Double Spin Asymmetry A_{LT} in Charged Pion Production from Deep Inelastic Scattering on a Transversely Polarized ^{3}He Target

by

Jin Huang

B.S., Univsersity of Science and Technology of China (2006)

Submitted to the Department of Physics
in partial fulfillment of the requirements for the degree of

Doctor of Philosophy in Physics

at the

MASSACHUSETTS INSTITUTE OF TECHNOLOGY

February 2012

Author .....
Department of Physics
October 21, 2011

Certified by .....
William Bertozzi
Professor of Physics
Thesis Supervisor

Certified by .....
Shalev Gilad
Principle Research Scientist
Thesis Co-Supervisor

Accepted by .....
Krishna Rajagopal
Associate Department Head for Education

Double Spin Asymmetry A_{LT} in Charged Pion Production from Deep Inelastic Scattering on a Transversely Polarized ^{3}He Target

by

Jin Huang

Submitted to the Department of Physics
on October 21, 2011, in partial fulfillment of the
requirements for the degree of
Doctor of Philosophy in Physics

Abstract

In this thesis I discuss the first measurement of the beam-target double-spin asymmetry A_{LT} for charged pion electroproduction in deep inelastic electron scattering on a transversely polarized ^{3}He target. These data were taken between October 2008 to February 2009 using a 5.9 GeV polarized electron beam at Thomas Jefferson National Accelerator Facility Experimental Hall A. The kinematics focused on the valence quark region, $0.16 < x < 0.35$ with $1.4 < Q^2 < 2.7\,\mathrm{GeV}^2$. The systematic uncertainties in this measurement due to acceptance, detector response drift, target density fluctuations and single spin asymmetries were suppressed to a negligible level by the frequent reversals of both beam helicity and target spin direction. Using the effective polarization approximation, the neutron A_{LT} asymmetries were extracted from the measured ^{3}He asymmetries and proton over ^{3}He cross section ratios.

The A_{LT} asymmetries probe the poorly known transverse momentum dependent parton distribution function g_{1T}^q, which describes the longitudinal polarization of quarks in a transversely polarized nucleon. The g_{1T}^q function requires an interference between wave function components differing by one unit of quark OAM, and therefore provide access to quark spin-orbit correlations in the nucleons. While the measured π^+ asymmetries are consistent with zero, these data indicate a positive azimuthal asymmetry for π^- production on ^{3}He and the neutron, which at leading twist leads to a non-zero g_{1T}^q. This work has laid the foundation for the future high precision mapping of the A_{LT} asymmetries, which is also discussed in this thesis.

Thesis Supervisor: William Bertozzi
Title: Professor of Physics

Thesis Co-Supervisor: Shalev Gilad
Title: Principle Research Scientist

Acknowledgments

Many people have helped me during my Ph. D. study, which made my journey to the finish line possible. At the beginning of my thesis, I want to express my deepest appreciation to them:

First of all, I want to thank my research advisors, William Bertozzi and Shalev Gilad, who offered me the intellectual freedom to pursue the research projects I enjoyed. I also appreciate the help and guidance I received from them during my course taking, the qualify exams, my Ph. D. research, thesis writing and finally the defense. In this process, Bill taught me how to become a good physicist while being happy every day, and Shalev have given me invaluable advices throughout every steps of my academic life. I am also grateful for the guidance I received from my academic advisors, Gunther Roland, and members of my thesis committee, William Donnelly and Ernest Moniz.

I also want to thank the E06-010 collaboration for this successful experiment and the opportunity for my thesis research. I would like to thank the co-spokespersons, Jian-ping Chen, Evaristo Cisbani, Haiyan Gao, Xiodong Jiang and Jen-Chieh Peng, for their leadership on this experiment, guidance on my work and advices on my career choices, especially for Jian-ping and Xiaodong who have supervised me through every step of my thesis work. I thank the postdocs of this experiment, Yi Qiang, Vincent Sulkosky, Andrew Puckett, Alexandre Camsonne, Brad Sawatzky and Bo Zhao, for their excellent service and kind help on my research, from the apparatus setup, data analysis to the publication. I wish the best of luck in their future endeavors to my fellow graduate students, Xin Qian, Kalyan Allada, Chiranjib Dutta, Joe Katich, Yi Zhang, Youcai Wang and Diana Parno. I will never forget the days and nights we worked together, which were filled with both challenges and fun. I would also like to thank the Hall A collaboration and the engineer divisions at Jefferson Lab, without whom this experiment would not have been possible.

I want to thank the Hall A SoLID collaboration for giving me the opportunity and honor to serve as the co-spokesperson for the newly approved experiment E12-

10-007. Your constant supports on this project are making this exciting measurement closer and closer to reality. I would like to thank Alexei Prokudin, Bernhard Musch, Barbara Pasquini, Alessandro Bacchetta, Rodolfo Sassot and Bo-Qiang Ma for kindly helping me understand the theory problem I bumped into and supporting both the past and future experiments that I have worked on. Meanwhile, I want to thank the APEX collaboration, especially Bogdan Wojtsekhowski, for the exciting test run in the summer of 2010, from which I experienced a direct search for new physics.

I want to thank other members of the MIT Nuclear Interaction Group, Yuan Xiao, Peter Monaghan, Xiaohui Zhan, Bryan Moffit, Navaphon Muangma, Nikos Sparveris, Kai Pan, Aidan Kelleher. I enjoyed very much the discussions we had and the work we did together. Our postdoc, Vincent Sulkosky and Aidan Kelleher reviewed this thesis and offered numerous valuable comments, and I am sincerely grateful for their help. And I would like to thank all my friends; life without you would be life without fun.

Finally, and most importantly, I would like to thank my parents, whose constant love cannot be matched with any word, and to thank my brilliant fiancee Yan for a happier future with a destination.

Contents

List of Figures

List of Tables

Nomenclature

A1	Short name for the Aerogel Cerenkov Detector used in Left-HRS during Experiment E06-010
ADC	analog-to-digital converter
AFP	adiabatic fast passage
amagat	density unit and 1 amagat is the gas density at 0°C and 1 atm pressure.
BCM	beam current monitor
beam-SSA	beam-SSA single spin asymmetry
BPM	Beam Position Monitor
BSPC	beam splitting polarizing cube
CEBAF	Continuous Electron Beam Accelerator Facility
CODA	CEBAF On-line Data Acquisition
CT	coincidence timing, also called coincidence time-of-flight, cTOF
cw	continuous-wave
DAQ	data acquisition
DIS	deep inelastic scattering
DSA	beam-target double spin asymmetry

DVCS	deeply virtual Compton scattering
E&M	Electromagnetic
EDT	electronic deadtime
EDTP	electronic deadtime pulse
EMC	European Muon Collaboration
EPICS	Experimental Physics and Industrial Control System
EPR	electron paramagnetic resonance
FAP	Coherent FAP (Fiber Array Package) laser system
FF	quark fragmentation function
FSI	final state interaction
GEM	Gas Electron Multiplier
GPD	generalized parton distribution
GTMD	generalized transverse-momentum dependent parton distributions
HRS	Hall A High Resolution Spectrometer
IHWP	insertable half-wave plate at the injector of CEBAF
Jefferson Lab	Thomas Jefferson National Accelerator Facility
JLab	Thomas Jefferson National Accelerator Facility
L1A signal	level-one-accept signal
LCCQM	light-cone constituent quark model
LCQDM	light-cone quark-diquark model
Left-HRS	Left High Resolution Spectrometer

LIR	Lorentz Invariance Relation
LO	leading-order
MLE	Maximum likelihood estimation
MRPC	Multi-gap Resistive Plate Chamber
MWDC	multi-wire drift chamber
NIM	Nuclear Instrumentation Module
NLO	next-to-leading order
NMR	nuclear magnetic resonance
nucleons	protons and neutrons
OAM	orbital angular momentum
parton	quark and gluon
PDF	parton distribution function
PID	Particle Identification
PID controller	proportional-integral-derivative controller
PMT	Photomultiplier Tube
psi	pound-force per square inch, approximately 6894 N/m^2
QCD	Quantum Chromodynamics
RICH	Ring Imaging Cerenkov Detector
SEOP	spin-exchange optical pumping
SIDIS	semi-inclusive deep inelastic scattering

SIMC	Hall C Monte Carlo code, which was updated to study the SIDIS process for the E06-010 experiment
SLAC	Stanford Linear Accelerator Center
SoLID	Solenoidal Large Intensity Device
srf	superconducting radiofrequency
target-SSA	target single spin asymmetry
TDC	time to digital converter
TMD	Transverse Momentum Dependent parton distributions
TOF	time-of-flight
VDC	vertical drift chamber
WW	Wandzura-Wilczek approximation

Chapter 1

Introduction

1.1 Nucleon Structure

The majority of the directly visible mass in the universe is contributed by nucleons (protons and neutrons). Therefore, nucleons are naturally a suitable object for our curiosity and dedicated studies. The fact, that a nucleon is not a point like particle but has substructure, was first indicated by their large anomalous magnetic moment [1]. More than half a century ago, the proton's finite radius is directly confirmed using electron scattering by the Nobel-prize-wining work of Hofstadter, *et.al.* [2]. In the 1950s and 1960s, a variety of hadrons was observed with multi-GeV accelerators, which lead to the birth of the quark model that hadrons are composed of more elementary spin one-half particles with fractional charges [3, 4]. In this model, a nucleon is made of three quarks as shown in Fig. 1-1a. The high energy electron scattering experiment at Stanford Linear Accelerator Center (SLAC) provided direct experimental probes to the nucleon's substructure, which supported the interpretation that the electrons were scattering off point like spin one-half constituents (partons) at large momentum transfers [5]. In the 1970's, the nucleon was further described by a new field theory called Quantum Chromodynamics (QCD), the contemporary standard theory that describes the strong interactions of colored quarks and gluons. As shown in Fig. 1-1b, gluons bond quarks together to form nucleons (as well as other hadrons). Currently neither quarks nor gluons have been observed as free particles.

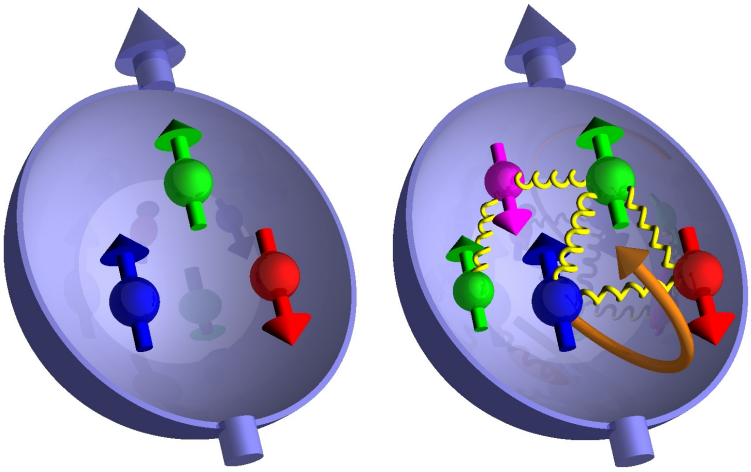

(a) (b)

Figure 1-1: Illustration of nucleon structure. (a): valence quarks only. (b): a more complete picture with gluons, sea quarks and the orbital motion of partons. These figures are from Ref. [8].

Although the QCD Lagrangian can be easily written down [6], the coupling constant of QCD α_S is large at the low energy scale of the nucleon system [7]. Therefore, the first principles of QCD can not be directly used to calculate nucleon structure. Meanwhile, due to the strong couplings, the QCD field energy and the quark kinetic energy accounts for most of the mass of the nucleon. Therefore, the experimental study of nucleon structure is still critical to test QCD in the low energy scale region and to understand the visible matter around us.

1.2 Experimental Probes for Nucleon Structure

Various experimental probes have been used to study the nucleon structure:

Electromagnetic (E&M) probes include charged lepton scattering (discussed in the following section) and the Drell-Yan process [9]. For both process the nucleon system is probed via virtual photons γ^*, which couple to the quark and lepton currents. In the Drell-Yan process, a quark and antiquark from two hadronic initial particles annihilate electromagnetically. Then a lepton-antileption pair is produced, which carries the information of the annihilating quarks. It is closely

related to E&M lepton scattering through a rotation in the time order.

Strong interaction probes utilize parton-parton scattering in hadron-hadron collisions to study the structure of the initial hadrons. Jets or particles (e.g. lepton, photon or meson) with a large transverse momentum are usually observed in the final state. The strong probes provide unique opportunities to study the gluon properties in nucleons, which are not directly observed in the E&M or weak processes.

Weak interaction probes study nucleon structure through the exchange of virtual W or Z bosons during the lepton nucleon scattering and through W or Z production in hadron-hadron collisions, which resembles the corresponding process with the E&M probes. The reactions involving W exchange are related to different quark flavor combinations compared to those with Z or γ^* exchange, and therefore provide complementary information on the flavor decomposition.

The following discussion in this Chapter will focus on the experimental study of the nucleon structure using lepton-nucleon scattering through E&M interactions, which is the process used by the experiment discussed in this thesis.

1.3 Unpolarized DIS and the Longitudinal Momentum Structure of Nucleon

As one of the most important experimental tools to study the nucleon structure, high energy leption-nucleon scattering, in particular deep inelastic scattering (DIS), has been extensively used to determine the structure of nucleon in the terms of its constituents (partons) and as an important testing ground for QCD. In the lepton-nucleon scattering, $\ell(l)+N(P) \to \ell(l')+X$, a lepton ($\ell$) scatters from a nucleon (N) with mass M, with four-momentums of the particles being denoted in the parentheses. In the single photon exchange approximation (Born approximation), a virtual photon is exchanged between the lepton and the nucleon with four-momentum transfer $q = l - l'$.

This process is referred to as DIS when the scattered electron is detected and the kinematics satisfy the deep (the four momentum transfer squared $Q^2 \equiv -q^2 \gg M^2$) inelastic (the virtual photon-nucleon invariant mass $W \equiv \sqrt{l - l' + P} \gg M$) criteria.

DIS is a particular useful tool to study the partonic structure of the nucleon. In the limit of large energy and four momentum transfer, the kinematic dependence of the DIS cross section was found to experimentally resemble that for elastic scattering off point-like charged particles. This feature of the DIS cross section is referred to as the Bjorken scaling [5]. The Bjorken scaling variable $x_{Bj} = \frac{Q^2}{2\,P\cdot q}$ is defined so that in a frame in which the nucleon's momentum is large, it represents the fraction x of the nucleon's momentum carried by the quark struck by the virtual photon. The number density of quarks in the nucleon with a longitudinal momentum of $x \cdot P$ is described by the unpolarized collinear parton distribution function (PDF) $q(x)$ or $f_1^q(x)$. In the simple parton model, the unpolarized DIS cross section is just the sum of scattering from individual quarks weighted by $q(x)$.

When the energy and momentum transfer is finite, this simple picture is modified by hard gluons radiated from the quark, which leads to a violation of the Bjorken scaling in a logarithmic order. At large Q^2 and small x, more gluons are radiated and produce into $q\bar{q}$ pairs and therefore changes the PDF. As an intuitive interpretation of this phenomena, the virtual photons at low Q^2 have larger wavelength and can not discern the detailed structure in the nucleon system; while Q^2 increases, the fine structure of the bare partons, in both time and space scales, begins to appear. In the framework of QCD, a scale dependent PDF is used to describe this mechanism, i.e., $q(x) \to q(x,\, Q^2)$. The Q^2-evolution of the PDF (relating $q(x,\, Q_1^2)$ and $q(x,\, Q_2^2)$) is described by the DGLAP equation [10, 11, 12, 13], and has been tested with data up to five orders of magnitude in the Q^2 coverage [6].

Many DIS experiments have been performed to study the parton momentum distribution inside the nucleons over the last forty years [6]. The $q(x)$ PDFs have been extracted using global analyses [23, 24, 25, 14], with additional complementary data from the related hard-scattering processes initiated by nucleons (e.g. Drell-Yan process, jet, W and Z production in hadron colliders). As an example, the MSTW 2008

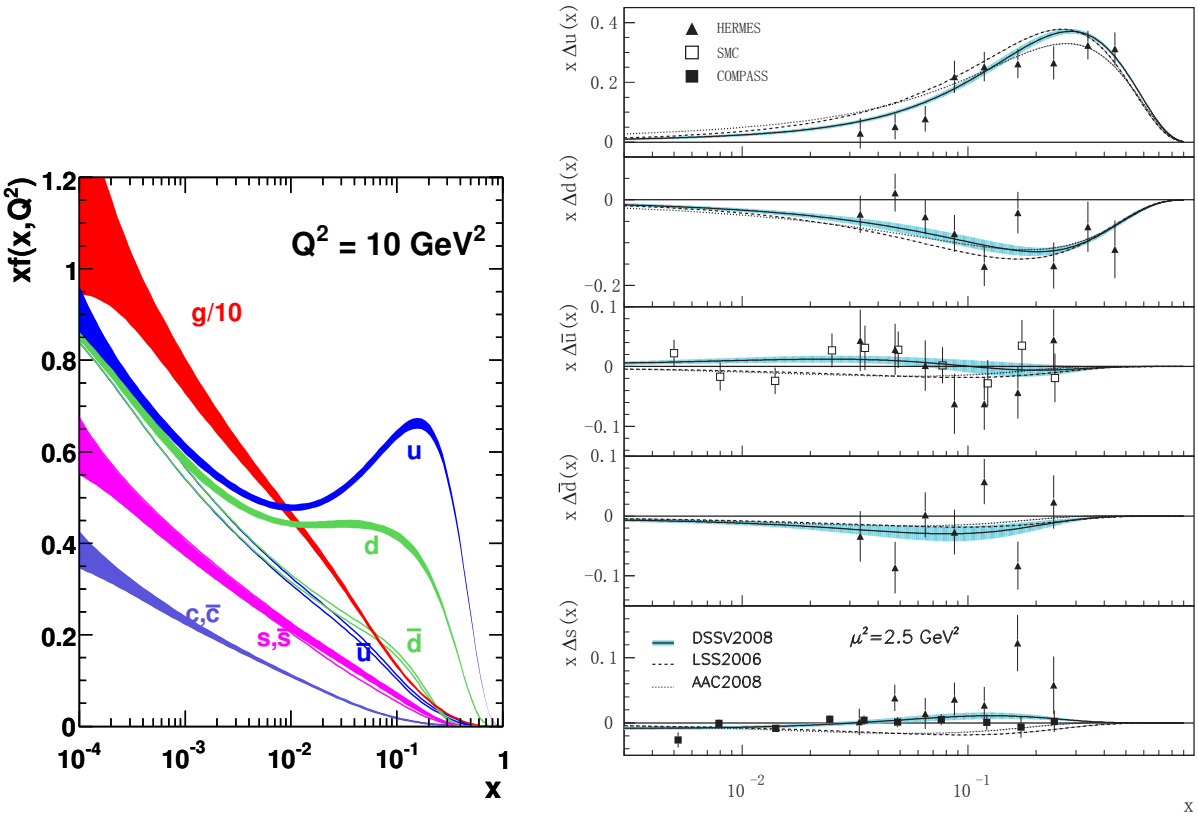

(a) (b)

Figure 1-2: The x times the (a) unpolarized and (b) polarized collinear PDF plotted against x. (a): $x \cdot q(x)$ from the MSTW 2008 NLO parametrization for different quark flavors and for gluons [14]. The width of the band represents the 68% (1σ) confidence level uncertainty. (b): $x \cdot \Delta q(x)$ from the global analysis (LSS2006 [15], AAC2008 [16] and DSSV2008 [17, 18]) and the semi-inclusive DIS data (HERMES [19, 20], SMC [21] and COMPASS [22]) at $Q^2 = 2.5\,\mathrm{GeV}^2$. The figure is taken from Ref. [6].

global fit and its uncertainty for $x \cdot q(x)$ at $Q^2 = 10$ GeV^2 is shown in Fig. 1-2a. The typical kinematic range for the global analyses covered five orders of magnitudes in both x and Q^2 [6].

1.4 Polarized DIS and Spin Structure of Nucleon

Like rest mass and charge, spin is a fundamental property of particles. Nucleons are spin one-half particles. Its spin structure, in terms of the parton spin and their orbital angular momentum, presents challenges for both the experimental and theoretical

studies, but with enriched rewards. The DIS process with both polarized leptons and nucleons has been one of the major experimental tools to study the nucleon spin structure.

The polarization of the initial lepton is transferred to the virtual photon that is exchanged between the lepton and the quark in the nucleon. Consider a nucleon whose spin is longitudinal, i.e., either parallel or antiparallel to that of the virtual photon momentum, the virtual photon can only be absorbed by its quark constituents with antiparallel helicity. Therefore, in the picture of the simple quark model, the difference in the number density of quarks with opposite helicity states, which is described by the polarized collinear PDF $\Delta q(x)$ or $g_1^q(x)$, can be extracted by forming the DIS cross section difference for leptons or nucleons with opposite spin. To help tag the flavor of the quark interacted with the virtual photon (struck quark), a final state hadron can be detected in coincidence with the scattered lepton in the semi-inclusive DIS (SIDIS, further discussed in Sec. 2.2.1).

In the 1980s, the European Muon Collaboration (EMC) collaboration measured Δq using DIS with a longitudinal polarized muon beam and a hydrogen target [26]. This measurement suggested that a surprising small fraction of the nucleon spin is carried by quarks. This observation is known as the "proton spin crisis" and stimulated intensive experimental and theoretical investigations. In the contemporary decompositions of the nucleon spin ("light-cone decomposition" in Ref. [27] or gauge invariant Ji's decomposition in Ref. [28]), total longitudinal spin can have contributions from the helicity of quarks, quark angular momentum and from gluons. The quark helicity distribution was extracted from the global analysis using inclusive polarized DIS data, and results from polarized pp scattering as shown in Fig. 1-2b. The current world data covered a range of approximately $x = 0.001 \sim 1$, the integrated spin contribution from the quark helicity was extracted $\Delta\Sigma^{[0.001\to1]} = \sum_q \int_{0.001}^1 dx\, \Delta q(x) = 0.366^{+0.042}_{-0.062}$ at $Q^2 = 10$ GeV^2 as concluded in the global analysis as discussed in Refs. [17, 18]. The same global study suggested that the spin contribution from the gluon helicity is also small. Therefore, the remaining piece of the spin puzzle, the contributions from the parton orbital angular momentum (OAM) have to be significant.

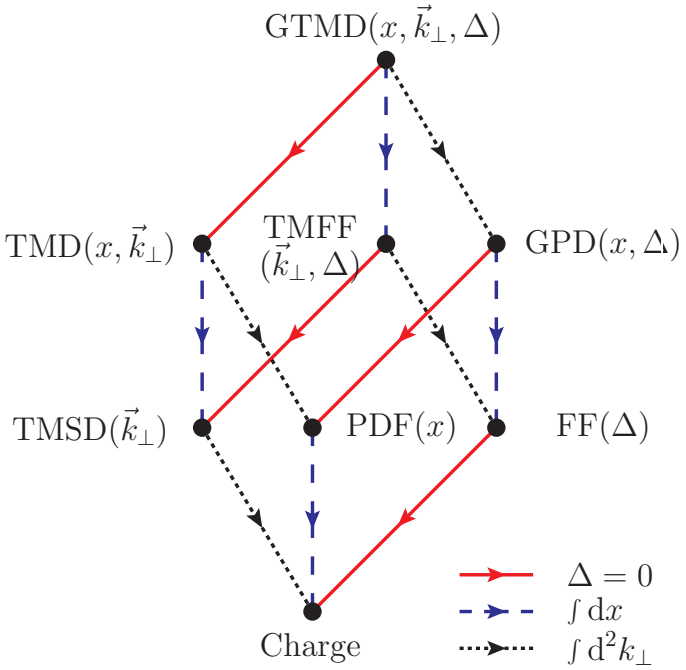

Figure 1-3: Representation of the projections of the GTMDs into parton distributions and form factors. The arrows correspond to different reductions in the hadron and quark momentum space: the solid (red) arrows give the forward limit in the hadron momentum, the dotted (black) arrows correspond to integrating over the quark transverse-momentum and the dashed (blue) arrows project out the longitudinal momentum of quarks. See text for the distributions. This figure is from Ref. [32], where the quark transverse momentum $\boldsymbol{p}_T$ is presented as $\vec{k}_\perp$.

1.5 Multidimensional Structure of Nucleon

To complete the picture of the nucleon structure, studies are required that go beyond the collinear PDF, which is integrated over the transverse dimension. In particular, a non-zero quark OAM indicates that quarks move in three dimensional space and therefore have non-zero transverse motion. The ultimate understanding of the partonic structure of the nucleon is the Wigner distributions $W_\Gamma(x, \boldsymbol{p}_T, \boldsymbol{r})$ [29, 30, 31], which can be also connected to the generalized transverse-momentum dependent parton distributions, GTMD$(x, \boldsymbol{p}_T, \Delta)$ [32]. Here, $\boldsymbol{p}_T$ is the transverse momentum, $\boldsymbol{r}$ is the phase-space position and Δ is the 4-momentum which is transferred by the probe to the hadron.

Wigner distributions and GTMD can be projected to generalized parton distri-

butions (GPDs), transverse-momentum dependent parton distributions (TMDs) and generalized form factors (TMFFs) as shown in Fig. 1-3. Although there is no known experiment at the moment that is capable of measuring them in the full unprojected phase space, GPDs and TMDs, which describe the parton's distribution in transverse coordinate and momentum space, respectively, can be experimentally studied. Both GPDs and TMDs provide three dimensional information of the nucleon system beyond the collinear picture and are complementary to each other. GPDs can be measured using, among others, the deeply virtual Compton scattering (DVCS) [33]; TMDs, which are experimentally studied using mainly the SIDIS and Drell-Yan process, will be discussed in details in the following chapter. Further following the cubic diagram of Fig. 1-3, projections of these distributions yields the standard collinear PDFs, form factors (FFs) which describe the charge and magnetic distributions in the nucleon, and the transverse-momentum dependent spin densities (TMSD). The nucleon charge (as well as its total momentum and spin) is the common limit for all of these distributions.

Systematic experimental studies on the nucleon multidimensional structure have just been started in the recent years [34]. The experiment discussed in this thesis contributes a unique piece of information to this global effort: this study provides the first SIDIS data using an effectively polarized neutron target (a polarized ^{3}He target) to probe the g_{1T} TMD distribution, which describe the longitudinal quark polarization in a transversely polarized nucleon. It also laid the foundation for the future experimental studies with much a higher precision and phase space coverage [35, 36].

Chapter 2

Physics Motivation

2.1 Transverse Momentum Dependent Parton Distribution (TMD)

A new phase of investigation of the nucleon structure has been started by studying physical observables that are sensitive to the transverse momentum structure of nucleons. This information is encoded in the Transverse Momentum Dependent parton distributions (TMDs), which describe the spin-correlated three-dimensional momentum[1] structure of the nucleon's quark and gluon constituents [37, 38]. At leading twist (twist-two), there are eight quark TMD distributions that can be grouped with their characteristic quark and nucleon spin combinations as shown in Table 2.1. They depend not only on the longitudinal momentum fraction x but also on the transverse momentum $\boldsymbol{p}_T$, thus providing a 3-dimentional description of the nucleon structure. The nomenclature of the distribution functions (also in Table 2.1) follows closely that of Ref. [37], which is sometimes referred to as "Amsterdam notation": f refers to unpolarized target; g and h to longitudinally and transversely polarized quark, respectively; a subscript 1 is given to the twist-two functions; subscripts L or T refer to the connection with the nucleon spin being longitudinal or transverse; and a symbol

[1]The three-dimensional momentum consists of the longitudinal momentum fraction, x, and the 2-D transverse momentum, $\boldsymbol{p}_T$.

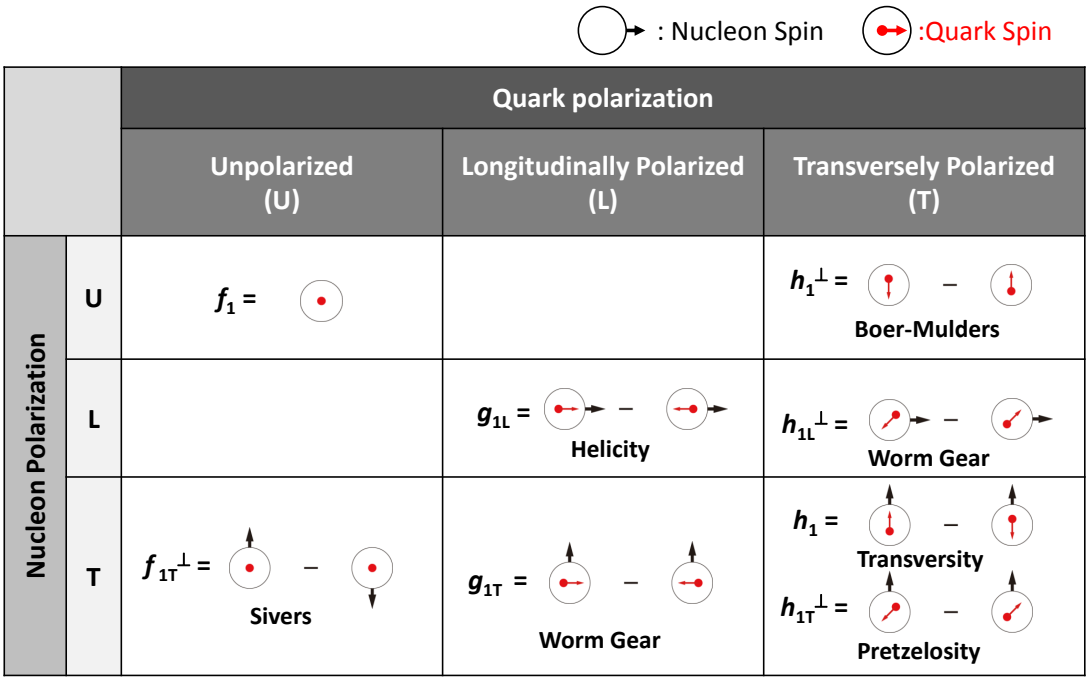

Table 2.1: Categorization and the intuitive probabilistic interpretation of all leading-twist transverse momentum distributions. The red arrows indicate the spin direction of the quarks and the black arrows indicate the spin direction of the parent nucleon. In the semi-inclusive deep-inelastic lepton-nucleon scattering (Sec. 2.2), the longitudinal direction defined along the momentum transfer of the probe (virtual photon) is horizontal in the paper.

$\perp$ signals the explicit presence of transverse momenta[2].

In the quark model, these quark TMD distributions have probabilistic interpretations, which are illustrated in Table 2.1:

- f_1, describes the probability of finding an unpolarized quark inside an unpolarized nucleon with longitudinal quark momentum fraction x and transverse momentum p_T.

- Similarly, helicity g_{1L} describes the probability of finding a longitudinally polarized quark inside a longitudinally polarized nucleon.

[2]There are a few exceptions traditionally accepted in the literature: the $\perp$ sign for the T-even and Chiral-even TMD, g_{1T}, is traditionally not included. In addition, g_{1L} is occasionally referred as g_1, following the notation for its collinear counterpart PDF $g_1(x)$ and the transversity h_1 do not contain "T" although it is related with a transversely polarized nucleon.

- In the case that both the quark spin and the nucleon spin are transverse, transversity h_1 describes the probability that their spins are along the same direction, while pretzelosity $h_{1T}^{\perp}$ describes the probability that their spins are perpendicular to each other.

- In a transversely polarized nucleon, there is certain probability that the quark with a non-zero transverse momentum is found polarized longitudinally and unpolarized, which are described by trans-helicity g_{1T} and the Sivers function $f_{1T}^{\perp}$, respectively.

- The transverse polarization of quark in a unpolarized and longitudinally polarized nucleon are described by the Boer-Mulders function $h_1^{\perp}$ and long-transversity $h_{1L}^{\perp}$, respectively.

More precisely, these eight TMDs are defined in using the decomposition of the quark-quark correlation function which contain a full description of the quarks distribution inside the nucleon. This is briefly summarized in Appendix A.1 and is shown in Refs. [37, 38] and in a review [39].

Three of the eight TMDs survive after integration over $\boldsymbol{p}_T$. Their integrals are related to the corresponding collinear PDFs:

$$q(x) = \int d^2\boldsymbol{p}_T f_1\left(x, p_T^2\right) , \tag{2.1}$$

$$\Delta q(x) = \int d^2\boldsymbol{p}_T g_{1L}\left(x, p_T^2\right) , \tag{2.2}$$

$$\Delta_T q(x) = \int d^2\boldsymbol{p}_T h_1\left(x, p_T^2\right) , \tag{2.3}$$

The other five vanish when integrated over $\boldsymbol{p}_T$ and therefore provide novel information regarding the transverse motion of the quarks. $h_1^{\perp}$ and $f_{1T}^{\perp}$ are odd under naive time reversal (naive T-Odd), i.e., merely the direction of all momenta and spins are reversed, without interchanging the initial and final states; the rest of the six TMDs are T-even. Combining the wealth of information from all these TMD distributions is invaluable for understanding the spin-orbit correlations in the nucleon wave function

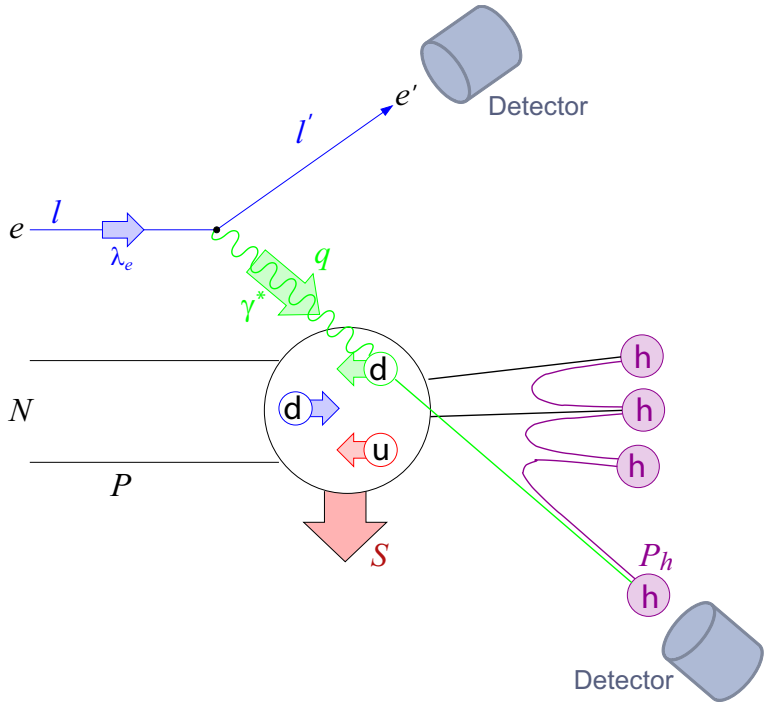

Figure 2-1: A schematic of the semi-inclusive deep inelastic scattering process using an electron beam (less or more hadron final state particles (h) can be produced). In the configuration for this experiment, the target is polarized transverse to the beam and the longitudinal quark polarization is probed using polarized electron beam. See text and Eq. (2.4) for definition of the symbols.

and thus provide important information about the quark orbital angular momentum [40], constraining an important part of the nucleon spin sum rule [27].

2.2 Semi-Inclusive Deep Inelastic Scattering (SIDIS)

2.2.1 Introduction

In recent years, semi-inclusive deep-inelastic lepton-nucleon scattering (SIDIS) and the Drell-Yan process have been recognized as direct experimental probes for TMDs [34]. In the SIDIS process,

$$\ell(l) + N(P) \to \ell(l') + h(P_h) + X\,, \tag{2.4}$$

a lepton (ℓ) scatters from a nucleon (N) and is detected in coincidence with a leading hadron (h)[3] with particle four-momenta denoted by l, P, l' and P_h, respectively, as shown in Fig. 2-1. The detected hadron carries the information of flavor, transverse momentum and the spin of the struck quark in the nucleon through a fragmentation process, which is described by fragmentation functions which will be discussed in Sec. 2.3.2. M and M_h are the masses of the nucleon and of the detected hadron h, respectively. The kinematic variables used in this thesis are defined following closely the notation used in the review work of Ref. [41]:

- $q = l - l'$, the four momentum transfer, and $Q^2 = -q^2$, four momentum transfer squared
- $x = \frac{Q^2}{2\,P\cdot q}$, the fraction of the nucleon's momentum carried by the struck quark in the parton model, which is called the Bjorken scaling variable[4]
- $y = \frac{P\cdot q}{P\cdot l}$, the fraction of the lepton's energy loss in the nucleon rest frame
- $z = \frac{P\cdot P_h}{P\cdot q}$, the fraction of the energy transfer carried by the observed hadron
- $W = \sqrt{l - l' + P}$, the virtual photon-nucleon invariant mass
- $W' = \sqrt{l - l' + P - P_h}$, the missing mass
- $\varepsilon = \frac{1-y-\frac{1}{4}\gamma^2 y^2}{1-y+\frac{1}{2}y^2+\frac{1}{4}\gamma^2 y^2}$, the ratio of longitudinal and transverse photon flux, where $\gamma = \frac{2Mx}{Q}$

The helicity of the lepton beam is denoted by λ_e. In the case that the polarization for the scattered lepton is unspecified, the cross section related to the transverse polarization for the lepton beam is suppressed kinetically by one over the lepton's Lorentz factor $1/\gamma_e$ [42], which is negligible with respect to the sensitivity of the E06-010 experiment and is not considered in the following discussions. S_L and S_T

[3]leading hadron carries a large portion of the moment of the struck quark, and pass out information including the quark's flavor and transverse momentum.

[4]In the discussion of SIDIS process using the parton model, the fraction of the nucleon's momentum carried by the quark struck and the Bjorken scaling variable coincide. Therefore, the difference in notation is dropped for the following discussion. The same arguments are also applied to z.

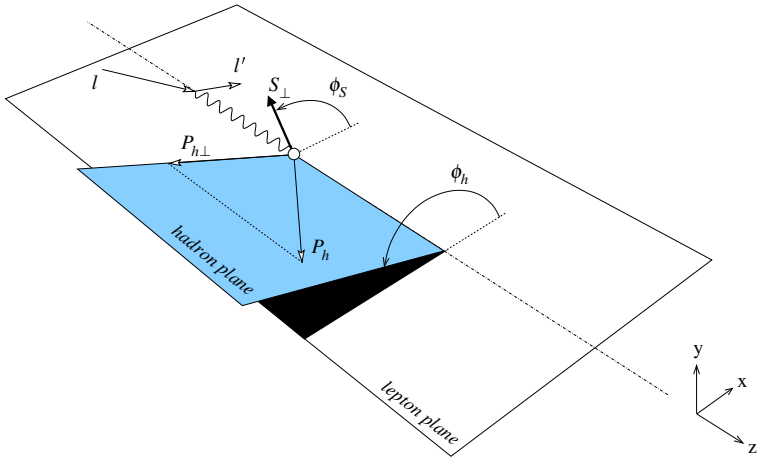

Figure 2-2: The Trento Conventions: Definition of azimuthal angles for SIDIS in the target rest frame [43]. $P_{h\perp}$ and $S_\perp$ (denoted as S_T in this thesis) are the components of P_h and S that transverse to the photon momentum.

are the longitudinal and the transverse target polarization, respectively. They are defined with respect to the virtual photon direction[5].The sign convention for the longitudinal spin component is such that the target spin is parallel to the virtual photon momentum for $S_L = -1$. The azimuthal and polar angles are defined as,

- ϕ_h (the azimuthal angle of the outgoing hadron) and ϕ_S (the azimuthal angle of target spin) are defined following the Trento conventions [43], which is shown in Fig. 2-2.

- $\theta_S \equiv \arctan\left(-\left|S_T\right|/S_L\right)$ is the polar angle of target spin[6].

2.2.2 Structure Functions and Asymmetries

Assuming single photon exchange, the lepton-hadron cross section can be expressed in a model-independent way by a set of structure functions (SFs). They can be measured experimentally. We follow the notation of reference [41] and define the

[5]In some literature (e.g., Ref. [41]), the notation of $S_\parallel$ and $S_\perp$ are used instead.

[6]$\theta_S \equiv \pi/2$ for a transversely polarized target with respect to the virtual photon, i.e., $S_L = 0$ and $|S_T| > 0$. $\theta_S \equiv 0, \pi$ for a longitudinally polarized target with respect to the virtual photon, i.e., $S_L = -1, +1$.

structure function as

$$
\begin{aligned}
\frac{d\sigma}{dx\,dy\,d\psi\,dz\,d\phi_h\,dP_{h\perp}^2} \;=\; & \frac{\alpha^2}{xyQ^2}\,\frac{y^2}{2\,(1-\varepsilon)}\left(1+\frac{\gamma^2}{2x}\right)\times \\
& \Big\{ F_{UU,T} + \varepsilon\, F_{UU,L} + \sqrt{2\,\varepsilon(1+\varepsilon)}\,\cos\phi_h\, F_{UU}^{\cos\phi_h} \\
& + \varepsilon\cos(2\phi_h)\, F_{UU}^{\cos 2\phi_h} + \lambda_e \sqrt{2\,\varepsilon(1-\varepsilon)}\,\sin\phi_h\, F_{LU}^{\sin\phi_h} \\
& + S_L \left[\sqrt{2\,\varepsilon(1+\varepsilon)}\,\sin\phi_h\, F_{UL}^{\sin\phi_h} + \varepsilon\sin(2\phi_h)\, F_{UL}^{\sin 2\phi_h} \right] \\
& + S_L\lambda_e \left[\sqrt{1-\varepsilon^2}\, F_{LL} + \sqrt{2\,\varepsilon(1-\varepsilon)}\,\cos\phi_h\, F_{LL}^{\cos\phi_h} \right] \\
& + |S_T| \Bigg[\sin(\phi_h-\phi_S)\left(F_{UT,T}^{\sin(\phi_h-\phi_S)} + \varepsilon\, F_{UT,L}^{\sin(\phi_h-\phi_S)} \right) \\
& + \varepsilon\,\sin(\phi_h+\phi_S)\, F_{UT}^{\sin(\phi_h+\phi_S)} + \varepsilon\,\sin(3\phi_h-\phi_S)\, F_{UT}^{\sin(3\phi_h-\phi_S)} \\
& + \sqrt{2\,\varepsilon(1+\varepsilon)}\,\sin\phi_S\, F_{UT}^{\sin\phi_S} \\
& + \sqrt{2\,\varepsilon(1+\varepsilon)}\,\sin(2\phi_h-\phi_S)\, F_{UT}^{\sin(2\phi_h-\phi_S)} \Bigg] \\
& + |S_T|\lambda_e \Bigg[\sqrt{1-\varepsilon^2}\,\cos(\phi_h-\phi_S)\, F_{LT}^{\cos(\phi_h-\phi_S)} \\
& + \sqrt{2\,\varepsilon(1-\varepsilon)}\,\cos\phi_S\, F_{LT}^{\cos\phi_S} \\
& + \sqrt{2\,\varepsilon(1-\varepsilon)}\,\cos(2\phi_h-\phi_S)\, F_{LT}^{\cos(2\phi_h-\phi_S)} \Bigg] \Big\}
\end{aligned}
\tag{2.5}
$$

All eight leading-twist TMD distributions can be accessed in SIDIS through these structure functions, which will be discussed in the following sections. The spin-dependent TMD distributions also lead to dependencies of the SIDIS cross-section on the hadron and the target spin azimuthal angles, i.e. non-zero polarized and/or azimuthal angle dependent structure functions. Azimuthal asymmetries with characteristic spin combinations and angular modulations are typically used to isolate the corresponding structure functions from the rest of the cross section terms (e.g. see discussion in Sec. 2.5.1).

The SIDIS asymmetries were first observed by SMC [44], HERMES [45, 46] and

CLAS [47, 48]. Further studies were performed both with transversely polarized targets by HERMES (proton) [49, 50], COMPASS (deuteron, proton) [51, 52, 53] and Jefferson Lab Hall A (^{3}He, this thesis) [54] and with longitudinally polarized targets by HERMES (proton, deuteron) [55, 56], COMPASS (deuteron) [57] and CLAS (proton) [58]. Nevertheless with the precision of the current world data, our knowledge of the TMDs is still very limited. Pioneering global analyses using SIDIS and e^+e^- data have been performed on the transversity and Sivers functions [59, 60]. However, limited by the available data, the current studies still depend heavily on the model assumptions. Therefore the fundamental properties of nucleon which are probed by TMDs (e.g. the Tensor Charge which is the lowest x moment of h_1^q [61]), are still poorly constrained. Future high statistics measurements have been planned to precisely study them [35, 36].

2.3 Interpreting SIDIS Cross Section using TMDs

2.3.1 Factorization Theorems

Several factorization theorems of the SIDIS cross section have been developed to interpret the SIDIS cross section. The applicable kinematic region for each theorem is closely related to the hadron transverse momentum by comparing to the photon-mass scale, Q, and the QCD scale, $\Lambda_{QCD} \approx 0.2$ GeV [62].

- When the transverse momentum is integrated over or when it is comparable to the hard photon-mass scale, $P_{h\perp} \sim Q$ and $\alpha_S(Q) \ll 1$, the cross sections can be calculated from the standard perturbative QCD formalism similar to inclusive DIS and parton distributions [63].

- In the case of $Q \gg P_{h\perp} \gg \Lambda_{QCD}$, the cross section can be calculated again with integrated parton distributions augmented by small non-perturbative QCD corrections [64, 65, 66].

- For the low $P_{h\perp}$ region of this thesis experiment, $Q \gg P_{h\perp} \sim \Lambda_{QCD}$, the SIDIS

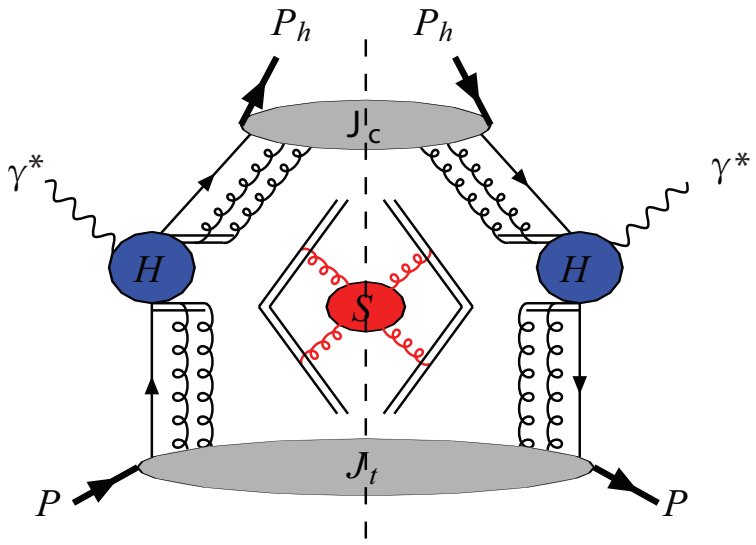

Figure 2-3: The leading region for SIDIS after soft and collinear factorizations at low $P_{h\perp}$ [67]. H (S) is the sub-diagram for the hard-interaction vertex (soft-gluon radiations). J_t (J_C) is the target (current) fragmentation jet.

cross section can be factorized into

- the TMDs, as discussed in Sec. 2.1,
- the transverse momentum dependent quark fragmentation function (FF) depending on, among others, the hadron momentum fraction z,
- the contribution H of parton hard scattering
- and the soft factor, which comes from soft-gluon radiations and is defined by a matrix element of Wilson lines in a QCD vacuum. [67, 68].

This factorization is illustrated in Fig. 2-3. Ref. [67] argues that factorization is valid to all orders of α_s. In addition, recent work [66] showed that the last two mechanisms (for $Q \gg P_{h\perp} \gg \Lambda_{QCD}$ and for $Q \gg P_{h\perp} \sim \Lambda_{QCD}$) are consistent in the overlap region for $P_{h\perp}$.

The experimental tests of the factorization theorems are still in the early stage. At leading order (LO) of α_S, an assumption of a naive $x - z$ factorization, i.e., assuming the SIDIS cross section can be described using the product of PDF $f(x)$ and fragmentation function $D(z)$, has been used by a number of collaborations (SMC,

HERMES, COMPASS, JLab, etc.; example refs are [20, 69]) to extract PDFs and FFs. The evidence for the z independence of the measured ratio of $(\bar{d}-\bar{u})/(u-d)$ in the range of $0.3 < z < 0.8$ was reported by the HERMES collaboration [70]; further studies [71] suggested a weak z-dependence, which can be attributed mainly to the next LO (NLO) effect. At Jefferson Lab, data from Hall C [72, 73, 74] with $0.35 < z < 0.65$ and from CLAS [47] in the region of $0.1 < x < 0.4$ and $0.5 < z < 0.8$ are consistent with the $x - z$ factorization.

2.3.2 Transverse Momentum Dependent Quark Fragmentation Functions

In the low $P_{h\perp}$ SIDIS factorization (at region of $Q \gg P_{h\perp} \sim \Lambda_{QCD}$) as discussed above, the transverse momentum dependent quark fragmentation functions (FFs) describe how the struck quark forms a final state hadron. They are functions of the fractional momentum z of the hadron and the transverse momentum $\boldsymbol{K}_T$ of the final-state hadron relative to the fragmenting quark. They can be defined using the parametrization of the fragmentation correlation function [37, 41], using a similar procedure as that for decomposing the quark-quark correlator as Eq. (A.2). Two leading-twist FFs contribute to the SIDIS spin-zero hadron production:

- the spin-independent FF, D_1, has an intuitive interpretation of a probability density of z and $\boldsymbol{K}_T$ for the final state hadron.

- the spin-dependent Collins FF [75], $H_1^\perp$, correlates the transverse spin of the fragmenting quark to the transverse momentum of the produced hadron. Moreover being chiral odd, the Collins function can be connected with, among others, the transversity distribution function, which is chiral odd too. Thus Collins FF can allow the measurement of this otherwise elusive property of the nucleon in SIDIS, which carries valuable information about the dynamics of confined quarks.

Besides, SIDIS data, the FFs can also be extracted from e^+e^- experimental data. Global analyses has been performed to extract $D_1(z, Q^2)$ as in Ref. [76, 77]. In the

recent years, H_1 has been studied using fit over global data as discussed in Ref. [78, 59, 79], although heavy assumptions were made during the study due to the scarce of experimental data. Moreover, the details of the K_T-dependence of FFs still remain unknown.

2.3.3 SIDIS Structure Functions in the Simple Quark Model

Under the low $P_{h\perp}$ factorization scheme as discussed in Sec. 2.3.1, the structure functions in Eq. (2.5) are parameterized as convolutions of TMD parton distribution functions with the transverse momentum dependent fragmentation functions [37, 38, 41]. The leading twist structure functions are listed below with quark interpretation at leading order; the complete list for all 18 structure functions can be found in Ref. [41].

$$F_{UU,T} = \left[f_1 \otimes D_1\right], \tag{2.6}$$

$$F_{UU,L} = 0, \tag{2.7}$$

$$F_{UU}^{\cos 2\phi_h} = \left[-\frac{2\left(\hat{\boldsymbol{h}}\cdot\boldsymbol{k}_T\right)\left(\hat{\boldsymbol{h}}\cdot\boldsymbol{p}_T\right)-\boldsymbol{k}_T\cdot\boldsymbol{p}_T}{MM_h}h_1^\perp \otimes H_1^\perp\right], \tag{2.8}$$

$$F_{UL}^{\sin 2\phi_h} = \left[-\frac{2\left(\hat{\boldsymbol{h}}\cdot\boldsymbol{k}_T\right)\left(\hat{\boldsymbol{h}}\cdot\boldsymbol{p}_T\right)-\boldsymbol{k}_T\cdot\boldsymbol{p}_T}{MM_h}h_{1L}^\perp \otimes H_1^\perp\right], \tag{2.9}$$

$$F_{LL} = \left[g_{1L} \otimes D_1\right], \tag{2.10}$$

$$F_{UT,T}^{\sin(\phi_h-\phi_S)} = \left[-\frac{\hat{\boldsymbol{h}}\cdot\boldsymbol{p}_T}{M}f_{1T}^\perp \otimes D_1\right], \tag{2.11}$$

$$F_{UT,L}^{\sin(\phi_h-\phi_S)} = 0 \tag{2.12}$$

$$F_{UT}^{\sin(\phi_h+\phi_S)} = \left[-\frac{\hat{\boldsymbol{h}}\cdot\boldsymbol{k}_T}{M_h}h_1 \otimes H_1^\perp\right], \tag{2.13}$$

$$F_{UT}^{\sin(3\phi_h-\phi_S)} = \left[\frac{2\left(\hat{\boldsymbol{h}}\cdot\boldsymbol{p}_T\right)\left(\boldsymbol{p}_T\cdot\boldsymbol{k}_T\right)+\boldsymbol{p}_T^2\left(\hat{\boldsymbol{h}}\cdot\boldsymbol{k}_T\right)-4\left(\hat{\boldsymbol{h}}\cdot\boldsymbol{p}_T\right)^2\left(\hat{\boldsymbol{h}}\cdot\boldsymbol{k}_T\right)}{2M^2M_h} \times h_{1T}^\perp \otimes H_1^\perp\right], \tag{2.14}$$

$$F_{LT}^{\cos(\phi_h-\phi_S)} = \left[\frac{\hat{\boldsymbol{h}}\cdot\boldsymbol{p}_T}{M}g_{1T} \otimes D_1\right], \tag{2.15}$$

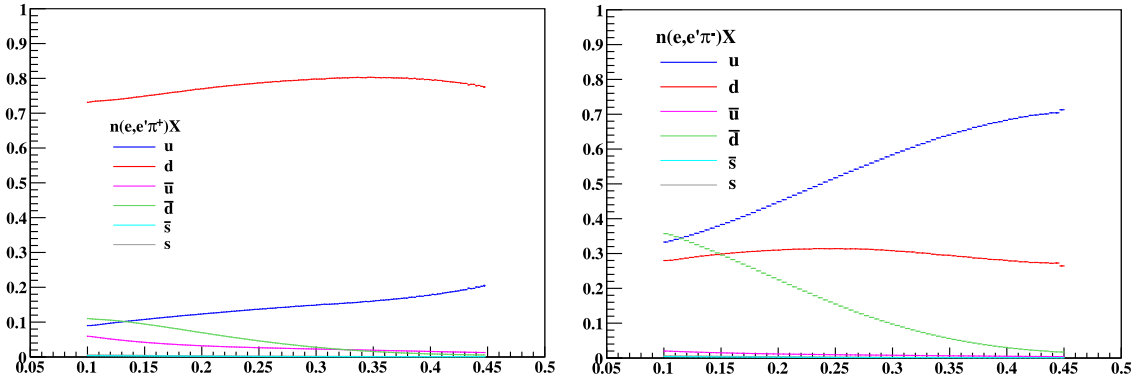

(a) (b)

Figure 2-4: The fractions that each quark flavor contributes to unpolarized cross section for the π^+ (2-4a) and π^- (2-4b) production on neutrons at the kinematics of experiment E06-010. The x-axsis is the quark's longitudinal momentum fraction, x. These fractions were calculated by Dr. A. Puckett (Los Alamos National Lab) using a simulation for this experiment (Sec. 5.4.1).

where $\hat{\boldsymbol{h}} \equiv \boldsymbol{P}_{h\perp}/|\boldsymbol{P}_{h\perp}|$, $\boldsymbol{k}_T \equiv -\boldsymbol{K}_T/z$. The convolution notation $\Big[w\,f \otimes D\Big]$ is defined as

$$\Big[w\,f \otimes D\Big] \equiv x \sum_a e_a^2 \int d^2\boldsymbol{p}_T\, d^2\boldsymbol{K}_T\, \delta^{(2)}\Big(z\boldsymbol{p}_T + \boldsymbol{K}_T - \boldsymbol{P}_{h\perp}\Big)\, w(\boldsymbol{p}_T, \boldsymbol{K}_T)\, f^a(x, p_T^2)\, D^a(z, K_T^2)\,, \tag{2.16}$$

where $\sum_a$ is sum over quark flavor index, a.

For the unpolarized neutron cross section at the kinematics of experiment E06-010, the fractions that each quark flavor contributes, σ^a/σ, were estimated using global parametrizations of the PDF and FFs (the CTEQ6 PDFs [80] and DSS07 FFs [77]) as shown in Fig. 2-4. The dominate flavors ($\sigma^a/\sigma > 10\%$) and their average fractions in parenthesis are d (78%), u (13%) for the π^+ production, and u (50%), d (30%), $\bar{d}$ (18%) for the π^- production.

2.4 the g_{1T} Distribution

The main physics topic of this thesis is to probe the g_{1T} distribution, which is one of the eight leading-twist TMDs. It was probed through the SIDIS beam-target double spin asymmetries $A_{LT}^{\cos(\phi_h - \phi_S)}$ with a transversely polarized target. The physics

related to the g_{1T} TMD, the experimental approach to access g_{1T} and the current experimental status will be discussed in the following two subsections.

2.4.1 g_{1T} and Its Relation to Quark Orbital Motion

The g_{1T} TMD, as defined in Eq. (A.4), is a twist-2 distribution related to the transverse motion of quark, nucleon spin and quark spin. It describes the distribution of a longitudinally polarized quark inside a transversely polarized nucleon [81, 37]. Therefore, it is also called transversal helicity[7] [82]. In addition, since both the g_{1T} and $h_{1L}^{\perp}$ functions[8] link two perpendicular spin directions of nucleons and quarks, they are also known as "worm-gear" functions [83].

The "worm-gear" functions provide unique information on the quark spin-orbital correlations. It represents the real part of an interference between nucleon wave functions that differ by one unit of orbital angular momentum; the corresponding imaginary part of the interference is related to the better studied $f_{1T}^{\perp}$ (Sivers functions) [84, 40]. Therefore, the observation of a non-zero g_{1T} would provide direct evidence that quarks carry orbital angular momentum, which help constrain an important part of the nucleon spin sum rule [27]. In a light-cone constituent quark model [85], g_{1T} is explicitly decomposed into a dominant contribution from the interference of S- and P-waves and a relatively smaller ($< 20\%$) contribution from the interference of P- and D- waves in the quark wavefunctions as shown in Fig. 2-5.

The spin-dependent distributions in transverse-momentum space have an analogy in terms of spin-dependent distributions in impact parameter space, which are described by generalized parton distributions (GPDs) [86]. This correspondence holds for 6 of the leading-twist TMDs, but not for the two "worm-gear" TMDs because of time-reversal symmetry [87, 88, 89]. Therefore, the "worm-gear" functions can not be generated dynamically from coordinate space densities by final-state interactions. Its appearance may be seen as a genuine sign of intrinsic transverse motion of the

[7] Also in Chinese: "横纵度"

[8] the $h_{1L}^{\perp}$ functions described the transverse polarization of quark inside a longitudinally polarized nucleon.

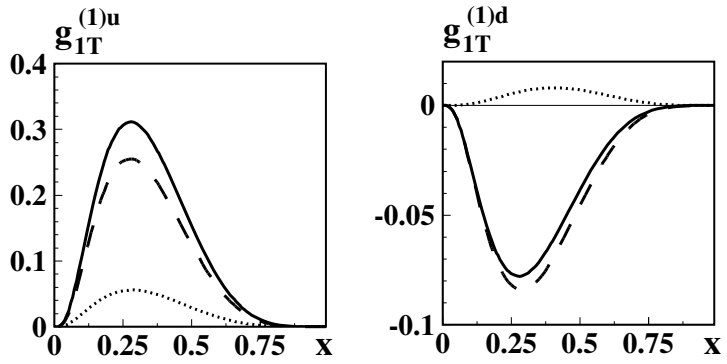

Figure 2-5: $g_{1T}^{(1)}$ functions (solid curves) and its component contributed from an interference between S- and P-waves (dashed curves) and an interference between P- and D- waves (dotted curves) as obtained from a light cone constituent quark model [91]. They are the integral of $g_{1T}(x, p_T)$ over $\boldsymbol{p}_T$ with a weight factor of $p_T^2/2M^2$ (Eq.. (A.7)). The quark flavors are left plot for up quarks and right plot for down quarks.

quarks [90].

g_{1T} is the only T-even and Chiral-even function among the five leading-twist TMDs which explicitly depend on the quark transverse momentum. Therefore, in the experimental cross sections, g_{1T} is not directly connected with T-odd (e.g. T-odd final state interactions) or Chiral-odd (e.g. Collins fragmentation) processes.

2.4.2 Lattice QCD Calculations

Recently, the TMDs have been explored in lattice QCD using a simplified definition of the TMDs with straight gauge links [90, 92]. The "worm-gear" functions were among the first TMDs addressed with this method. The results showed a rise to a dipole deformation of the density of quarks in the transverse momentum plane, clearly visible in Fig. 2-6 (distributions for proton are shown in this specific plot), where the x-integrated densities obtained from lattice QCD at $m_\pi \approx 500\,\text{MeV}$. The size of the dipole deformation can be characterized by an average transverse momentum shift:

- In a transversely polarized nucleon for a longitudinally polarized quark (TL), the shift is

$$\langle p_x \rangle_{TL}^q = \frac{M}{n_q} \int_0^1 dx \ \left(g_{1T}^{q(1)}(x) - \bar{g}_{1T}^{q(1)}(x) \right) \tag{2.17}$$

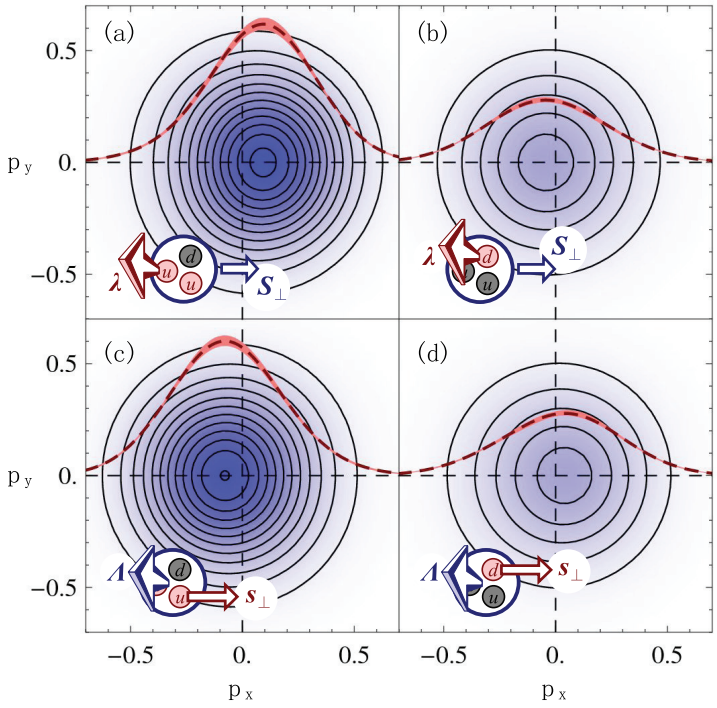

Figure 2-6: x-integrated quark density in the transverse momentum space, calculated using lattice QCD [90] at $m_\pi \approx 500$MeV. (a)\(b): a longitudinally ($+\boldsymbol{z}$ direction) polarized quark $u\backslash d$ density for a proton polarized in $+\boldsymbol{x}$ direction, which is related to the lowest x-moment of g_{1T}. (c)\(d): transversely ($+\boldsymbol{x}$ direction) polarized quark $u\backslash d$ density for a longitudinally ($+\boldsymbol{z}$ direction) polarized proton, which is related to the lowest x-moment of $h_{1L}^{\perp}$.

where $n_u = 2$ and $n_d = 1$ denote the number of valence quarks in the nucleon, and where $\bar{g}_{1T}^q$ is the anti-quark TMD PDF corresponding to g_{1T}^q. Based on a Gaussian parametrization of the transverse momentum dependence, the lattice study [92] finds $\langle p_x \rangle_{TL}^u = 69.7 \pm 4.5$ MeV and $\langle p_x \rangle_{TL}^d = -30.9 \pm 5.1$ MeV.

- In a longitudinally polarized nucleon for a transversely polarized quark (LT), the shift is

$$\langle p_x \rangle_{LT}^q = \frac{M}{n_q} \int_0^1 dx \, \left(h_{1L}^{\perp q(1)}(x) - \bar{h}_{1L}^{\perp q(1)}(x) \right) \tag{2.18}$$

  The lattice calculation yields $\langle p_x \rangle_{LT}^u = -59.1 \pm 3.8$ MeV and $\langle p_x \rangle_{LT}^d = 18.3 \pm 4.1$ MeV.

One finds that the u-quarks have a larger shift than d-quarks with opposite sign. Also the current lattice calculation supports that $g_{1T} \approx -h_{1L}^{\perp}$. Both of the observations

support corresponding results from quark models [93, 94, 95, 96, 97, 82, 98].

2.4.3 Model Predictions

g_{1T} have been estimated by many quark models [93, 94, 95, 96, 97, 99, 82, 98]. Common features of these models suggest that g_{1T}^u is positive and g_{1T}^d is negative. Both reach their maxima in the valence region at the few-percent level relative to the unpolarized distribution f_1^q. At the $x \to 1$ limit, g_{1T} has power behavior $(1-x)^4$, which is one power of $(1-x)$ suppressed relative to the unpolarized quark distribution [100].

2.4.3.1 TMD Relations

Recently, C. Lorcé and B. Pasquini reviewed the model relations among TMDs and their origins, which were predicted by a large class of models [101]. These model relations have essentially a geometrical origin and can be traced back to properties of rotational invariance of the rotational invariance of the system system. Generally, however, the relations do not necessarily hold in QCD. Experimental information on these TMDs can test the generic model assumptions.

The most simple one of the model relations,

$$g_{1T}^q = -h_{1L}^{\perp q}\,, \tag{2.19}$$

which is flavor-independent. Pioneering calculations in lattice QCD have indicated that the relation (2.19) may indeed be approximately satisfied [90, 92]. In addition, there are two more flavor independent relations for g_{1T}^q:

$$h_1^q + \tfrac{\boldsymbol{k}_\perp^2}{2M^2}\, h_{1T}^{\perp q} = g_{1L}^q\,, \tag{2.20}$$

$$\left(g_{1T}^q\right)^2 + 2h_1^q\, h_{1T}^{\perp q} = 0\,. \tag{2.21}$$

These relations can be further used to make constraints in a generic model-supported way on the Pretzelosity distribution, $h_{1T}^{\perp q}$, which is experimentally challenging to

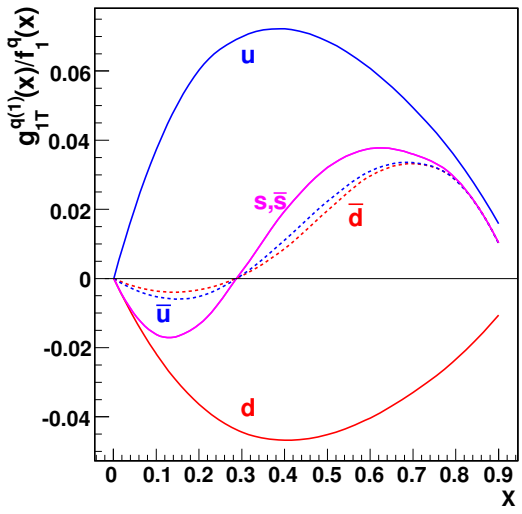

Figure 2-7: WW-type prediction of $g_{1T}^{q(1)}/f_1(x)$ [105, 106, 107] as function of x.

measure due to the small values of the predicted asymmetries. In addition, the QCD parton model suggested approximate TMD relations, which link g_{1T}^q with the quark transversity distribution h_1^q and the pretzelosity distribution, $h_{1T}^{\perp q}$ [102, 103, 104].

2.4.3.2 WW-type Calculations

One can establish, among others, the following two so-called Lorentz Invariance Relations (LIRs) [37, 105] between p_T weighted "worm-gear" functions (Eq. (A.7)) and $\boldsymbol{p}_T$ integrated twist-3 "collinear" PDFs (which, however, are not valid in general [108] and in QCD satisfied only in an approximation analogous to the Wandzura-Wilczek (WW) approximation [109, 110]):

$$g_T^q(x) \;=\; g_1^q(x) + \frac{d}{dx} g_{1T}^{q(1)}(x) \tag{2.22}$$

Then, using the Wandzura and Wilczek (WW) approximation [111, 112, 109]

$$g_T^q(x) \;\overset{WW}{\approx}\; \int_x^1 \frac{dy}{y} g_1^q(y)\,, \tag{2.23}$$

the g_{1T} functions can be related to better understood collinear PDFs, g_1, through following WW-type relations:

$$g_{1T}^{q(1)}(x) \overset{WW-type}{\approx} x \int_x^1 \frac{dy}{y} g_1^q(y)\,. \tag{2.24}$$

With Eqs. (2.24), numerical evaluations have been performed based on experimental data of g_1 [105, 106, 107], as shown in Fig. 2-7. Similar calculation can also performed for the other "worm-gear" function $h_{1L}^{\perp}$. which is related to the transversity distribution under the same type of approximation

$$h_{1L}^{\perp q(1)}(x) \overset{WW-type}{\approx} -x^2 \int_x^1 \frac{dy}{y^2} h_1^q(y). \tag{2.25}$$

The WW approximation and LIRs are based on assumptions that the twist-3 "interaction dependent" terms due to quark-gluon-quark correlations and current quark mass terms are small [112, 109]. However, it was estimated that the violation on WW can be as large as $15 \sim 40\%$ [113]. A precise extraction of g_{1T} and comparison to these calculation can verify these approximations experimentally.

2.4.3.3 More Models Predictions

The following models and reference papers also provided numerical evaluation of g_{1T}^q. g_{1T}^q for u and d quarks with a similar order of magnitude as that calculated using WW-approximation (Fig. 2-7) was shown in the following models:

- Diquark spectator models [93, 114]
- a Light-Cone Constituent Quark Model (LCCQM) [94, 85], also shown on Fig. 2-5 with the OAM interference decomposition.
- a covariant parton model framework with intrinsic orbital motion [96]
- a quark-model framework provided by the Bag Model [97]
- a light-cone quark-diquark model (LCQDM) [82]

2.5 Probing g_{1T} through SIDIS Asymmetries

2.5.1 Double Spin Asymmetry A_{LT}

g_{1T} leads to a dependence of the SIDIS cross-section on the beam helicity, the target spin, the hadron and target spin azimuthal angles through the leading twist structure function $F_{LT}^{\cos(\phi_h-\phi_S)}$, Eq. (2.15). The dependency can be experimentally measured by the beam-target double spin asymmetry (DSA) with a transversely polarized target, $A_{LT}\left(\phi_h,\phi_S\right)$,

$$A_{LT}\left(\phi_h,\phi_S\right) \equiv \frac{1}{|P_B S_T|}\frac{Y^+\left(\phi_h,\phi_S\right)-Y^+\left(\phi_h,\phi_S+\pi\right)-Y^-\left(\phi_h,\phi_S\right)+Y^-\left(\phi_h,\phi_S+\pi\right)}{Y^+\left(\phi_h,\phi_S\right)+Y^+\left(\phi_h,\phi_S+\pi\right)+Y^-\left(\phi_h,\phi_S\right)+Y^-\left(\phi_h,\phi_S+\pi\right)}\,, \tag{2.26}$$

where P_B is the polarization of the lepton beam, S_T is the transverse polarization of the target w.r.t. the virtual photon direction, and $Y^{\pm}\left(\phi_h,\phi_S\right)$ is the normalized yield for beam helicity of ± 1. Using Eq. (2.5), $A_{LT}\left(\phi_h,\phi_S\right)$ can be expressed as ratios of the structure functions,

$$\begin{aligned} A_{LT}\left(\phi_h,\phi_S\right) \;=\; & \frac{1}{1+\cos\phi_h\, A_{UU}^{\cos\phi_h}+\cos(2\phi_h)\, A_{UU}^{\cos 2\phi_h}} \times \Big[\cos(\phi_h-\phi_S)\, A_{LT}^{\cos(\phi_h-\phi_S)}+ \\ & \cos\phi_S\, A_{LT}^{\cos\phi_S}+\cos(2\phi_h-\phi_S)\, A_{LT}^{\cos(2\phi_h-\phi_S)}\Big]\,, \end{aligned} \tag{2.27}$$

where the azimuthal asymmetries are defined as

$$A_{LT}^{\cos(\phi_h-\phi_S)} \equiv \sqrt{1-\varepsilon^2}\,\frac{F_{LT}^{\cos(\phi_h-\phi_S)}}{(1+\varepsilon R)\; F_{UU,T}}\,, \tag{2.28}$$

$$A_{LT}^{\cos\phi_S} \equiv \sqrt{2\,\varepsilon(1-\varepsilon)}\,\frac{F_{LT}^{\cos\phi_S}}{(1+\varepsilon R)\; F_{UU,T}}\,, \tag{2.29}$$

$$A_{LT}^{\cos(2\phi_h-\phi_S)} \equiv \sqrt{2\,\varepsilon(1-\varepsilon)}\,\frac{F_{LT}^{\cos(2\phi_h-\phi_S)}}{(1+\varepsilon R)\; F_{UU,T}}\,, \tag{2.30}$$

$$A_{UU}^{\cos\phi_h} \equiv \sqrt{2\,\varepsilon(1+\varepsilon)}\,\frac{F_{UU}^{\cos\phi_h}}{(1+\varepsilon R)\; F_{UU,T}}\,, \tag{2.31}$$

$$A_{UU}^{\cos 2\phi_h} \equiv \varepsilon\,\frac{F_{UU}^{\cos 2\phi_h}}{(1+\varepsilon R)\; F_{UU,T}}\,. \tag{2.32}$$

The longitudinal-transverse cross section ratio is

$$R \equiv \frac{F_{UU,L}}{F_{UU,T}}\,, \tag{2.33}$$

In the quark/parton models (Sec. 2.3.3), the $A_{LT}^{\cos(\phi_h-\phi_S)}$ and $A_{UU}^{\cos 2\phi_h}$ are the only two leading twist azimuthal asymmetries in Eq. (2.27) and $R = 0$. In addition, if the experiment acceptance for ϕ_h is complete, the terms of $\cos\phi_h\, A_{UU}^{\cos\phi_h}$ and $\cos(2\phi_h)\, A_{UU}^{\cos 2\phi_h}$ vanish after summing yield over ϕ_h. Under these assumptions, Eq. (2.27) can be simplified to

$$A_{LT}\left(\phi_h, \phi_S\right) \approx A_{LT}^{\cos(\phi_h-\phi_S)} \times \cos\left(\phi_h - \phi_S\right) \tag{2.34}$$

By substituting the structure functions defined in Eqs. (2.6) and (2.15) to Eq. (2.28), the asymmetries can be expressed as convolution of TMDs,

$$A_{LT}^{\cos(\phi_h-\phi_S)} \;=\; \sqrt{1-\varepsilon^2}\,\frac{\left[\frac{\hat{\boldsymbol{h}}\cdot\boldsymbol{p}_T}{M} g_{1T} \otimes D_1\right]}{\left[f_1 \otimes D_1\right]}\,, \tag{2.35}$$

where the asymmetries are functions of, among others, x, y, z, $P_{h\perp}$ and Q^2. The y dependency is kinematic, i.e., it is related to depolarization factor $\sqrt{1-\varepsilon^2}$. If the unfavored fragmentation and sea quark contribution is ignored, $\pi^{+(-)}$ asymmetries are directly proportional to the corresponding $u(d)$ TMD distributions.

Besides the $A_{LT}\left(\phi_h, \phi_S\right)$ DSA, $A_{LT}^{\cos(\phi_h-\phi_S)}$ and g_{1T} can also be studied by forming the target single spin asymmetry (target-SSA) with a fixed non-zero beam helicity or the beam single spin asymmetry (beam-SSA) with a transversely polarized target at fixed spin direction. The DSA approach provides the most clean access to $A_{LT}^{\cos(\phi_h-\phi_S)}$ in terms of the contamination from other single spin structure functions as in Eq. (2.5). The target-SSA method has been used by the COMPASS and HERMES collaborations. This thesis work is the first measurement of $A_{LT}^{\cos(\phi_h-\phi_S)}$ using the DSA method and is also the pioneer $A_{LT}^{\cos(\phi_h-\phi_S)}$ experiment using an effective polarized neutron target.

2.5.2 Weighted A_{LT}

The convolution in Eq. (2.35) can be simplified using a technique of weighted asymmetries and TMDs. The $P_{h\perp}$ weighted asymmetries are defined [105, 106, 99] as

$$A_{LT}^{|P_{h\perp}|\cos(\phi_h-\phi_S)} \equiv \sqrt{1-\varepsilon^2}\frac{\int d^2\boldsymbol{P}_{h\perp}\frac{|P_{h\perp}|}{zM}F_{LT}^{\cos(\phi_h-\phi_S)}}{\int d^2\boldsymbol{P}_{h\perp}F_{UU,T}}\,. \tag{2.36}$$

Then a simpler relation using the weighted $g_{1T}^{(1)}$ (Eq. A.7) can be expressed [105, 106, 99] as

$$A_{LT}^{|P_{h\perp}|\cos(\phi_h-\phi_S)} = 2\sqrt{1-\varepsilon^2}\frac{\sum_q e_q^2 g_{1T}^{q(1)}(x)D_1^q(z)}{\sum_q e_q^2 f_1^q(x)D_1^q(z)}\,. \tag{2.37}$$

In Eq (2.37), the TMD factorization of Eq (2.15) has been assumed to hold even though $A_{LT}^{|P_{h\perp}|\cos(\phi_h-\phi_S)}$ by definition is integrated to large $P_{h\perp}$ (detailed discussion in [115]). A new weighted asymmetry [116, 117] using Bessel functions has been proposed to avoid this issue.

For measurements with an infinite $P_{h\perp}$ coverage, this weighted asymmetry could be directly extracted from data:

$$A_{LT}^{|P_{h\perp}|\cos(\phi_h-\phi_S)} = \frac{\left\langle\frac{|P_{h\perp}|}{zM}\cos(\phi_h-\phi_S)\right\rangle_{LT}}{\langle\cos^2(\phi_h-\phi_S)\rangle_{UU}}\,. \tag{2.38}$$

For measurements with a limited $P_{h\perp}$ coverage, the transverse momentum dependency of TMD PDFs and FFs will become an indispensable ingredient in interpreting measured asymmetries. As shown in Appendix. A.3, under an assumption of Gaussian-like transverse momentum dependence, a similar relation as Eq. (2.37) can be established between $g_{1T}(x)$ and $A_{LT}^{\cos(\phi_h-\phi_S)}$, as well as between $h_{1L}^{\perp}(x)$ and $A_{UL}^{\sin 2\phi_h}$ [105, 106, 107]. A measurement with a large coverage over $P_{h\perp}$ will also help to test and to characterize this Gaussian dependency.

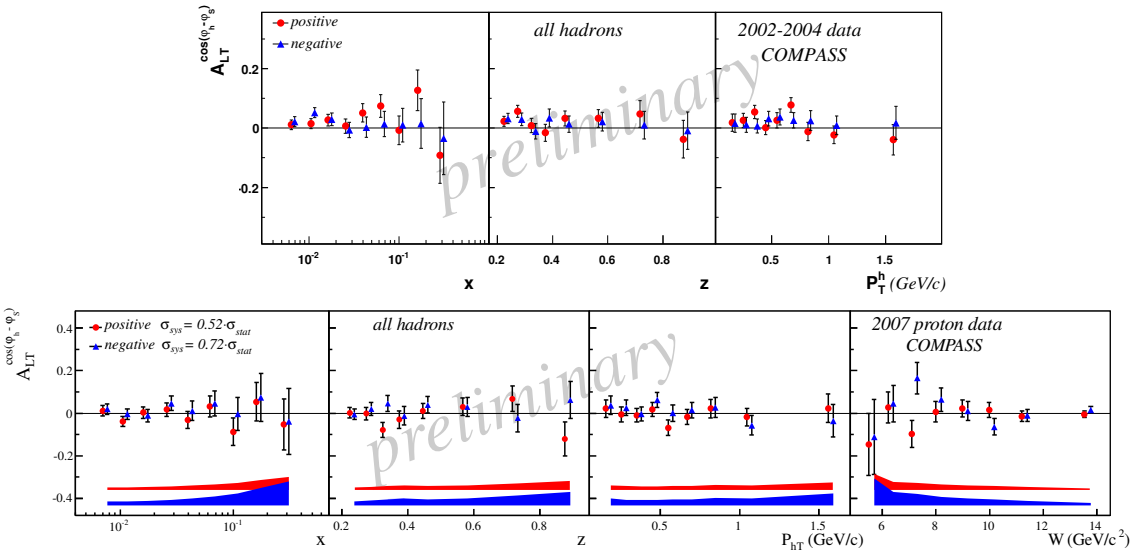

Figure 2-8: The COMPASS preliminary results of $A_{LT}^{\cos(\phi_h - \phi_S)}/\sqrt{1-\varepsilon^2}$ as function of x, z, $P_{h\perp}$ and/or W, using transversely polarized targets and muon beam. Top: deuteron target [118]; bottom: proton target [119].

2.5.3 Experimental Status

There were no experimental data on $A_{LT}^{\cos(\phi_h - \phi_S)}$ until recent years. Over the last decade, measurements have been made by the COMPASS collaboration [118, 53, 119], the HERMES collaboration [121, 120], and the Hall A Neutron Transversity Collaboration (this thesis work):

- The COMPASS collaboration previously reported preliminary results for $A_{LT}^{\cos(\phi_h - \phi_S)}$ in positive and negative charged hadron production using a muon beam scattered from transversely polarized deuterons [118, 53] and protons [119], as shown in Fig. 2-8. The kinematics favored the sea quark region. Within the uncertainties, the preliminary results are consistent with zero and various model predictions.

- Recently, the HERMES collaboration reported the preliminary results of $A_{LT}^{\cos(\phi_h - \phi_S)}$ on a transversely polarized proton target. The detected hadron species include $\pi^{\pm}$, π^0 and $K^{\pm}$ [121, 120]. The data indicated a positive $A_{LT}^{\cos(\phi_h - \phi_S)}$ asymmetry for the π^- electroproduction as shown in Fig. 2-9.

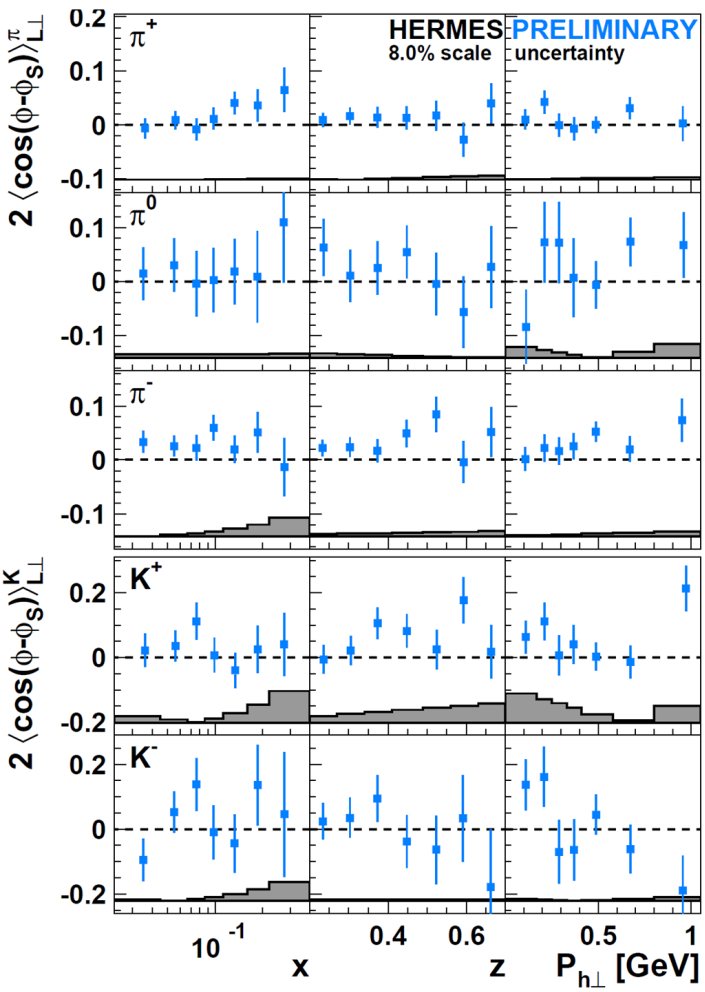

Figure 2-9: The HERMES preliminary results of $A_{LT}^{\cos(\phi_h-\phi_S)}$ on transversely polarized protons as a function of x, z, $P_{h\perp}$ [120].

- This thesis work will present the first measurement of the double-spin asymmetry A_{LT} of charged pion electroproduction in deep inelastic electron scattering on a transversely polarized ^{3}He target, obtained with fast electron helicity reversal and target spin reversal.

2.5.4 Theory Parametrization

As shown on Fig. 2-10, at the kinematic region of this thesis work, $A_{LT}^{\cos(\phi_h-\phi_S)}$ has been predicted using several model calculations, including WW-type approximations with parametrizations from Ref. [106] (Par. 1) and Ref. [106, 107] (Par. 2), a light-cone constituent quark model (LCCQM) [94, 85] and a light-cone quark-diquark

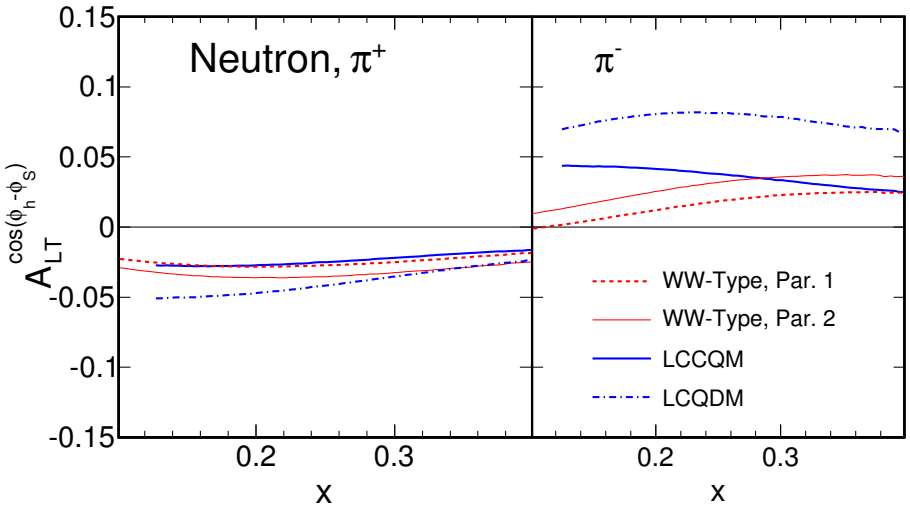

Figure 2-10: Theory predictions of neutron $A_{LT}^{\cos(\phi_h-\phi_S)}$ asymmetries, evaluated at the kinematic centers of the E06-010 experiment. See text for details.

model (LCQDM) evaluated using Approach Two[9] in Ref. [82]. The common features suggest that the asymmetries are at a level of a few percent, and π^+ and π^- asymmetry have opposite signs for the neutrons. However, due to the lack of experimental information on the g_{1T}^q function, these models are not directly experimentally constrained, and can have considerable uncertainties associated with the model assumptions. Therefore, experimental information on $A_{LT}^{\cos(\phi_h-\phi_S)}$ is essential to constrain the a large possible range of this asymmetry, and proble the g_{1T}^q function, which are sensitive to the quark spin-orbital correlations.

[9]Two approaches on the estimation of the TMDs were introduced in Ref. [82]: Approach One directly calculated the TMD functions using the LCQDM model; Approach Two utilized the information on the unpolarized distributions and the transverse movement dependencies, which were extracted from experimental data using global analyses [80, 60]. The author argued that Approach Two give more reasonable predictions and provided prediction for this experiment according to this approach.

Chapter 3

Experimental Setup

3.1 Overview

Experiment E06-010 measured the double spin asymmetry (DSA) A_{LT} and the target single spin asymmetries (target-SSA) [54] in deep-inelastic charged pion production on a transversely polarized ^{3}He target. This experiment took data at Thomas Jefferson National Accelerator Facility (or JLab) Experimental Hall A from Oct 2008 to Feb 2009. A schematic diagram and a 3-D model of the experimental apparatuses are shown in Fig. 3-1, which consisted of the Hall A beam line elements (Sec. 3.2), the polarized ^{3}He target (Chap. 4), the Left-HRS spectrometer (Sec. 3.3) and the BigBite spectrometer (Sec. 3.4).

The experiment used a longitudinally polarized 5.9 GeV electron beam with an average current of 12 μA. Polarized electrons were excited from a superlattice GaAs photocathode by a circularly polarized laser [122] at the injector of the CEBAF accelerator. The average beam polarization was $(76.8 \pm 3.5)\,\%$, which was measured periodically by the Møller polarimeter. Through an active feedback system [123], the beam charge asymmetry between the two helicity states was controlled to less than 150 ppm over a typical 20 minute period between target spin-flips and less than 10 ppm for the entire experiment. A high luminosity polarized ^{3}He target was used in this measurement as an effective polarized neutron target, which is discussed in detail in Chap. 4.

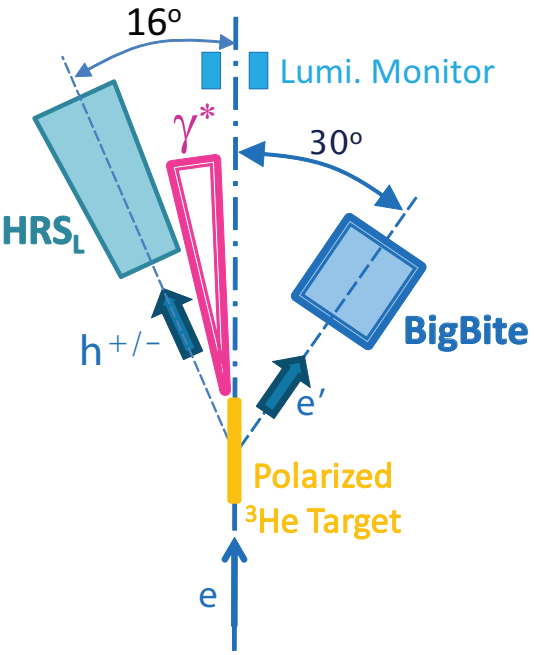

(a)

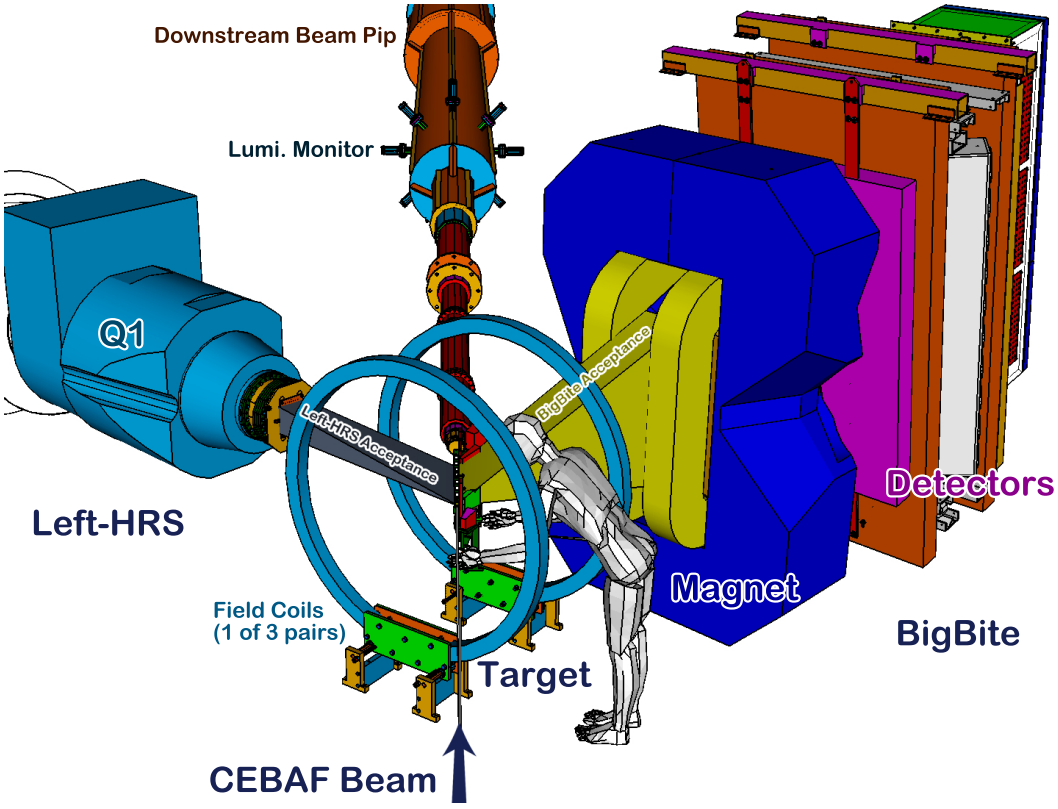

(b)

Figure 3-1: (a) Schematic diagram and (b) 3-D model of the E06-010 experimental apparatuses. Only a small part of the target system is shown, including the target ladder, collimators and one of the three field coils (more complete model: Fig. 4-5). The acceptance for both spectrometers is visualized as the grey and yellow blocks for Left-HRS and BigBite, respectively.

Scattered electrons from the target were detected in the BigBite spectrometer, which consisted of a single dipole magnet for momentum analysis, three multi-wire drift chambers for tracking, a scintillator plane for time-of-flight measurement and a lead-glass calorimeter divided into pre-shower and shower sections for electron identification (ID) and triggering. Its angular acceptance was about 64 msr for a momentum range from 0.6 GeV to 2.5 GeV. The left High Resolution Spectrometer (Left-HRS) [124] was used to detect hadrons in coincidence with the BigBite Spectrometer. Its detector package included two drift chambers for tracking, two scintillator planes for timing and triggering, a gas Cerenkov detector and a lead-glass counter for electron ID. In addition, an aerogel Cerenkov detector and a ring imaging Cerenkov detector were used for hadron ID. The HRS central momentum was fixed at 2.35 GeV with a momentum acceptance of $\pm 4.5\%$ and an angular acceptance of $\sim$6 msr.

3.2 Accelerator and Beam Line Components

3.2.1 Continuous Electron Beam Accelerator Facility

The Jefferson Laboratory's superconducting radiofrequency (srf) Continuous Electron Beam Accelerator Facility (CEBAF) provides multi-GeV continuous-wave (cw) polarized electron beams for experiments at the nuclear and particle physics interface [126]. Since the first beam on target on July 25, 1994, a wide spectrum of physics programs have been carried out at this facility. These include: measurements of the charge distributions in the nuclei and nucleons, studies of nuclear and nucleon structure, studies and searches for excitation states of the nucleon, studies of parity-violating asymmetries, which are reviewed in Ref. [125].

As required by many experiments, the CEBAF beam is usually highly polarized. Polarized electrons are excited from a superlattice GaAs photocathode by a circularly polarized laser [122] at the injector of the CEBAF accelerator. The laser polarization, and therefore the electron beam helicity, was reversed at 30 Hz using a Pockels cell.

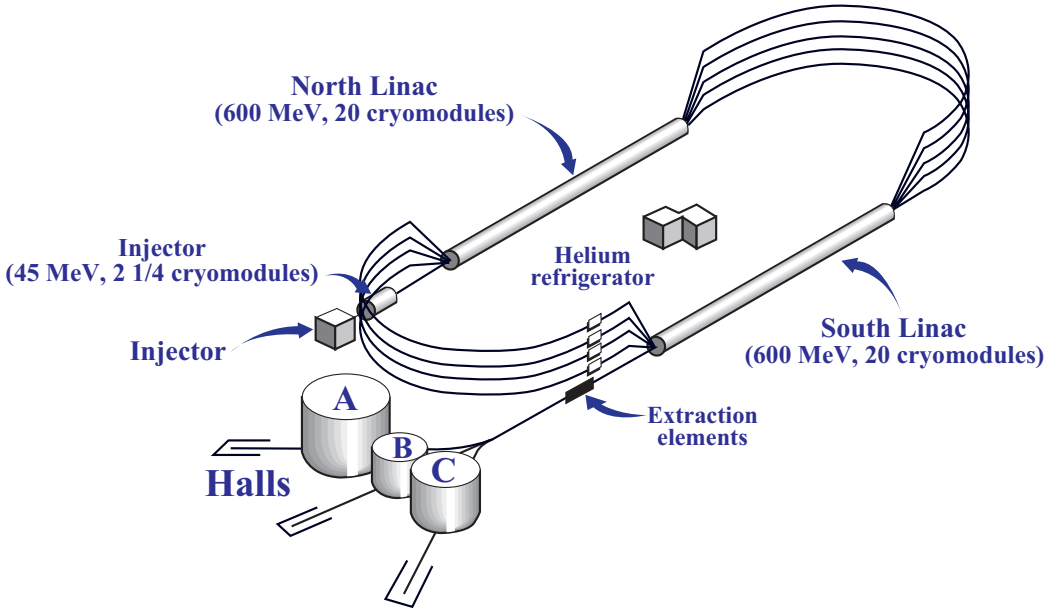

Figure 3-2: Sketch of the CEBAF accelerator [125]. The beam travels once through the North and South linacs with each recirculation, when it can be extracted into any of the three Halls.

During the E06-010 experiment, the sequence for beam helicity states followed a quartet structure, ie $+--+$ or $-++-$, and the sequence of the quartet was random. The typical electron polarization at JLab has been about 85%.

The electrons are injected into the accelerator after initial acceleration to 45 MeV. As shown in Fig. 3-2, the main acceleration section consists of two antiparallel linacs linked by nine recirculation beam lines for up to five passes. Because the electrons are ultrarelativistic and travel with essentially the same speed through their journey, a single linac on each side can be used to accelerate electrons for all passes. CEBAF has been providing simultaneous beams at different but correlated energies to three experimental halls (named A, B and C). By the mid-1990s, the maximum beam energy was around 4 GeV ; and since 2000, with the state-of-arts superconducting radiofrequency technologies, CEBAF has been providing electron beams with energies up to nearly 6 GeV at 1-150 μA for experimental Hall A and C and 1-100 nA for experimental Hall B.

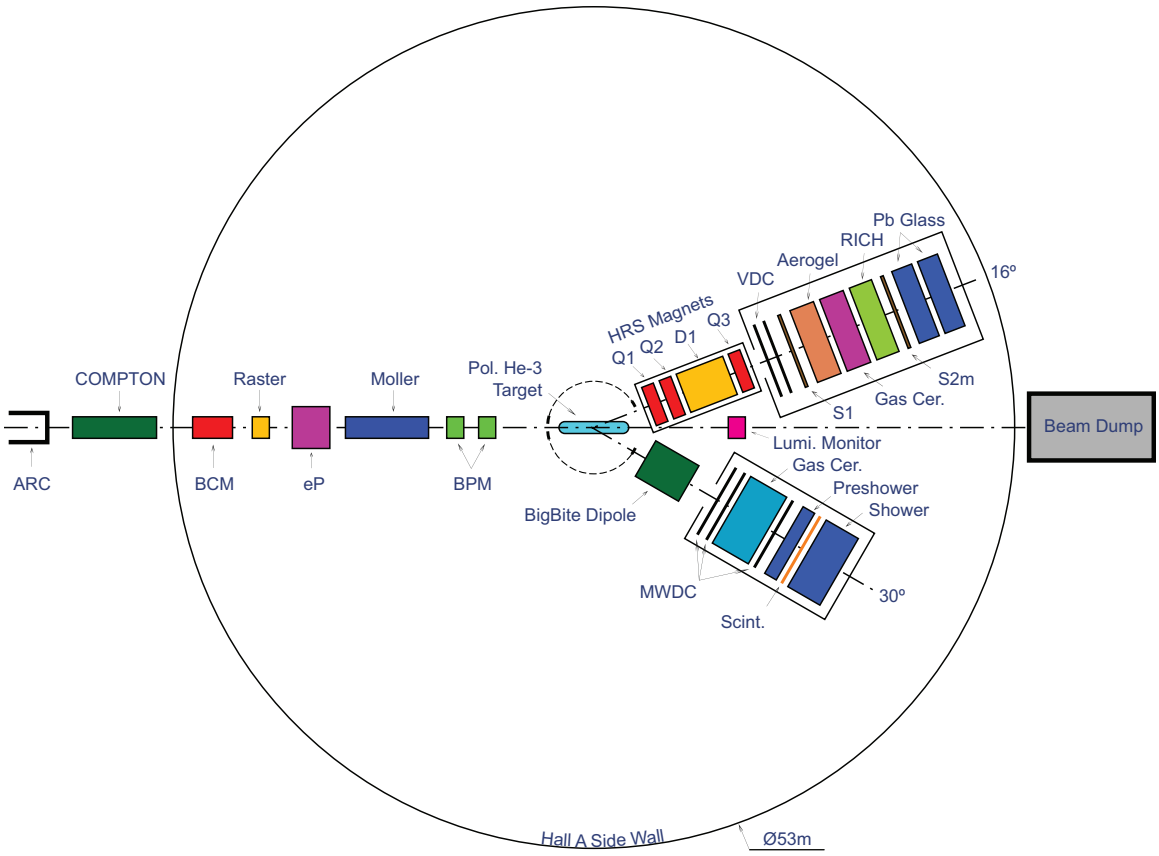

Figure 3-3: Hall A floor plan for experiment E06-010

3.2.2 Hall A

Experimental Hall A [124] (or Hall A in short) is the largest one of the three experiment Halls at Jefferson Lab, with a diameter of 53 m. The central components of Hall A are two identical high resolution spectrometers (HRSs), which allow the vertical drift chambers in the focal plane to provide a momentum resolution of better than 2×10^{-4}. A newer BigBite spectrometer was installed, which provided significant larger acceptance than the HRSs. The facility has been operated successfully at a luminosity well in excess of $10^{38}\,\mathrm{cm}^{-2}\mathrm{s}^{-1}$.

The floor plan during the E06-010 experiment is shown in Fig. 3-3. The key elements included the beamline, the polarized ^{3}He target, the left High Resolution Spectrometers (Left-HRS) and the BigBite spectrometer. The right HRS, which was rolled to a backward angle, was not used for this experiment and is not shown in

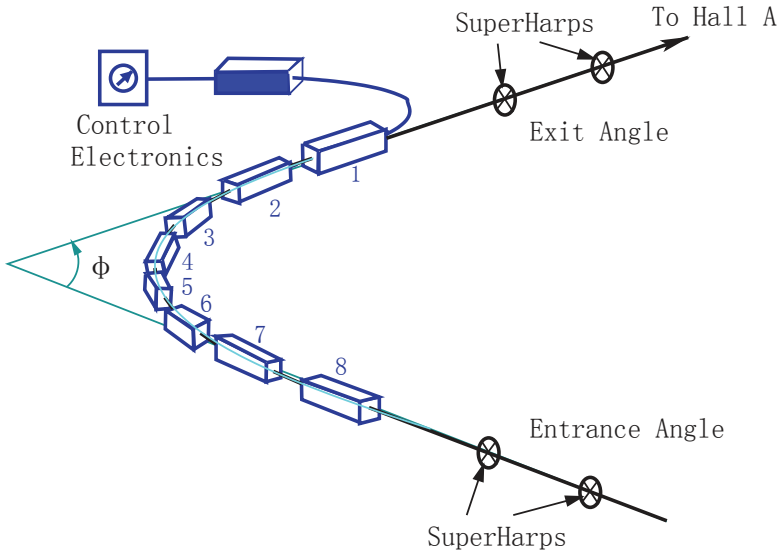

Figure 3-4: Schematic of the arc energy measurement [127]

Fig. 3-3. The beam components will be discussed in the following subsections.

3.2.3 Beam Energy Measurement

Two methods were used to determine the electron beam energy during experiment E06-010:

- Arc energy method [124], precisely measured the bending angle of the beam ($\theta = \pi - \phi$) when it passed through a given magnetic field which bended the electron beam into Hall A. The Arc setup is illustrated in Fig. 3-4. The beam momentum p can be calculated by

$$p = k\frac{\int \boldsymbol{B}\cdot\boldsymbol{dl}}{\theta}\,, \tag{3.1}$$

  where $\int \boldsymbol{B}\cdot\boldsymbol{dl}$ (in Tm) is the integral of transverse magnetic field along the trajectory of the beam and $k = 0.299792\,\mathrm{GeV\,rad\,T^{-1}\,m^{-1}}/c$. The Arc energy method is an invasive measurement, i.e., it cannot be made in parallel to the production data taking. For experiment E06-010, one Arc measurement was

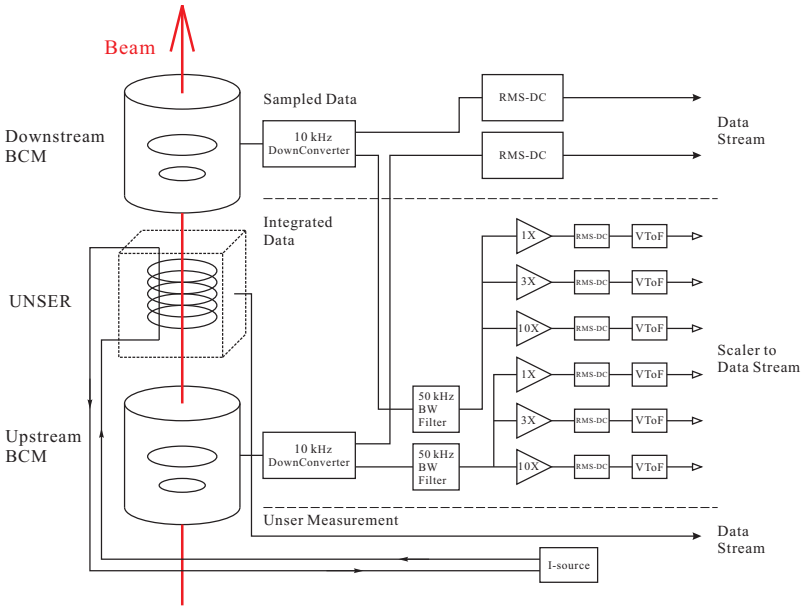

Figure 3-5: Schematic of beam current monitors [129]

performed at the production beam configuration [128]:

$$E_{Arc} = 5889.4 \pm 0.5(Stat.) \pm 1.0(Sys.)\,\text{MeV} \tag{3.2}$$

- The beam energy during the experiment was monitored by the "Tiefenbach" value and cross checked by the Arc measurement. This value is calculated by $\int \boldsymbol{B} \cdot \boldsymbol{dl}$ of Hall A arc and Hall A arc beam position monitors. This number is continuously recorded in the data stream and was used in the data analysis. The Tiefenbach energy corresponding to the Arc measurement was 5891.3±2.5 MeV, consistent with the Arc results (Eq. 3.2). The uncertainty for the "Tiefenbach" beam energy introduced a negligible systematic uncertainty on the azimuthal asymmetry results (Sec. 6.1.5).

3.2.4 Beam Current and Luminosity Measurement

Beam Current Monitor

The beam current is measured by the beam current monitors (BCMs) in Hall A, which provides a stable, low-noise, no-invasive measurement [124]. As shown in Fig. 3-5,

it consists of an Unser monitor, two RF cavities and supporting electronics system. The cavities and the Unser monitor are located 25 m upstream of the target and are enclosed in a temperature-stabilized magnetic shielding box.

- The Unser monitor [130] is a Parametric Current Transformer which provides an absolute reference with a nominal output of 4 mV/μA. Unser monitor's output signal drifts significantly on a time scale of several minutes, it cannot be used to continuously monitor the beam current and was not directly used in this experiment.

- The two resonant RF cavity monitors are located on either side of the Unser monitor as shown in Fig. 3-5. They are stainless steel cylindrical high-Q (3000) waveguides which are tuned to the frequency of the beam (1497 MHz). The voltage levels at their outputs which are proportional to the beam current. Each of the RF output signals from the two cavities is split into two parts, to be sampled or integrated:

  - The sampled signal was digitalized by a high-precision digital multi-meter, HP3458A and recorded to the data stream.

  - The integrated signal are sent to an RMS-to-DC[1] converter to produce an analog DC voltage level, and this level drives a Voltage-To-Frequency converter. These frequency signals are logged by scalers (details in Sec. 3.5.3) accumulate during the run and provide a number proportional to the total delivered charge. The regular RMS-to-DC output is linear for currents from about 5 μA to 200 μA. So a set of amplifiers has been introduced to produce three signals with gain factors of 1, 3, and 10. The higher-gain signals are used for lower currents experiments, at the expense of saturation at high currents; and the gain= 1 copy works best for the higher beam currents. Hence, there is a set of three signals coming from each of the upstream (u) and downstream (d) RF BCMs. These six signals (named

[1]RMS-to-DC: root mean square (RMS) to direct current (DC)

u1, u3, u10, d1, d3 and d10) are fed to scaler inputs of both BigBite and Left-HRS DAQs, providing redundant beam charge information.

During the E06-010 experiment, the an average current was 12 μA. The gain-3 copies (u3 and d3) of the integrated signal from the resonant RF cavity monitors were used as the primary signal source to calculate the beam charge, which was calibrated using the "OLO2" cavity at the injector, as discussed in Ref. [131].

Beam Charge Feedback

The beam helicity was reversed at 30 Hz during the experiment. The yield difference between two helicity states was the basis to extract the helicity asymmetries, e.g., Eq. (2.26); a large beam charge asymmetry between the two helicity states can bias the measurement. Therefore the charge asymmetry between two helicity states was minimized through an active feedback system [123]. The final beam charge asymmetry was controlled to less than 150 ppm over a typical 20 minute period between target spin-flips and less than 10 ppm for the entire experiment.

Luminosity Monitor

As shown in Fig. 3-1 and 3-3, a luminosity monitor (or Lumi for short) was placed about 6.5 meters downstream of the target to measure the relative overall luminosity of the experiment. As shown in the downstream view of Fig. 3-6, it consisted of 8 quartz bars (shown in brown) oriented symmetrically around the electron beam pipe at 45° intervals. The scattering angles from the target were between 0.5°-0.7°. For each bar, the Cerenkov photons from the quarts were read out by a photo-multiplier tube. The PMT housing is shown as blue tubes in Fig. 3-6. A standalone parity DAQ was used to read the data from the luminosity monitors. For data summed over the whole experiment, the luminosity asymmetry between two beam helicity states was not larger than $10\,ppm$, negligible compared to the uncertainty of this experiment. Therefore, no direct correction from the luminosity monitor was made.

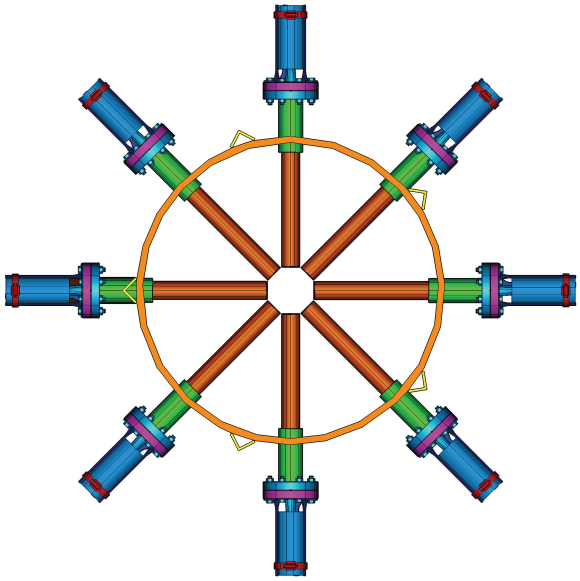

Figure 3-6: Schematic of the luminosity monitor mounted on the downstream beam pipe (orange ring from this view point), viewed from target center along the central beam line of Hall A. Unscattered beam goes through the center of this setup.

3.2.5 Beam Position and Direction

Two Beam Position Monitors (BPMA and BMPB) were used to measure the central beam position [124]. They are placed 7.345 m and 2.214 m upstream of the Hall A beam center line center, respectively. The standard difference-over-sum technique is used to determine the relative position of the beam to 100 μm for currents above 1 μA [132]. The absolute position of the beam can be determined from the BPMs by calibrating them with respect to wire scanners (superharps), which are located adjacent to each BPM. The signal from each BPM is recorded to DAQ for each event. The central beam position and direction at the target are linearly extrapolated using the beam position at both BPMs.

The E06-010 experiment used a high luminosity polarized ^{3}He target. Around 10 atm of target gas was contained in glass target cells, whose window thickness was around 0.1 mm. To avoid overheating on a single spot of the target cell window, the narrow (<0.3mm wide) CEBAF beam was rastered to homogeneously cover a square shape with a size around 3 mm $\times$ 3 mm. The beam raster consisted of two sets of steering magnets, located about 23 meters upstream of the target. The shift of the

beam relative to the average beam position was proportional to the current in the raster magnets, which was recorded by analog-to-digital converters for each event.

3.2.6 Beam Polarization Measurement

An important part of the experimental program in Hall A uses a polarized electron beam, with a typical beam polarization of 75-90%. In order to measure the polarization of the electron beam delivered to the hall, the beamline is equipped with two polarimeters, whose functions are partly overlapping and partly complementary:

Compton Polarimeter utilizing the process of Compton scattering, was designed to measure the beam polarization concurrently with experiments running in the hall to a 1% statistical error within an hour [133]. The polarization is extracted from the measurement of the counting rate asymmetry for opposite beam helicities in the scattering of a circularly polarized photon beam by the electron beam. During the E06-010 experiment, the Compton polarimeter was in the process of being upgraded to and commissioning with a new setup with improved detection system [134]. Only intermediate and unstable data were taken for the production data. Therefore, the Compton data was not used to determine the final beam polarization for this analysis.

Møller Polarimeter provided an invasive measurement of the beam polarization, which was performed approximately once every week during Experiment E06-010. The principle of the measurement and the results will be discussed for the rest of this section.

Principle of Møller Polarimeter

Polarized Møller scattering, in which polarized electron beam scatters off polarized atomic electrons in a magnetized foil $\vec{e}^{\leftarrow} + \vec{e}^{\leftarrow} \rightarrow e^- + e^-$, was utilized to measure the beam polarization for this experiment [135, 124]. The coordinate system is defined that the beam direction is along the Z-axis and the scattering happens in the $Z - X$ plane. Then the beam and target polarizations can be projected to the axises of i

$= X, Y, Z$, i.e., $P_{beam,\,i}$ and $P_{target,\,i}$. The Hall A Møller polarimeter measures the Z component of the beam polarization. i.e., the longitudinal beam polarization. There are also smaller transverse beam polarizations, i.e., the X or Y projections of the beam polarization. For the deep inelastic scattering studied in the E06-010 experiment, i.e., polarized electron scattering on a nuclear target and the polarization for the scattered electron is unspecified, the cross section dependence on the transverse polarization for the electron beam is suppressed kinetically by one over the lepton's Lorentz factor $1/\gamma_e$ [42]. Therefore the contributions due to the transverse beam polarization was negligible for this experiment and they are not related to the main physics goals for this thesis.

The cross section for the Møller scattering depends on the beam and target polarizations as

$$\sigma \propto (1 + \sum_{i=X,Y,Z} (A_{ii} P_{bean,\,i} P_{target,\,i})) \tag{3.3}$$

$$A_{ZZ} = -\frac{\sin^2\theta_{CM} \cdot (7 + \cos^2\theta_{CM})}{(3 + \cos^2\theta_{CM})^2} \tag{3.4}$$

$$A_{XX} = -\frac{\sin^4\theta_{CM}}{(3 + \cos^2\theta_{CM})^2} \tag{3.5}$$

$$A_{YY} = -A_{XX}\,, \tag{3.6}$$

where A_{ii} is the analyzing power and θ_{CM} is the scattering angle in the center of mass (CM) frame [124]. At $\theta_{CM} = 90°$, the analyzing power for the longitudinal polarization reaches its maximum $A_{ZZ,\,max} = 7/9$, therefore the Hall A Møller polarimeter was designed to cover 75$<$ θ_{CM} $<$105 and the average analyzing power is about$|< A_{ZZ} >| = 0.76$ [129], close to the maximum $A_{ZZ,\,max}$. The Møller cross section is less sensitive to the transverse polarizations, i.e., the maximum of the transverse analyzing power $A_{XX,max}$=$A_{YY,max}$ = $A_{ZZ,max}/7$. For the Hall A Møller polarimeter which measures the longitudinal beam polarization, the data with opposite target transverse polarizations are averaged to cancel the transverse contributions as discussed in the following paragraph.

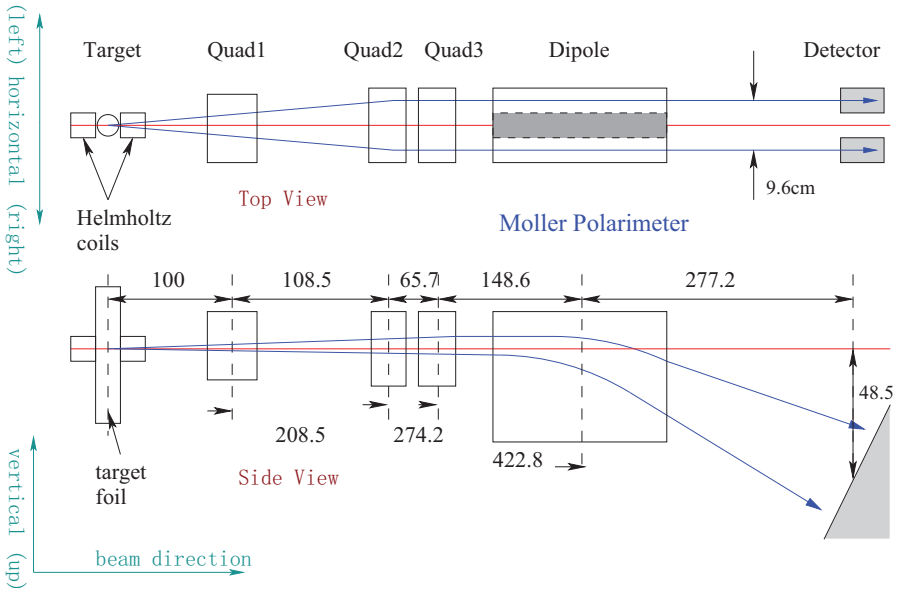

Figure 3-7: Layout of the Møller polarimeter [124, 127]

Measure Beam Polarization Using Møller Polarimeter

The setup for the Møller polarimeter is shown in Fig. 3-7. A thin magnetically saturated ferromagnetic foil is used as the polarized electron target. An average electron polarization of about 8% was obtained [124]. A pair of asymmetries are measured at two target angles of about $\theta_t = \pm 20^\circ$ with respect to the beam direction and the average is taken to cancel the transverse contributions, whose asymmetries have opposite signs for these target angles. In addition, at a given target angle, two sets of measurements with opposite directions of the target polarization are taken. The false asymmetries that coming from the residual helicity-driven asymmetry of the beam flux, are canceled in the averaged results for opposite target polarization directions.

The spectrometer coincidentally detects both scattered and target electrons which are close to the horizontal plane. It consists of a sequence of three quadrupole magnets and a dipole magnet as shown in shown in Fig. 3-7 and covered the kinematic range of $75 < \theta_{CM} < 105$ and $5 < \phi_{CM} < 5$; where θ_{CM} and ϕ_{CM} are the polar and azimuthal angle in the center of mass frame. The detector consists of scintillators and lead-glass calorimeter modules. The estimated background level of the coincidence rate is below

0.5% as discussed in Ref. [124].

The beam longitudinal polarization is measured as:

$$P_{beam} = \frac{1}{P_{target} \cdot \cos\theta_t \cdot < A_{ZZ} >} \times \frac{N_+ - N_-}{N_+ + N_-}, \tag{3.7}$$

where N_+ and N_- are the measured counting rates with two opposite mutual orientation of the beam and target polarization. Using a Monte-Carlo calculation of the Møller spectrometer, the average analyzing power $< A_{ZZ} >$ is obtained. The target polarization P_t is derived from measurements of the magnetization of the foil samples, and the target angle θ_t is measured using a scale, engraved on the target holder and seen with an TV camera, and also using the counting rates measured at different target angles.

The Møller polarimeter can be used at beam energies from 0.8 to 6 GeV. A lower beam current ($\sim 0.5\,\mu$A) than the typical running condition ($\sim 12\,\mu$A) was used by Møller and it is an invasive measurement. A typical running time was an hour providing a statistical accuracy of about 0.2%. The total error (~2%) was dominated by the determination of target polarization [135]. During the E06-010 experiment, Møller polarimetry was performed about once every week. It was usually scheduled immediately after a longer unavailable period of the beam or configuration change in the accelerator.

Issues for Beam Polarization

In general, the uncertainty for Hall A Møller polarimeter is dominated by the uncertainty of the polarization for the Møller target, which leads to a beam polarization uncertainty for $\delta P \approx 2\%$ (absolute) [135]. The statistical uncertainty is negligible. However, two additional factors increased the uncertainty during this experiment:

- During the Møller measurements of Nov-Dec 2008, the electron beam energy measurement was less precise due to the overall low beam current in the accelerator. This effect increased the systematic uncertainty for the beam polarimetry to $\delta P \approx 3\%$ (absolute) for this run period [135].

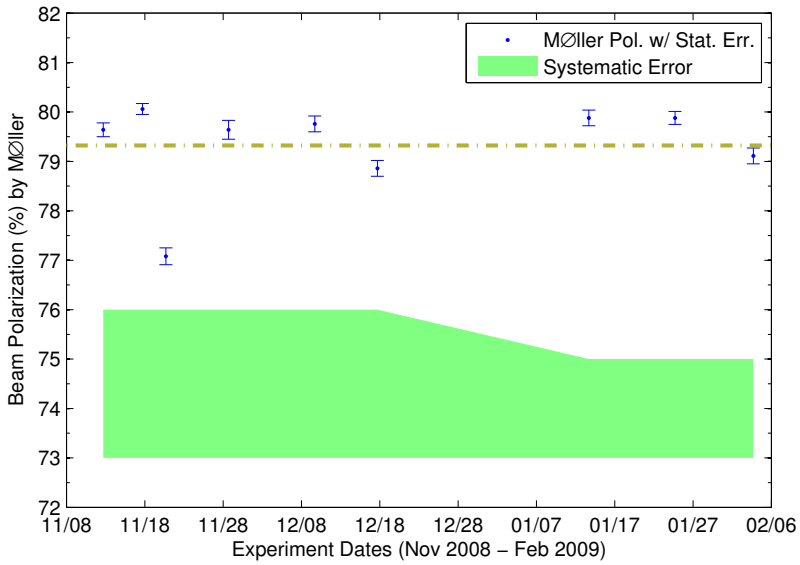

Figure 3-8: Beam polarization history measured using the Møller polarimeter [135], except the measurement with $P = 54\% \pm 3\%$ on Dec 08, 2008 as discussed above. The statistical uncertainty is shown as the error bar for each measurement; the systematic uncertainty is shown as the green band.

- There was a Pockels cell problem at the beam injector during Dec 2-8, 2008 (~10% of the data) [136], which reduced the beam polarization from 80% to 54%. This problem was discovered and fixed before production run 4306. During this period, a systematic uncertainty equal to the possible range of polarization (54% to 80%) was used, due to the unknown start date of the problem. A possible first run with this problem is run 4287, after service work on an related injector power supply. The contribution to the average polarization was $\delta P/P \approx 3.3\%$, conservatively.

In summary, the uncertainty for average beam polarization was $\delta P/P \approx 4.6\%$ as quoted in the manuscript.

Beam Polarization History

The beam polarization history measured using the Møller polarimeter [135] is shown in Fig. 3-8, except the measurement of $P = 54\% \pm 3\%$ on Dec 08, 2008 as discussed above. Since the measured beam polarizations are consistent within the uncertainties except the problematic period around Dec 08, the polarization in normal beam conditions

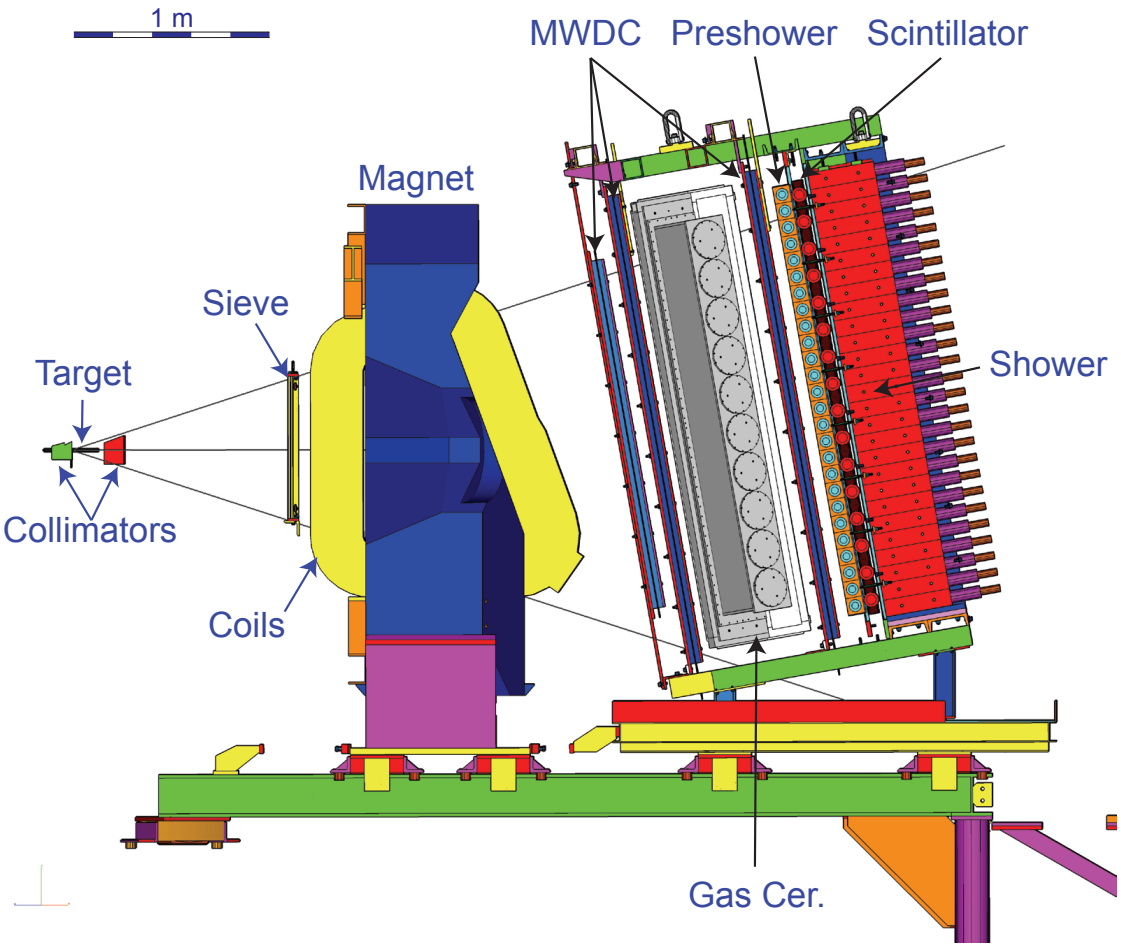

Figure 3-9: A side view of the BigBite detector package during the E06-010 experiment. A magnetic field shielding plate was installed between the "Sieve" and "Coils", which is not shown in this figure.

was averaged for the 2008 and 2009 data, respectively; and the Dec 08 measurement was used for runs 4287-4306. The average beam polarization was $(76.8 \pm 3.5)\,\%$.

3.3 BigBite Spectrometer

3.3.1 Overview

During the E06-010 experiment, the BigBite spectrometer was used to detector the DIS electrons. BigBite provided a momentum range of 0.6-2.5 GeV and an angular acceptance about 64 msr for 1.0 GeV negatively charged particles. The large coverage

of the out-of-plane angle was essential to provide a larger coverage in azimuthal angles and improve the separation of the SIDIS angular modulations.

A side view of the BigBite spectrometer during the E06-010 experiment was shown in Fig. 3-9 and a simulation of an electron event is shown in Sec. 5.4.2 Fig. 5-17. Near the beam windows of the ^{3}He target cell, two target collimators were installed to shield the high energy electrons and photons generated from the windows. The spectrometer used a simple dipole magnet, which was followed by three sets of multi-wire drift chamber (MWDC) to provide tracking information, a scintillator plane to provide the timing information, and a shower counter system including a preshower and a shower for PID. The scintillator plane was sandwiched between the layers of the preshower and shower. A gas Cerenkov detector was installed between the second and third MWDC. During experiment E06-010, it was under commissioning for the subsequent E06-014 experiment, and its data were not used for this thesis analysis.

3.3.2 BigBite Magnet

The spectrometer used a large acceptance, non-focusing dipole magnet to analyze the momentum of particles . It was originally designed and built for use at NIKHEF in the Netherlands [137, 138]. The gap between pole-faces is 25 cm in the horizontal and 84 cm in the vertical directions, which allows for a ten-times larger "bite" in the acceptance compared with the Hall A HRS spectrometers.

During Experiment E06-010, the current in the coils was about 710 A, which corresponds to a 1.2 T magnetic field inside the BigBite magnet [131]. A field shielding plate was installed in front of the BigBite magnet during the experiment in order to shield the target from the fringe magnetic field from the BigBite magnet. The residual field on the target was a few Gauss. It did not affected the operation of the polarized ^{3}He target by taking account of this contribution when configuring the holding magnetic field ($\sim$ 25 Gauss, see in Sec. 4.2.2).

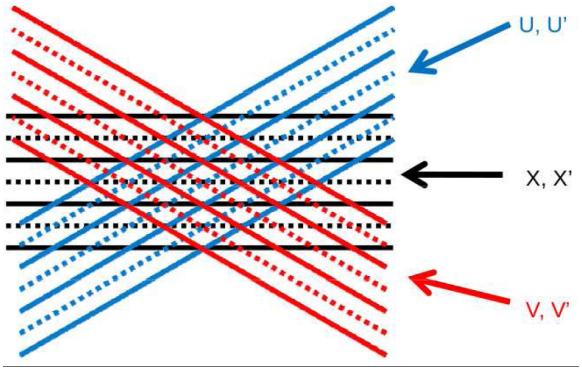

Figure 3-10: Illustration of the MWDC plane orientations: u, v and x (see text for details) [131]. The wire planes are parallel to the paper and x is the horizontal direction. In BigBite, the typical track indenting angle relative to the perpendicular direction is not more than 40°. .

3.3.3 Detector Package

Multi-Wire Drift Chamber

The tracking for the charged particles was provided by three sets of multi-wire drift chamber (MWDC), which were constructed at the University of Virginia [139]. The active area of the first chamber is about 140 cm×35 cm. The active area of the second and the third chamber is the same, which is about 200 cm×50 cm. Each wire chamber consists of six wire planes, which are divided into three groups with orientations of u (+30° with respect to the horizontal direction), v (-30°) and x (0°). The group configuration is illustrated in Fig. 3-10, where the solid and dash lines are the signal wires from the two planes in each group. Within each group, the second plane (labeled u', v' and x') is shifted by half of the signal-wire-spacing relative the the first plane (labeled u, v and x) to distinguish the left and right ambiguities. The distance between two adjacent signal wires in a single wire plane is 1 cm, and in between two signal wires a field wire is inserted. Each wire plane is sandwiched by two cathode planes. The field wires and the cathode planes were set at a voltage of about -1600 V during the experiment. A gas mixture of 50%/50% argon-ethane was kept flowing through the MWDC system. When a charged particles pass through the wire plane, they ionize the surrounding gas atoms and produce ions and electrons. The ionized electrons will drift to the closest signal wire. The time they take to

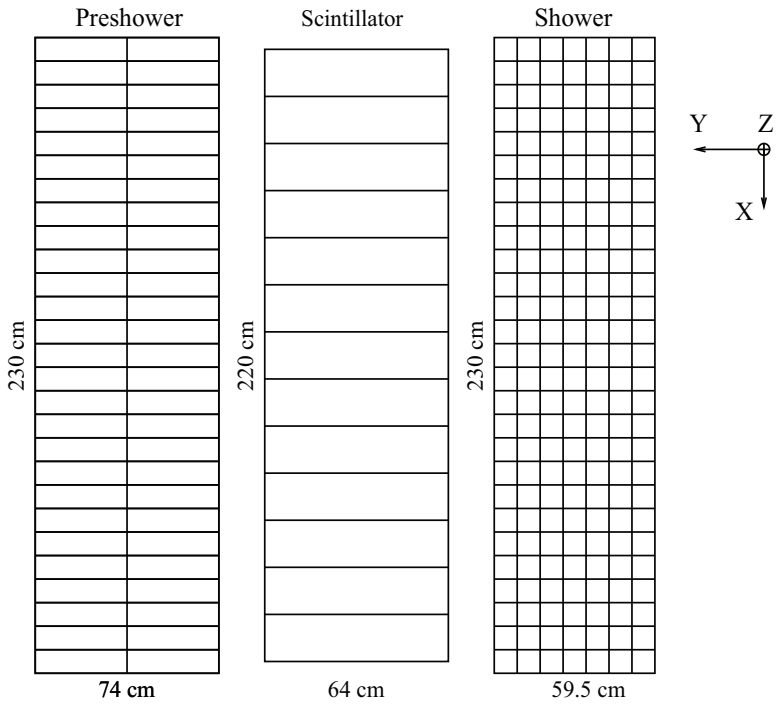

Figure 3-11: Geometry of the BigBite preshower, scintillator, and shower detectors as labeled on the top [140]. $+x$ is the dispersive direction of the BigBite magnet (towards down) and the central negatively charged track in BigBite is along +z direction. In the detector package, these three detectors were stacked together along the z direction as shown in Fig. 3-9.

reach the wire is proportional to the distance traveled. The signal from the wires is recorded using time-to-digital converters (TDCs), which was used to construct the track (Sec. 5.2.2.1). A detailed discussion can be found in Ref. [139].

Scintillator

The timing information was provided by a plastic scintillator detector [140, 141], which was mounted between the preshower and shower detectors as shown in Fig. 3-9. Fig. 3-11 shows the detector consisted of 13 bars with dimensions of 17 cm×64 cm×4 cm. Each bar was connected to two PMTs, one on each side. The signal from each PMT was amplified 10 times and recorded by a time-to-digital converter (TDC) and a analog-to-digital converter (ADC) for timing and amplitude information, respectively. Since this detector was behind the preshower, an electron shower had a large probability of firing two scintillator bars, which was used to perform the relative timing

alignment between bars. The timing resolution for the scintillator plane was better than 300 ps as discussed in Sec. 5.2.3.

Calorimeters

The EM calorimeter with a preshower-shower splitting provided the electron particle identification (PID) by measuring the energy deposition of the EM shower [140, 141]. The reconstructed energy had a resolution of about $\delta E/E = 8\%$. They also provided the PID trigger for the BigBite spectrometer, which preferred electron (and high energy photon) events.

The preshower blocks were made of TF-5 lead-glass blocks, each measuring 8.5 cm× 34 cm × 8.5 cm in the X, Y, and Z directions (defined in Fig. 3-11), respectively. There were 54 preshower blocks arranged in two columns of 27 rows each, as shown on the left side of Fig. 3-11. The active area was 210×74 cm^2, with 8.5 cm (3 radiation lengths) along the normal indenting direction. The photons were read out using PMTs on the outer side for each block.

The shower blocks were made of TF-2 lead-glass material, each measuring 8.5 cm× 8.5 cm × 34 cm in the X, Y, and Z directions, respectively. It covered an active area of 221×85 cm^2, with 34 cm (13 radiation lengths) along the normal indenting direction. There were 189 shower blocks arranged in 7 columns of 27 rows each, as shown on the right side of Fig. 3-11. The photons were readout from the backside for each block using PMTs as shown in Fig. 3-9.

3.4 Left High Resolution Spectrometer (HRS) Spectrometer

3.4.1 Overview

The Left High Resolution Spectrometer (Left-HRS or L-HRS) is one of the standard experimental apparatuses in Hall A [124]. As shown in Fig. 3-12, the vertically

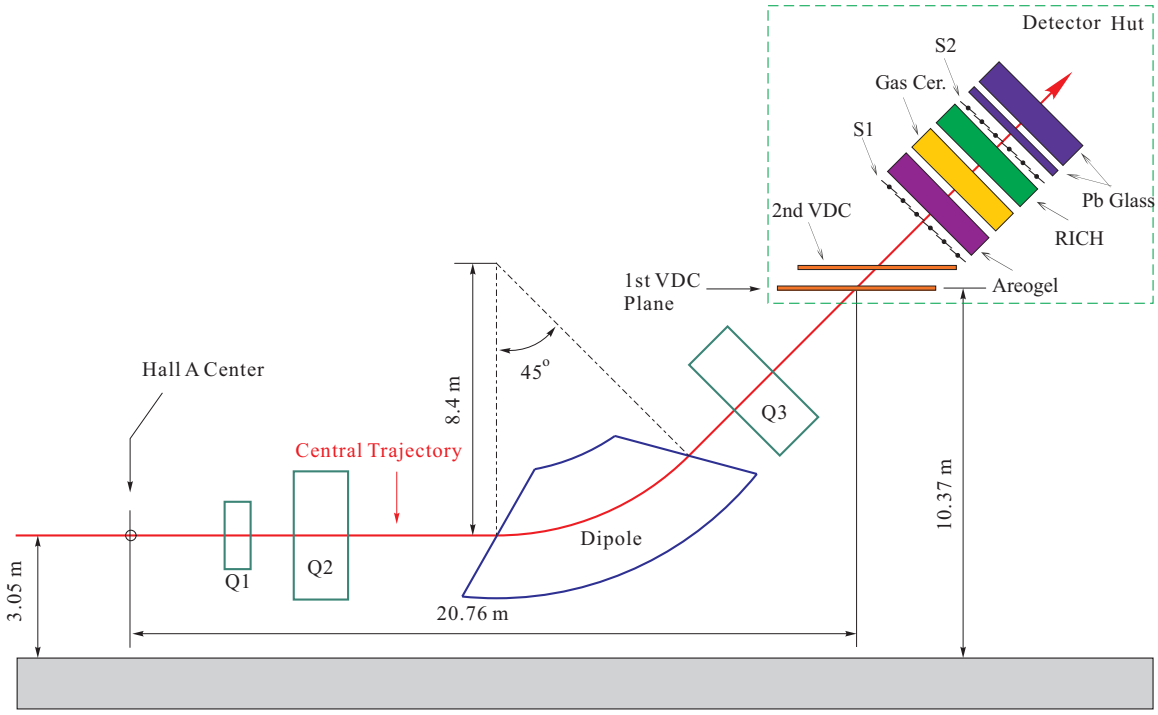

Figure 3-12: Schematic of Hall A High Resolution Spectrometer and the detector package for the E06-010 experiment

bending design includes a pair of superconducting $\cos(2\theta)$ quadrupoles followed by a 6.6 m long dipole magnet with focusing entrance and exit pole faces, including additional focusing from a field gradient in the dipole. Following the dipole is a third superconducting $\cos(2\theta)$ quadrupole. The first quadrupole Q1 is convergent in the dispersive (vertical) plane. Q2 and Q3 are identical and both provide transverse focusing. The main design characteristics of the spectrometers are shown in Table 3.1.

3.4.2 Detector Packages

As shown in Fig. 3-12, the detectors and all of the Data-Acquisition (DAQ) electronics are located inside a detector hut to protect them against radiation background. The detector package was configured to provide tracking and optimized particle identification for pions, as discussed in this subsection. The calibration and PID cuts will be discussed in Sec. 5.2.1.1 and Sec. 5.3.3, respectively.

Configuration	QQDQ vertical bend
Bending angle	45°
Optical length	24.2 m
Momentum range	0.3-4.0 GeV
Momentum acceptance	$\frac{\lvert p-p_0\rvert}{p_0}$<4.5%
Momentum resolution	2×10^{-4}
Horizontal angular acceptance	±30 mrad
Vertical angular acceptance	± 60 mrad
Horizontal resolution	1.5 mrad
Vertical resolution	4.0 mrad
Central Solid angle	6 msr
Transverse length acceptance	±5 cm
Transverse position resolution	2.5 mm

Table 3.1: Main characteristics of the Left-HRS [124]. The resolution values are for the FWHM. The central solid angle corresponds to the target center and for charged particles with the central HRS momentum p_0. The transverse length and position are along the line, which is horizontal, perpendicular to the central line of Left-HRS acceptance and passing the target center.

VDC

The tracking information on the Left-HRS was provided by a pair of vertical drift chambers (VDCs) [142], which was the first device in the Left-HRS detector package as shown in Fig. 3-12. The Top and side view of the VDCs is shown in Fig. 3-13. The two VDC chambers are placed horizontally with the long edge along the dispersive direction, and with a separation of about 335 mm. In each chamber, there are two wire planes, oriented at 90° to one another, and at 45° with respect to the dispersive directions. In each plane as shown in Fig. 3-14, the sense wires is sandwiched between two cathode planes. There are a total of 368 sense wires for each plane, spaced 4.24 mm apart. The chambers are filled with a gas mixture of argon (62%) and ethane (38%). A 4.0 kV high voltage is applied, which produced the electric field lines as shown by the black arrows in Fig. 3-14. For a typical track, the charged particle passes through the chamber at an angle of about 45° as shown by the red arrow and produces electron and ion pairs along its pass. The ionized electrons drift along the electric field lines (magenta arrows) at a velocity of $\sim 50\,\mu m/ns$ [142] and fires an average of five sensor wires (orange dots in the view of Fig. 3-14). The drift distance

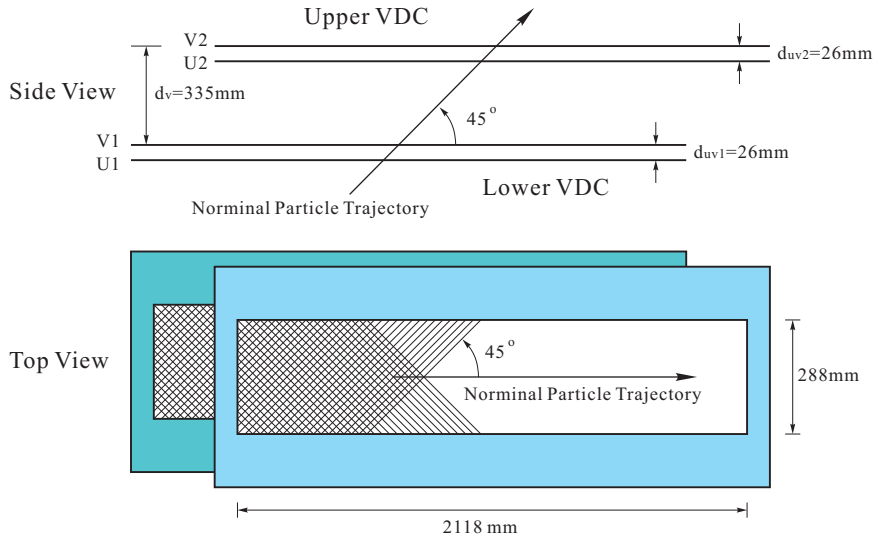

Figure 3-13: Top and side view of VDCs [142]

is calculated using the drift time, which is measured using TDCs. The cross-over point that the track pass through the sense wire plane is determined using a linear fit of the drift distances. The position resolution for VDCs is $\sigma_{x(y)} \sim 100$ μm; and using the cross-over points on the two chambers, the angles of the track are determined to a precision of $\sigma_{\theta(\phi)} \sim 0.5$ mrad. The typical wire efficiency during the E06-010 experiment was close to 100%.

Scintillator Planes

There were two planes of trigger scintillators S1 and S2m in the left HRS, separated by a distance of about 2 m. Both layers was used to form the main trigger for the Left-HRS and S2m was used to provide the timing measurement.

The S1 plane contains 6 thin (5 mm) plastic (BC408) scintillators as shown in Fig. 3-7. Each scintillator is read by two PMTs attached to both ends. The active volume of S1 is 36 cm (length)×29.3 cm (width)×0.5 cm (thickness). The S1 plane is designed to be thin in order to minimize particle absorption, and it provided the first component of the main trigger.

The S2m plane is made of 16 fast plastic scintillator bars with dimensions of 43.2 cm (length)×14 cm (width)×5.08 cm (thickness). Besides forming trigger on the

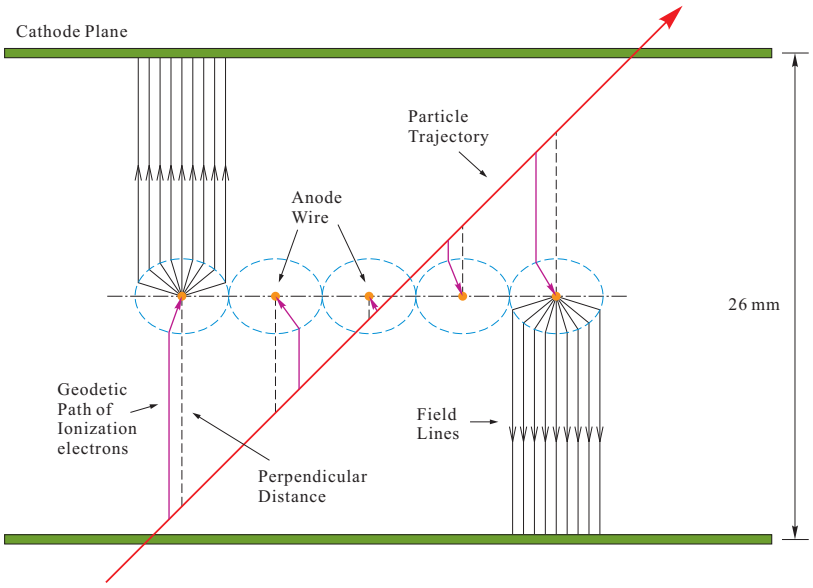

Figure 3-14: Configuration of wire chambers in VDCs [142]. See text for the description.

Left-HRS side, it provided the accurate timing of when the charged particle passed through the detector. The resolution for the Left-HRS time-of-flight[2], was around 160 ps as discussed in Sec. 5.2.3.

Cerenkov Detectors

As shown in Fig. 3-12, three Cerenkov detectors were mounted between the two scintillator planes to provide particle identification for the Left-HRS. From upstream to downstream, they are:

Aerogel Cerenkov Counter (A1): a diffusion-type aerogel Cerenkov counter (A1) was installed in experiment E06-010 to provide hadron identification [124]. As shown in Fig. 3-16, a 9 cm thick radiator is used in A1 with an index of refraction of 1.015, which provides a threshold of 2.84 and 0.803 GeV for kaons and pions, respectively. 24 PMTs are attached to A1 to collect the Cerenkov light. The average number of photo-electrons for GeV-level-energy electrons in A1 is about eight. In the E06-010 experiment, the HRS momentum setting was 2.35 GeV. Therefore, pions would fire the A1, while kaons and protons were below the

[2]time-of-flight for the Left-HRS is the time for charged particles to fly from the reaction point to the S2m timing plane.

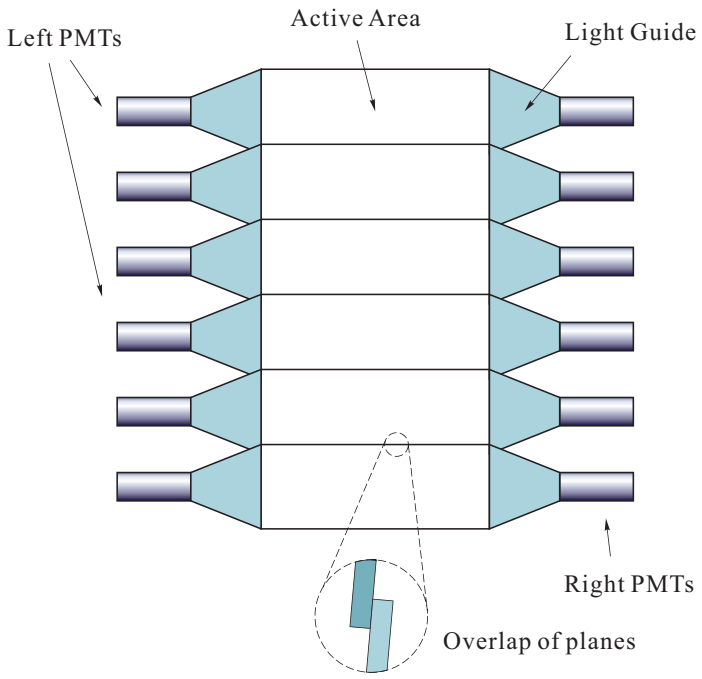

Figure 3-15: Layout of the S1 scintillator counter [143]

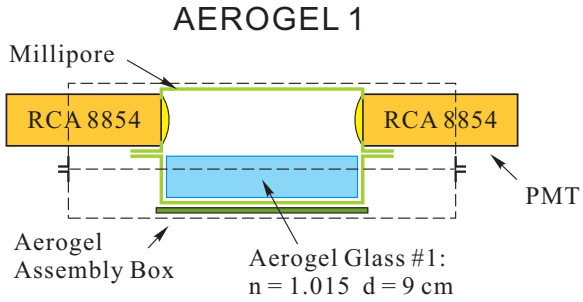

Figure 3-16: Structure for the aerogel counter A1 [143]. Particles enter from the bottom of the figure.

threshold. A1 provided a kaon and proton rejection better than 10:1 for the pion identification [131].

Gas Cerenkov Counter: a 80 cm long gas Cerenkov detector was used to provided electron-hadron separation [144]. With one atmospheric pressure of CO_2, it allows a 99% electron identification with a pion momentum threshold of 4.8 GeV. The total amount of material in the particle path is about 1.4% radiation lengths. There are in total 10 mirrors, together with 10 PMTs to collect the signal. During this experiment, an average of ~6 photo-electrons were observed

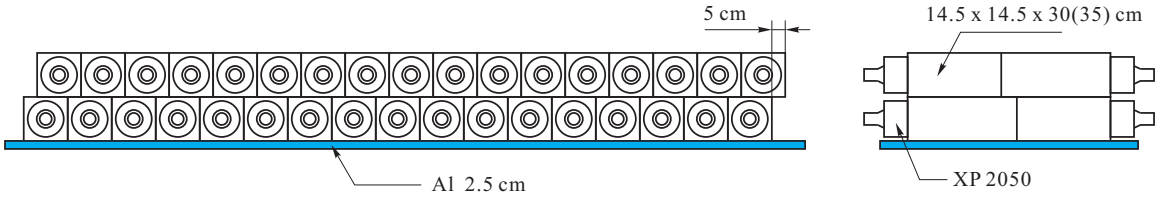

Figure 3-17: Schematic lay-out of the shower detectors [124]. Particles enter from the bottom of the figure.

for an electron event [145].

Ring Imaging Cerenkov Detector (RICH): the Hall A RICH detector was upgraded and installed to provide additional PID for the kaons. A detailed description and analysis of the RICH can be found in Ref. [146]. The data from RICH is essential for the kaon PID and its pion contamination study, but not necessary for the pion PID. Therefore, it was not used in the data analysis of this thesis.

Lead Glass Shower Detector

Two layers of the lead glass shower detectors were installed in the left HRS. Both layers were oriented perpendicular to the particle's velocity direction. Both layers were composed of 34 lead glass blocks of 14.5 cm×14.5 cm× (30 or 35) cm as shown in Fig. 3-17. The goal of the shower system was to provide additional electron rejection capability beyond that of the gas Cerenkov counter by detecting the large energy deposition of the EM showers.

3.5 Data Acquisition (DAQ)

3.5.1 Hall A DAQ

The Hall A data acquisition (DAQ) system uses CEBAF On-line Data Acquisition (CODA) [147] developed by the Jefferson Lab Data Acquisition Group. CODA consists of a set of software and hardware packages which manages the acquisition, monitoring and storage of experiment data. The major components for CODA are

Digitization devices, including time-to-digital converter (TDCs), a analog-to-digital converters (ADCs) and scalars (Sec. 3.5.3). They are installed on front-end crates and convert electronic signal into digitalized information, which is send out through the crates.

Readout controllers (ROCs) which runs on the front-end crates and manages its communication through Ethernet networks.

Trigger supervisor (TS) is the central control point for the data acquisition activity. It is the link between the experiment specific triggering system and the ROCs. External triggers are accepted through the eight input channels, usually known as T1 to T8 (Table 3.2). It accepts and prescales multiple triggers and maintains the "system busy" signal while a trigger is being processed. During this time no additional triggers are accepted until all the ROCs are finished processing the data, which cause DAQ deadtime (analyzed in Sec. 5.2.4) when the trigger rate is not negligible compared with the maximum event processing rate.

Software package which run on a control computer to cache incoming buffers of events from the different ROCs, merge them into the data streams, and write the streams into temporary data disk array. Approximately once per day of data taking, the data on the temporary disk are sent to a mass storage tape silo (MSS) for long-term storage. In addition, a graphical user interface (Run Control) is used to set experimental configuration, control runs, and monitor CODA components.

Besides CODA, the Experimental Physics and Industrial Control System (EPICS) is used to manage the majority part of CEBAF and records assisting information at a slower update rate [148]. The information provides by EPICS, such as beam position, beam current, beam energy, and magnet status, are combined and written to the CODA data stream every few seconds.

Trigger type	Description
T1	Low threshold on BigBite lead-glass
T2	BigBite gas Cerenkov singles
T3	Left HRS singles (S1.AND.S2m)
T4	Left HRS efficiency
T5	Coincidence between BigBite and Left HRS (T1.AND.T3)
T6	High threshold on BigBite lead-glass
T7	BigBite Cerenkov and lead-glass overlap
T8	1024 Hz clock

Table 3.2: Triggers used during E06-010 experiment [140].

3.5.2 Trigger Formation

The triggers were formed in the hardware layer and input into the TS. All eight trigger types provided by TS were used in this experiment and their assignment is shown in Table 3.2. The major triggers used for the physics analysis for this thesis are:

Single BigBite triggers (T1 and T6) were designed to select electrons by triggering on a large total energy deposited in the calorimeter using lower and higher thresholds, respectively [140]. In order to measure the total energy deposited by a particle in the lead-glass detector, a total hardware sum (TSUM) of the two overlapping rows of preshower (2×2=4 blocks) and shower (2×7=14 blocks) was formed, as shown in Fig. 3-18. The TSUM signal was proportional to the total energy deposited by the particle in the calorimeter. This analogue signal then passed through a discriminator, whose threshold could be remotely controlled. Any TSUM that passed the threshold form a BigBite trigger.

Single HRS trigger (T3) was formed by requiring that both S1 and S2m scintillator planes (Sec. 3.4.2) had a paddle with a hit on both sides (a total of four PMTs), as shown in Fig. 3-19. In order to have a constant reference time, the timing of this trigger was tied to the leading edge of the right side PMT signal of the S2m scintillator bars.

Coincidence trigger (T5) was constructed by overlapping T1 and T5 triggers in time. The SIDIS events were based on the T5 trigger. The cable delays were

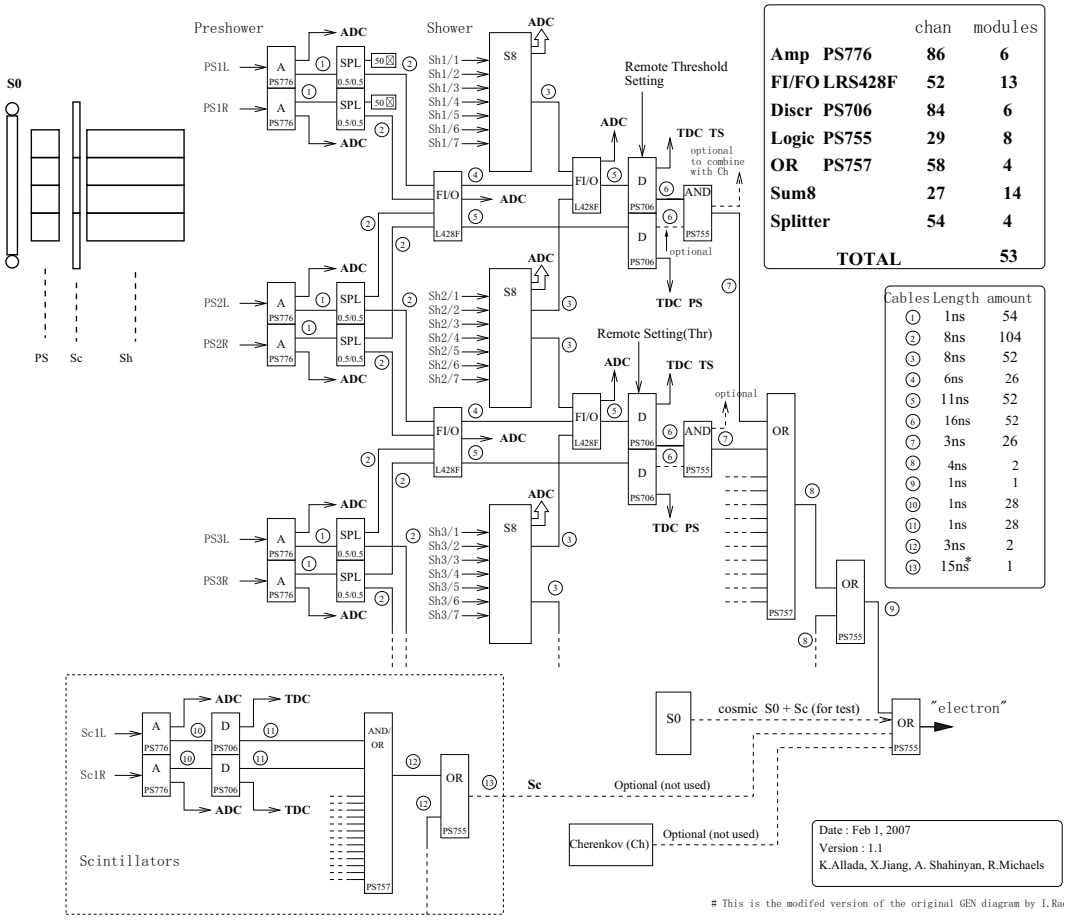

Figure 3-18: The BigBite trigger diagram [140].

set such that T1 arrives 40 ns after T3 and a logic AND between T1 and T3 defines the T5 trigger. The timing of T5 was given by the leading edge of the T1 trigger. After the T5 signal was formed it was fed to the trigger supervisor (TS) which generated an level-one-accept (L1A) signal. This L1A signal was sent to both spectrometers where it was re-timed with respect to the local triggers to form gates for TDCs and ADCs. This setup was shown in Fig. 3-20.

3.5.3 Scaler measurements

Scalers count raw digitalized signals without deadtime. They were used for recording accumulated information including clock (time), the raw counts for various triggers and beam charge. They were needed to normalize the experimental data (e.g.

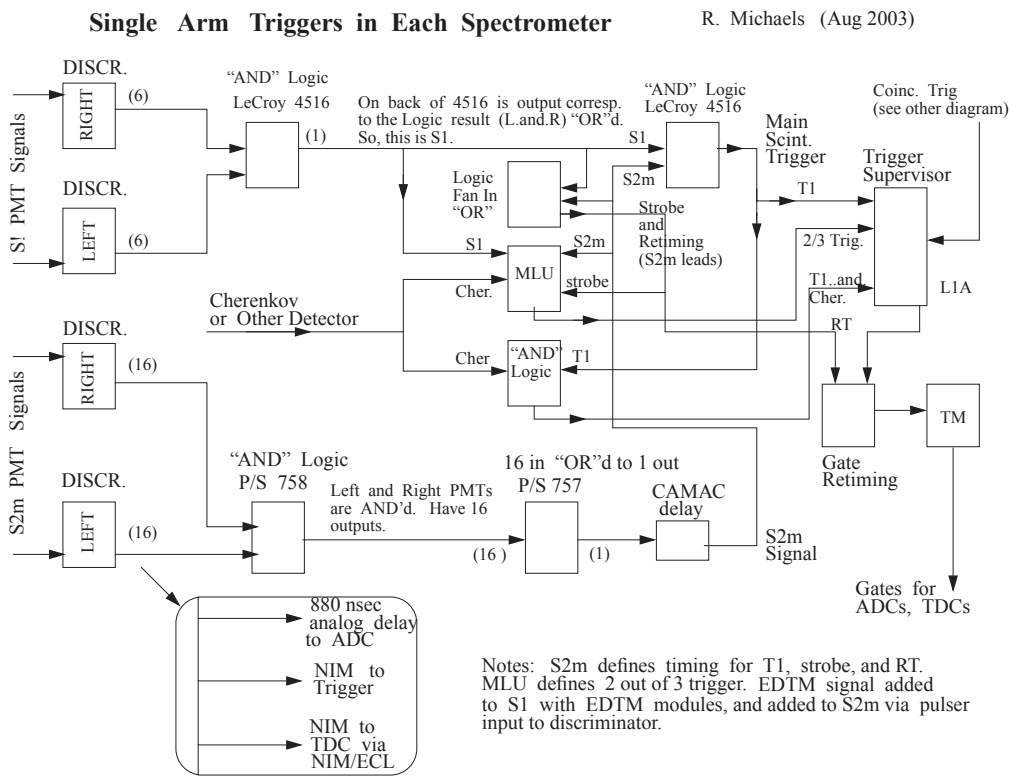

Figure 3-19: Diagram for the left HRS single arm triggers.

Eq. (5.17)) and calculating the DAQ deadtime and livetime (Sec. 5.2.4). In addition, this information was very useful for real time monitoring of the trigger rates, beam current, and raw rates on the individual PMTs.

As shown in Fig. 3-21, a new setup for scalers was used in the E06-010 experiment by gating the scalers based on both beam helicity and target spin states [140]. All five scaler modules had the same input signal, while their gates were different: four scalers were gated with complete combination of the target-spin (Sec. 4.6) and helicity (Sec. 5.6.2) signals: Target+ Helicity+, Target+ Helicity-, Target- Helicity+, Target- Helicity-, and one was ungated. Additionally, all five scalers were also gated with a run gate, which allowed the scalers to count only during the period between run-start and run-stop. For the redundancy and cross-checking purposes, identical scaler setups were constructed in both spectrometers(BigBite and Left-HRS). The scaler

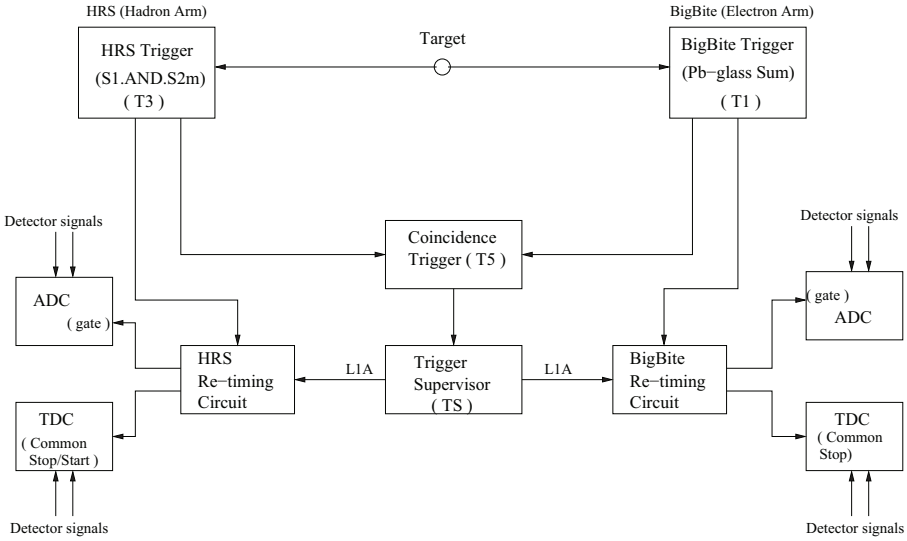

Figure 3-20: Schematic diagram of the setup of the two-spectrometer coincidence trigger (T5) [140]. The signal input the Left-HRS re-timing circuit is (S1 OR S2m) and L1A.

information was inserted into CODA data stream periodically in synchronization to the event flow.

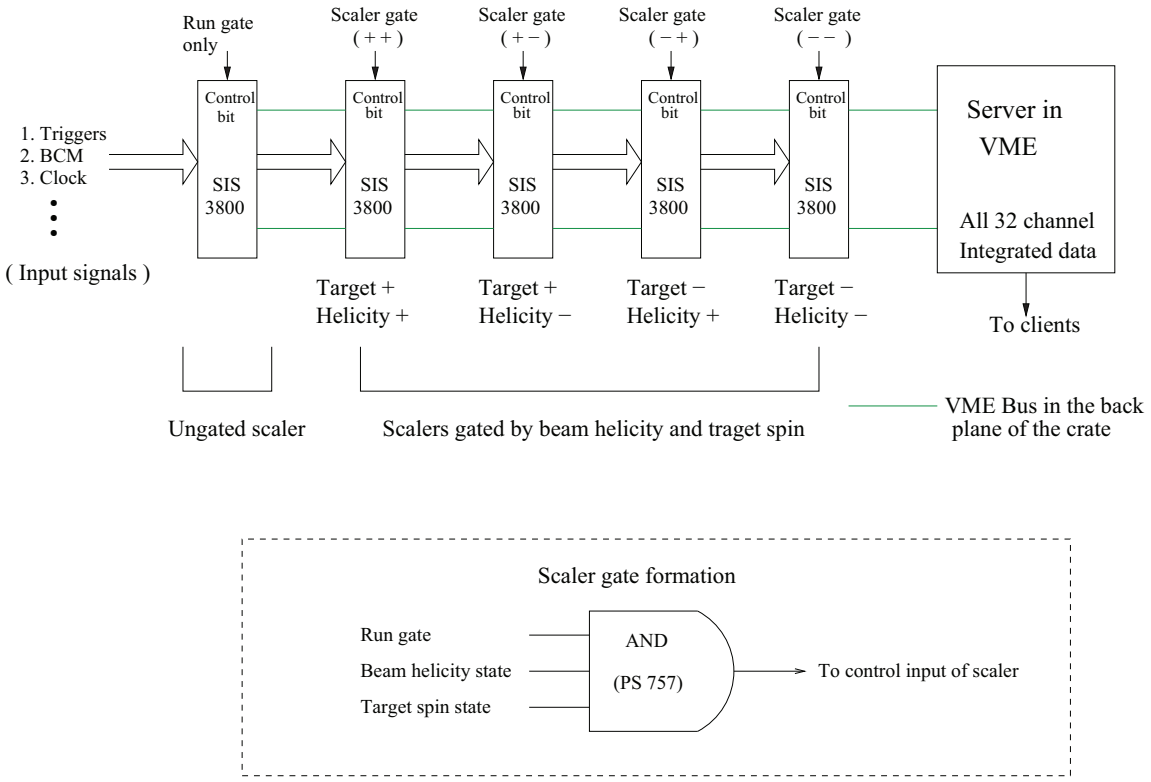

Figure 3-21: Scaler setup and gating scheme using the target spin and beam helicity [140]

Chapter 4

Polarized ^{3}He Target

The ground state ^{3}He wavefunction is dominated by the S-state, in which the two proton spins cancel and the nuclear spin resides entirely on the single neutron [149]. Therefore, a polarized ^{3}He target is the optimal effective polarized neutron target. The target used in this measurement is polarized by spin-exchange optical pumping of a Rb-K mixture (Sec. 4.1.2). A significant improvement in target polarization compared to previous experiments was achieved using spectrally narrowed pumping lasers (Sec. 4.2.3), which improved the absorption efficiency. The ^{3}He gas of ~10 atm pressure was contained in a 40-cm-long glass vessel (Sec. 4.2.1), which provided an effective electron-polarized neutron luminosity of $10^{36}\,\mathrm{cm}^{-2}\mathrm{s}^{-1}$. The beam charge was divided equally among two target spin orientations transverse to the beamline, parallel and perpendicular to the central $\vec{l}$-$\vec{l}'$ scattering plane[1], which was controlled by the directions of the holding magnetic field (Sec. 4.2.2). Within each orientation, the spin direction of the ^{3}He was flipped every 20 minutes through adiabatic fast passage (Sec. 4.6). The average in-beam polarization was $(55.4 \pm 2.8)\%$ and was measured during each spin reversal using nuclear magnetic resonance (Sec. 4.3), which in turn was calibrated regularly using electron paramagnetic resonance (Sec. 4.4).

[1] In this experiment, the central l-l' scattering plane is defined using the nominal electron beam $l = e$ and the central line of the BigBite spectrometer which detected the scattered electron $l' = e'$. This plane is horizontal at the height of the Hall A target center.

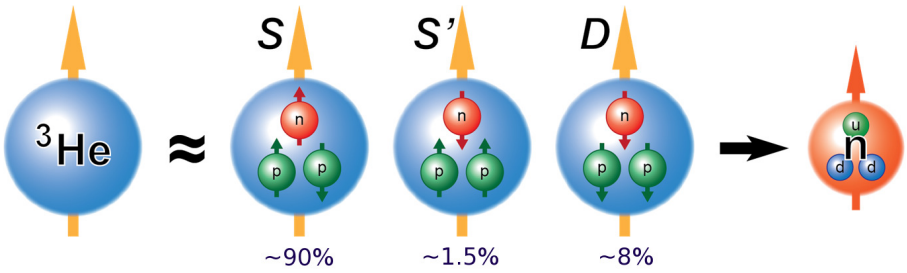

Figure 4-1: Illustration of ^{3}He wave function [150]. The probability for each state was reviewed in Ref. [151].

4.1 Principal of Operation

4.1.1 Polarized ^{3}He as Effective Polarized Neutron Target

Information from both the proton and neutron is essential to study the structure of the nucleon. However, experiments on free neutrons are difficult due to its short life time (885.7±0.8 s [6]). Therefore, in order to achieve the luminosity required to make precise measurements of asymmetries, stable light nuclei, such as deuteron or ^{3}He, are typically used as effective neutron targets.

The idea of using polarized ^{3}He nuclear target as an effective neutron target was first investigated by Blankeider and Woloshyn in the closure approximation [152]. The ground state of the polarized ^{3}He is dominated by the S wave [152, 153], in which the spin of the two protons cancel due to the Pauli exclusion principle and the neutron contributes to the entire spin of ^{3}He. Additionally, there are small components of D state and S' state in the ground state of ^{3}He as shown in Fig. 4-1. The contribution of the P state is small enough to essentially ignore.

Polarized ^{3}He targets have been used at MIT-Bates, SLAC, DESY, MAMI, and Jefferson Lab to study the neutron electromagnetic structure and its longitudinal spin structure functions. In experiment E06-010, transversely[2] polarized ^{3}He was first used to probe the transverse spin structure of the neutron.

[2]the target is polarized perpendicular to the electron scattering plane.

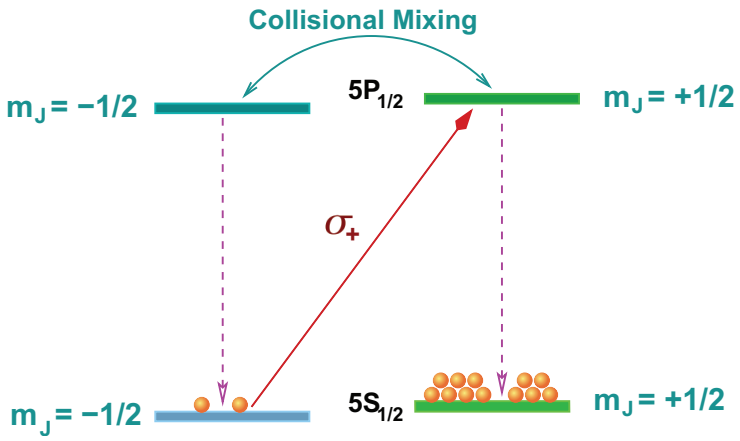

Figure 4-2: Optical pumping of Rb by a circularly polarized laser towards the + spin state. The figure is taken from Ref. [141].

4.1.2 Spin-Exchange Optical Pumping (SEOP)

The term spin-exchange optical pumping (SEOP) refers to a two-step process. First alkali metal atoms (heated to the vapor form) are optically pumped with a polarized laser, and quickly polarized. Second, that polarized alkali metal atom exchanges its spin with a noble gas nucleus, such as ^{3}He.

As a technical breakthrough, a new spectrally narrowed laser [154] was first used at Jefferson Lab with this experiment, which improved the laser absorption and maximum achievable ^{3}He polarization. The details will be further discussed in Sec. 4.2.3.

4.1.2.1 Optical Pumping

As the first step to polarize ^{3}He nucleus, a polarized electron source is generated, which can transfer its spin to ^{3}He. The polarized electron is provided by the outermost shell in the Rb and K atoms which are vaporized and mixed with the ^{3}He gas. In the optical pumping process, circularly polarized photons are used to polarize the outermost-shell electrons in Rb, which subsequently transfer its polarization to the K atoms and the ^{3}He nucleus.

To help illustrate the concept of optical pumping, the spin of Rb nucleus is first ignored. There is a single outermost shell electron in the Rb atom, whose ground state is the $5S_{1/2}$ state. Using 795 nm infrared lasers, the ground state Rb can be

excited to the $5P_{1/2}$ state. In an external magnetic field, both states split through Zeeman splitting to two sub-levels, $m_J = \pm 1/2$. As illustrated in Fig. 4-2, given a polarized laser light, whose spin direction is parallel to the magnetic field, the excitation is selected from $5S_{1/2}\,(m_J = -1/2)$ to $5P_{1/2}\,(m_J = +1/2)$ only, and vice verse. The excited atoms decay to both $m_J = \pm 1/2$ sub-levels. By pumping with right circularly polarized light, the alkali sample quickly becomes highly polarized.

The nuclear spin of Rb is $I = 5/2$ for ^{85}Rb and $I = 3/2$ for ^{87}Rb, which further complicates the picture. Therefore, the $5S_{1/2}$ state splits through hyper-fine interaction to levels with quantum number of $F = I \pm J$, which further splits into levels of $m_F = -F, F+1, \cdots, F$ with the weak holding field (25 Gauss) used for this target. The exact energy level is described by the Breit-Rabi formula [155], Eq. (4.11). Using similar arguments as in the last paragraph, the Rb atom is polarized to the $m_F = \pm F = \pm(I + 1/2)$ states depending on the direction of the laser spin.

When the excited atoms spontaneously decay back to the $m_J = -1/2$ state, they emit photons, which have the same wavelength as the pumping laser. These photons can depolarize Rb atoms and reduce the pumping efficiency. Therefore, a small amount (~1% in pressure) of nitrogen gas is added to the sample. As a diatomic molecule, nitrogen has vibrational and rotational degrees of freedom to absorb energy and enables radiation-less decay of the Rb atoms, which is the dominant process (95% [156]) in the decay.

4.1.2.2 Spin Exchange

The idea of spin exchange is illustrated in Fig. 4-3. After Rb atoms are polarized by optical pumping, they subsequently transfer their polarization to the K atoms and finally to the ^{3}He nucleus. The spin-exchange cross section between the two alkali-metals is very large, and the spin-exchange rate is over 200 times faster than the typical alkali spin-relaxation rates [157, 158, 159]. Therefore, the K vapor has an electron polarization approximately equal to that of the Rb vapor.

When polarized alkali gas (Rb and K) coexists with ^{3}He, the atoms can transfer their electron polarization to the ^{3}He nuclei, which was first discovered by Bouchiat,

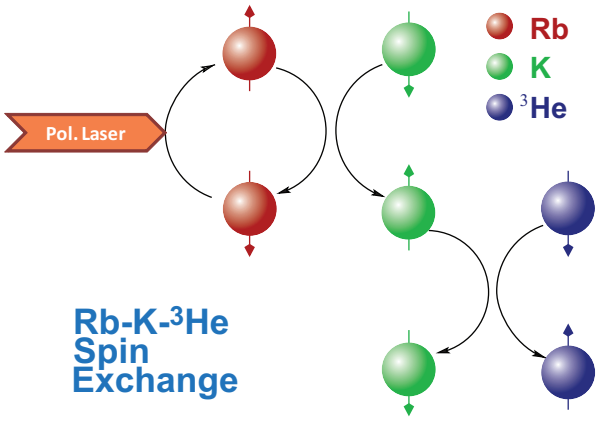

Figure 4-3: Spin exchange in a Rb-K hybrid cell. The figure is taken from Ref. [141].

et. al. [160]. The transfer of angular momentum is dominated by the binary collision between atoms. During the collision, the spin-exchange is due to hyperfine interaction between the alkali electron and the ^{3}He nucleus [161],

$$H_{SE} = \alpha \boldsymbol{I} \cdot \boldsymbol{S}, \tag{4.1}$$

where $\boldsymbol{I}$ is ^{3}He nuclear spin, $\boldsymbol{S}$ is the spin of alkali electron and α is the coupling function. This interaction also shifts the alkali Zeeman frequency proportionally to the ^{3}He polarization, which is used as one of the target polarimetries as discussed in Sec. 4.4.

Although it is difficult to calculate the exact value of α, the spin-exchange rates for ^{3}He, γ_{SE}, were measured experimentally as function of alkali density,

$$\gamma_{SE} = k^A_{SE}[A], \tag{4.2}$$

where $[A]$ is the alkali density and k^A_{SE} is the spin-exchange rate constant for the corresponding alkali metal. For Rb, several measurements were reported, as summarized in Table I of Ref. [162]. The average result of the repolarization [162, 163] and rate balance methods [162] is $k^{Rb}_{SE} = 6.8 \times 10^{-20}\,\mathrm{cm}^3/s$. For K, $k^K_{SE} = 5.5 \times 10^{-20}\,\mathrm{cm}^3/s$ was reported in Ref. [164, 165].

Another important parameter of SEOP is the spin-exchange efficiency, η, where

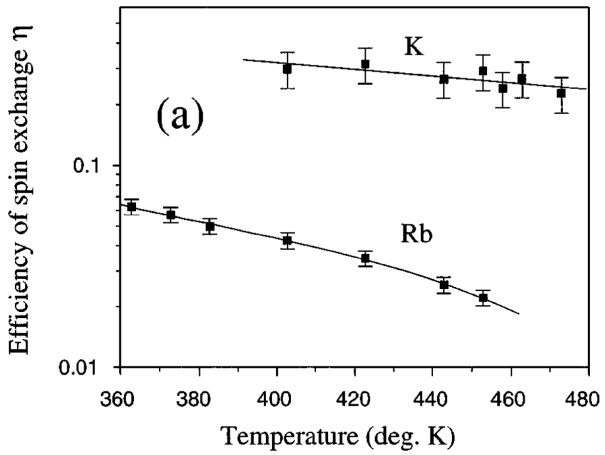

Figure 4-4: Spin-exchange efficiencies (note logarithmic scale) for ^{3}He-Rb (7.0 amagat of ^{3}He) and ^{3}He- K (6.9 amagat of ^{3}He) versus temperature [163].

$1/\eta$ is the minimum number of photons needed to provide $\hbar/2$ units of spin to an initially unpolarized ^{3}He nucleus and fully polarize it [163]. Therefore, η is the ratio of spin-exchange rate and the total spin relaxation rate. It has been measured for both K and Rb as in Fig. 4-4.

Although the efficiency for K is one order of magnitude higher than that of Rb [163, 165], there is still no source of commercially available lasers of sufficient power and narrow linewidth to polarize K for an electron target. A method of hybrid polarization may be adopted to achieve high polarizations [158, 159]. The method involves a mixture of Rb and K vapors. Since K and Rb spin exchange rate is large, their polarizations are similar. The efficiency with a mixture of alkali vapors was studied for various K/Rb density ratios as in Ref. [165]. For the E06-010 target, the ratio is around $[K]/[Rb] \sim 5$.

The evolution of ^{3}He polarization using SEOP will be described in Sec. 4.5 with a two-chambered cell model. Starting from a low polarization, the ^{3}He polarization can be monitored as a function of time as shown in left plot of Fig. 4-17. For the most part[3], the curve can be described with a exponential fit as shown in Eq. 4-17, whose time constant is related to the spin exchange rate. The typical time constant is ~4 hour.

[3]The initial part of the curve contains another fast-decaying component as described in Eq. (4.21).

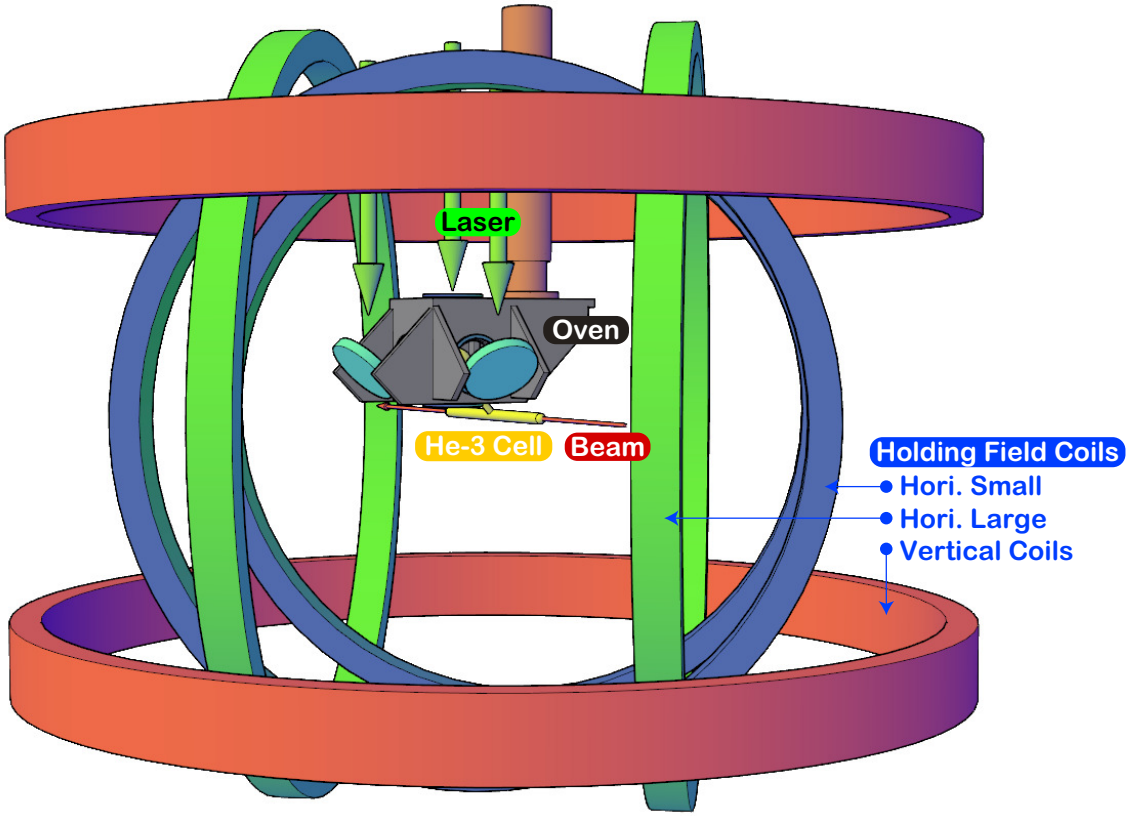

Figure 4-5: Polarized ^{3}He target setup [150]. The holding field coils are three pairs of Helmholtz coils as discussed in Sec. 4.2.2.

4.2 Target Setups

A polarized ^{3}He target system has been successfully used for the E06-010 experiment. The target was upgraded with hybrid Rb-K cells and spectrally narrowed pumping lasers. Additionally, new features include an automated rapid spin-flip subsystem and capability of polarizing in the vertical direction.

Fig. 4-5 shows the core part of target. It includes the polarized ^{3}He cell, the oven, the pumping laser beams and the Helmholtz coils, which provide the holding magnetic field. These elements of the target will be discussed in this section.

4.2.1 ^{3}He Cell

The polarized ^{3}He gas was contained in hand-blown glass cells, which were made of GE180 aluminosilicate glass [170]. Before the cell was sealed, it was filled with ~8 atm

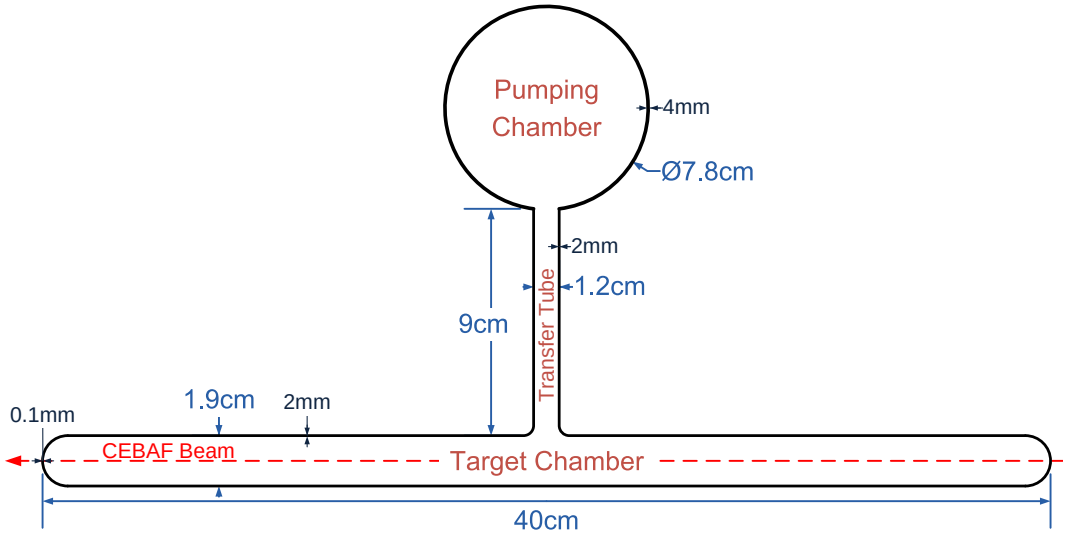

Figure 4-6: Glass cell used for the polarized^{3}He gas. Typical (outer) dimensions and wall thickness for E06-010 cells are shown. The "pull off", which is a small tube with one end attached to the pumping chamber and sealed at the other end, is not drawn.

of ^{3}He, ~1% of N_2 gas and a mixture of rubidium and potassium metal. As shown in Fig. 4-6, a typical cell used in Jefferson Lab consists of three parts

The pumping chamber (*pc*)**,** which is a three-inch sphere with a typical wall thickness of 4 mm. There is a small (~4 cm long) tube or "pull off", attached to the pumping chamber, which was used to seal the cell and detach it from the rest of the cell filling apparatus.. Cells made for this experiment oriented the "pull off" parallel to the target chamber to avoid intruding into the laser beam. In the working setup, the pumping chamber was heated to ~270°C and the alkali metal was vaporized. Then the laser polarization was transferred to the alkali atoms and eventually to the ^{3}He nuclei.

The target chamber (*tc*) is a 40 cm long glass tube with an typical diameter of 1.9 cm. During the experiment, the CEBAF electron beam passed through this chamber's glass windows and interacted with the polarized ^{3}He nuclei. The thickness of the beam window on both ends of the tube was minimized to 0.10−0.15 mm. The side walls were around 1.6 mm thick. This chamber was cooled with ^{4}He jets on both beam windows to an average of 50~70°C. The

Name	Astral	Maureen	Brady
Used Dates	Oct-Nov 08	Nov-Dec 08	Jan-Feb 09
Filled at	UVa [166]	W&M [167]	UVa [166]
V_{pc} (cm^3)	164.92	180.75 [167]	169.27
V_{tc}(cm^3)	79.47	78.97 [168]	74.57
V_{tt}(cm^3)	6.77	5.81 [168]	5.98
n_0 (amagat) [168]	8.12	7.80	7.95
Lifetime (hour) [166]	49	29	36
$N_2/^3He$ (filling)	1.36%	1.32%	1.4%
$N_2/^3He$ (pressure curve) [169]	1.48 ± 0.07%	1.6 ± 0.3%	1.0 ± 0.29%

Table 4.1: Characteristics of ^{3}He cells used by experiment E06-010 [166, 167]. n_0 is the ^{3}He density when the cell is at room temperature. Amagat is a density unit and 1 amagat is the gas density at 0°C and 1 atm pressure.

average density of the ^{3}He gas was around 10 amagat[4].

The transfer tube (*tt*) connected the pumping and target chambers. Its outer diameter was around 12-13 mm; the wall thickness[5] was around 1.6 mm; the overall length was around 9 cm. The higher polarization ^{3}He gas diffused from the pumping chamber to the target chamber at a rate of around 1 circulation per hour. Temperature in the tube dropped from the pumping chamber end (~270°C) to the target chamber end (~100°C) and the majority of alkali vapor condensed before exiting the pumping chamber.

The main characteristics of the cells used in this experiment are summarized in Table 4.1. The ratio of N_2 to ^{3}He filling densities of all three target cells are compared with those obtained from pressure curve data. The difference was used as the systematic uncertainty for this ratio which is used in the N_2-dilution analysis (Sec. 5.5.3).

4.2.2 Holding Magnetic Field

A uniform holding magnetic field, which had an average strength of 25 G and a typical gradient of 10-30 mG/cm, covered the ^{3}He cell. The direction of ^{3}He spin was either parallel or antiparallel to this magnetic field, for ^{3}He spin state +1 or −1,

[4]Amagat is a density unit and 1 amagat is the gas density at 0°C and 1 atm pressure.

[5]Transfer tube wall thickness was measured to be 1.627 ± 0.013 mm for a cut-open cell, Hamlet [171] and 1.6 mm for cell Maureen, one of the three production cells [172].

Coil Name	Inner Diameter (m)	Number of turns	Resistance (Ω)	Power Supply
Hori. Small	1.27	256	3	KEPCO BOP 36-12D
Hori. Large	1.45	272	3	
Vertical	1.83	355	4.4	Agilent 6675A

Table 4.2: Basic characteristics and power supplies of Helmholtz coils, which generate the holding magnetic field.

Field	I_{Small} (A)	I_{Large} (A)	I_{Vertical} (A)
Transverse	6.234	-4.621	0.712
Vertical	0.329	-0.958	14.093

Table 4.3: Current set points for each coil (Table 4.2) for generating two standard 25 G holding fields with different direction.

respectively. The holding magnetic field was generated using three pairs of Helmholtz coils, oriented in three mutually orthogonal directions as shown in Fig. 4-7, i.e., the Horizontal Small Coils (Hori. Small), the Horizontal Large Coils (Hori. Large) and the Vertical Coils. The basic characteristics of these coils are shown in Table 4.2. The magnitude and direction of the holding magnetic field were controlled by the electrical currents in these coils. Two holding magnetic field directions were used in experiment E06-010:

Transverse: in the central scattering plane[6] and perpendicular to the nominal beam direction. The field direction was towards the BigBite side.

Vertical: perpendicular to the central scattering plane and upwards.

The set current in each pair of coils to generate these two fields was listed in Table 4.3. The direction of the holding field was measured to a precision of better than 0.5° using two compass systems:

- The transverse field direction was measured by the longitudinal compass, which was a 40 cm long iron bar covering the target length.

[6]The central scattering plane was defined by the Hall A central beam line and the central line of the BigBite spectrometer which detected the scattered electrons.

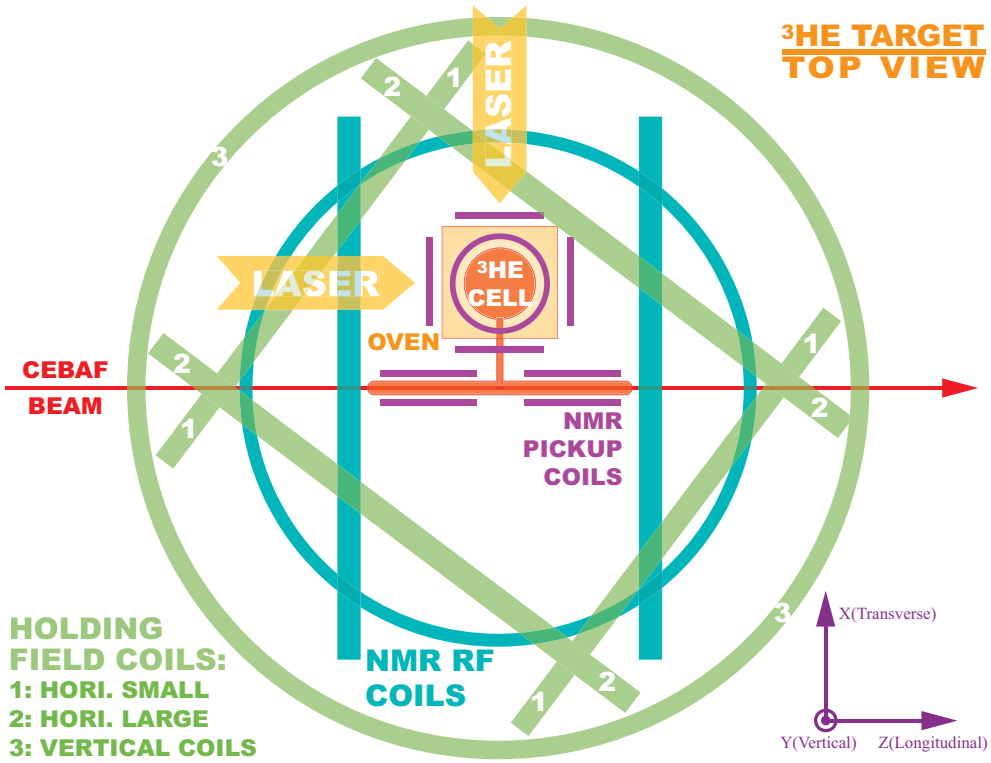

Figure 4-7: Top view of the coil setup for the ^{3}He target. $+\hat{X}$ direction is towards left HRS. A pick-up coil at the bottom of the oven is not shown. The holding field coils are shown in green; the NMR RF coils are shown in blue; the NMR pickup coils are shown in purple (see Sec. 4.3 for the NMR polarimetry). The two vertical holding field coils overlap each other from this viewpoint. A 3-D view is shown in Fig. 4-5.

- The vertical field direction was measured by a vertical compass, which was a floating device in air with a magnetic cylinder and an optical encoder attached to it [145]. The angular resolution for the optical encoder was 0.09°. The calibration procedures using this compass was discussed in details in Ref. [145].

4.2.3 Laser System

Experiment E06-010 was the first to use a spectrally narrowed laser system, which significantly improved the target polarization. This experiment started with a Coherent FAP (Fiber Array Package) system with spectral widths of $\Delta\nu \approx 2$ nm, which was used by previous experiments at Jefferson Lab [173, 141, 127]. A few days into the production data taking, the FAP lasers were gradually replaced by Newport/Spectra-Physics COMET lasers. The new lasers have volume Bragg grat-

ings (VBG) coupled directly to the output of the laser diode bars. A narrow slice of the gain profile is amplified by reflecting wavelength-selected light by the VBG back into the laser diode bar. The resulting output laser beam has a spectral width of $\Delta\nu \approx 0.2$ nm for 90% of the total power [154], which significantly improved the absorption of the laser light by Rb atoms and the ^{3}He polarization. The central wavelength can be fine tubed by adjusting the temperature to better match the absorption peak for the rubidium atoms. For the E06-010 target, the typical target polarization increased from $40-45\%$ to around 60% after the pumping lasers were switched from FAP system to the COMET lasers. More than 97% of the production data benefited from this new laser technology. At typically working conditions, three COMET lasers with a combined CW[7] power of 75 W were used.

The lasers were installed in an interlocked room outside the experimental hall for the reasons of safety, radiation and ease of maintenance. Fifteen 75 m long fibers were used to connect the laser source to the target setup. A typical power loss in a 75 m long fiber was around 6%. At the target end, five fibers were combined to one output through a 5-to-1 combiner before entering the optics setup.

Three lines of lasers existed for three possible pumping directions: vertical, horizontal transverse-to-beam (or transverse) and longitudinal-to-beam (or longitudinal)[8]. Each line used a separate but similar optics setup. The vertical-pumping optics is shown in Fig. 4-8. The purpose of the optics is to deliver the laser light to the pumping chamber of the ^{3}He cell and to circularly polarize the light. A two-lens system was used to focus the light exiting from the 5-to-1 combiner. The lenses were tuned in such a way that the diameter of the laser spot on the pumping chamber is slightly smaller than the diameter (~3 inch) of the pumping chamber. A balance was found between covering the majority of the chamber and avoiding hitting the edges, which can scatter the light and increase the depolarization effect. Two six-inch dielectric mirrors (top left of Fig. 4-8) were used to reflect the light to the pumping chamber. To preserve the circular polarization of the laser, the orientation of the mirrors was

[7] continuous wave (CW)

[8] The first two directions were used by E06-010. The longitudinal polarization was used by the sister experiments, E06-014 [174] and E05-102 [175].

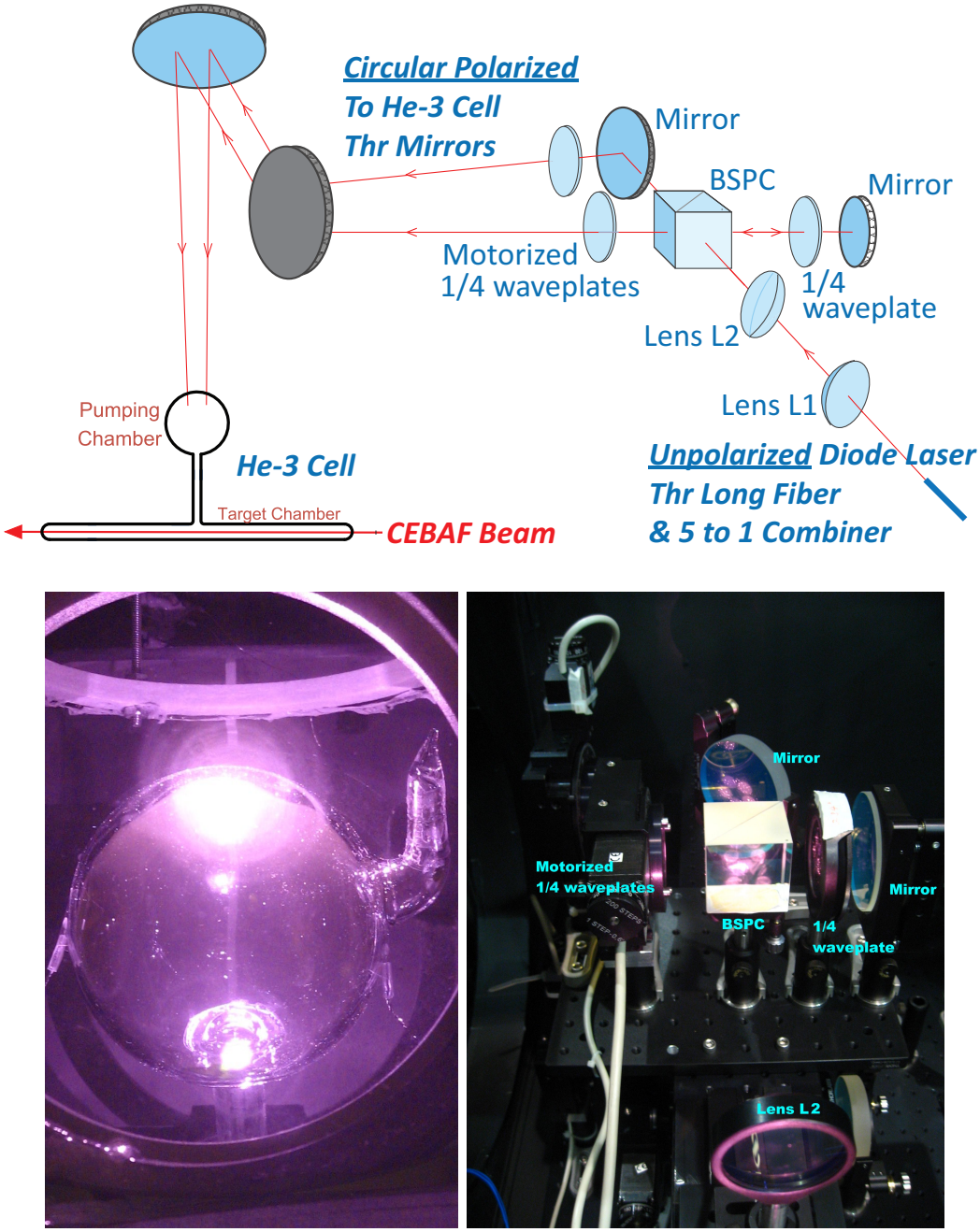

Figure 4-8: Top: schematic diagram of the optics setup for the vertical pumping laser line. Bottom right: photo of the polarizer (for vertical polarization, identical to that for transverse) from a similar viewing angle as the top diagram. Bottom left: photo of the pumping chamber of cell Astral under a vertical laser beam coming from the top. The magenta color of the infrared laser light was due to the imperfect infrared filtering of the camera (Canon SD 700SI).

designed to reflect the laser by 90 degree with two scattering planes perpendicular to each other[9].

Between the lens and six-inch mirrors, there was a set of optics components, which circularly polarized the laser light. The sign of the laser polarization was remotely controlled to enable frequent spin reversal (detailed in Sec. 4.6). Following Fig. 4-8, the principal of the polarizer will be discussed as following: after lens L2, the unpolarized laser beam was split and linearly polarized by a beam splitting polarizing cube, or BSPC: the majority of the P-wave component, which is parallel to the reflecting plane, transmits through the cube and is reflected towards the six-inch mirror. All the S-wave component, which is perpendicular to the reflecting plane, is reflected 90 degrees to the right side of the beam. Then the S-wave passes through a quarter-wave plate, is then reflected from a flat mirror, and passes through the quarter-wave plate again. The result of these two passes is that the light is now in the P-wave state and passes back through the BSPC. At this point, both beams are linearly polarized P-waves heading towards the first six-inch mirror. Before hitting of the mirror, each beam pass through a motorized quater-wave plate, whose light axises are 45 degrees relative to the laser polarization direction, and attains a circular polarization. By remotely rotating both motorized quater-wave plate by 90 degrees, the helicity sate of the laser is flipped, therefore, flipping the rubidium states of $m_F = \pm 3$ and the pumping spin state of ^{3}He nuclei.

Due to the use of high power infrared laser, the target system was optically isolated from the rest of experimental setup. Sensors were placed on the optics enclosure, which would trip the lasers if the container was inadvertently opened. During laser alignment work, the whole experimental hall was placed under laser controlled access.

[9] An exception was the longitudinal mirrors, whose scattering planes were parallel to each other. A special technique that required an additional quarter-wave plate was invented to recover the laser polarization [176].

4.2.4 Other Elements of Target System

4.2.4.1 Oven System

In working conditions, the pumping chamber of the ^{3}He cell was heated through hot air at 230°C to produce alkali vapors. The heating and the mechanical support of the cell was provided by the oven system (Fig. 4-5). The ^{3}He polarization was sensitive to the external magnetic field. Therefore, a calcium-silicate based nonmagnetic material of CS85 was used to construct this oven. Five glass windows were placed on the sides to allow the pumping laser light to enter and exit the oven.

The heating for the oven was provided by a flow of pressurized air. The air was filtered and passed through two heaters before entering the oven. Both the inlet and the exhaust pipe were enclosed in a tube that supported the oven and was wrapped with insulation material. the internal air temperature for the oven was measured using a resistance temperature detector (RTD). The RTD read back was input into a digital proportional–integral–derivative (PID) controller, which controlled the power on the heater and therefore the temperature of the oven. Through out the experiment, the oven air temperature readout was kept stable at 230 ± 2 degrees.

4.2.4.2 Target Ladder

A target ladder was attached below the oven to provide several additional choices of target other than polarized ^{3}He. The ladder can move with the oven system vertically to place the chosen target in the height of the electron beam. The assembly and side view of the ladder is shown in Fig. 4-9. The available targets in experiment E06-010 ordered from top to bottom are as following:

Polarized ^{3}He, which was the 40 cm long target chamber of the ^{3}He cell

"Holey" carbon target, which is a single carbon foil with a hold drilled in the horizontal center. By scanning the detector rate verses the beam position around this hole, the relative alignment between the beam and target ladder can be performed at a precision of about 1 mm.

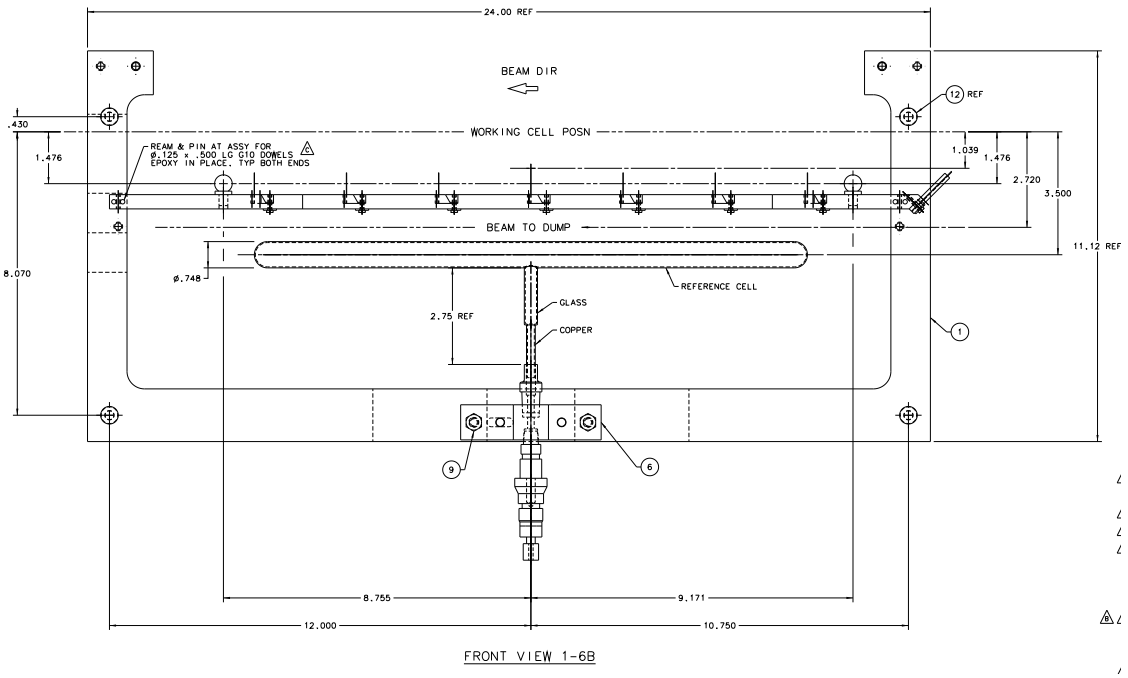

Figure 4-9: The side view of the target ladder

Multi-carbon target plus BeO foil: Seven carbon foils, averagely spaced and covering the 40 cm length of the target chamber, were used to provide optical alignment data for the spectrometers. Special structures on the support bars of the foils can be used to survey the location of the foil relative to the predefined hall center. In addition, a beryllium oxide (BeO) foil was placed upstream to the carbon foils and outside the normal acceptance of the spectrometers. It was used to visually inspect the beam spot and correct the beam position at a precision of few millimeters.

The empty target was a special gap on the ladder to allow beam pass straight though during beam tuning.

The reference cell was a glass tube, similar to the target chamber of the ^{3}He cell, but with an intake/outtake pipe connected to a gas system. It provided calibration data from various pure gas targets with known pressures, which included nitrogen, hydrogen and ^{3}He (unpolarized).

4.2.4.3 Collimator

During the experiment, target collimators were installed to shield the high energy electrons and high energy photons generated from the two beam windows of the target scattering chamber. Each collimator was made of tungsten powder, and their thickness was about 10 cm in the nominal particle's momentum direction.

4.3 NMR Polarimetry

There were two primary types of polarimetry used in experiment E06-010: nuclear magnetic resonance (NMR) polarimetry and electron paramagnetic resonance (EPR) polarimetry. This section will discuss the NMR polarimetry, which determines the target polarization by measuring the ^{3}He NMR signal during spin reversal of the ^{3}He nuclei through the adiabatic fast passage (AFP) [177] technique.

4.3.1 Principle

In a classical picture, consider a free particle with spin $\vec{I}$ and magnetic moment $\overrightarrow{M} = \gamma\vec{I}$, where γ is the gyro-magnetic ratio. When placed inside a magnetic field $\vec{H}_0$, the particle experiences a magnetic torque and follows a rotation equation of

$$\frac{d\overrightarrow{M}}{dt} = \gamma\overrightarrow{M} \times \vec{H}_0 \tag{4.3}$$

We can further add an additional small field of $\vec{H}_1$, which is transverse to $\vec{H}_0$ and rotates around with an angular frequency, $-\vec{\omega}$, which is parallel to $\vec{H}_0$. It is more convenient to represent Eq. (4.3) in a rotational coordinate system with the same angular frequency ($-\vec{\omega}$) relative to the lab frame, in which $\vec{H}_0 = H_0\hat{z}$, $-\vec{\omega} = -\omega\hat{z}$ and $\vec{H}_1 = H_1\hat{x}$,

$$\frac{d\overrightarrow{M}}{dt} = \gamma\overrightarrow{M} \times (\vec{H}_0 - \frac{\vec{\omega}}{\gamma} + \vec{H}_1) \tag{4.4}$$

$$= \gamma\overrightarrow{M} \times \left(\left(H_0 - \frac{\omega}{\gamma}\right)\hat{z} + H_1\hat{x}\right) \tag{4.5}$$

Then the effective field the particle experiences in this frame can be defined as

$$\vec{H}_e \equiv \left(H_0 - \frac{\omega}{\gamma}\right)\hat{z} + H_1\hat{x} \tag{4.6}$$

Consider that the spin is originally along $\vec{H}_e$ and $\left(H_0 - \frac{\omega}{\gamma}\right)$ begins to slowly vary with time from $\left(H_0 - \frac{\omega}{\gamma}\right) \ll -H_1$, passing zero and ending at $\left(H_0 - \frac{\omega}{\gamma}\right) \gg H_1$. If $\left(H_0 - \frac{\omega}{\gamma}\right)$ changes slow enough to satisfying the quantum adiabatic limit [178], $\frac{d}{dt}\left(H_0 - \frac{\omega}{\gamma}\right)/H_1 \ll \gamma H_1$, the spin will stay in the same quantum state, follow the direction $\vec{H}_e$ and reverse its direction.

During adiabatic fast passage, the rotational H_1 field was provided by a linear oscillating magnetic field (usually called the RF field) perpendicular to $\vec{H}_0$ with a angular frequency of $|\omega|$ and magnitude of $2H_1$. It can be decomposed into two rotational components with the same magnitude H_1 and opposite rotations $\pm\omega\hat{z}$. The $+\omega\hat{z}$ component does not play any role during an AFP and will not be considered here. In the typical conditions of experiment E06-010, $H_1 \sim 10^{-1}$ Gauss.

There are two general types of AFP techniques used to introduce a time dependent $\left(H_0 - \frac{\omega}{\gamma}\right)$. Both were used in experiment E06-010:

- AFP field sweep, during which, the RF field was fixed at a angular frequency of $|\omega| = \omega_0 \sim (2\pi) \times 91$ kHz and the holding field scanned at $H_0(t) \sim 25\,\text{Gauss} + t \times 1.2\,\text{Gauss}/s$[10], sweeping from lower than $\omega_0/\left|\gamma_{^3\text{He}}\right| \sim 28\,\text{Gauss}$ to higher fields, where $\gamma_{^3\text{He}} = g_{^3\text{He}}\mu_N/\hbar = -20.4 \times 10^3\,\text{rad}\,s^{-1}\,\text{Gauss}^{-1}$.

- AFP frequency sweep, during which, the holding field remains fixed at $H_0 \sim 25\,\text{Gauss}$ and the RF frequency sweeps at $\frac{|\omega(t)|}{2\pi} \sim 77\,\text{kHz} + t \times 4\,\text{kHz}/s$, which passes through the resonance around 81 kHz.

Besides the adiabatic relation as discussed above, the sweep speed was set fast enough so that $\left|\vec{H}_e\right|$ passed through the minimum quickly and the ^{3}He relaxation was small.

[10] 25 Gauss is the nominal field strength

To summarize, the sweep speed limits are

$$\frac{D\left|\nabla H_0\right|^2}{H_1^2} \ll \frac{\frac{d}{dt}\left(H_0 - \frac{\omega}{\gamma}\right)}{H_1} \ll \left|\gamma_{^3\mathrm{He}}\right| H_1. \tag{4.7}$$

Using the typical conditions of experiment E06-010,

$$\left(10^2 \text{ s}\right)^{-1} \ll \frac{\frac{d}{dt}\left(H_0 - \frac{\omega}{\gamma}\right)}{H_1} \ll \left(10^{-3} \text{ s}\right)^{-1}, \tag{4.8}$$

which was satisfied by our sweeping speed as shown above.

If a pick-up coil is placed in a transverse direction to $\vec{H}_0$, the ^{3}He magnetic moment, which rotates with $\vec{H}_e$, induces a signal in the coil. The orientation of the coil is usually perpendicular to the RF field, to reduce the pickup of the source RF signal, which is irrelevant to the polarization. The signal is proportional to the transverse component of ^{3}He magnetic moment, and therefore its average polarization, $\langle P \rangle$,

$$S_{NMR} \propto \langle P \rangle \frac{H_1}{\sqrt{(H_0 - \frac{\omega}{\gamma})^2 + H_1^2}} \tag{4.9}$$

The signal is maximum at the resonance, $H_0 = \frac{\omega}{\gamma}$. Typical NMR signals with both sweep methods are shown in Fig. 4-11.

The sign of the NMR signal for a given pick-up coil is related to the initial spin direction of ^{3}He. This was very important to determine the spin direction during the experiment, since it frequently flips. The following condition will flip the sign of NMR signal,

- Flip of initial spin direction
- Change of sweep direction, e.g. for the frequency sweeps, the signal changes sign between a sweep of lower frequency to higher and that of higher frequency to lower
- Change from frequency sweep to field sweep with same sweep direction.

The absolute sign of the spin, which is defined relative to the holding magnetic field,

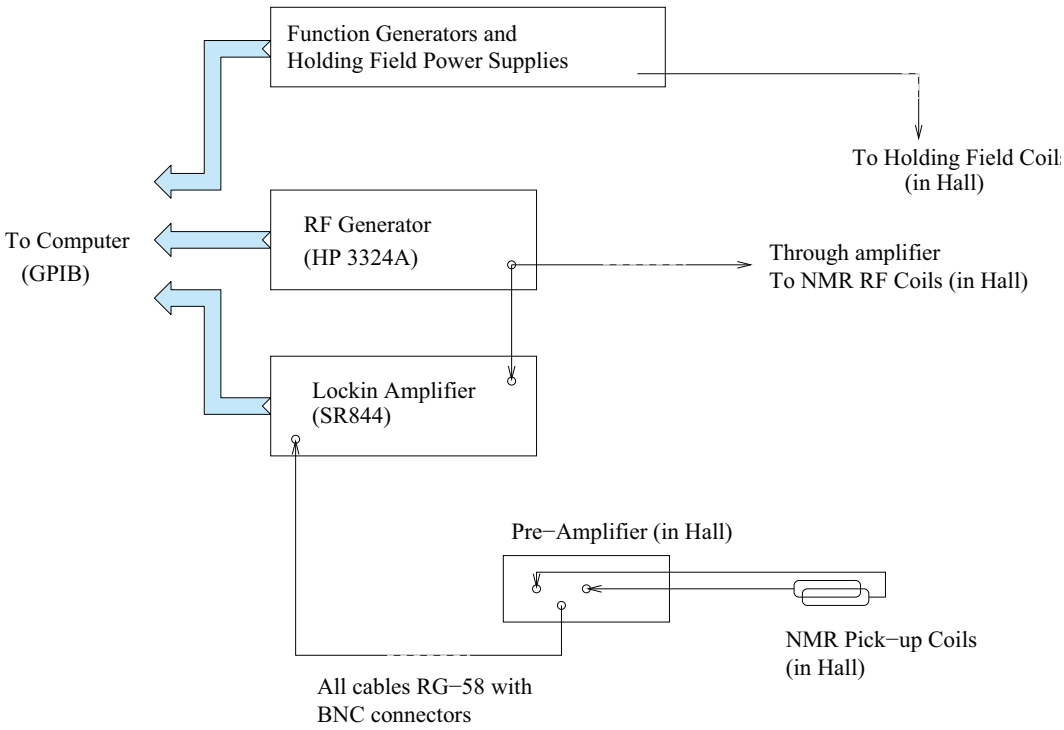

Figure 4-10: The electronic set up for the NMR measurements. This figure is updated from the original version in Ref. [141].

can be calibrated with the EPR polarimetry, which is discussed in Sec. 4.4.

4.3.2 Setup

The target was upgraded to support polarizing and polarimetry for three target spin directions, two of which were used for experiment E06-010: horizontal transverse-to-beam and vertical. For each spin directions, the coils were setup so that the holding field, RF field and pick-up coils were orthogonal to each other. The top view of the coil setup is shown in Fig. 4-7. The pick-up coils were installed in pairs on opposite sides of the chambers, to cancel the background RF signal and double the NMR signal. Five pairs[11] of pick-up coils were placed near the pumping chamber and along the sides of the target chamber.

For each pair of pick-up coils, the electronics were similar, as shown in Fig. 4-

[11]The five pairs were: two pairs on the upstream and downstream ends of the target chamber (a 40-cm long tube) and three pairs around the pumping chamber (a 3" sphere), which were orthogonal to each other.

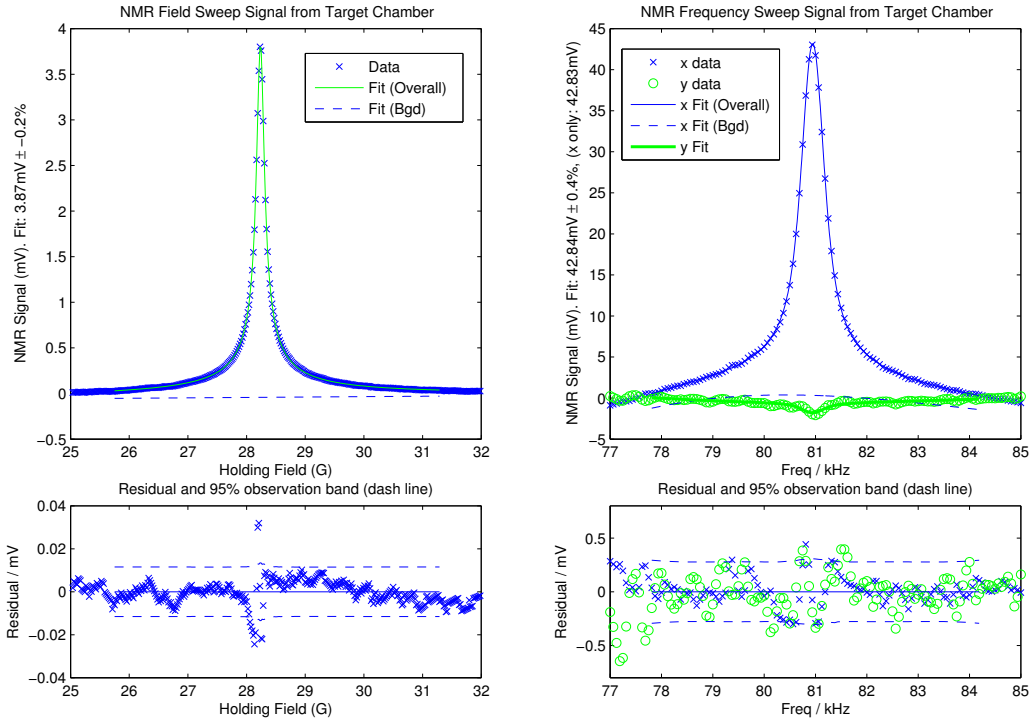

Figure 4-11: Signal of a typical NMR field (left) and frequency (right) sweep, plotted against the holding field strength and the NMR RF frequency, respectively. The fit curve (top) and the residual=signal−fit (bottom) were shown. Each signal was fit with a Gaussian convoluted NMR signal function (see text) plus a background function and the fit signal height is recorded on the label of the y-axis. The background function, shown as the blue dashed lines, was assumed to be linear VS the holding field strength for the field sweep, and a third-order polynomial of the NMR RF frequency for the frequency sweeps.

10. The power supplies for the holding field provided the necessary current to the Helmholtz coils to maintain a constant field. The RF function generator, HP 3324A, generates a constant or sweeping RF signal, which was amplified and sent to the RF coils inside the targets. The NMR signals from both pick up coils were then sent into low-noise pre-amplifier (Model SR620) input A and input B. The output (A-B) was then connected to the input of a lock-in amplifier (Model SR844). It was essential at the beginning of the experiment to adjust the pick-up coil pairs so that the background RF signal canceled in the output (A-B), while the NMR signal doubles. The lock-in amplifier measured the NMR signal, which had the same frequency as

the reference, RF signal. The signal was integrated and stored every ~10 ms and the data were sent to a computer via a GPIB interface.

4.3.3 Analysis

Typical NMR signals with both field and frequency sweep methods are shown in Fig. 4-11. During production running, one AFP frequency sweep was performed every 20 min to flip the target spin and measure the target polarization with the NMR signal. Compared to the field sweep NMR, the signal had a larger background within a smaller sample window. Several ansatz functions were used for the fit. They reproduced the average target polarization with-in 1%, which was included as a part of the systematic uncertainty. The particular fit function shown in Fig. 4-11 is the raw NMR signal as of Eq. (4.9) convoluted with a Gaussian smearing,

$$S_{NMR,Gaussion} \propto \langle P \rangle \int dt \frac{H_1}{\sqrt{(H_0 - \frac{\omega}{\gamma} + t)^2 + H_1^2}} \exp\left(-\frac{t^2}{2\sigma^2}\right) \tag{4.10}$$

This smearing effect can stem from the field gradient and the lock-in sampling uncertainty at a leading-order approximation. A linear and third-order polynomial background were added to the signal during fitting for the field and frequency sweep, respectively. The residual (signal−fit) was significantly improved with this Gaussian smearing technique compared to the raw signal fits.

There were two methods used to calibrate the NMR signal, which is proportional to the signal height to the absolute ^{3}He polarization: (1) perform the same measurement on a water sample, whose thermal polarization due to the holding magnetic field can be calculated [145]; (2) calibrate with EPR polarimetry, which is discussed in Sec. 4.4.4. The method (2) has been the major one for polarimetry analysis of this thesis, while final analysis for method (1) is still in progress. The target polarimetry was cross-checked using dedicated data of elastic ^{3}He scattering, whose asymmetry is known [42]. The measured elastic physics asymmetry was consistent within an 8% relative uncertainty (statistics limited) with the expected asymmetry based on a simulation [145], which roughly verified the reliability of the target polarimetry.

4.4 Electron Paramagnetic Resonance (EPR) Polarimetry

4.4.1 Principal

The method of electron paramagnetic resonance (EPR) measures both the sign and absolute polarization of the ^{3}He nuclei using the shift of the rubidium or potassium Zeeman resonance due to the magnetic field created by the polarized ^{3}He nuclei [179]. There are two effects, which shift the EPR frequency in the presence of ^{3}He polarization. First, the alkali-^{3}He spin exchange interaction shifts the EPR frequency proportionally to the ^{3}He polarization. Second, the Zeeman resonance frequency is shifted classically due to the presence of the ^{3}He magnetization. In a typical running condition of experiment E06-010, the size of the shift is around 0.4% for potassium EPR. By flipping the ^{3}He spin with AFP frequency sweep and isolating the shift of EPR frequency, the frequency shifts ($2\Delta\nu_{EPR}$) can be measured to a precision of $\delta\left(\Delta\nu_{EPR}\right)/\left(\Delta\nu_{EPR}\right) \approx 0.2\%$.

4.4.2 Measuring EPR Frequency

The EPR transition was excited by broadcasting a RF frequency signal through a small coil near the pumping chamber. In the first step of the EPR polarimetry, the RF frequency was scanned to find the transition (EPR FM sweep). Then it was locked to that transition This step was followed by the second step (EPR AFP sweep), which continuously tracked and recorded the EPR transition frequency while an even number of AFP frequency sweeps were performed. The EPR frequency shift at each AFP was analyzed to give the polarization in the pumping chamber. The diagram of the EPR electronics setup is shown in Fig. 4-12.

EPR FM sweep: Exciting the EPR transition depolarizes the alkali metal (Rb or K, chosen by central frequency). Once either alkali metal depolarizes, both metal species become depolarized due to their fast spin exchange. Then, the Rb atoms begins to re-polarize, which produces florescence. The 780 nm D2

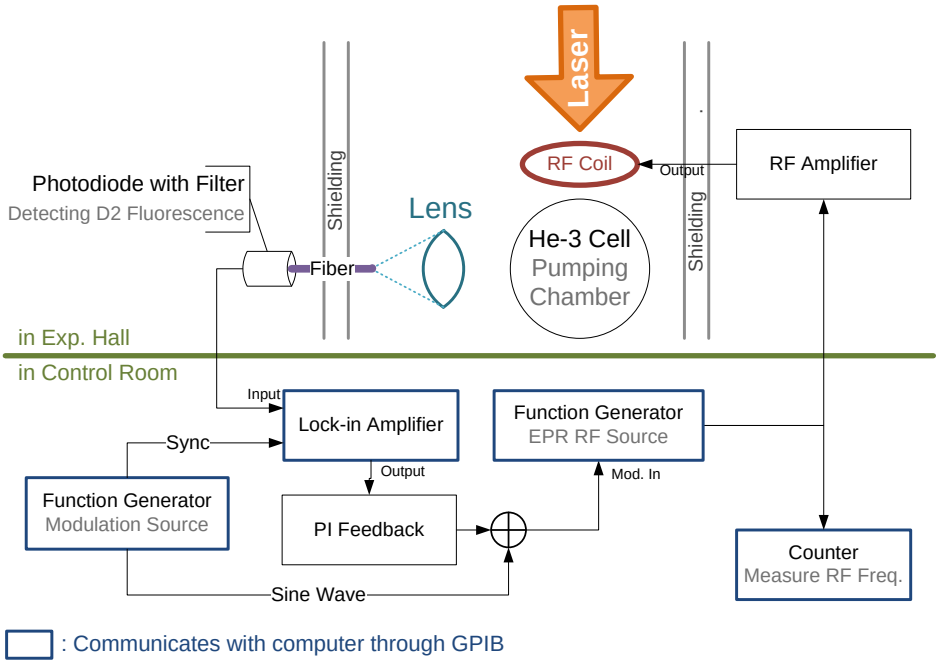

Figure 4-12: Schematic diagram of the EPR setup. The proportional-integral (PI) feedback was disabled during EPR FM sweeps; it was turned on before the EPR AFP sweeps.

florescence, due to the Rb atom decay from the $5P_{3/2}$ state to the $5S_{1/2}$ state, was detected using photodiodes. During the EPR measurement, the RF was frequency-modulated (FM) with a 100 Hz sine wave. The D2 florescence signal was measured by a lock-in amplifier, which was synchronized to the 100 Hz modulation signal (Fig. 4-12). The signal from the lock-in output is approximately the derivative of the EPR florescence curve as a function of the RF frequency. Therefore, at the EPR resonance, the florescence reaches maximum and the derivative is zero. During the EPR FM sweep, the central RF frequency is scanned to search for the resonance by finding this zero derivative point as shown in Fig. 4-13.

EPR AFP sweep: Before the AFP sweeps, EPR RF frequency was locked to the resonance by a proportional-integral (PI) feedback loop, which utilized the linear shape of the EPR FM curve (Fig. 4-13) around the resonance and locked the signal to the zero point. Then typically four NMR AFP frequency sweeps were

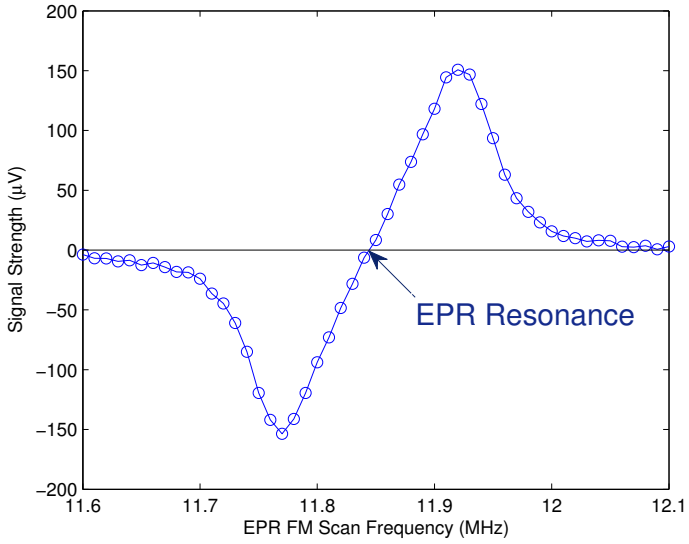

Figure 4-13: A typical data of EPR FM sweep with potassium when the pumping spin direction is anti-parallel to the holding magnetic field.

performed; each flipped the ^{3}He spin once and returned to its initial spin state after the measurement. typical EPR AFP sweep data are shown on the top plot of Fig. 4-14.

4.4.3 EPR Analysis

The energy spectrum of a ground state alkali atom (^{39}K and^{85}Rb in the analysis) in a magnetic field, B, can be described by the Breit-Rabi formula [155]:

$$E_{F=I\pm\frac{1}{2},m_F} = -\frac{\Delta E_{hfs}}{2(2I+1)} - g_N\mu_N B m_F \pm \frac{\Delta E_{hfs}}{2}\sqrt{1+\frac{2m_F}{I+\frac{1}{2}}x+x^2}, \quad (4.11)$$

where ΔE_{hfs} is hyper fine splitting energy, which was measured for alkali atoms in Ref. [180]. $x \equiv (g_N\mu_N - g_e\mu_B)\,B/\Delta E_{hfs}$, represents the relative strength of the Zeeman interaction comparing to that of hyper-fine splitting.

The EPR frequency, $\nu_{EPR,\pm}$, which corresponds to the energy difference between the $m_F = \pm F$ and $m_F = \pm(F-1)$ states with $F = I + \frac{1}{2}$, can be calculated using

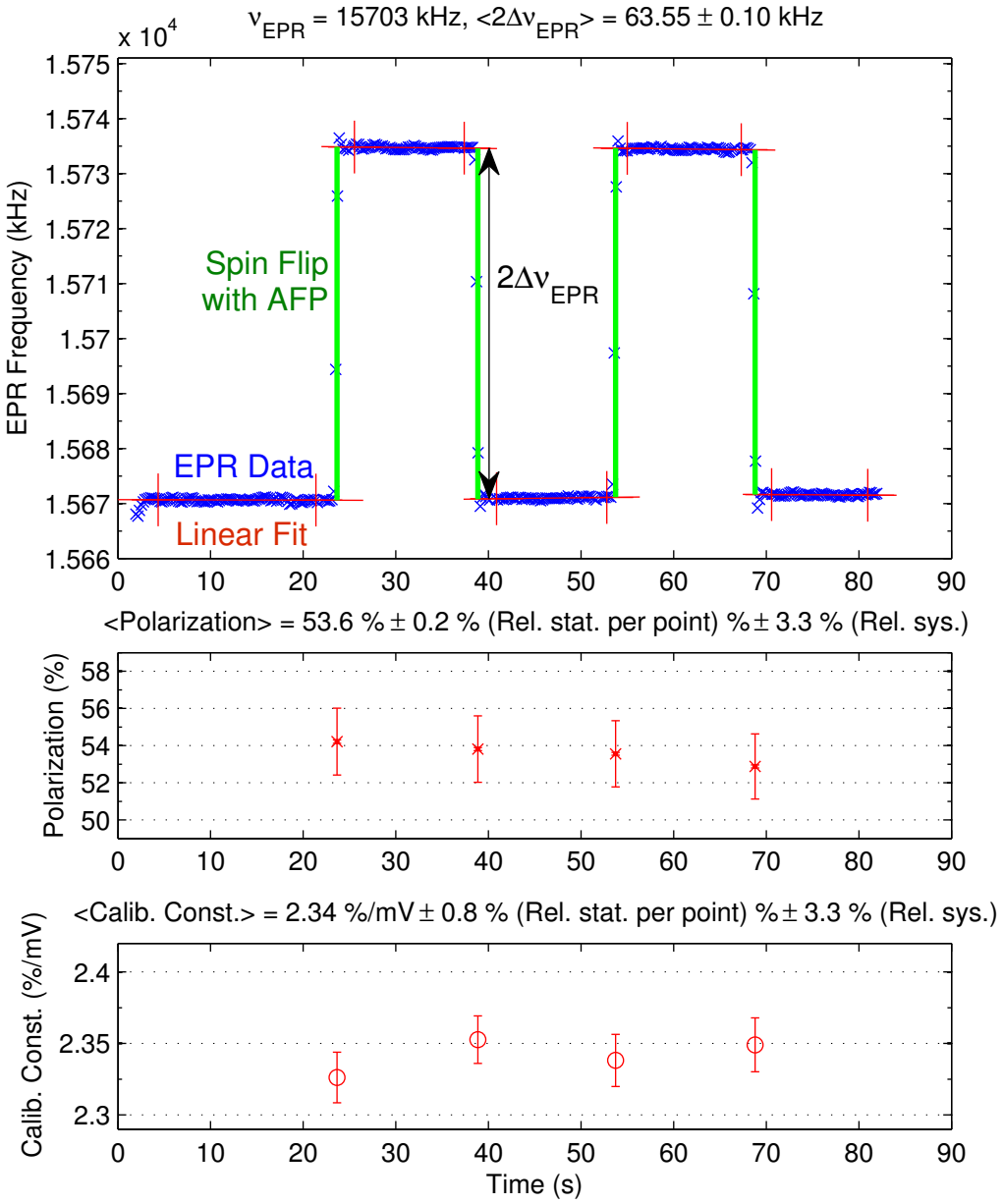

Figure 4-14: Top: Typical EPR data with four AFP frequency sweeps using linear fit. Middle: EPR polarization at each AFP flip. The inner error bar is statistical and outer one is total uncertainty with overall scaling errors. The polarization drops 0.6% during each AFP. The average polarization and the relative uncertainties ($\delta P/P$ in percentage) are shown above the plot. Bottom: Pumping chamber NMR calibration constant calculated for each AFP. Only the statistical error bar is shown.

Eq. (4.11):

$$h\nu_{EPR,\pm} \equiv \left| E_{F,m_F=\pm F_F} - E_{F,m_F=\pm(F-1)} \right| \tag{4.12}$$

$$= -\frac{B}{2}\left(g_N\mu_N + g_e\mu_B\right) \pm \frac{\Delta E_{hfs}}{2}\left(1 - \sqrt{1 \pm 2\frac{2I-1}{2I+1}x + x^2}\right). \tag{4.13}$$

By inverting Eq. (4.11), the magnetic field can be expressed a function of the EPR frequency, $B_\pm\left(\nu_{EPR}\right)$, where $\pm$ is determined by $m_F = \pm F$, and ultimately by the helicity sign of the laser light relative to the holding magnetic field.

As shown in Fig. 4-14 for each AFP flip during EPR, the shift of EPR frequency $2\Delta\nu_{EPR}$ was measured. The shift is proportional to the polarization of ^{3}He [179],

$$2\Delta\nu_{EPR} = 2 \times \frac{2\mu_0}{3}\left(\frac{dB_\pm\left(\nu_{EPR}\right)}{d\nu_{EPR}}\right)^{-1} \kappa_0\mu_{^3\mathrm{He}}[^3\mathrm{He}]P_{^3\mathrm{He}}, \tag{4.14}$$

where the ^{3}He magnetic moment is given by $\mu_{^3\mathrm{He}} = -2.12762\mu_N$ [181]. $[^3\mathrm{He}]$ and $P_{^3\mathrm{He}}$ are the density and polarization of ^{3}He in the pumping chamber, respectively. κ_0 is a constant that depends on temperature, but not on density. It has been measured experimentally [179, 182],

$$\kappa_0^{^{39}K}(T) = (5.99 \pm 0.11) + (0.0086 \pm 0.0020)(T - 200^\circ C) \tag{4.15}$$

$$\kappa_0^{^{85}Rb}(T) = 6.39 + (0.00916 \pm 0.00026)(T - 200^\circ C) \tag{4.16}$$

The uncertainty for $\kappa_0^{^{39}K}(T)$, extrapolated to the typical working temperature of $270^\circ C$, is around 2.7% and is the dominate uncertainty for the pumping chamber polarization. The reliability of this extrapolation was cross checked by comparing the potassium-39 EPR results with that from the rubidium-85, for which $\kappa_0^{^{85}Rb}(T)$ was measured to $T > 300^\circ C$ [182]. The results were consistent within the systematic uncertainties.

During experiment E06-010, EPR polarimetry was performed regularly for all three cells in each pumping direction. The results of the EPR polarimetry are shown in Fig. 4-15, which was used to calibrate the NMR signals as discussed in the following

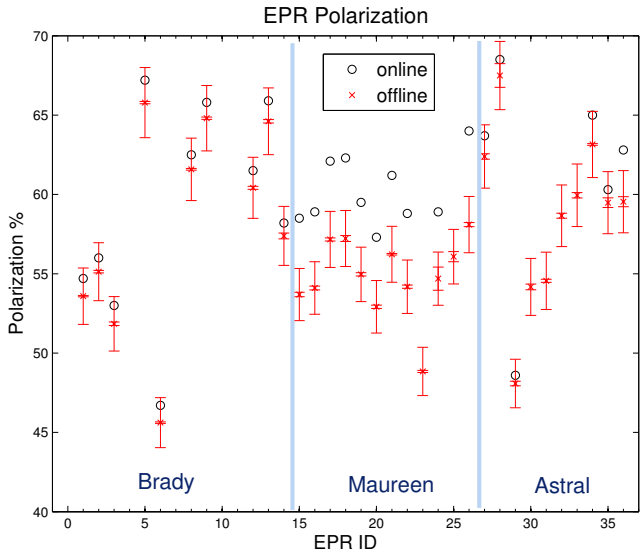

Figure 4-15: EPR results of pumping chamber polarization. The polarization shown corresponds to the moment when the EPR polarimetry was performed, which was an invasive measurement. This is not polarization history of running condition. Both statistical (inner) and systematical (outer) errors are shown for the off-line results. There were major shifts between on-line and off-line number for the cell Maureen due to the update of its density measurement [168].

subsection.

The sign of the ^{3}He spin can be determined by the sign of $\Delta\nu_{EPR}$. Since $\mu_{^3\mathrm{He}} < 0$, ν_{EPR} will be smaller when the ^{3}He spin is parallel to the holding magnetic field. Taking Fig. 4-14 as example, the positive shift of ν_{EPR} during the first AFP indicated that the initial ^{3}He spin state is $+1$, or its spin was parallel to the holding field.

4.4.4 Calibration of NMR with EPR

To reduce systematic errors, the target spin was reversed every 20 minutes by AFP. During these spin reversals (or spin flips), an NMR signal at the pumping chamber was recorded. The polarization is proportional to the NMR signal height: $P_{PC} = C \times S_{NMR}$. C is a calibration constant of NMR, which can be determined using the EPR polarimetry.

For each AFP during the EPR measurements, an NMR signal was measured using the identical settings compared to the AFP spin flips for production running.

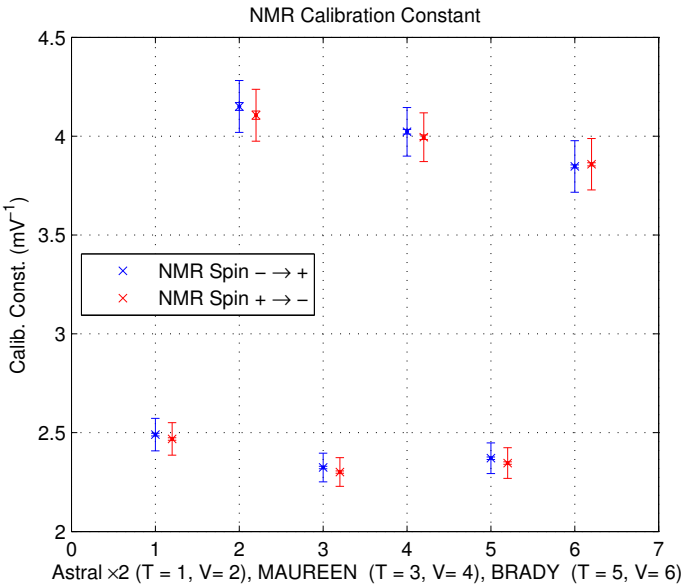

Figure 4-16: NMR calibration constant for all three cells. The constant was averaged separately in regards to the two pumping directions for each cell and the two spin states for each pumping direction. The inner error bar is statistical error and the outer one shows the systematic error.

A calibration constant was calculated for each flip $C_i = P_{EPR,i}/S_{NMR,i}$, where $P_{EPR,i}$ is the EPR polarization evaluated for this flip and $S_{NMR,i}$ is the NMR signal height, which was fit using the same procedure as that used for the production data analysis. C_i is then averaged for the two spin states, ± 1, and weighted by the statistical uncertainty:

$$\bar{C}_{\pm} = \sum_{i,\pm} w_i C_i \tag{4.17}$$

$$w_i = \left(\tfrac{1}{\Delta C_i}\right)^2 / \textstyle\sum_{j,\pm}\left(\tfrac{1}{\Delta C_j}\right)^2. \tag{4.18}$$

The result of calibration constant is shown in Fig. 4-16.

4.5 Polarization Gradients

During the production runs, NMR polarimetry measured the pumping chamber polarization, P_{pc}, every 20 min. However, the electron interacted with ^{3}He in the target

chamber, which carried a polarization of P_{tc}. Since the ^{3}He gas was polarized in the pumping chamber, and diffused down to the target chamber, there was a polarization gradient between the two chambers. The gradient, which was quantified as P_{tc}/P_{pc}, is discussed in this section using a two-chamber polarization model.

4.5.1 Two Chamber Polarization Model

The polarized ^{3}He cells used at Jefferson Lab consists of a pumping chamber and a target chamber, which are connected with a small transfer tube (Fig. 4-6). ^{3}He is polarized in the pumping chamber and the polarization diffuses to the target chamber. The polarization dynamics can be described by a two-chamber model [183, 184, 185],

$$\frac{dP_{pc}}{dt} = \gamma_{SE}\left(P_A - P_{pc}\right) - \Gamma_{pc}P_{pc} - d_{pc}(P_{pc} - P_{tc}) \tag{4.19}$$

$$\frac{dP_{tc}}{dt} = d_{tc}(P_{pc} - P_{tc}) - \Gamma_{tc}P_{tc} \tag{4.20}$$

where the parameters during typical E06-010 running conditions are

- P_A, P_{pc} and P_{tc} are the polarizations of alkali, pumping chamber and target chamber, respectively. P_A can be close to 100% in the region where optical absorption occurs.

- $\gamma_{SE} \sim (4\ \text{hour})^{-1}$ is the spin-exchange rate in the pumping chamber.

- $\Gamma_{pc} \sim (10\ \text{hour})^{-1}$ and $\Gamma_{tc} \sim$ (10~20 hours)$^{-1}$ are the ^{3}He spin relaxation rates in each chamber due to effects other than spin-exchange and diffusion.

- The diffusion rates, d_{tc} (d_{pc}), are the probability per unit time per nucleus that a nucleus will exit the target (pumping) chamber and enter the pumping (target) chamber. They are both $(1 \sim 2\ \text{hour})^{-1}$ for the E06-010 cells.

The solution to Eq. (4.19) and (4.20) is a superposition of two exponential terms, one slower (s) and one faster (f), decaying towards an equilibrium polarization for each

chamber:

$$P_{pc}(t) = P_{pc}^{\infty} + C_{pc}^{s}\exp\left(-\Gamma_s t\right) + C_{pc}^{f}\exp\left(-\Gamma_f t\right) \tag{4.21}$$

$$P_{tc}(t) = P_{tc}^{\infty} + C_{tc}^{s}\exp\left(-\Gamma_s t\right) + C_{tc}^{f}\exp\left(-\Gamma_f t\right) \tag{4.22}$$

$$P_{pc}^{\infty} = P_A \frac{\gamma_{SE} f_{pc}}{\gamma_{SE} f_{pc} + \Gamma_{pc} f_{pc} + {}^{\Gamma_{tc} f_{tc} d_{tc}}/_{(d_{tc}+\Gamma_{tc})}} \tag{4.23}$$

$$P_{tc}^{\infty} = P_{pc}^{\infty}\frac{d_{tc}}{d_{tc}+\Gamma_{tc}} \tag{4.24}$$

where f_{pc} (f_{tc}) is the fraction of ^{3}He nuclei in the pumping (target) chamber. The amplitude of exponential terms, $C_{tc,\,pc}^{s,\,f}$, are related to the initial polarization of both chambers. The exact expression for $C_{tc,\,pc}^{s,\,f}$ and $\Gamma_{s,\,f}$ can be found in Refs. [183, 184, 185]. Our data with various conditions can be described with this model as shown in Fig. 4-17.

The meaning of both exponential terms is more clear at the fast diffusion limit, i.e. d_{tc}, $d_{pc} \gg \gamma_{SE}$, Γ_{pc}, Γ_{tc}. At this limit, the slower time constant, $\Gamma_s \approx \langle\gamma_{SE}\rangle + \langle\Gamma\rangle$, represents the average spin exchange ($\langle\gamma_{SE}\rangle \equiv f_{pc}\gamma_{SE}$) and relaxation ($\langle\Gamma\rangle \equiv f_{pc}\Gamma_{pc} + f_{tc}\Gamma_{tc}$) of the whole cell; and the faster time constant, $\Gamma_f = d_{tc}+d_{pc}+\mathcal{O}\left(\gamma_{SE},\,\Gamma_{pc},\,\Gamma_{tc}\right)$, represents the diffusion between the two chambers. After a short time ($t \gg 1/\Gamma_f$) of diffusion, the polarization of both chambers become the same and can be represented using a single function $P(t)$,

$$P(t) \approx C\exp\left(-(\langle\gamma_{SE}\rangle + \langle\Gamma\rangle)t\right) + P_A\frac{\langle\gamma_{SE}\rangle}{\langle\gamma_{SE}\rangle + \langle\Gamma\rangle}, \tag{4.25}$$

which resembles the spin evolution of a single-chambered cell.

Eq. (4.24) shows that at equilibrium, the target chamber polarization is always lower than that of the pumping chamber by ${}^{\Gamma_{tc}}/_{(d_{tc}+\Gamma_{tc})}$. Therefore the target chamber diffusion rate and life time are needed to estimate the polarization gradient. They will be discussed in the following subsections.

4.5.2 Diffusion Rate

The ^{3}He gas with higher polarization diffuses from the pumping chamber towards the target chamber through the transfer tube. For the transfer tube of a typical E06-010 cell, the crosssectional area, $A_{tt} \sim 0.7$ cm^2, and its length, $L_{tt} \sim 9$ cm. Consider a one dimensional polarization flux at a given z position in the transfer tube,

$$J_{tt}(z) = -n(z)D(z)\frac{dP(z)}{dz}, \tag{4.26}$$

where n is the density, P is the polarization and D is the diffusion constant. The temperature and density dependence of D can be described with a model based on a classical gas of hard spheres [183]

$$D(z) = D_0 \left(\frac{T(z)}{T_0}\right)^{m-1} \frac{n_0}{n(z)}, \tag{4.27}$$

where the parameters were fit from experimental data on ^{4}He [186] with a scale of ^{4}He to ^{3}He mass ratio [156, 127]: $D_0 = 2.789 \pm 0.007$ cm$^2/s$ at $T_0 = 353K$ and $m = 1.705 \pm 0.003$.

We further assume that the temperature and density distributions reached a stable state, the flux is a constant (J_{tt}) along the transfer tube[12] and the temperature in transfer tube changes linearly. Then Eq. (4.26) can be integrated along z , and

$$J_{tt}(z) = J_{tt} = (P_{pc} - P_{tc})\frac{n_{tc}D_{tc}K}{L_{tt}} \tag{4.28}$$

$$D_{tc} = D_0 \left(\frac{T_{tc}}{T_0}\right)^{m-1} \frac{n_0}{n_{tc}} \tag{4.29}$$

$$K = \frac{(2-m)(t-1)}{t^{2-m}-1} \tag{4.30}$$

$$t = {}^{T_{pc}}/_{T_{tc}} \tag{4.31}$$

[12] It is implied that there is no polarization loss in transfer tube.

Therefore, the diffusion rates in Eq. (4.19) and (4.20) can be calculated with J_{tt} as

$$d_{tc} = \frac{J_{tt}A_{tt}}{V_{tc}n_{tc}(P_{pc}-P_{tc})} = \frac{A_{tt}}{V_{tc}L_{tt}}D_{tc}K \tag{4.32}$$

$$d_{pc} = \frac{J_{tt}A_{tt}}{V_{pc}n_{pc}(P_{pc}-P_{tc})} = \frac{V_{tc}n_{tc}}{V_{pc}n_{pc}}d_{tc} \tag{4.33}$$

The same model was crosschecked by calculating the diffusion rates measured in Ref. [184]. The calculation and data are consistent within 10% . For experiment E06-010, the typical value of d_{tc} is around $(1.2 \text{ hour})^{-1}$. The uncertainty was estimated as $\delta d_{tc}/d_{tc} \approx 20\%$.

4.5.3 Target Chamber Life Time

The cell lifetime, which is inversely proportional to the spin relaxation rate, is one of the main characteristics used to evaluate the quality of the cell. The cold cell lifetime, $\tau_{lifetime}$, is usually measured as one of the steps to characterize the target cell (Table 4.1). However, during production run condition, additional factors contributed to the target chamber spin relaxation rate,

$$\Gamma_{tc} = \Gamma_{dip} + \Gamma_{wall} + \Gamma_{beam} + \Gamma_{AFP} + \Gamma_{\Delta B}, \tag{4.34}$$

where the relaxation mechanisms are

Γ_{dip} **(Nuclear dipolar interaction)** stems from a direct coupling between two nearby ^{3}He nuclei. It was calculated by Newbury, et. al. [187] as

$$\Gamma_{dip} = \frac{n}{(744 \text{ amagat} \cdot \text{hour})} \tag{4.35}$$

at $23°C$, where n is the density of ^{3}He. Amagat is a density unit and 1 amagat is the gas density at 0°C and 1 atm pressure. A small temperature dependence was also predicted and an empirical formulas based on Newbury's study including the temperature dependence [183] was used to calculate the Γ_{dip}.

Γ_{wall} **(Wall relaxation)** is the relaxation due to collisions between the ^{3}He nucleus

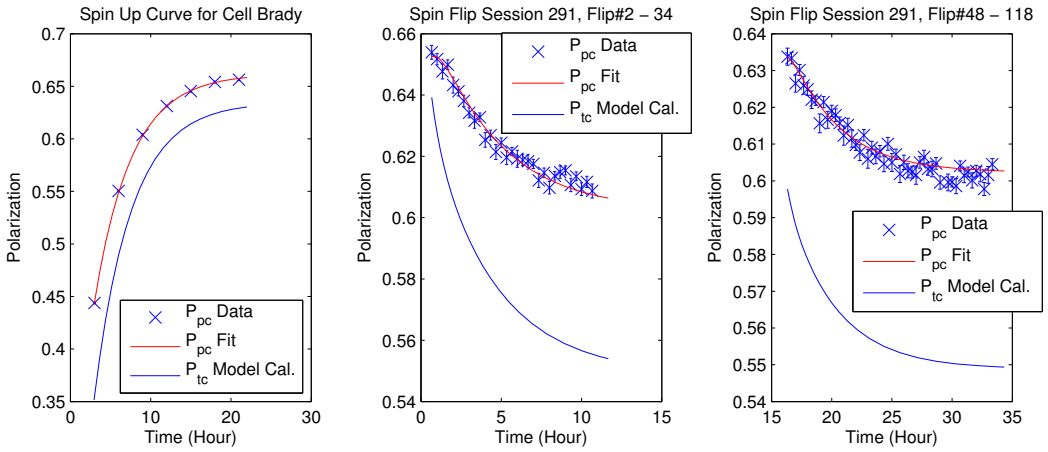

Figure 4-17: Fit for the beam depolarization effect using the two-chambered model. The spin up test started with low polarization with 2 AFP NMR measurement ever 3 hours and no beam. Data in spin flip session 291 was taken with one AFP NMR measurement every 20 min and a ~13 μA beam.

and the cell glass wall. The average wall relaxation for both chambers can be found with $\Gamma_{wall} = 1/\tau_{lifetime} - \Gamma_{dip}$. In addition, if one assumes the glass relaxation in both chambers is the same, the Γ_{wall} for both chambers will be proportional to their surface area to volume ratio S/V, and the wall relaxation for the target chamber, $\Gamma_{wall,\,S/V}$, can be calculated. The difference between Γ_{wall} and $\Gamma_{wall,\,S/V}$ were used as the uncertainty of Γ_{wall}, i.e., $\delta\Gamma_{wall} = \left|\Gamma_{wall,\,S/V} - \Gamma_{wall}\right|$.

Γ_{beam} **(Beam depolarization):** Ionizing radiation increases the nuclear spin relaxation in the target chamber. The beam depolarization effect was extracted with a fit of the two-chambered model to our data (Fig. 4-17). The best fit showed that $\Gamma_{beam} = {}^{I}/_{(414\ \text{hour}\cdot\mu\text{A})}$, where I is the average beam current. By varying the input parameters of the fit, an uncertainty of 40% was quoted.

Γ_{AFP} **(AFP loss):** During the production runs, an AFP spin flip was performed every 20 min. The spin loss for each AFP was measured by performing many (~10) AFPs in few minute and monitoring the exponential polarization drop. The average result is $\Gamma_{AFP} \sim 0.56\%/20$ minuites[188].

$\Gamma_{\Delta B} = D\frac{|\nabla B_x|^2+|\nabla B_y|^2}{B_z^2}$ is the relaxation due to the magnetic field gradient [189, 190], where $D \sim 0.2\ \text{cm}^2/s$ is the ^{3}He self diffusion coefficient. The overall magnitude

NIM Logic Level	"Spin+" = 1	"Spin+"= 0
"Spin-"= 1	Electronically impossible	^{3}He spin anti-parallel to hold field
"Spin-"= 0	^{3}He spin parallel to hold field	Target spin unknown

Table 4.4: Definition of target spin signals in NIM logic levels

of $\Gamma_{\Delta B}^{-1} \sim 10^3$ hour, which is a much smaller effect than the rest of the relaxation mechanisms.

4.5.4 Polarization Gradient Results

In summary, the polarization gradient was calculated based on Eq. (4.24),

$$\frac{P_{tc}^{\infty}}{P_{pc}^{\infty}} = \left(1 + \frac{\Gamma_{tc}}{d_{tc}}\right)^{-1} \tag{4.36}$$

$$\begin{aligned}\Gamma_{tc} &= 1/\tau_{lifetime} - \Gamma_{dip}(\text{Filling condition}) + \Gamma_{dip}(\text{Target chamber}) \\ &\quad + \Gamma_{beam} + \Gamma_{AFP} + \Gamma_{\Delta B}.\end{aligned} \tag{4.37}$$

The result shows $P_{tc}^{\infty}/P_{pc}^{\infty}$ is around 92%, which varies from cell to cell. Its uncertainty is 3.4%.

4.6 Automatic Target Spin Reversal

During experiment E06-010, the ^{3}He target spins were reversed every 20 minutes using the AFP spin flip technique to reduce possible false asymmetries. A more frequent spin flip (also called spin reversal) would further reduce the possible systematic uncertainties and possible false asymmetries. However, spin flips reduce the target polarization due to the AFP loss of each flip. Therefore, a 20 min spin flip was adopted to balance both effects. During each spin flip, an NMR signal was acquired and the target polarization was measured. The sign of the new spin state was determined by the sign of NMR signal (Sec. 4.3.1), which was calibrated from the sign of EPR $\Delta\nu_{EPR}$ as discussed in Sec. 4.4.3.

A new spin flip subsystem was developed to automatically flip the target spin and

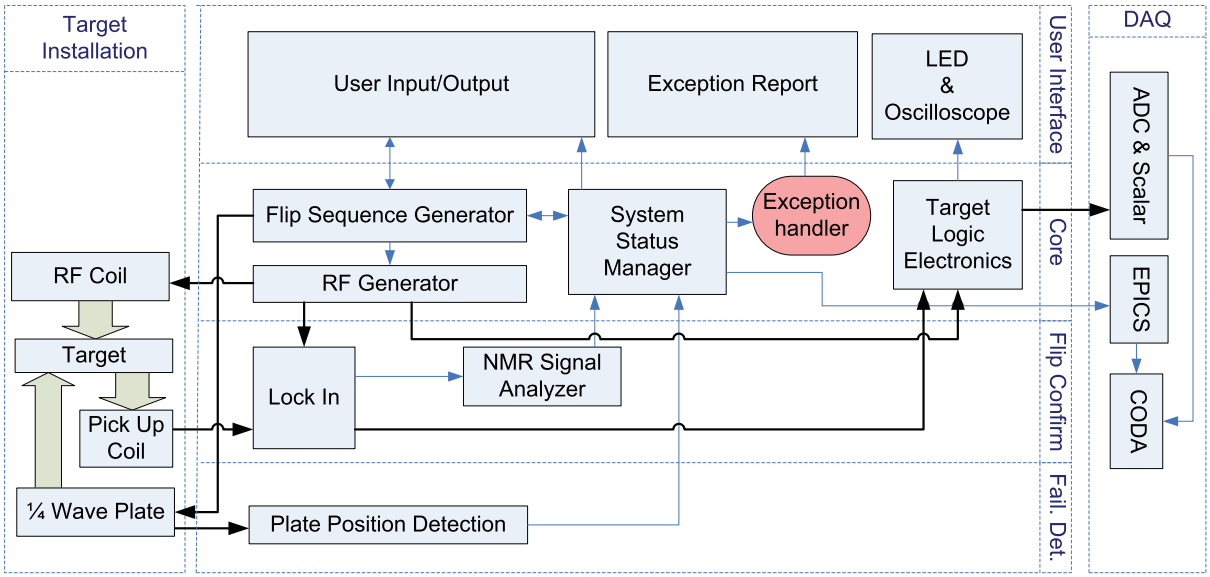

Figure 4-18: Diagram of spin flip subsystem. The blue arrows are digitalized data flow; the black arrows are hardware signal; the wide arrows are laser beams and NMR RF waves.

monitor the target status. The diagram of the subsystem is shown in Fig. 4-18. The software, System Status Manager (Fig. 4-20), collects the target status and controls its running. When the software sent out a command for spin flip every 20 min, the NMR subsystem performed an AFP frequency sweep, flipped the target spin and recorded the NMR data. Simultaneously, the motorized quater-wave plates (Fig. 4-8) were rotated by 90 degrees, which flipped the laser polarization and pumping direction. The subsystem communicated with the data acquisition (DAQ) system with real-time target spin information through hardware and software channels. The primary channel was based on the hardware NIM signal, which was generated by the Target Logic Electronics as shown in Fig. 4-19. The input of the Target Logic Electronics was a TTL signal, which flags whether an AFP was in progress and an analog NMR signal[13], which was then digitalized and the target spin state information was locked through two flip-flops [191]. The primary output consisted of two channels of NIM logic signal, spin±, whose meaning is shown in Table 4.4. The signals flipped to an "unknown target state", starting from shortly before the spin flip, until the flip was finished, and the target spin state was confirmed with the sign of the NMR signal.

[13]It can also directly take input signal from the System Status Manager.

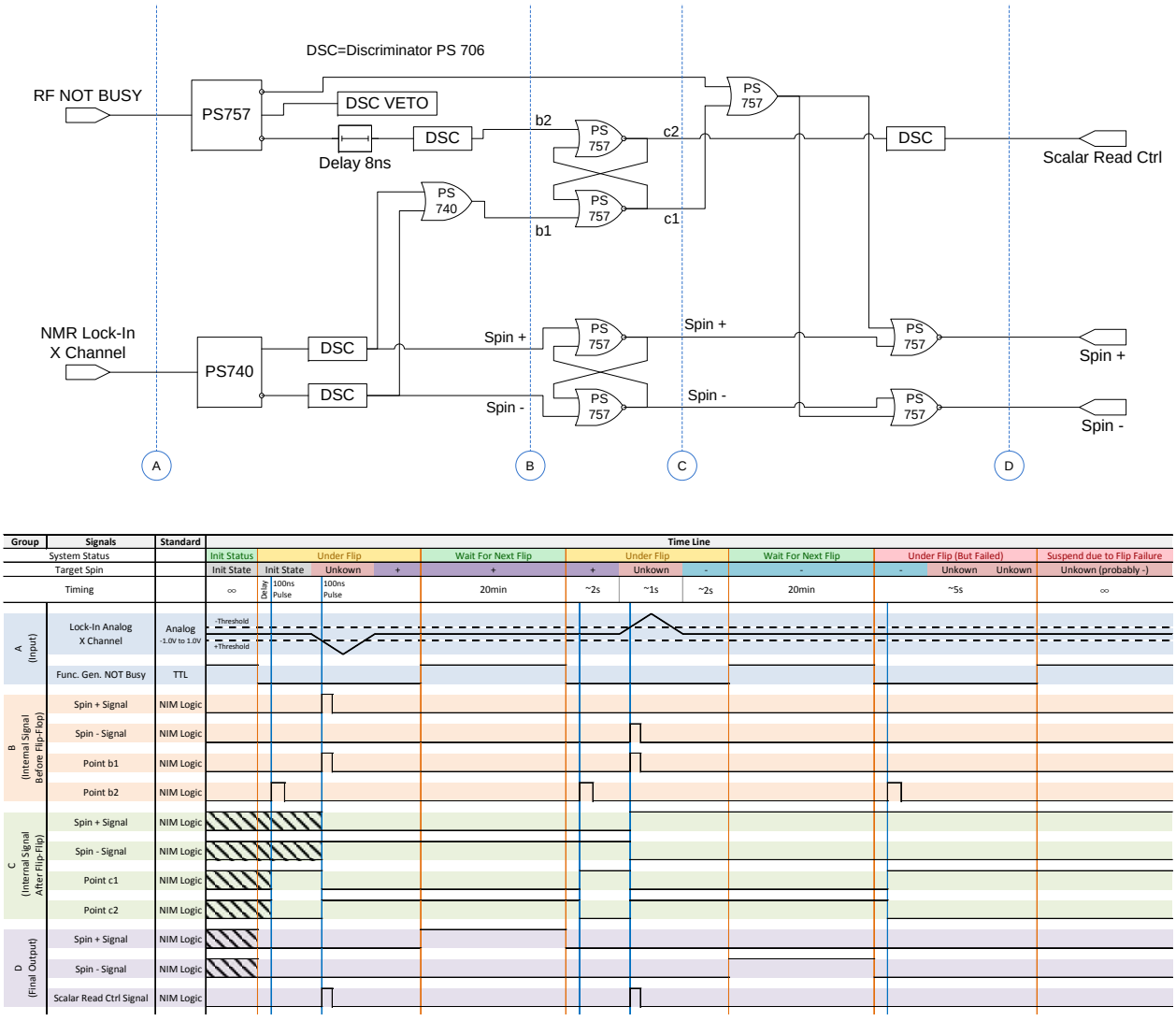

Figure 4-19: Target logic electronics (top) and timing diagram (bottom)

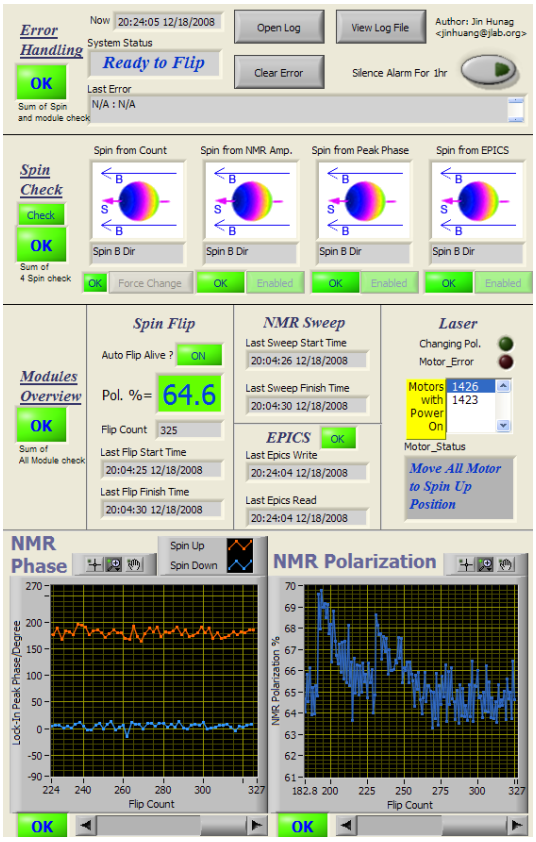

Figure 4-20: One of the Labview-based graphical user interface of the on-line target control software. This GUI is the front panel of "system status manager" as labeled in Fig. 4-18.

The signals were used to form the scalar gate signal to flag each event, which enabled synchronization of the luminosity and event information with the real-time target spin states. Besides the primary channel, more complete target information was archived to the data stream through a slower software system known as Experimental Physics and Industrial Control System (EPICS) [148].

4.7 Target Performance

The target chamber polarization is shown in Fig. 4-21, which was measured by NMR for each spin flip. With the new spectrally narrowed laser, the in-beam polarization was between 50~65%, a world record for the high luminosity polarized ^{3}He targets. By comparing to the previous experiments in Fig. 4-22, the figure-of-merit was signif-

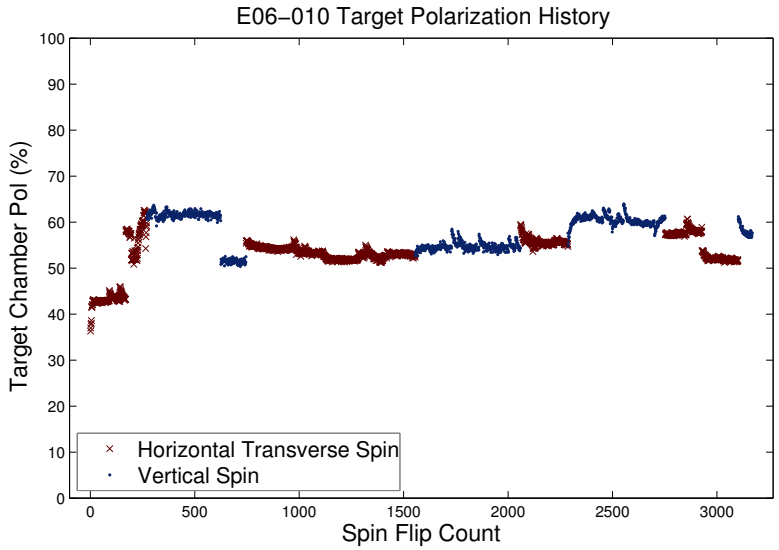

Figure 4-21: Target Polarization History

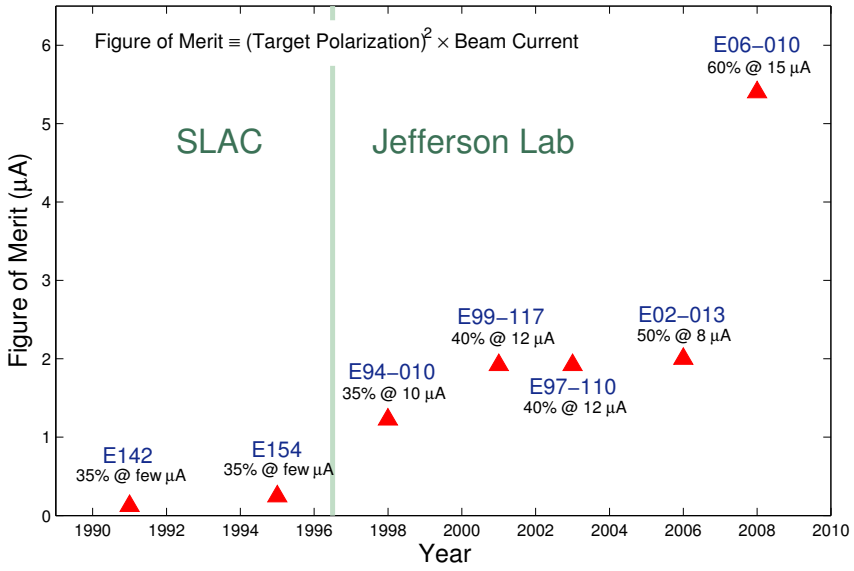

Figure 4-22: Figure-of-Merit history for high luminosity polarized ^{3}He targets. A 60% stable target polarization with 15 μA electron beam was achieved by the E06-010 target.

Items		Rel. Pol. Error
Pumping Chamber	K-^{3}He EPR κ_0	2.7%
	Pumping chamber density	1.8%
	NMR signal fit	0.8%
	Pumping chamber temperature	0.5%
	Density fluctuation	0.4%
	Stat. error of NMR calib. constant	0.3%
Polarization Gradient	Diffusion rate	2.3%
	Target chamber intrinsic lifetime	2.0%
	Beam depolarization	1.6%
	Transfer tube depolarization	0.5%
	Spin flip loss	0.2%
Sum all		**4.9%**

Table 4.5: Systematic uncertainty budget for target polarization. The average relative statistical uncertainty for each NMR is 0.8%.

icantly improved with higher polarization and beam current. In addition, a pumping chamber polarization of 73% was observed after a long period of pumping without beam and target spin reversals, which is also a record polarization for this type of target cells. For the production runs, the average polarization for pumping (pc) and target (tc) chambers are

$$\langle P_{pc} \rangle = 60.4\% \pm 0.5\% \,(\text{average stat. per NMR}) \pm 2.1\% \,(\text{sys.}) \quad (4.38)$$

$$\langle P_{tc} \rangle = 55.4\% \pm 0.4\% \,(\text{average stat. per NMR}) \pm 2.7\% \,(\text{sys.}), \quad (4.39)$$

where the statistical uncertainty is averaged for each spin flip.

The systematic uncertainty is summarized in Table 4.5. The dominant uncertainty for the pumping chamber polarization is from the limitation of world data on the potassium EPR constant κ_0 and the uncertainty of the overall density in the pumping chamber. To obtain the polarization for the target chamber, the polarization gradient was calculated with a data-calibrated model (Sec. 4.5), which lower the polarization by $(P_{pc} - P_{tc})/P_{pc} = 7$ 9% (cell dependent) with an uncertainty of $\delta(P_{pc} - P_{tc})/(P_{pc} - P_{tc}) = 3.4\%$. The overall systematic uncertainty for the target chamber polarization is $\delta P_{tc}/P_{tc} = 4.9\%$.

Through out the experiment, the target was extremely stable with no major inci-

dents. The target software performed automatic spin reversals every 20 minutes for more than three thousand reversals, for which only few exceptions occurred. These exceptions were captured by the exception handler, reported and fixed with minimal loss of beam time.

THIS PAGE INTENTIONALLY LEFT BLANK

Chapter 5

Data Analysis

5.1 Overview of the Data Analysis

The primary goal for this analysis is to extract the ^{3}He $A_{LT}^{\cos(\phi_h-\phi_S)}$ azimuthal asymmetries in semi-inclusive deep inelastic electron scattering on a transversely polarized ^{3}He target and extract the corresponding neutron asymmetry using the effective polarization approximation. The flow chart of the data analysis is shown in Fig. 5-1. Using the Hall A analyzer package [192] and the detector calibration database (Sec. 5.2), the raw data were converted to ROOT files [193] which contained the reconstructed events. The raw azimuthal asymmetry in each kinematic bin was extracted directly using an azimuthally unbinned maximum likelihood estimator with corrections for the accumulated beam charge, the data acquisition livetime, and the beam and target polarizations (Appendix C). The result was confirmed by an independent binning-and-fitting procedure [131, 54] as shown in Sec. 6.1.2. In Sec. 6.1.3, the ^{3}He $A_{LT}^{\cos(\phi_h-\phi_S)}$ asymmetry (Fig. 6-14) was corrected for the N_2 dilution, A_{LL} contribution, charge-symmetric background and radiative effects. The corresponding neutron A_{LT} asymmetries (Fig. 6-16) were extracted from the measured ^{3}He asymmetries and proton over ^{3}He cross section ratios using the effective polarization approximation (Sec. 6.2). Using the simple quark models, naive extractions of the parton distributions are discussed (Sec. 6.3).

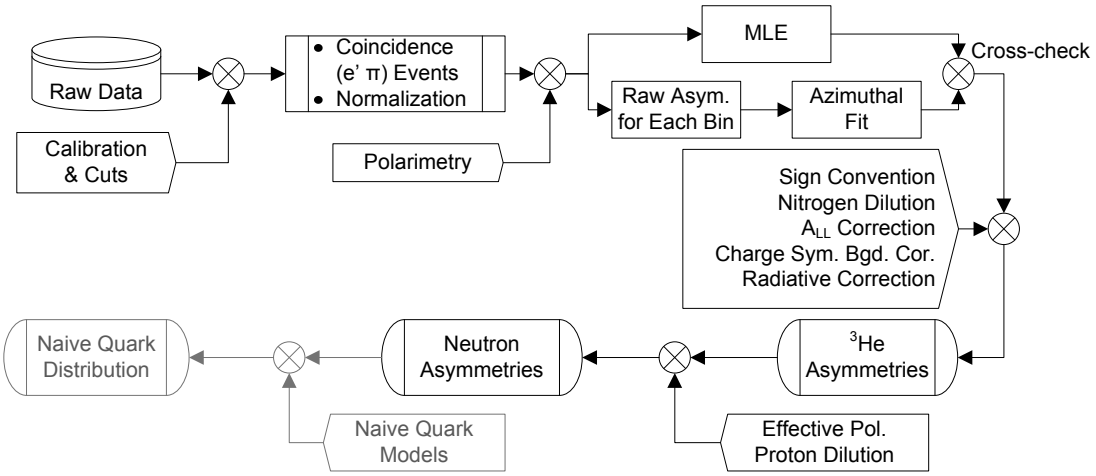

Figure 5-1: Flow chart of the analysis for the $A_{LT}^{\cos(\phi_h-\phi_S)}$ azimuthal asymmetries, where the primary results are the ^{3}He (Fig. 6-14) and neutron A_{LT} (Fig. 6-16) asymmetries.

5.2 Detector Calibration

5.2.1 Left HRS

The detector package on the Left-HRS was calibrated using the standard techniques as discussed in Sec. 5.2.1.1, except that the calibration of the timing detector, which is discussed in Sec. 5.2.3 for the integrity of coincidence timing analysis. A new set of software was developed to calibrate the Left HRS Optics [194], which will be discussed in the second part of this section (5.2.1.2).

5.2.1.1 Detector Calibration

The Left-HRS detectors used in this analysis were mainly calibrated by C. Dutta [145], Y. Wang [195], *et.al.* The description of the detector is given in Sec. 3.4.2. The calibration is summarized in this subsection.

Vertical Drift Chambers (VDC), which provided particle tracking, are a standard equipment in Hall A. The calibration mainly consisted of aligning the timing offset of each wire, which was extracted by identifying the rising edge of the drift time spectrum.

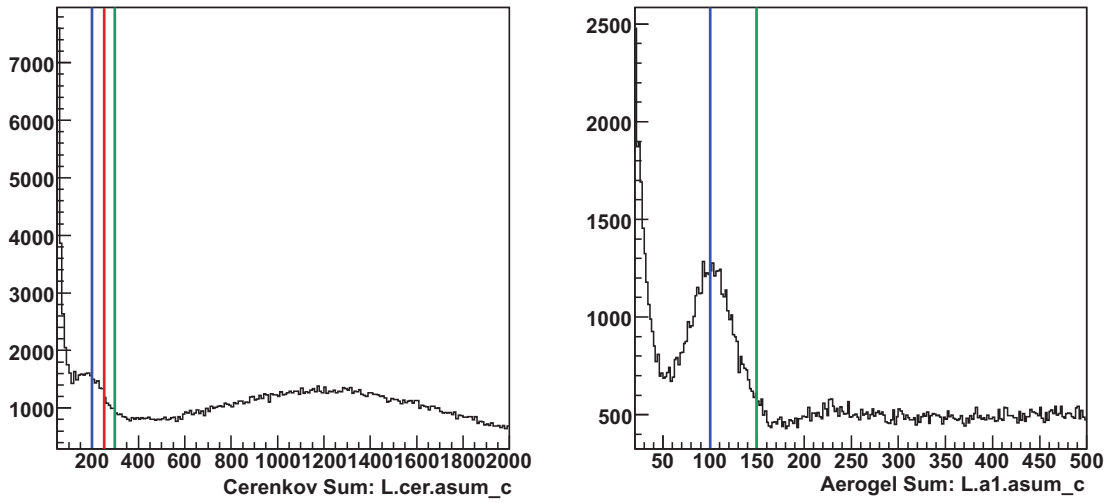

(a) (b)

Figure 5-2: Spectrums for (a) the Gas Cerenkov Detector and (b) the Aerogel Cerenkov Detector [131]. The single photon peaks were marked as blue lines and the PID cuts are marked in green or red lines (see Sec. 5.3.3).

Gas Cerenkov Detector: electrons produced Cerenkov light in the Gas Cerenkov Detector, while hadrons were below the threshold. The photons were focused to ten PMTs, and the signals were read-out by the ADCs. The calibration of ADCs involved mainly aligning their amplitudes by scaling the single photon peak to a value of normalized ADC Sum $L.cer.asum\_c = 200$ as shown in Fig. 5-2a. The value 200 was chosen so that the average scale on all PMTs are close to 1. In a typical electron event, an average of ~6 photo-electrons were observed; and typical $L.cer.asum\_c$ was close to zero or at the single photon peak for hadron events.

Aerogel Cerenkov Detector (A1) detected Cerenkov light for pions and electrons, while kaons and protons were below the threshold. It was calibrated by scaling and aligning the single photon peak to a normalized ADC Sum of $L.a1.asum\_c = 100$ as shown in Fig. 5-2b. The value 100 was also chosen so that the average scale on all PMTs are close to 1. For kaon and proton events, the typical $L.a1.asum\_c$ was close to zero or at the single photon peak.

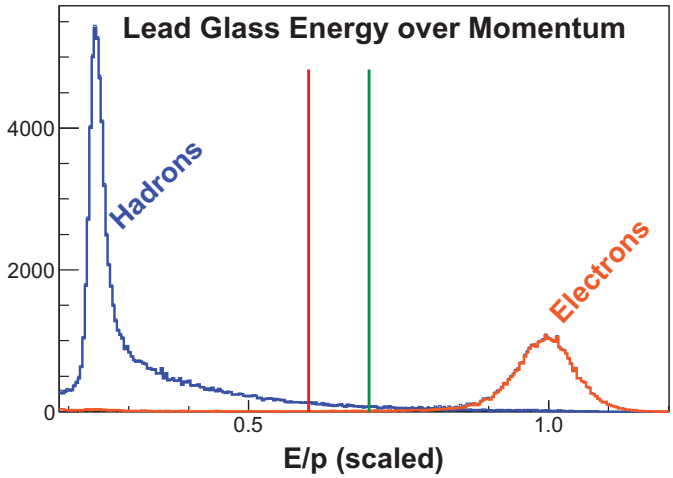

Figure 5-3: Spectrum for scaled E/p in the lead-glass shower detector [145]. The electron and hadron cuts are marked by the red and green lines, respectively, which will be discussed in Sec. 5.3.3.

Lead-Glass Shower Detector consist of two layers of lead-glass detectors, in which electrons deposit more energy than hadrons due to the EM shower. During the calibration, the pion peaks in the ADCs for both layers were aligned to channel 100. As shown in Fig. 5-3, a clear separation of pions and electrons was achieved on the energy over momentum E/p spectrum, where E is the scaled sum of energy deposition in both layers, $E = C \cdot (L.prl1.e + L.prl2.e)$. The scale constant C was calibrated so that the electron peak was centered at $E/p = 1$.

5.2.1.2 Optics Reconstruction

During experiment E06-010, the Left-HRS was used to measure the 3-D momentum and vertex of the charged particles produced at the target. The spectrometer was configured to detect one particle charge at a time, and it can be reconfigured to detect the opposite charge by reversing the magnetic fields in all of its magnets. The optics of the Left-HRS describes the transportation of charged particle from the target side to tracking detector, vertical drift chamber (Sec. 3.4.2); and the optics reconstruction describes the inverted optics transportation property of the magnet, i.e., using the tracking information at the detector side and beam location to reconstruct

the momentum and vertex of the scattered particle at the target side. The optics reconstruction for the Left HRS is parameterized using a set of polynomial expansions. The polynomial coefficients are also known as the optics matrix. Descriptions of the standard HRS optics reconstruction can be found in Ref. [196, 143]. The optics calibration for Experiment E06-010 will be discussed in this section.

General Approach

The goal of this study is to calibrate the reconstruction of the following HRS optics variables, which describes the particle trajectory at the target interaction point:

θ_{tg} and ϕ_{tg}, the tangent[1] of the vertical and horizontal angles relative to the HRS central line.

δ_{tg}, the relative momentum magnitude, i.e., $\delta_{tg} = (p - p_0)/p_0$, where p_0 is the central momentum. The above three variables allow a 3-D reconstruction of the particle momentum at the reaction vertex.

y_{tg} and z_{react}, are the horizontal track position in the target coordinate system and the vertex position along the ideal beam direction, respectively. They are directly related geometrically [196, 143]. One of the purposes for this calibration is to exclude the contamination due to the scattering on the target cell windows. z_{react} on the Left HRS also provides a vertex coincidence with the BigBite spectrometer, which helps to suppress the random coincidence background.

As illustrated in Fig. 5-4, the available optics calibration data included elastic scattering data on a multi-carbon target (Sec. 4.2.4.2) with sieve plate[2] installed and removed and elastic scattering on the multi-carbon foil target and pure ^{3}He, H_2 and N_2 gas targets.

A new optimization routine was established for general HRS optics calibrations. This new code features:

[1] tangent trigonometric function

[2] The sieve plate was a 0.25 inch-thick tungsten plate with holes drilled in a matrix pattern.

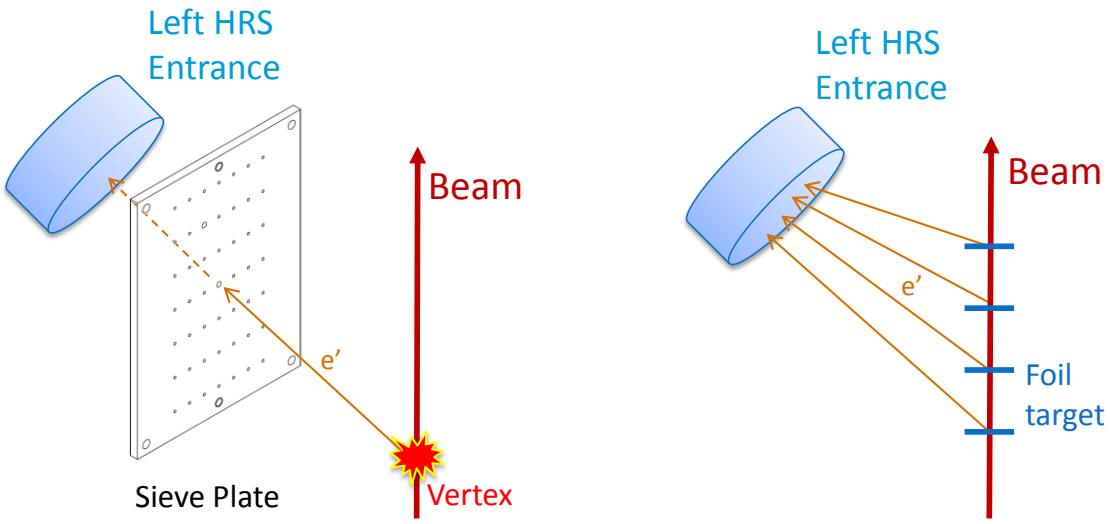

Figure 5-4: Schematics diagram of the setup for optics calibration. Left: setup for calibration of $\delta_{\rm tg}$, $\theta_{\rm tg}$ and $\phi_{\rm tg}$, for which a tungsten plate with holes (sieve slit) was inserted in between the reaction vertex and the Left-HRS entrance window; right: setup for the vertex calibration using the multi-carbon foil target whose location was surveyed.

- To ensure the code reproduce exact the same optics reconstruction as the analyzer, the subroutine is converted from the optics reconstruction subroutine THAVDC in the standard ANALYZER [192]. This subroutine is called for thousands of times during the optimization and the coefficients for the optics reconstruction (i.e., optics matrix) are gradually adjusted to minimize the square error defined in Eq. (5.1).

- Minimization routine is based on the `MINUIT2` package [197].

- Automatically visualize results after optimization, e.g. Fig. 5-5 and 5-6.

- Multiple self-consistency checks, including checks on the array size limits, on the input file formats and on the internal results.

Calibration Procedure

The optics calibration requires data sets for which the optics variables are known at both the vertex and detector locations. The optics matrix was obtained by minimizing

$$\chi^2 = \sum_{\text{Event}} (\text{reconstruction target variable} - \text{nominal target variable from survey})^2 \tag{5.1}$$

Three calibration data sets were taken at the beginning of the experiment using a 1.2 GeV electron beam. Each of them provided a calibration for one or two of the target variables. Each target variable was fitted independently, except for the vertex calibration, which also depends on a good reconstruction of horizontal angle ϕ_{tg}:

The angular calibration used the quasi-elastic scattering on the multi-carbon foil target with the sieve-slit inserted as shown on the left side of Fig. 5-4. The momentum distribution of the quasi-elastic electrons was wider than the momentum acceptance of the HRS spectrometer (~ 1 GeV$\pm$4.5%), so that the calibration data covered all the momentum acceptance. As shown in Appendix B.1, the sieve-slit plate was a 0.25 inch-thick tungsten plate with holes drilled in a matrix pattern. Electrons lost enough energy passing through tungsten, so that only the particle trajectories that went through the sieve holes could reach the detectors. Each selected event corresponded to a specific carbon foil and one of the holes in the sieve slit, whose location was surveyed before the experiment (Fig. B-3). Therefore the actual angle of the vertex trajectory was known for each event. The vertical (θ_{tg}) and horizontal (ϕ_{tg}) tangent angles were independently fit. The final reconstructed sieve-slit plate is shown in Fig. 5-5. Two of the sieve holes are larger than the rest to allow identifying the center and orientation of the sieve as shown in Appendix B.1; and the corresponding reconstructed larger holes in Fig. 5-5 have more statistics than the surrounding holes. The sieve-slip plate is larger than the acceptance of the Left-HRS so that the full acceptance can be calibrated. At the edge foils (e.g., the most upstream foils #0 and downstream foil #5), the HRS acceptance is very limited as shown in Fig. 5-5.

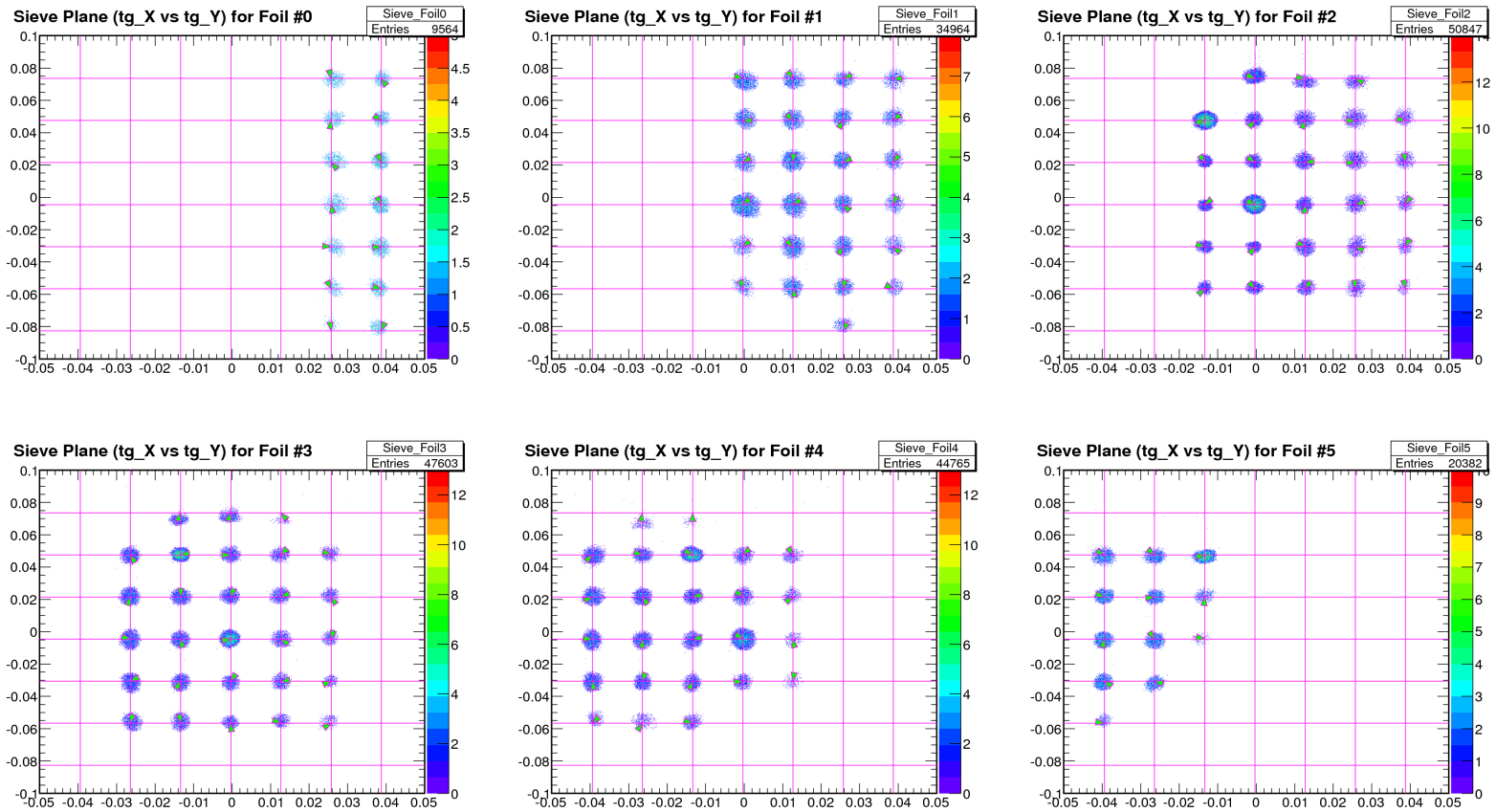

Figure 5-5: The reconstructed sieve-slit pattern (vertex trajectory projection at the sieve-slit plane): each plot is for a single carbon foil; each crossing of the pink lines corresponded to the location of a sieve hole.

The momentum calibration used the elastic scattering data and a similar setup as that for the angular calibration (left side of Fig. 5-4). The full coverage of the HRS momentum acceptance was achieved by scanning the HRS central momentum p_0 around the carbon elastic peak, i.e., δ-scans at $p_0 = p_{\text{Elastic}}$, $\pm 2\%$ and $\pm 4\%$. For each momentum setting, events from a specific carbon ground state or an excitation state were selected. The real momentum was calculated using the scattering angle and the corrections due to the collision energy losses in the target material (Appendix B.3). An global fit was performed using data from all δ-scan points. The final momentum reconstruction results are shown in Fig. 5-6, with a resolution better than 5×10^{-4} was achieved[3].

Vertex calibration used DIS scattering data on the multi-carbon foil target . The setup is shown on the right side of Fig. 5-4. All reconstructed foil vertex peaks were aligned to their actual positions as shown in Fig. 5-7. The average z_{react} resolution was 6 mm with the spectrometer at 16° for a 40 cm long target. The Left HRS and BigBite vertices are consistent to the level of 1 cm (1σ) for the coincidence events.

Extended Target Correction and Raster Correction

The optics matrix, which was calibrated as described earlier, does not include all the information for the optics reconstruction: it give the first order approximation of the optics reconstruction by assuming the spectrometer at the angle of 90° and the beam propagates along the hall center line. However, for the Left-HRS whose acceptance is small, a set of simple corrections on these first order results, so called Extended Target Correction, can be applied. It has been shown in Ref. [198] that the Extended Target Correction is linearly correlated with the vertical beam position. Therefore, this correction is also called the beam raster correction. This correction was applied using the Hall A analyzer [192], subroutine THAEXTTARCOR.

[3]The ^{4}He gas and air in the target area limited the momentum resolution. The intrinsic momentum resolution for HRS is 1×10^{-4} as shown in Sec. 3.4.

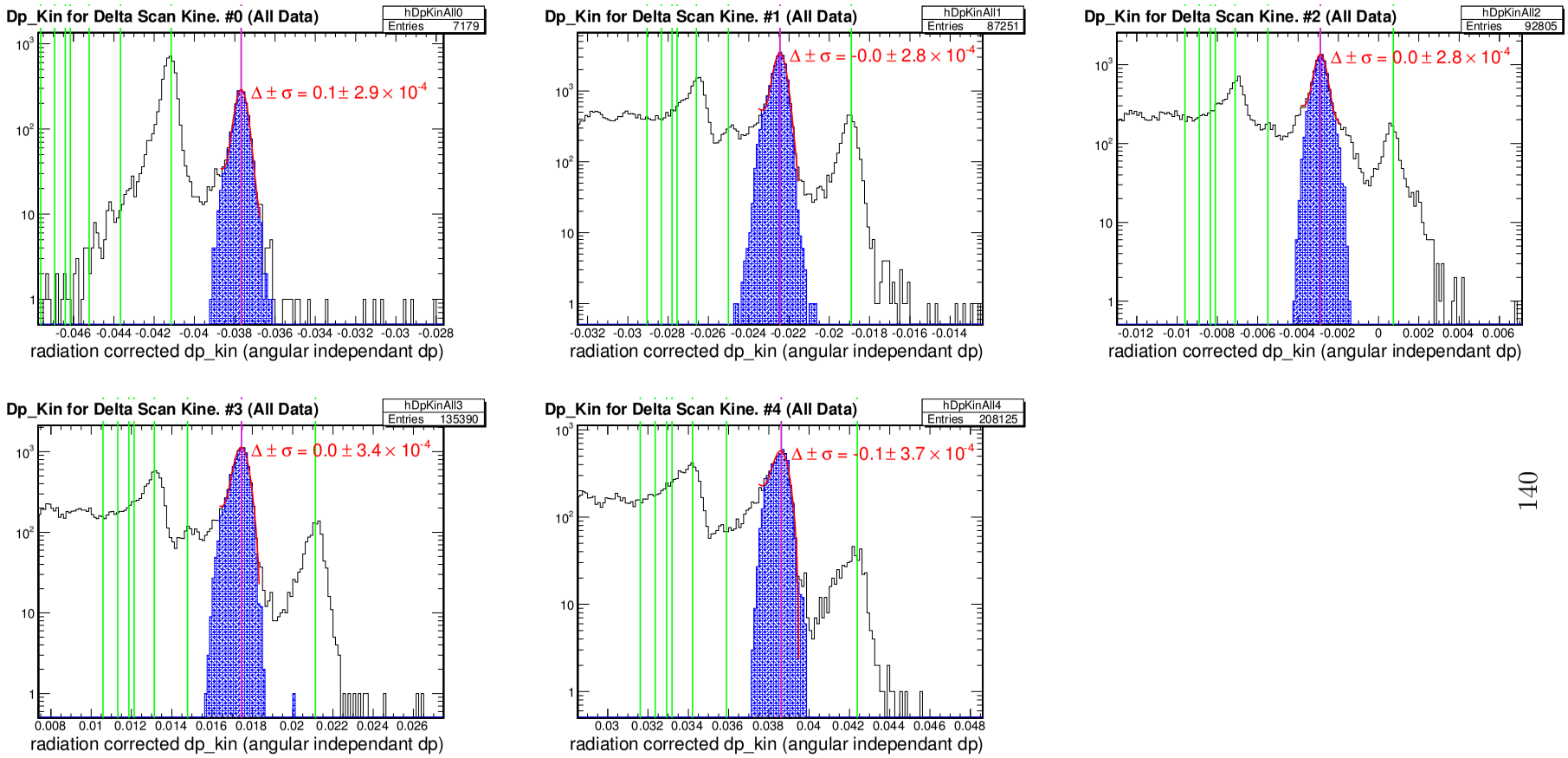

Figure 5-6: The reconstructed normalized momentum of carbon elastic data for five central momentum settings. The black curve is data, within which, the blue shaded area shows the data used for the calibration, whose expected momentum is marked by magenta vertical lines. The blue areas are fitted (red curves) and compared to the expectation, with its mean deviation (Δ) and width (σ) labeled. The green lines mark out ground and other excitation states that were not used for the calibration. The excitation states automatically agree with the expected value, which demonstrates the stability of the fit.

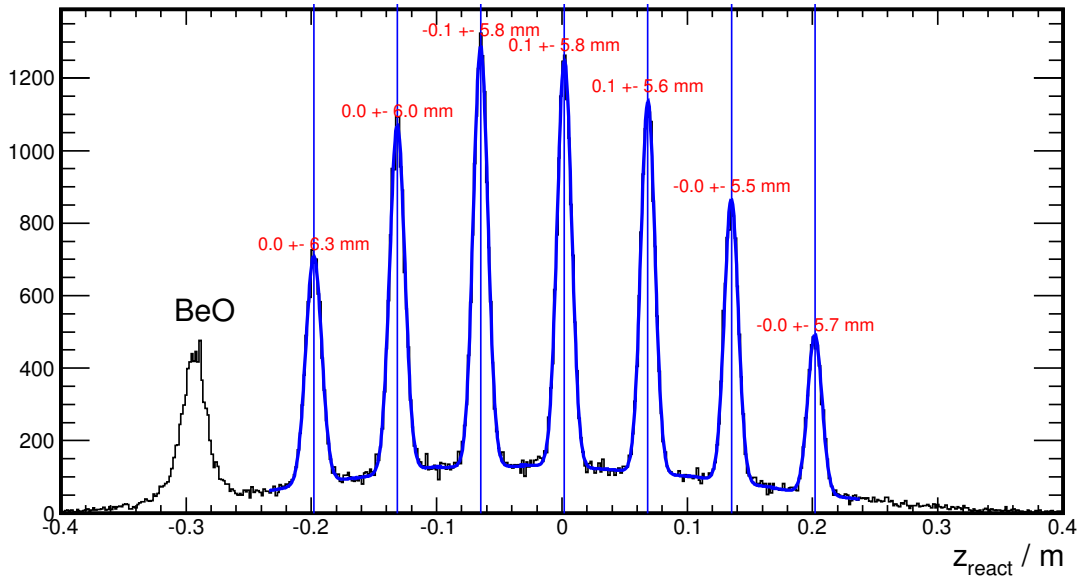

Figure 5-7: Reconstructed vertex position z_{react}: each carbon vertex peak is fitted and compared to its surveyed location, which is marked by vertical blue lines. The leftmost peak is a beryllium oxide foil (see also Fig. 4-9).

5.2.2 BigBite Spectrometer

5.2.2.1 Detector Calibration

Multi-Wire Drift Chamber (MWDC)

The procedure of the BigBite wire chamber calibration mainly involves checking the cable map, calibrating the location of each wire, determination of TDC timing offset and parametrization of the drift time to distance conversion [131]. The resolution of tracking residual, which is defined as the distance between the actual hit position and the projected hit position from the reconstructed track, was 180 μm (σ). The average chamber hitting efficiency, which represents the efficiency that wire chamber plane responds to a actual charge track going through the chamber, was 98% on an average. The tree search pattern match algorithm [199], which matches the hit pattern in all planes with templates of increasing granularity and resolution, was used to reconstruct tracks from the wire chamber raw hits. The overall tracking efficiency[4] was estimated to be higher than 95% with low background ($1 - 2\,\mu A$ beam) by

[4]The tracking efficiency is defined as the probability of reconstructing a correct track for a charged particle passing through the active areas of all the MWDC planes and produced a trigger in BigBite.

comparing the simulated and reconstructed yield with hydrogen elastic scattering process, and higher than 85% with the background at production running ($\leq 14\,\mu A$ beam) by studying the yield dependence of the beam current [131].

Calorimeters

The BigBite calorimeter was used for identifying the scattered electrons by rejecting pions and the photons. The calibration was performed using the reconstructed momentum from the elastic hydrogen scattering at two different beam energies (1.230 GeV and 2.396 GeV), which provided electron events with precisely known energy deposition in the calorimeter. The calibration procedure for the calorimeter system was mainly about aligning the gain for each ADC [140]. The energy for a shower cluster was reconstructed by identifying the block with maximum energy deposition and summing the deposition with 8 blocks surrounding it The energy resolution of about $\sigma_{\frac{E}{p}} = 8\%$ was achieved [140].

5.2.2.2 Optics Calibration

The procedure of the BigBite optics calibration followed the same principle as discussed in Sec. 5.2.1.2. The calibration procedure as described in Ref. [131] is summarized as following: the interaction vertex reconstruction was calibrated using the multi-foils carbon target, whose locations were precisely known from the accurate survey conducted for the experiment. The scattering angles were calibrated using a removable sieve slit placed in front of the BigBite magnet (Fig. 3-9). The momentum was calibrated using the elastically scattered electrons from a hydrogen target, for which the electron momentum can be precisely calculated using the two-body kinematics. The quality of the calibration is demonstrated in Fig. 5-8 and the sieve pattern reconstruction can be seen in Fig. 5-9.

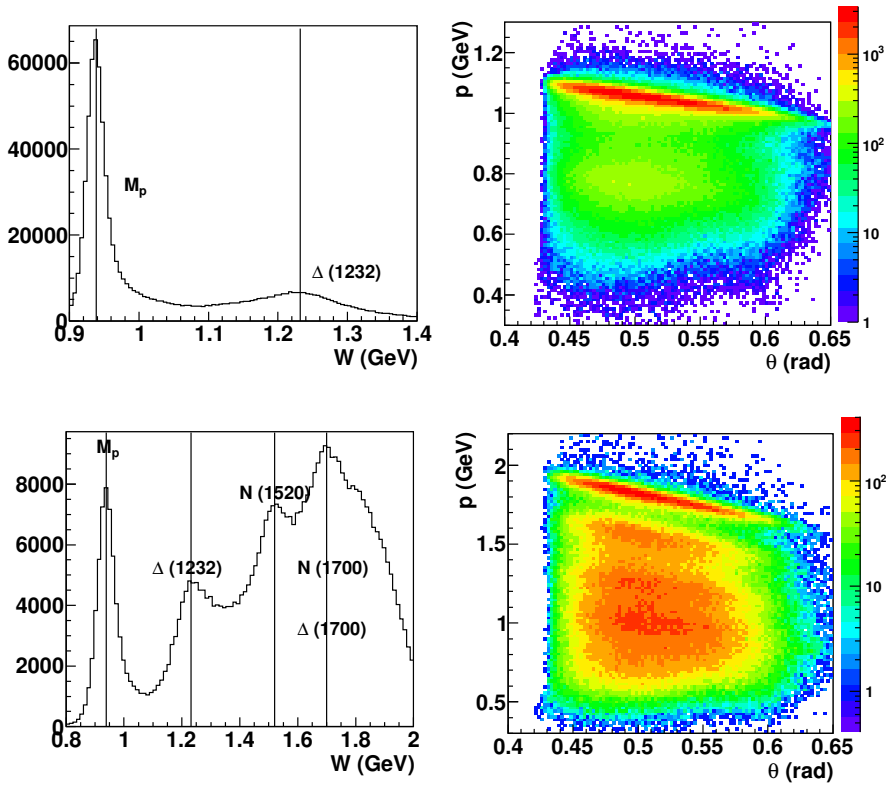

Figure 5-8: Demonstrating the quality of the BigBite momentum reconstruction by reconstructing electrons scattered on a hydrogen target [131]. Left: the reconstructed invariant mass spectrum of the nucleon and its resonances; right: the scattered electron momentum VS scattering angle. The color represents event densities with the color axis shown on the right side. The electron beam energy is top: 1.230 GeV and bottom: 2.396 GeV.

5.2.3 Coincidence Timing

General Approach

For experiment E06-010, the asymmetries were measured by detecting the hadrons in the Left-HRS, which are in coincidence with the electrons detected in the BigBite spectrometer. A coincidence timing (CT, also called coincidence time-of-flight, cTOF) between these two spectrometers is defined as the time difference between the production of the two particles at the reaction point as determined by these two spectrometers. Therefore, a perfect system should show a CT with a sharp peak at 0 ns. In the case of multiple final states, a CT is calculated with respect to a specific species of particle in each arm. The coincidence of different species of particle would

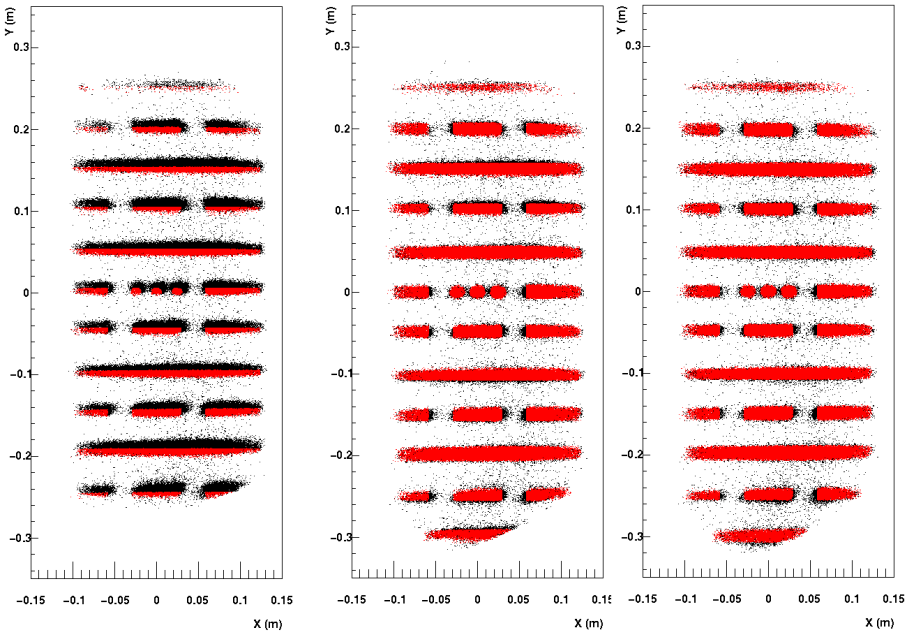

Figure 5-9: The left panel shows the reconstructed sieve pattern with the first order optics model [131]. The middle panel shows the sieve pattern after adding offsets. The right panel shows the sieve pattern after applying the higher order corrections. The red points indicates the location of sieve holes/slots.

appear at different locations in that CT spectrum due to the time difference of flight time for different particles.

The major goal of the CT calibration for Experiment E06-010 is zeroing the offsets for the $(e, e'h)$ CT peaks and optimizing the resolution. As discussed in Sec. 6.1.4, the CT was used in the later stage of analysis for:

- Reducing random coincidence background by requiring the particle detected in both spectrometers were produced at the target within a few ns.

- Improving particle identification (PID) on the hadron arm (the Left-HRS): assuming electron events are selected with the Bigbite spectrometer, the CT peak location will be related to the time-of-flight (TOF) of hadrons detected by the L-HRS. Therefore, the kaon peak will be separated by $\sim$ 1.8 ns from that of the pion, and the proton-pion peak separation is $\sim$ 6 ns. This separation is especially important to obtain a clean kaon data sample.

In the calculation, the CT can be separated into three parts and each was calibrated independently:

$$\text{CT} = \text{RF Time}_{\text{LHRS}} - \text{RF Time}_{\text{Bigbite}} - \text{Trigger Time Difference}\,, \tag{5.2}$$

where Trigger Time Difference is the time difference between two single arm triggers. RF $\text{Time}_{\text{Spectrometer}}$ is defined as the amount of time between a vertex reaction and the single arm trigger. RF $\text{Time}_{\text{Spectrometer}}$ includes contributions from

- Time-of-Flight (TOF): amount of time for a particle to travel from the reaction point to the timing detector, which was calculated using the flight path length and speed, $\frac{\text{Pathlength}}{v}$.
- Response time of timing detector: including detector response time, cable delay and electronic process time, which is a constant for each scintillator bar.
- Time difference between timing detector signal and the trigger signal. This information was recorded using high resolution (60.2 ps on Bigbite and 50.0 ps on L-HRS) TDCs.

"RF Time" is named after its calibration procedures: during E06-010, the beam radio frequency (RF) signal, which characterizes the beam bunch timing, was recorded in a TDCs (noted as t_{RF}), relative to the single arm trigger signal. Therefore, when the spectrometer's central scattering angle is small, RF $\text{Time}_{\text{Spectrometer}} - t_{\text{RF}}$, which is called RF Structure, should appear as sharp peaks repeating every 2 ns (beam bunch spacing). RF $\text{Time}_{\text{Spectrometer}}$ is calibrated independently for each arm, as discussed in the following text.

Left-HRS Single Arm Timing Calibration

In the Left-HRS, the timing detector was the S2m scintillator. RF $\text{Time}_{\text{LHRS}}$ was calculated using

$$\text{RF Time}_{\text{LHRS}} = \frac{(t_{\text{Left}} + t_{\text{Right}})}{2} - \frac{\text{Pathlength}}{c \cdot \beta}\,, \tag{5.3}$$

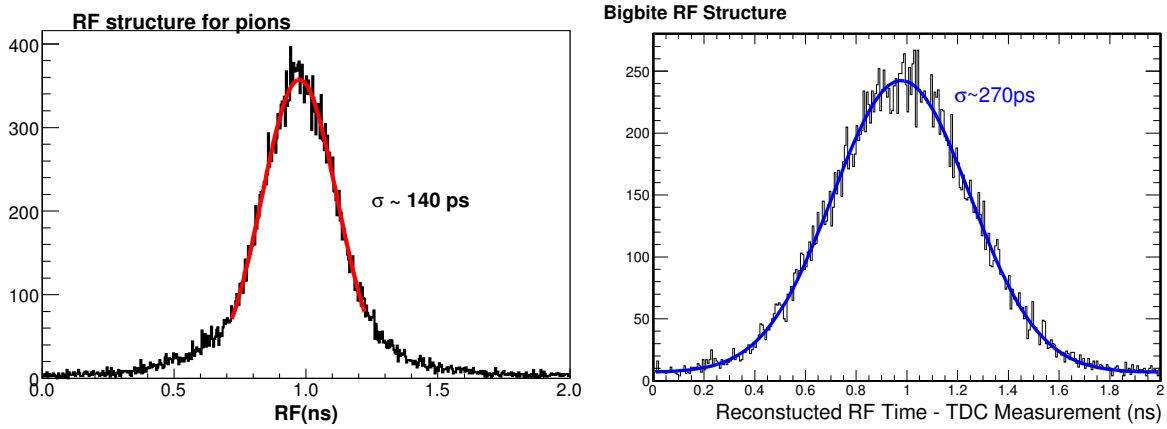

(a) (b)

Figure 5-10: RF Structures, RF $\text{Time}_{\text{Spectrometer}} - t_{\text{RF}}$, which was arbitrarily centered at 1 ns. (a) Left HRS:RF $\text{Time}_{\text{LHRS}} - t_{\text{RF}}$ for the pion samples. The fit shows a timing resolution of $\sim$ 140 ps. (b) BigBite: RF $\text{Time}_{\text{Bigbite}} - t_{\text{RF}}$ for the electron events.

where t_{Left} (t_{Right}) is the calibrated scintillator time from the left-side (right-side) of the paddle, and c is the speed of light. β was calculated using the measured momentum in Left-HRS and the mass of the particle. The following factors were corrected or implemented: path-length corrections, scintillator time offset corrections and the time-walk corrections. The time-walk correction for each paddle was calibrated by looking at the dependence of the RF Structure as a function of the average of the left and right ADCs. A final iteration of the alignment of timing offsets was performed following the time-walk correction. The final resolution from the L-HRS side was $\sim$140 ps for the pions (Fig. 5-10a).

BigBite Single Arm Timing Calibration

For the BigBite spectrometer, timing was calibrated for electron and photon candidates. The timing detector inside the BigBite spectrometer was a 13-bar scintillator plane inserted between the pre-shower and shower lead glass detectors. A PMT was mounted on each end of the scintillator bars, whose signals were recorded by digitalizing both the timing and amplitude information. The achieved timing resolution for a single bar was $\sim$ 230 ps. For an electron event, the primary electron, as well as secondary particles from electromagnetic shower inside the pre-shower detector, fired

at least one of the scintillator bars and probably one of the neighboring bars.

The calibration procedure was separated into the following major steps:

1. Scintillator bar offset and time-walk effect correction. First, events firing only two neighboring scintillator bars were selected. The timing difference between these two bars were optimized toward 0 by applying a time offsets for each PMT as well as the time walk correction. The time walk effect on each PMT was found to be similar. and was reasonably described by

$$\Delta t_{\text{time walk}} = -17.9(\text{ADC} - \text{pedestal})^{-0.140}\text{ns}\,. \tag{5.4}$$

2. Path-length calibration: a simple linear correlation was used to correct the path-length differences: (Eq. 5.5)

$$\Delta L_{\text{time walk}}/c = 1.4\,\text{ns} * \theta_{\text{MWDC}}\,, \tag{5.5}$$

   where θ_{MWDC} is the tangent[5] of the vertical angle for the track as measured by the MWDC. Up to the second order, no notable improvement was found by adding further polynomial terms.

3. A second iteration of bar by bar offset alignment was performed to remove the vertical position dependence.

The final resolution for the RF time for the BigBite spectrometer was ~ 270 ps (1σ), as shown in Fig. 5-10b.

In a parallel study, the BigBite trigger detector (total shower detector) timing was also calibrated to achieve a better tracking performance in the drift chambers. The full width at half maximum (FWHM) uncertainty of the trigger was reduced from ~ 8 ns down to ~ 4 ns, which leads a $\sim 10\%$ improvement on the squared tracking residual[6].

[5] tangent: trigonometric function tan ()

[6] Tracking residual, which is defined as the distance between track projections on the hit wire plane and the hit position calculated using time-of-drift, is a flag of the tracking precision. Calibration of

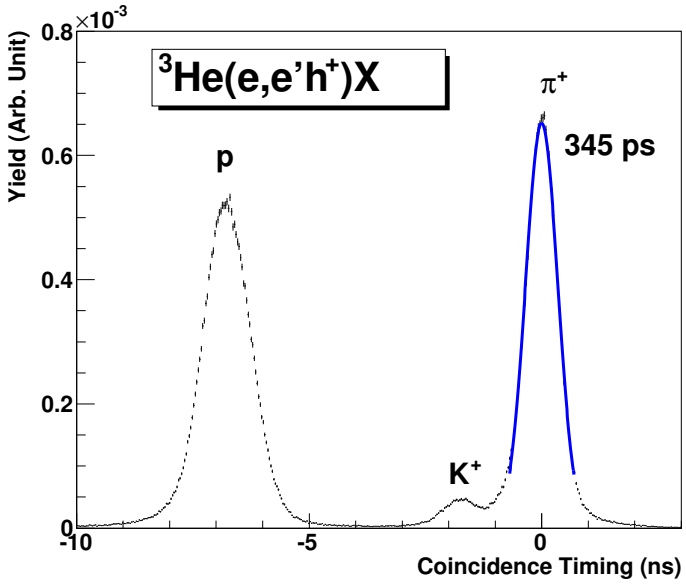

Figure 5-11: ^{3}He$(e, e'h^+)X$ coincidence time spectrum, where h^+ represents positively charged hadron. The pion mass was used in the calculation of RF Time$_{\text{LHRS}}$ in Eq. (5.3) and therefore the pion peak was narrower and centered at 0 ns. The blue curve is a Gaussian fit.

Two Arm Coincidence Time

For the last term in Eq. 5.2, Trigger Time Difference was measured by a TDC with a resolution of 60.2 ps. A typical CT spectrum with the L-HRS detecting positive hadrons is shown in Fig. 5-11. The final CT reached a resolution of $\sim$ 345 ps (1σ) for $(e, e'\pi)$ reaction and $\sim$ 400 ps (1σ) for $(e, \gamma\pi)$ events. The impacts of this calibration are

- Compared to the coincidence window[7] of $\sim$ 200 ns, a $\pm$1 ns (3σ) cut will suppress random coincidence events by an factor of 100.

- For the analysis of the coincidence kaon productions[8], by cutting on the kaon CT peak with a window of $\pm$1 ns, pion rejection can reach $\geq 25:1$. Most of the pion leakage comes from non-Gaussian tails in the timing peaks.

the trigger timing improved the precision of time-of-drift and therefore reduced the tracking residual for the MWDC.

[7]If the trigger time between the Left-HRS and BigBite is within this window, the event will be recognized as a coincidence event (T5) by the DAQ as discussed in Sec. 3.5.2.

[8]Kaon production is not the topic for this thesis.

5.2.4 DAQ Livetime

Not all the good events in the detector were recorded in the data stream due to the imperfect working cycle of the DAQ system, or DAQ deadtime, which was dominated by two factors:

- The front-end electronics, e.g. discriminators, may lose some events in high rate conditions due to effects such as signal pileup. This effect is also known as electronic deadtime (EDT).

- The DAQ electronics were not accepting triggers at all times. When an event occurs, the trigger supervisor accepted the trigger and sent an L1A signal to all the read-out controllers (ROCs) which digitalized the signal. The trigger supervisor maintained a busy state while all the ROCs were being read out. This busy state could last $300 - 500$ μs. The time cost was related to the specific set of channels and ROCs to read out, therefore it was related to the type of event trigger. This waiting period caused a loss of events that occurred during this period.

During Experiment E06-010, the typically DAQ deadtime was much higher than the electronic deadtime.

The deadtime effect was measured and corrected during data analysis. The complementary part of the deadtime, the DAQ live time for each trigger is defined as:

$$LT = \frac{N_{data}^{recorded}}{N_{scaler}^{trigger}} , \tag{5.6}$$

where $N_{data}^{recorded}$ is the number of events recorded for each trigger and $N_{scaler}^{trigger}$ is the number of raw triggers counted by the scalers, which have no deadtime.. Live time usually depends on the pre-scale factors of the trigger and the number of total rates recorded by the DAQ. In the trigger design of Experiment E06-010, an electronic deadtime pulse (EDTP), with a frequency of 12.5 Hz, was plugged into each trigger type to mimic a real trigger. The goal of this EDT pulser was to monitor the

electronics deadtime. Thus the livetime formula will be modified as:

$$LT = \frac{N_{data}^{recorded} - N_{EDTP}^{recorded}}{N_{scaler}^{trigger} - N_{scaler}^{EDTP}}. \tag{5.7}$$

The livetime normalization was applied to the yield (Sec. 5.5.1) and asymmetry (Sec. 5.6 and Sec. 6.1.2) calculations.

5.3 Event Selection and Kinematic Distribution

5.3.1 Data Quality Cuts

Multiple procedure and cross check were employed to exclude unreliable runs and events, which included

Run List: a MYSQL database[9] was used to organize run information [131]. Good production runs were selected by checking the detector response, trigger rate, scaler consistency between multiple copies, yield stability and the original experiment logs.

Unstable Periods Cuts: within each run, unstable periods were removed in the event stream and scaler counts synchronously. The excluded unstable periods were beam trips, detector trips, magnet trips and localized high DAQ deadtime periods as discussed in Ref. [131].

5.3.2 Cuts for BigBite Electron Sample

The electron-hadron identification in the BigBite spectrometer was provided by the calorimeter, together with the reconstructed momentum information from MWDC. It consisted of the lead-glass detector in a preshower-shower configuration.

Track Quality Cut: the quality of the reconstructed track was determined by the quantity: χ^2/N_{dof}. A cut of $\chi^2/N_{dof} < 2.4$ was applied to remove the reconstructed tracks with poor fit quality.

[9] URL: `http://nedm.tunl.duke.edu/db/`

Track Matching Cut: the calorimeter provided the center position of the reconstructed shower cluster. For any charged particle, the position of the reconstructed cluster center (x and y) should match with the projected position from the reconstructed track on the shower. Since the profile of energy deposition for electron and hadrons were quite different in the calorimeter, separate cuts were applied.

Optics Validity Cut: at the top and bottom edges of the BigBite magnet, the magnetic field is weaker than that in the central region. The optics reconstruction deviated in these extreme regions. Therefore a 2-D graphic cut was used for excluding these extreme regions.

Momentum Cut: BigBite optics was calibrated using two elastic energies around 1 and 2 GeV. Therefore, a cut on the momentum range was applied to avoid over extrapolation and avoid the high-pion-contamination region at the lower momentum side:

$$0.6 \text{ GeV} < p < 2.5 \text{ GeV} \tag{5.8}$$

Charge Type Cut: the BigBite magnet separated particles of opposite charges through the vertical bending. The bending direction was measured using the reconstructed tracks. Since the BigBite magnet provided a simple dipole field, the negatively charged particles were bent upwards and the positively charged particles were bent downwards. Therefore, they were clearly separated in the plot of vertical position X and the vertical slope dX/dZ in the first MWDC, as illustrated in Fig. 5-12, where $+X$ is in the plane of wire chamber and downward; +Z is perpendicular to the chamber plane towards the calorimeter.

Calorimeter PID cut: for each track, a shower cluster was identified by matching its center with the projected track position. The PID in the calorimeter system was performed with a 2-D cut on the energy deposited in preshower vs. the E/p, which is the ratio of the total energy deposited in the shower system to the reconstructed track momentum. Fig. 5-13 shows a typical PID plot with

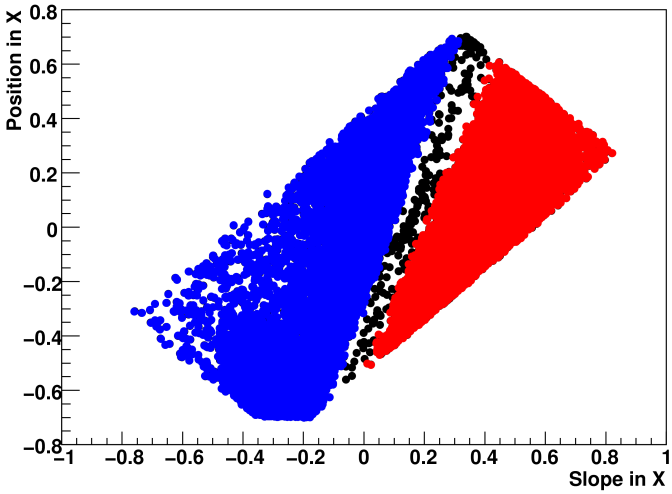

Figure 5-12: Vertical position (Position in X) vs. the vertical slope dX/dZ (Slope in X) in the first MWDC (Up is towards $-X$ and +Z is perpendicular to the chamber plane towards the calorimeter) [131]. All particles are likely to have a more positive dX/dZ at a positive X and vice versa, due to the geometrical constrains for particle to reach MWDC from the target (Fig. 3-9). The blue points are the negative charged particle, which are bended towards $-dX/dZ$ (more upwards). The red points are the positive charged particles, which are bended towards $+dX/dZ$ (more downwards). The black points include everything.

the T6 trigger (higher shower-threshold single BigBite trigger as discussed in Sec. 3.5.2). The corresponding regions for electrons and pions are labeled. For the electron sample, two cuts were applied: $E_{\text{preshower}} > 200$ MeV as the red line in Fig. 5-13 and a 2.5-σ E/p cut around 1. From the smaller-x bins to larger ones, the pion contamination in the electron sample ranged from 1.7% to 0.2% for the coincidence π^+ in HRS and from 0.5% to $< 0.1\%$ for the coincidence π^- in HRS, which was estimated by fitting the pion spectrum in the preshower detector ($E_{\text{preshower}}$) with a Gaussian convoluted Landau function and counting its tail in the electron cut ($E_{\text{preshower}} > 200$ MeV) [131, 140]. An excluding cut, $E_{\text{preshower}} < 150$ MeV, was used to select pion like events.

Interaction Vertex cut: A 40-cm-long target cell was used, and a cut was applied to the interaction vertex to exclude events from the target beam window at ±20 cm: $|z_{\text{Vertex}}| < 0.185$ m.

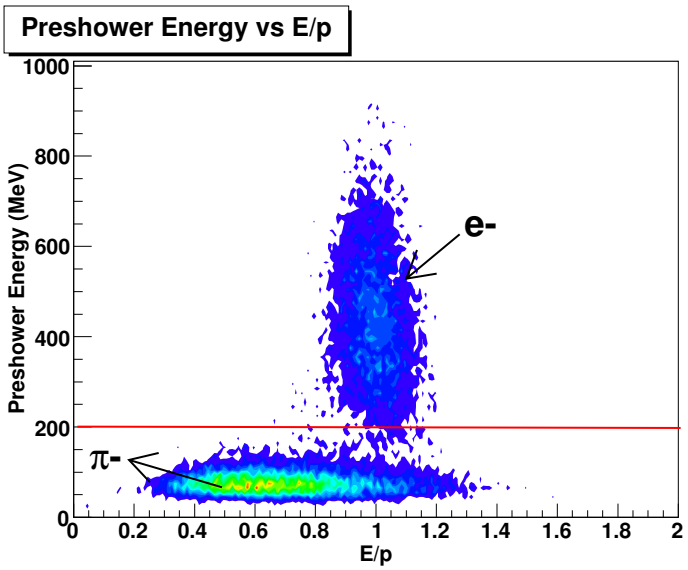

Figure 5-13: Energy deposition in the preshower vs. the E/p. Electrons and pions (hadrons) are labeled.

5.3.3 Left-HRS Cuts

General Cuts

Spectrometer Acceptance: for the Left-HRS, its small acceptance and the heavy shielding provided a low background environment. Only particles with selected charged and momentum can reach the detector package. Simplified residual cuts were used to remove events far from the main acceptance, which can be rescattered at the edge of the acceptance. The cuts are shown in Fig. 5-14, which are placed on six 2-D projections of the 4-D acceptance space for the Left-HRS The cut was placed close to but outside the rough edges of the event distribution to maximize the statistics.

Vertex: consistent with the BigBite vertex cuts as discussed in the last section, cuts were placed on the Left-HRS vertex to avoid beam window at $z_{\text{Vertex}} = \pm 0.20$ m. For single arm events, $|z_{\text{Vertex}}| < 0.175\,\text{m}$; for the coincidence events, the cut was modified to $|z_{\text{Vertex}}| < 0.185\,\text{m}$.

VDC Single Track: only events with single tracks in VDC were used in the analysis, which excluded ~3% events with multiple tracks.

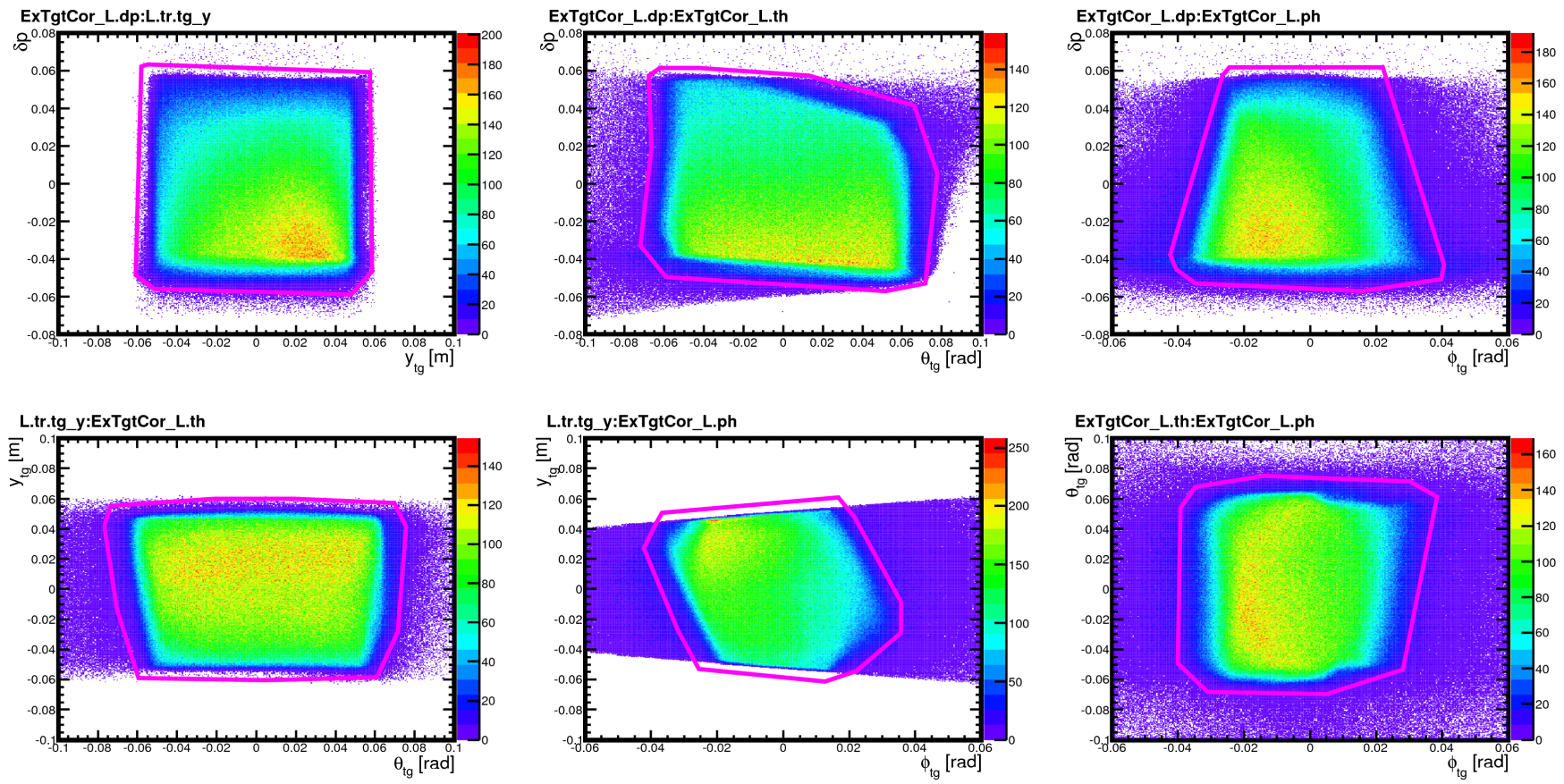

Figure 5-14: Left-HRS acceptance cuts (magenta lines) on 2-D projections of 4-D phase space for relative momentum $\delta p = (p - p_0)/p_0$, horizontal angle ϕ_{tg}, vertical angle θ_{tg} and horizontal position y_{tg}.

Lead-Glass Counter Acceptance: the track projection on the lead-glass detector was limited within the detector coverage:

$$-1.5\,\mathrm{m} < \quad L.prl1.trx \quad < 1.0\,\mathrm{m}, \tag{5.9}$$

$$-0.24\,\mathrm{m} < \quad L.ptrl1.try \quad < 0.24\,\mathrm{m}, \tag{5.10}$$

where $L.prl1.trx$ is in the projection in the dispersive direction and $L.prl1.try$ is for the non-dispersive direction.

PID Cuts

Three detectors were used for this purpose in the Left-HRS: lead glass, gas Cerenkov, and the aerogel Cerenkov detectors. Their cuts for different particles are listed below:

Gas Cerenkov Detector: the single photon peak was aligned to normalized ADC Sum $L.cer.asum\_c = 200$ during the calibration (Sec. 5.2.1.1). $L.cer.asum\_c > 300$ as marked by the green line in Fig. 5-2a was used to select electrons which produced Cerenkov light in the detector; $L.cer.asum\_c < 250$ was used to select hadrons, which was marked by the red line.

Aerogel Cerenkov Detector (A1): the single photon peak was aligned to normalized ADC Sum $L.a1.asum\_c = 100$ during the calibration (Sec. 5.2.1.1) as shown in Fig. 5-2b. $L.a1.asum\_c > 150$ was used to select pions in the hadron sample; other hadrons were selected by the inverted cut $L.a1.asum\_c < 125$.

Lead-Glass Shower Detector: electrons were selected using E/p>0.7 and hadrons were cut by $E/p < 0.6$ as marked by the red and green lines in Fig. 5-3, respectively.

For the pion events, there were several sources of contamination, which are largely suppressed using the above cuts:

- the first one was from electrons and the second one was from kaons and protons. The gas Cerenkov and lead-glass detector gave a combined electron rejection

factor of better than $10^4 : 1$. Since the yield for coincidence pion in the Left-HRS was larger than that for electrons, the contamination of e^- to the π^- sample was negligible leading to a negligible systematic uncertainty in the asymmetry results (Sec. 6.1.4).

- For kaons, the estimated K^+/π^+ rate was about 6% and K^-/π^- was not larger than 3%. The aerogel Cerenkov gave a kaon and proton rejection factor better than $10 : 1$, which was estimated using the cross calibration of CT. Therefore, the contamination of kaons into the pion sample was well below 1% ,which lead a minor systematic uncertainty in the asymmetry results (Sec. 6.1.4).

- Protons were largely rejected with the TOF cut in the coincidence channel (see TOF spectrum in Fig. 5-11). The residual was included in the random coincidence background ($< 1\%$ total). The corresponding systematic uncertainty for the asymmetry results due to the random coincidence background was very minor (Sec. 6.1.4).

5.3.4 SIDIS Events Cuts

Coincidence Cuts

Coincidence timing: the coincidence timing (CT) depended on the species of particle in each spectrometer. As an example, the CT spectrum for electrons in BigBite and π^+ in the Left-HRS is shown in Fig. 5-11. The cuts depended on the particle species as shown in Table 5.1.

Coincidence vertex cuts selected events for which the vertex for both spectrometers were close to each other. The 1σ width for the vertex coincidence peak was $1.8 \sim 1.2$ cm for lower momentum particles in the Bigbite to higher momentum ones. A momentum dependent cut was used to select the coincident events:

$$|z_{\text{react, BigBite}} - z_{\text{react, HRS}} - z_{\text{offset}}\left(p_{\text{BigBite}}\right)| \;<\; 3 \times \sigma\left(p_{\text{BigBite}}\right) , \quad (5.11)$$

where $z_{\text{offset}}\left(p_{\text{BigBite}}\right)$ and $\sigma\left(p_{\text{BigBite}}\right)$ are function of the BigBite electron mo-

Particle Species		Cuts	
BigBite	Left-HRS	Real Coincidence	Random Coincidence
electron	pion	-3 ns < pi_t < 3 ns	8 < pi_t < 65 or -65 < pi_t < -14
electron	kaon	-1 ns < K_t < 1 ns	9 < K_t < 59 or -73 < K_t < -43
electron	proton	-3 ns < p_t < 3 ns	73 < p_t < -23 or 11 < p_t < 61
photon	pion	-3 ns < pi_photon_t < 3 ns	9 < pi_photon_t < 59 or -69 < pi_photon_t < -19
photon	kaon	-1 ns < K_photon_t < 1 ns	9 < K_photon_t < 59 or -73 < K_photon_t < -43
photon	proton	-3 ns < p_photon_t < 3 ns	-73 < p_photon_t < -23 or 11 < p_photon_t < 61
hadron	pion	-2.5 ns < pi_t < 3.5 ns	9.5 < pi_t < 59.5 or -69.5 < pi_t < -19.5
hadron	proton	-2.5 ns < p_t < 3.5 ns	-73.5 < p_t < -23.5 or 11.5 < p_t < 61.5

Table 5.1: Coincidence time cuts, which depended on the particle species.

mentum p_{BigBite} in the unit of GeV,

$$z_{\text{offset}}\left(p_{\text{BigBite}}\right) = 2.5\,\text{mm} - 3.5\,\text{mm} * p_{\text{BigBite}} + 1.2\,\text{mm} * p_{\text{BigBite}}^2 \quad (5.12)$$

$$= 0 \sim 1\,\text{mm} \quad (5.13)$$

$$\sigma\left(p_{\text{BigBite}}\right) = 27\,\text{mm} - 17\,\text{mm} * p_{\text{BigBite}} + 5\,\text{mm} * p_{\text{BigBite}}^2 \quad (5.14)$$

$$= 1.2 \sim 1.8\,\text{mm} \quad (5.15)$$

These two functions were extracted by fit the coincidence vertex distribution using a Gaussian ansatz as described in Ref. [131].

Kinematic Cuts

The SIDIS event sample was selected with particle identification and kinematic cuts, including the four momentum transfer squared $Q^2 = -(l - l')^2 > 1$ GeV^2, the virtual photon-nucleon invariant mass $W = \sqrt{l - l' + P} > 2.3$ GeV, and the mass of the undetected final-state particles $W' = \sqrt{l - l' + P - P_h} > 1.6$ GeV. The cuts are shown as the horizontal yellow lines in Fig. 5-15a.

5.3.5 Kinematic Distribution

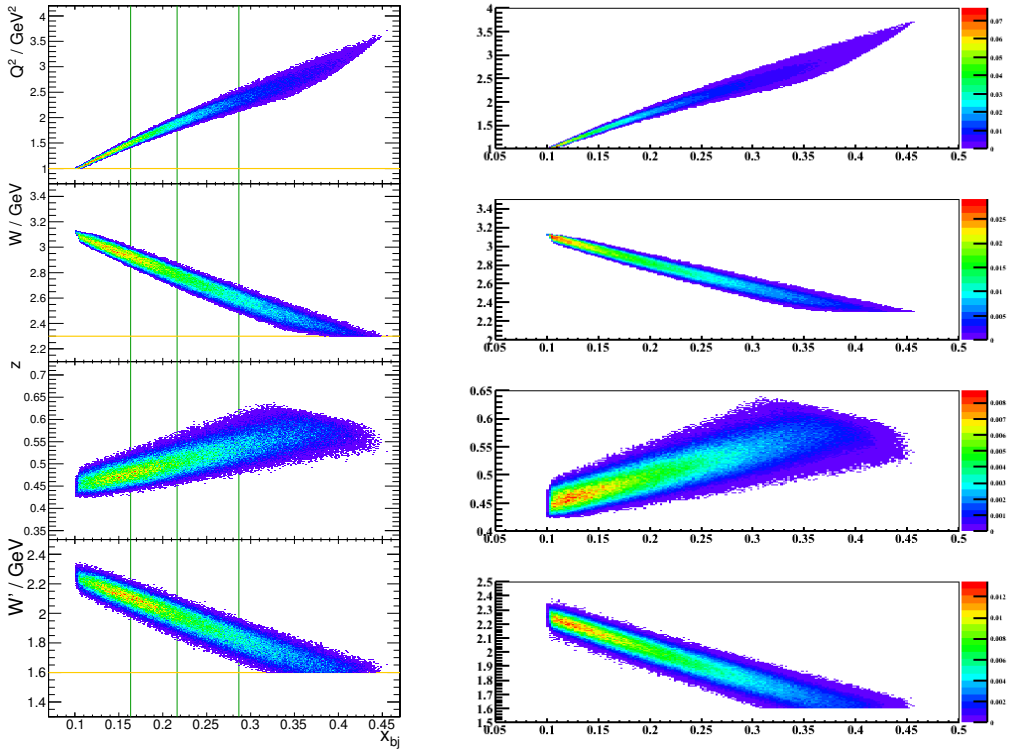

(a) Data (b) SIMC simulation

Figure 5-15: Kinematic phase space, (a) from data and (b) using the SIMC simulation (Sec. 5.4.1)

As shown in Fig. 5-15a, the kinematic coverage was in the valence quark region: the Bjorken scaling variable covered $0.16 < x < 0.35$ and the four momentum transfer squared covered $1.4 < Q^2 < 2.7\,\mathrm{GeV}^2$. The range of the measured hadron transverse momentum $P_{h\perp}$ was 0.24-0.44 GeV. The fraction z of the energy transfer carried by the observed hadron was confined by the HRS momentum acceptance to a small range about $z \sim 0.5$-0.6. Using the x cuts marked by green vertical lines in Fig. 5-15a, events were divided into four x-bins with equivalent statistics. The azimuthal angle distribution is shown in Fig. 5-16a. As shown in Fig. 5-16b, the azimuthal acceptance in $\phi_h - \phi_S$ was close to 2π at high x, while at lower x, roughly half of the 2π range was covered, including the regions of maximal and minimal sensitivity to $A_{LT}^{\cos(\phi_h-\phi_S)}$ at $\cos(\phi_h - \phi_S) \sim \pm 1$ and zero, respectively. The central kinematics, which were

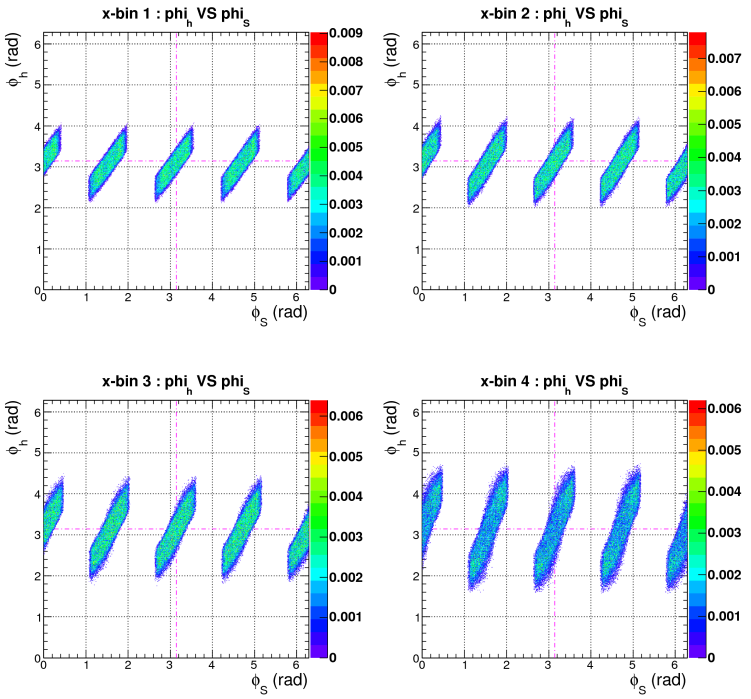

(a)

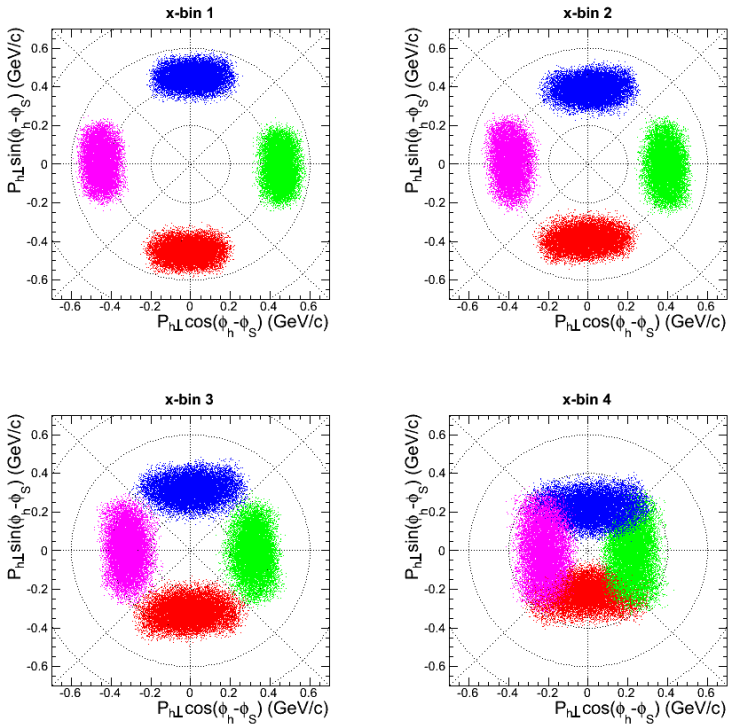

(b)

Figure 5-16: Azimuthal distribution for the SIDIS events. (a): ϕ_h VS ϕ_S; (b): polar plot of $P_{h\perp}$ (radius) VS $\phi_h - \phi_S$ (angle), where different color represents events from four target-spin directions.

x	Q^2 GeV^2	y	z	$P_{h\perp}$ GeV	W GeV	W$'$ GeV	ε	$\sqrt{1-\varepsilon^2}$
0.156	1.38	0.81	0.50	0.435	2.91	2.07	0.27	0.96
0.206	1.76	0.78	0.52	0.38	2.77	1.97	0.33	0.94
0.265	2.16	0.75	0.54	0.32	2.63	1.84	0.40	0.91
0.349	2.68	0.70	0.58	0.24	2.43	1.68	0.47	0.87

Table 5.2: Radiative corrected central kinematics for the four x bins. The depolarization factor $\sqrt{1-\varepsilon^2}$ as defined in Ref. [41] is included in the definition of $A_{LT}^{\cos(\phi_h-\phi_S)}$ as in Eq. (2.28).

averaged for each x-bin and corrected with mean radiative shifts (Sec. 5.4.1) are presented in Table 5.2.

5.4 Simulation of the Experiment

Two Monte Carlo (MC) simulation tools were developed for the E06-010 experiment, which is briefly summarized in the following two subsections:

- Sec. 5.4.1: SIMC was used to simulate the coincidence process, for which the detector responses were simplified (the simplification will be discussed in Sec. 5.4.1).
- Sec. 5.4.2: a GEANT3 based simulation was used to study the response and background for the BigBite spectrometer which was a relatively new apparatus in Hall A.

5.4.1 SIMC Simulation

General Features

The standard Hall C Monte Carlo code (SIMC) was modified by Dr. A. Puckett (Los Alamos National Lab), *et. al.* to include a realistic model of the BigBite spectrometer and a physics event generator [169]. The standard SIMC already includes

- a realistic model of the acceptance and resolution of the Hall A High Resolution Spectrometers (HRSs), and a model for the unpolarized semi-inclusive

$N(e, e'h^{\pm})X$ cross sections..

- radiative corrections to the SIDIS process
- a model for exclusive ρ production, an important physics background.

These features makes SIMC a natural option for a Monte Carlo simulation of coincidence $(e, e'h^{\pm})$ for the analysis of the E06-010 experiment. As discussed in Ref. [169], new features were developed:

- a model for the BigBite spectrometer was added
- realistic descriptions were developed for the materials of the polarized ^{3}He target for purposes of energy loss, multiple scattering and radiation of the incident and scattered particles and a simplified geometry of the target collimators.

In SIMC, an unpolarized event is generated in the following steps:

1. Simulated particles are "thrown" at the spectrometers in which all independent vertex variables (interaction vertex, particle angles, particle momenta) are generated randomly.
2. Using spectrometer optics models, each scattered particle is then transported to the detectors. Along the way, checks are made against numerous apertures and the decay of unstable particles is simulated.
3. If the particle reaches the detector, its trajectory is then "smeared" for detector resolution. The "smeared" track is then reconstructed back to the target using the optics models (Sec. 5.2.1.2 and 5.2.2.2) and is used as the input for the yield and asymmetry analysis.
4. If both the scattered electron and hadron tracks pass all apertures of Bigbite and the left HRS, respectively, the cross section corresponding to the randomly generated kinematics of both particles is calculated.

In the case of SIDIS, the unpolarized cross section is fully differential in x, y, z, Q^2, $P_{h\perp}$, but averaged over ϕ_h. An unpolarized physics event generator for SIDIS reactions on a transversely polarized ^{3}He target was used. The SIDIS cross section model for polarized ^{3}He assumed a simple incoherent sum over free nucleons at rest; i.e., $\sigma_{^3\mathrm{He}} = 2\sigma_p + \sigma_n$. The proton and neutron unpolarized SIDIS cross sections were calculated using an ideal leading-order approximation following Eq. (2.6), where the leading-order versions of the MSTW2008 PDFs [14] and DSS2007 FFs [200] were used. Following Appendix A.3 and the global analysis of [201], the transverse momentum dependence of the cross section was included assuming the following factors:

- Gaussian ansatz, as shown in Eq. (A.10) and (A.11).
- Quark flavor-independent width $\langle p_T^2 \rangle = 0.25$ GeV^2 for the intrinsic quark transverse momentum relative to the momentum transfer $\vec{q}$
- Hadron species-independent width $\langle K_T^2 \rangle = 0.20$ GeV^2 for the intrinsic transverse momentum of produced hadrons relative to the fragmenting quarks.

The similarity between the real and simulated experimental acceptances is illustrated in Fig.5-15b, which shows the correlations between Bjorken x and Q^2, the invariant mass W, the hadron energy fraction z, and the missing mass W'.

Two-Step Event Generators for Asymmetry Simulation

To efficiently use the CPU time, the event generation for the polarized scattering was separated into two steps:

Step 1: an unpolarized phase space (large amount of unpolarized events) was generated as discussed above and the result was saved to a intermediate data file. This step was expensive in the terms of CPU time.

Step 2: events in the phase space were stochastically rejected according to an input asymmetry model (listed below).

The final data file was analyzed using the same analysis algorithm as used for the experimental data and compared to the input asymmetries. The same phase space from step 1 was reused for different asymmetry models[10].

At the second step, events were rejected stochastically. The probability that it passed was

$$P = \frac{\sigma}{\sigma_0} / \max\left[\frac{\sigma}{\sigma_0}\right], \tag{5.16}$$

where σ is the SIDIS cross section as given in Eq. (C.1), which depended on the beam helicity, target spin and the vertex kinematic variables including x, y, z, Q^2, $P_{h\perp}$ and azimuthal angles. σ_0 is the unpolarized cross section averaged over azimuthal angles. The asymmetry models used in the simulation were:

- To simulate the SSAs corresponding to the Collins and Sivers effects, we used the phenomenological global fits of Anselmino and collaborators: Ref. [59] for the Collins moments and Ref. [202] for the Sivers moments.
- For DSAs, the WW-type estimation of A_{LT} was used following the discussion of Refs. [106, 107].
- The ^{3}He asymmetry was formed based on the asymmetry for protons and neutrons and followed the effective polarization approximation (Eq. (6.22)).

The final MC data followed the full SIDIS cross section model of Eq. (C.1).

Asymmetry Analysis

Equal integrated luminosities were simulated in each of the four target spin directions used in the transversity experiment. The output of SIMC is an ntuple with events distributed according to the acceptance-convoluted cross section, which was used for the following analyses:

- Target-SSA analysis, which was discussed in a recent paper Ref. [54] and Ph. D. theses of Refs. [140, 145, 131, 195].

[10]It is worth noticing that, for studies which shared the same intermediate data of Step 1, the statistics were not independent.

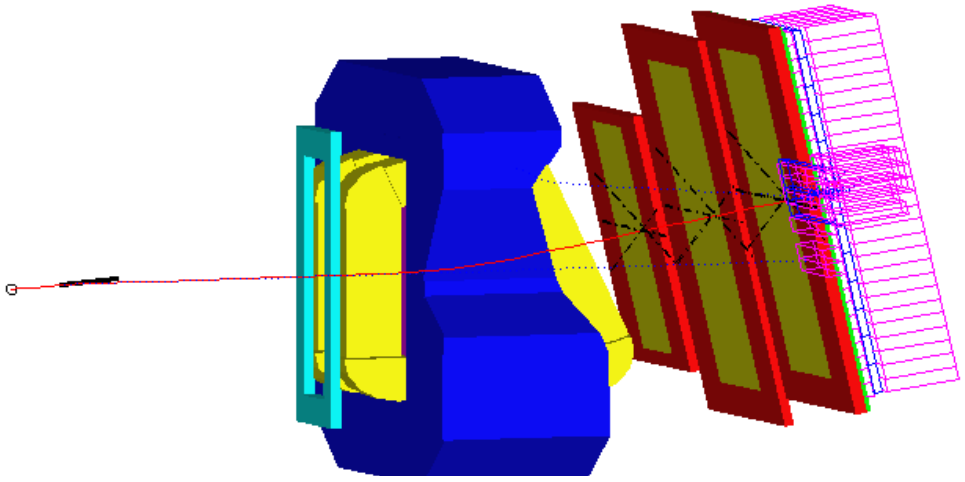

Figure 5-17: An event display of BigBite in COMGEANT. The fired wires are labeled by dashed lines. The hit preshower/shower blocks are illustrated [131].

- Systematics studies for the DSA measurement as discussed in Sec. 6.1.4: estimating the effect of reconstruction errors, bias due to extra azimuthal modulations, bin centering effect, radiative effects and low-W contamination.
- A systematics study for the charge-difference DSA, as discussed in Sec. 6.3.1.
- Test of ML estimator as discussed in Appendix C.4.3.

5.4.2 The GEANT3 Simulation for BigBite

During the data analysis, a GEANT3 based BigBite spectrometer simulation code was developed by Dr. X. Qian (Duke Univ.), *et.al.* [131] to understand the low energy background in the MWDC, to evaluate the tracking efficiency of the newly developed Pattern Match Tree Search tracking algorithm [199], to design the BigBite optics sieve slit, and to estimate the solid angle of BigBite. The software is based on "COMGEANT" [203], which is an interface to GEANT3.21 program.

The initial BigBite Model was constructed by Dr. E. Chudakov (Jefferson Lab) based on BigBite engineering drawings. The model was later updated in the data analysis of the Experiment E06-010 in order to describe the data. In the simulation, events are uniformly generated from a 40 cm long ^{3}He target. The interaction between

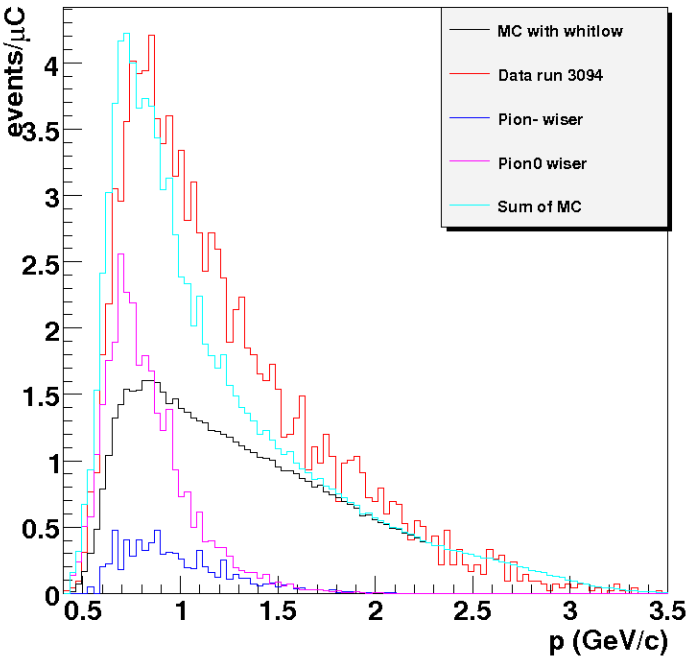

Figure 5-18: Data (red) and simulated (light blue) yields for the electron sample in the single BigBite trigger. The contributions for π^- and $\pi^0(\rightarrow \gamma) \rightarrow e$ contamination were shown as the blue and magenta curves, respectively.

the particle and the defined material is provided by standard GEANT3 and the motion of a charged particle inside the magnetic field is performed step-by-step. The detector responses are digitalized and stored in data files, which are analyzed using the same software tool for the real data [192]. One event display is shown in Fig. 5-17.

To study the rates in BigBite, particles were first simulated in a flat phase space; then a weight proportional to the a cross section was calculated for each event: the cross sections of single hadron electroproduction including protons and pions were calculated using the Wiser code [204] and the electron production was reasonably described by Ref. [205]. Hadron transverse momentum dependencies were added and tuned according to the data to better describe the observed distribution. The hadron rates for both BigBite and HRS hadrons were consistent with these models [131]. The observed yield for the electron sample was compared with the simulation as shown in Fig. 5-18, which agreed with the data. This study confirmed that the contamination for the electron events drops as the momentum in BigBite increased. And at the low

momentum region, which corresponds to the lower x region in the DIS kinematics, the dominant contamination was the pair-production background from the π^0 decay. For the single BigBite trigger[11], this contamination was about 50% in the electron sample, which was consistent with the estimation based on the real data [131]. In Sec. 5.5.2, this background in the coincidence data sample is studied using the E06-010 data and it was corrected for the asymmetry analysis as discussed in Sec. 6.1.3.

5.5 Unpolarized Data Analysis

5.5.1 Yield

As shown in Eq. (2.26), the yield (Y) was the basis for the asymmetry analysis:

$$Y = \frac{N}{C \cdot LT} \tag{5.17}$$

where N, C and LT was the event count, beam charge and DAQ livetime[12], respectively. The yield for the coincidence ($e'\pi^{\pm}$) channel are plotted against run numbers in Fig. 5-19, where the left column is for target spin state = +1 and the right column is for the -1 spin state. From top row to bottom, they are for the sum regardless of the helicity states (± 1 and unknown), for the beam helicity = +1 and the -1 beam helicity states. For each of the six combinations of spin-helicity states, a different set of scalers was used to measure C and LT[13]. The yellow vertical lines corresponded to target cell changes, when the target density and overall yield changed. The blue vertical lines are Left-HRS magnet polarity flips; runs between 4219 and 5456 were taken with positive charged particles detected in the Left-HRS. The Yields for runs with similar running conditions were checked for consistency to screen abnormal runs.

[11] The single BigBite trigger was not directly used in this thesis analysis.

[12] The electronics deadtime (1-livetime) for E06-010 was much smaller than the DAQ deadtime.

[13] The unpolarized scaler was reused for both target spin states. Since the target spin states interchange every 20 min and are well separated, it is effectively used as two scalers, each of which is associated with one spin state.

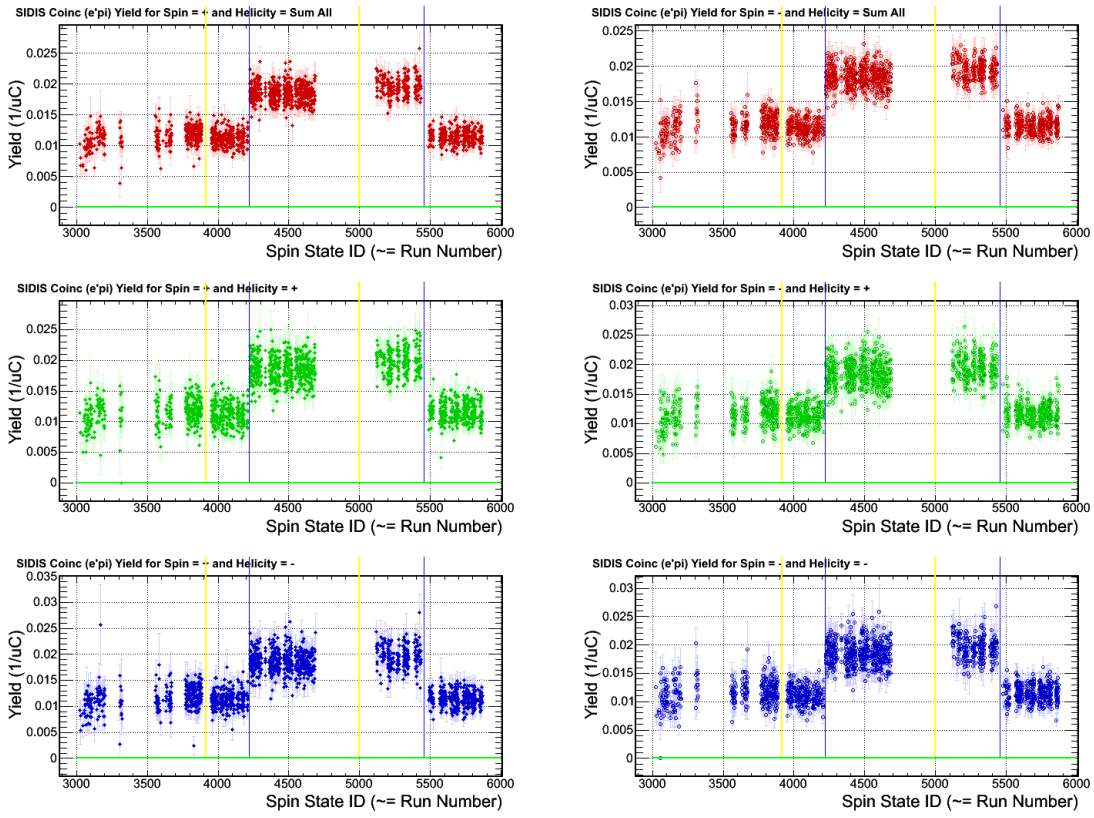

Figure 5-19: Yield history for all the production run

5.5.2 Pair-Produced Background

During the E06-010 experiment, a large fraction (70%) of the single BigBite low-threshold T1 triggers were observed that had a large deposition of energy in the calorimeter, but without tracks. These events were interpreted as photons, dominated by the decay products of the π^o mesons produced in the collision. This was supported by the GEANT3 simulation of the BigBite spectrometer as discussed in Sec. 5.4.2. There were two major mechanism for this background to be misidentified as an DIS electron events:

- The dominant mode of decay is $\pi^o \rightarrow 2\gamma$. When these photons pass through material, such as the target cell side wall, they can produce an electron and positron pair.

- In addition, the π^o mesons have about 1% decay branching ratio to $(\gamma e^- e^+)$ [6].

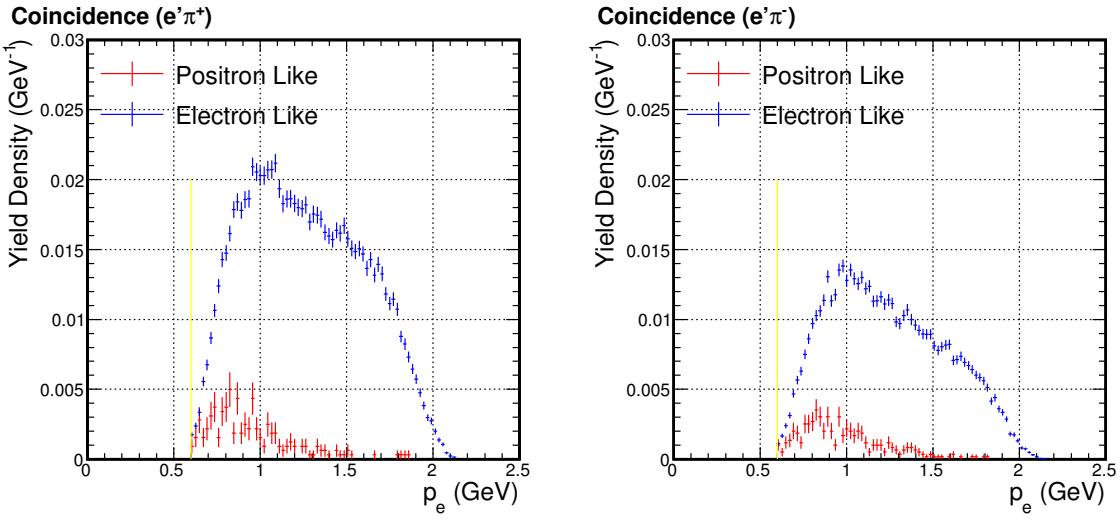

(a) (b)

Figure 5-20: Coincidence yield for electron with the BigBite negative mode (blue) and positron in the BigBite positive mode (red), plotted against the momentum in BigBite. A π^+ (left) or π^- (right) was detected in coincidence using HRS. The vertical yellow lines are the lower momentum cut at 600 MeV.

x	$f_{pair}^{\pi^+}$	$f_{pair}^{\pi^-}$
0.156	22.0±4.4%	24.0±4.8%
0.206	8.0±2.0%	14.0±2.0%
0.265	2.5±0.9%	5.0±1.8%
0.349	1.0±0.5%	2.0±1.0%

Table 5.3: The contamination ratio for the pair production background $f_{pair}^{\pi^\pm}$ [54].

These events are referred to as the pair-produced background or charge-symmetric background. The yield and distribution of the produced electrons and positrons are expected to be symmetric. It is the major source of contamination to the DIS electrons for the BigBite spectrometer.

Dedicated data were used to measure the contamination for this background by inverting the magnetic field of the BigBite spectrometer (from negative mode to positive mode) and measuring the positron yield. In the positive mode, the acceptance for the positrons was the same as the one for the electrons in the negative mode. Therefore the positron yield in the positive mode was the same as the pair-produced electrons in the negative mode. The yield was measured for the coincidence chan-

x	$1 - f_{N_2}^{\pi^+}$	$1 - f_{N_2}^{\pi^-}$
0.156	0.907 ± 0.011	0.923 ± 0.009
0.206	0.906 ± 0.011	0.904 ± 0.012
0.265	0.909 ± 0.010	0.898 ± 0.012
0.349	0.915 ± 0.009	0.916 ± 0.010

Table 5.4: Nitrogen dilution factor f_{N_2} [169]

nel as shown in Fig. 5-20. By subtracting the pion background, the percentage of pair-production background in the coincidence data $f_{pair}^{\pi^\pm}$ was estimated in Table 5.3.

5.5.3 Nitrogen Dilution Factor

In the target cell, a small amount of N_2 was required by the spin-exchange optical pumping of ^{3}He as discussed in Sec. 4.1.2.1. The N_2 ratio was roughly 1% in pressure and ~10% in DIS cross section. The unpolarized nitrogen introduced a dilution effect to the asymmetry measurement, which was corrected by the nitrogen dilution factor f_{N_2}:

$$A_{^3\mathrm{He}} = \frac{A_{\mathrm{Observed}}}{1 - f_{N_2}} \tag{5.18}$$

$$f_{N_2} \equiv \frac{N_{N_2}\sigma_{N_2}}{N_{^3\mathrm{He}}\sigma_{^3\mathrm{He}} + N_{N_2}\sigma_{N_2}}, \tag{5.19}$$

where N is the density and σ is the unpolarized SIDIS cross section for either N_2 of ^{3}He. The density ratios $N_{N_2}/N_{^3\mathrm{He}}$ are listed in Table 4.1. The amount of N_2 from the target cell fill and the measured one using the standard pressure curve method[14] are consistent within the uncertainties as discussed in Ref. [169]. The ratio $\sigma_{^3\mathrm{He}}/\sigma_{N_2}$ was measured periodically using dedicated data on the reference cell target filled with known amounts of pure unpolarized ^{3}He or N_2. The systematic uncertainty include

- a relative 10% uncertainty in $N_{N_2}/N_{^3\mathrm{He}}$
- uncertainty in the filling pressure of the reference cell for 1 psi[15]

[14] During a pressure curve measurement, the yield for elastically scattered electron is measured both for the production cell and for a set for reference cell target, whose pressure is known. By taking account of the radiative corrections, the yield ratio is proportional to the density of the target gas.

[15] psi: pound-force per square inch ≈ 6895 N/m^2

- yield drifts determined using linear fits of the yield VS time

The results are shown in Table 5.4.

5.5.4 Proton Dilution Factor

In the effective polarization approximations as given in Eq. (6.22), the neutron asymmetries were extracted from the ^{3}He asymmetries using the corrections of the proton asymmetry and the proton dilution factor $f_p \equiv 2\sigma_p/\sigma_{^3\mathrm{He}}$. f_p was measured using the yield ratios of the hydrogen and ^{3}He targets. Dedicated data using the hydrogen reference cell were taken regularly through out the experiment to measure the hydrogen yield. The production ^{3}He data were combined with the reference cell ^{3}He data to obtain the ^{3}He yield with maximum statistics. As discussed in Ref. [169], the systematic uncertainties include:

- For the reference cells, the uncertainties of the filling pressure was 1 psi, which was the uncertainty of the pressure gauge.

- For the production runs, the uncertainties include the density uncertainties and that for the nitrogen dilution as discussed in the last section.

- Yield drift due to the preshower degrading: similar to the nitrogen dilution calculation, the effect of yield drift is estimated and summarized.

- Radiative corrections, which took into account the thickness difference between the reference cell and the production cells.

- Nuclear effects: the cross section for protons in the ^{3}He nuclei can be modified due to nuclear effects, including the shadowing effects and the final state interactions (FSI).

  - In general, the shadowing effects are pronounced at small Bjorken x. In the experiment E06-010, the probed x range is between 0.1 and 0.4, and the effects caused by nuclear shadowing are less than 5% [206, 131].

x	$1 - f_p^{\pi^+}$	$1 - f_p^{\pi^-}$
0.156	0.212 ± 0.032 (0.027)	0.348 ± 0.032 (0.022)
0.206	0.144 ± 0.031 (0.029)	0.205 ± 0.037 (0.027)
0.265	0.171 ± 0.029 (0.028)	0.287 ± 0.036 (0.024)
0.349	0.107 ± 0.026 (0.030)	0.220 ± 0.032 (0.026)

Table 5.5: The proton dilution factors with their experimental uncertainties [169]. The numbers in parentheses represent the model uncertainties corresponding to the unpolarized FSI effects [54].

– FSIs are expected to be small at high pion momentum (2.35 GeV at $z \sim 0.5$). The possible effect of FSI was estimated using pion multiplicity data [207] and the Lund string model-based calculation of the pion absorption probability [208], which was estimated to be 3.5% in the change of SIDIS cross section at our kinematics.

The extracted f_p are summarized in Table 5.5.

5.5.5 π^+ over π^- Cross-Section Ratio for ^{3}He

Data Analysis

The HRS spectrometers are ideal devices to measure the cross section ratios of particles of opposite charges. During a polarity flip, the directions of the magnetic fields in the spectrometer are inverted by inverting the polarities of magnet power supplies. To setup HRS magnetic field at each polarity, the currents in the magnets were increased to a large value before dropped to the set points to avoid inconsistency in the field strength due to hysteresis. At both polarities, the magnetic field in the dipole magnet was locked at the same amplitude using NMR magnetometers. For a perfect reversal of the magnetic fields, the acceptance for opposite charged particles are identically reproduced at the same running condition. Using the polarity flip of the Left-HRS, this experiment measured the π^+/π^- cross section ratio of SIDIS pion productions, $R \equiv \sigma(\pi^+)/\sigma(\pi^-)$.

As shown in Fig. 5-19, two polarity flips for the Left-HRS were performed: Flip 1 for $\pi^- \to \pi^+$ around run 4220 and Flip 2 for $\pi^+ \to \pi^-$ around run 5450, which are

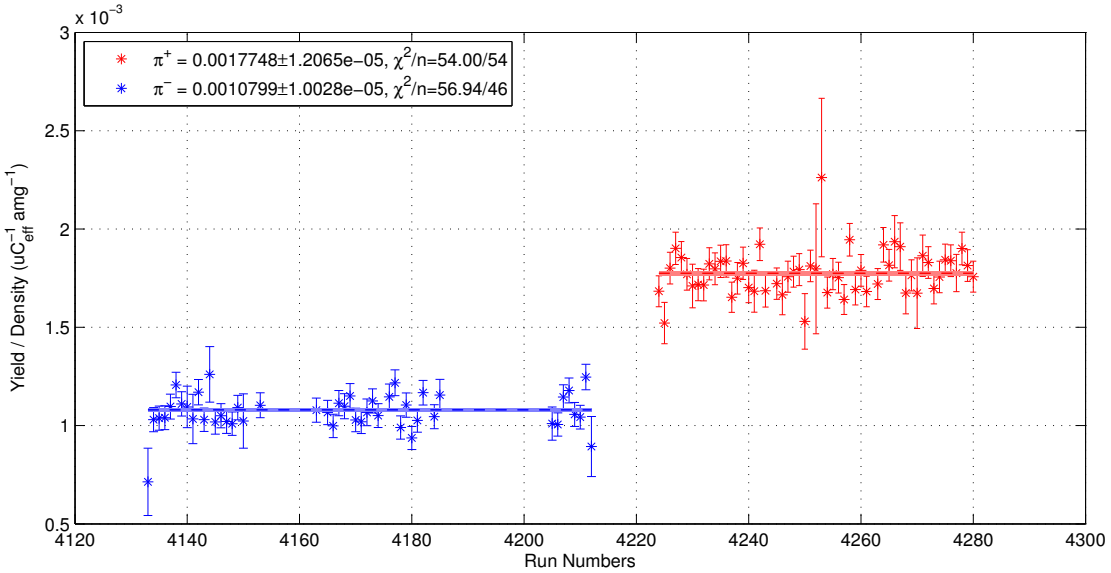

(a) Flip 1

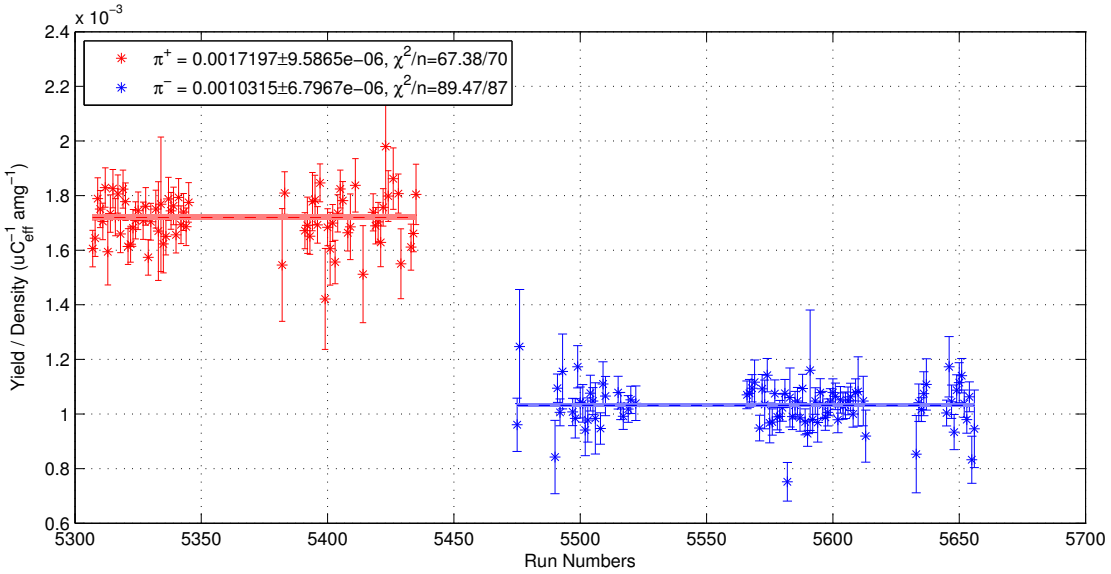

(b) Flip 2

Figure 5-21: Fit of density-normalized yield $\widetilde{Y}$ for SIDIS π^+ (red) and π^- (blue) production.

magnified and fit in Fig. 5-21a and 5-21b to obtain the average value of the yield, respectively. The running conditions, including beam current, target cell, temperature, target spin direction and detector setting, were similar for the selected runs adjacent to each polarity flip. Before and after each polarity flip, $\sim 2 \times 10^4$ events ($\sim 5\%$ of the total events) were used to measure the density-normalized yields

$$\widetilde{Y} = \frac{Y}{\rho} = \frac{N}{C \cdot LT \cdot f_{\mathrm{VDC}} \cdot (1 - f_{\mathrm{N}_2}) \cdot \rho}\,, \tag{5.20}$$

where N is the event count, C is beam charge, LT is the DAQ livetime, f_{N_2} is the nitrogen dilution as Eq. (6.11) and ρ is the average density of target. Only single track events in the Left-HRS were used in this analysis, which was corrected by the probability for single track events in the Left-HRS for a T3 or T5 trigger, f_{VDC}. In Fig. 5-21, $\widetilde{Y}$ was formed for each run as shown by the data points. $\widetilde{Y}\,(\pi^+)$ and $\widetilde{Y}\,(\pi^-)$ were fit separately for each flip (horizontal lines) and $\widetilde{Y}\,(\pi^+)\,/\widetilde{Y}\,(\pi^-)$ of two flips were averaged to give the measured value for R (data points in Fig 5-22 and 5-23).

Systematic Effects

Acceptance: the acceptance for π^+ and π^- in the Left-HRS can be slightly different due to imperfect reversal of the magnetic fields. Although there is no full set of data which can quantify the difference, the vertex reconstruction before and after the polarity flips can be used to estimate the magnitude of this effect. For the carbon foil target covering the (center$\pm$200 mm) vertex range, the shift in any of the seven foils was not larger than 0.8 mm or less than 0.5% relative to the vertex acceptance. The overall difference for the acceptance of opposite charges was cited as $\delta R/R \leq 4\%$ conservatively.

Bin Centering Effect was studied using a high statistics SIMC simulation as shown in the top panel of Fig. 5-22a. The input R which was plotted in fine grained x-bins (green points) was compared to the extracted value in four x-bins (blue points). The bottom panel shows the residual, which was $\delta R/R \leq 0.6\%$ and was quoted in the systematic uncertainty.

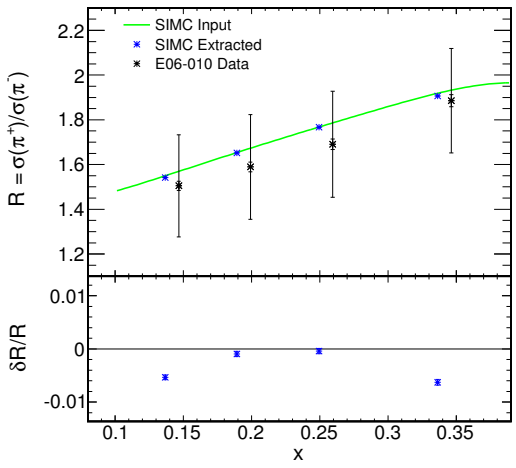

(a)

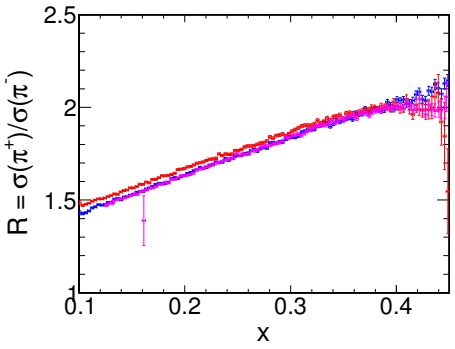

(b) Blue: radiative effect off; Red: radiative effect on; Magenta: Red points with radiative kinematic correction on x.

Figure 5-22: SIMC simulations of R: (a) for the bin centering effect and (b) for the radiative correction using kinematic shift.

Radiative Effects: as shown in Fig. 5-22b by correcting the kinematics using the average kinematic shift on x, the simulated R with radiation effects was mainly overlapped with that at Born level. The residual averaged in each x-bin was $\delta R/R < 1\%$, which was included in the systematic uncertainty.

Random Coincidence events consisted of about 0.5%. Therefore, $\delta R/R = \sqrt{2} \times 0.5\%$ was included in the uncertainty.

Contamination from Low-W Events the low-W events, which have significantly lower W or W' than the SIDIS events, are mainly from resonance and exclusive productions. They can be misidentified as SIDIS events due to the energy loss of the beam or scattered electron. Estimated using the SIMC simulation, the upper limit for the contamination was 3% and 4% for π^+ and π^-, respectively:, $\delta R/R = 3\% \oplus 4\% = 5\%$.

HRS PID Contamination: the proton contamination in the pion sample was included in the random coincidence background; electron contamination was negligible due to high PID rejection ($10^4 : 1$); the kaon contamination was less than 0.6% for π^+ and 0.2% for π^-, with $\delta R/R = 0.6\% \oplus 0.2\% = 0.6\%$.

Yield Drift: at each flip, the data taking period was roughly 10% of data and about one week of beam time. Drifts in detector efficiency and acceptance would bias the measurement. Using a linear fit of the yield dependence over time, the corresponding uncertainty on R was estimated as $\delta R/R \sim 2\%$.

Density Determination the relative target density was calculated using RTD temperature readings, whose uncertainty was around $2^{\circ}C$. The uncertainty was roughly 0.4% for each pion charge and $\delta R/R = 0.6\%$.

Detector Efficiency: The difference on the detector efficiency and trigger efficiency was assumed to be negligible due to identical detector and DAQ settings.

Azimuthal Modulations: the beam and target spin asymmetries canceled in this measurement due to frequent reversal of the beam helicity and target spin. However, as shown in Eq. (2.5) the unpolarized azimuthal asymmetries, the Cahn effect ($F_{UU}^{\cos\phi_h}$) and the Boer-Mulders effect ($F_{UU}^{\cos 2\phi_h}$), do not canceled due to the limited acceptance for ϕ_h. This bias was estimated using the SIMC simulation. For the Cahn effect, $\delta R/R = 14\% \sim 11\%$ for the smaller-x bins to higher ones and for the Boer-Mulders effect, $\delta R/R \sim 4\%$.

Results

The results are shown in Fig. 5-23, where R is measured in 4 x-bins (red data points) and for all data (the blue data point). The systematic uncertainties are presented in the grey band below the points. They are dominated by the Cahn effect contributions. The results are compared with various calculations using different parametrization of fragmentation functions. This measurement can not distinguish between these curves due to the systematic uncertainties. These results will be used in the quark model extractions as discussed in Sec. 6.3.

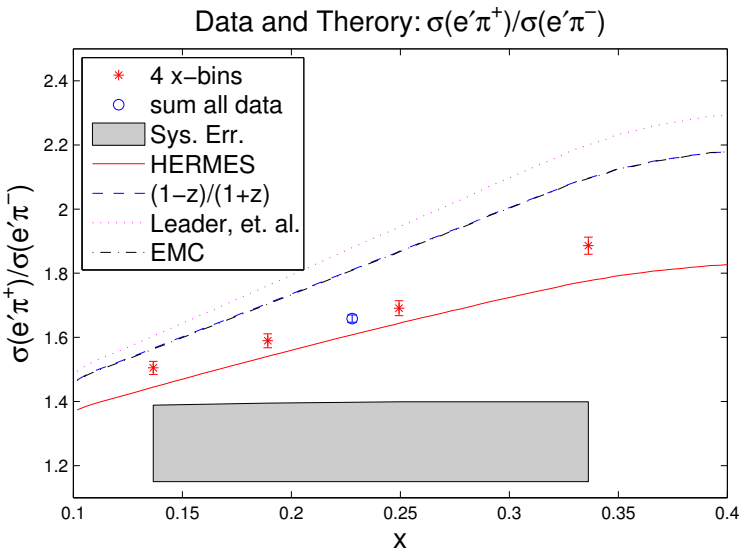

Figure 5-23: π^+/π^- cross-section ratio, R

5.6 Helicity Based Asymmetries

5.6.1 Definition

The beam-target double spin asymmetries (DSA) discussed in this section are based on the overall yields Y^+ (Y^-) for beam helicity $\lambda_e = +1(-1)$:

$$A = \frac{1}{|P_{\text{Beam}} P_{\text{Target}}|} \frac{Y^+ - Y^-}{Y^+ + Y^-}, \tag{5.21}$$

where P_{Beam} and P_{Target} are the polarization for the beam and target, respectively. As discussed in Sec. 4.2.2, two target spin orientations were used (transverse and vertical). For each orientation, two opposite target spin states (Spin= ± 1 state) were defined:

Transverse: in the central scattering plane[16] and perpendicular to the beam line. Spin= $+1$ state was towards the BigBite spectrometer; the Spin= -1 state was towards the Left-HRS spectrometer.

Vertical: perpendicular to the central scattering plane[17]. Spin= $+1$ state was up-

[16]The central scattering plane was defined by the Hall A central beam line and the central line of the BigBite spectrometer which detected the scattered electrons.

[17]The central scattering plane was horizontal.

wards; Spin= -1 state was downwards.

The DSAs as defined in Eq. (5.21) were calculated for specific target spin directions. It can also be combined with data using opposite target spin directions, which is effectively in a double cancellation form (e.g. Eq. (2.26)) due to the frequent target spin reversals. For a combined asymmetry, the sign convention follows that for the target Spin= $+1$ states, and the sign of the yield difference $Y^+ - Y^-$ for target Spin= -1 was inverted.

5.6.2 Sign of Beam Helicity

Overview

The CEBAF accelerator reverses the helicity of the beam at 30 Hz. A NIM logic signal (the helicity-sign signal) is fed into the DAQ from the beam injector to flag the helicity sign for each event. However, this signal only provides a relative sign because the beam helicity is reversed multiple times during the laser and electron transportation in CEBAF. The sign of the signal can also be flipped in the electronics as well as in the analysis software. Therefore, the relative phase ($\Phi_{\rm DAQ} = \pm 1$) between helicity-sign signal ($\lambda_{\rm DAQ} = \pm 1$) and the physical beam helicity ($\lambda_e = \pm 1$) needs to be calibrated,

$$\lambda_e = \Phi_{\rm IHWP} \cdot \text{sign}\left[\cos\phi_{\rm HallA}\right] \cdot \Phi_{\rm DAQ} \cdot \lambda_{\rm DAQ}\,, \tag{5.22}$$

where $\Phi_{\rm IHWP}$ is an additional phase introduced by the insertable half-wave plate (IHWP) at the beam injector, which provided a passive helicity reversal for an independent cross-check of the systematic uncertainty. The convention for IHWP during this analysis is

$$\Phi_{\rm IHWP} = \begin{cases} +1 & \text{, when IHWP was inserted} \\ -1 & \text{, when IHWP was taken out} \end{cases} \tag{5.23}$$

$\phi_{\rm HallA}$ is the extra phase the electron gained when transported through the accelerator to Hall A due to the non-zero ($|g_e| - 2$) [209].

Once the electronics and software setup was fixed, $\Phi_{\rm DAQ}$ has a fixed value. λ_e

can be measured by the Møller polarimeter (Sec. 3.2.6). However, since the helicity-sign signal analyzed by the Møller subsystem can be reversed relative to the main DAQ and analysis software[18], the Møller polarimeter can only provide a relative monitoring of the helicity sign. Nevertheless, it was useful for monitoring the change of $\Phi_{\rm IHWP}$ and sign $[\sin\phi_{\rm HallA}]$. As discussed in the following text of this subsection, the calibration of $\Phi_{\rm DAQ}$ was mainly based on measuring the known inclusive asymmetry of $^3\overrightarrow{\rm He}(\vec{e},e')$ elastic and quasi-elastic scattering on longitudinally and transversely polarized targets [42, 210] and the result was extensively crosschecked.

Beam Phase $\phi_{\rm HallA}$ Calculation

At the injector, the beam from the photocathode is only polarized in the longitudinal direction [209]. Then during the transportation of the beam through the accelerator, the electron spin was rotated by the following beam components:

- A single dipole at injector rotated the electron spin by $\phi_g = -0.01^\circ$ [209].
- A Wien filter [211], which located in the 100 keV beam line following the electron gun, rotated the electron spin by a preset angle, $\eta_{\rm Wien}$.
- At the n-th pass, the electrons were transported through the accelerator with $2n-1$ bending of $\theta = 180.000^\circ \pm 0.002^\circ$. The beam was finally bended into Hall A by an angle of $\theta_A = 37.491 \pm 0.002^\circ$ [209]. At each angle bend θ_0, the spin of electrons with energy E was rotated by $\left(\frac{|g_e|-2}{2m_e}\right)\cdot E\cdot\theta_0$. Therefore, the total rotation ψ_n is given in Ref. [209]:

$$\begin{aligned}\psi_n &= \left(\frac{|g_e|-2}{2m_e}\right)\Big[(2n-1)\,\theta\,E_0 + n^2\,\theta\,E_1 \\ &\quad n\,(n-1)\,\theta\,E_2 + \theta_A\,(E_0 + n\,(E_1+E_2))\Big]\,, \end{aligned} \tag{5.24}$$

  where E_0, E_1 and E_2 are the energy gains of the injector, north linac and south linac, respectively.

[18] There was no direct check on the sign convention between the main DAQ and Møller during experiment E06-010, which used a relatively new configuration of the DAQ system. This new system featured scalers separated in five bands gated by a combination of target spin and beam helicity signals, which defined the new sign of observed helicity signal.

The overall rotation is

$$\phi_{\rm HallA} = \eta_{\rm Wien} + \psi_n + \phi_g \,. \tag{5.25}$$

The calculation of $\phi_{\rm HallA}$ was verified using the relationship for the longitudinal polarization measured by the Møller polarimeter $P = P_0\,\Phi_{\rm IHWP}\,\cos\phi_{\rm HallA}$, where P_0 is the maximum polarization in Hall A. Twenty-eight Møller measurements from Apr 30, 2008 through Dec 18, 2009 were used for this cross check. The calculated P was consistent with the measured polarization within 15% , which verified the calculation of sign $[\cos\phi_{\rm HallA}]$. For experiment E06-010, two beam configurations (1-pass/1.2 GeV and 5-pass/5.9 GeV) were used and for both configurations sign $[\cos\phi_{\rm HallA}] = +1$.

Elastic Asymmetries and Determination of $\Phi_{\rm DAQ}$

During experiment E06-010, the double spin asymmetry (DSA) of elastic scattering on a longitudinally polarized ^{3}He target was used to determine the sign for the beam helicity λ_e and therefore the phase $\Phi_{\rm DAQ}$. The sign of DSA was calculated based on Ref. [42] and used the ^{3}He form factors G_E and G_M [210]:

$$A_{\rm Elastic} = \frac{\left(\frac{d\sigma}{d\Omega dE'}\right)_{\lambda_e=+1} - \left(\frac{d\sigma}{d\Omega dE'}\right)_{\lambda_e=+1}}{\left(\frac{d\sigma}{d\Omega dE'}\right)_{\lambda_e=+1} + \left(\frac{d\sigma}{d\Omega dE'}\right)_{\lambda_e=+1}} = \frac{\Delta}{\Sigma}\,, \tag{5.26}$$

where E' is the energy of scattered electron. Σ is the unpolarized cross section and Δ is the helicity dependent part. Under the one-photon-exchange approximation, Δ can be expressed as

$$\Delta = -\frac{Z^2\alpha^2\cos^2\frac{\theta}{2}}{4E^2\sin^4\frac{\theta}{2}}\left(V_{T'}R_{T'}\cos\theta_S + V_{TL'}R_{TL'}\sin\theta_S\cos\phi_S\right)\,, \tag{5.27}$$

$$V_{T'} = \sqrt{\frac{Q^2}{|\vec{q}|^2} + \left(\tan\frac{\theta}{2}\right)^2}\,\tan\frac{\theta}{2}\,, \tag{5.28}$$

$$R_{T'} = \frac{2\tau E'}{E}G_M^2\,, \tag{5.29}$$

$$V_{TL'} = -\frac{1}{\sqrt{2}}\,\frac{Q^2}{|\vec{q}|^2}\,\tan\frac{\theta}{2}\,, \tag{5.30}$$

$$R_{TL'} = -\frac{2E'\sqrt{2\tau(1+\tau)}}{E}G_E G_M\,, \tag{5.31}$$

where $\tau = Q^2/(4M^2)$; θ is the electron scattering angle; E and E' are the energy for electron before and after the scattering, respectively. The definition of kinematic variables follows that of Sec. 2.2.1, where Q^2 by definition in this thesis has an opposite sign compared with the Q^2 defined in Ref. [42, 212]. For a polarized target, whose spin is parallel to the beam direction, $\cos\theta_S = (E - E'\cos\theta)/|\vec{q}|$ and $\phi_S = 0$. At $\theta = 16.0^\circ$, $E = 1.23$ GeV and $Q^2 = 0.115$ GeV^2 , $\Delta > 0$, and therefore $A_{\rm Elastic} > 0$.

This asymmetry was measured using the data from runs 2771 and 2773, for which the IHWP was inserted ($\Phi_{\rm IHWP} = +1$). The ^{3}He target spin direction was parallel to the beam direction, which was determined using the EPR measurement of the target spin state [213] and the target field direction [214][19]. The raw asymmetry was measured by selecting elastic electrons using an invariant mass W cut of $|W - M_{^3\rm He}| < 1\,$MeV.

$$A_{\rm Raw} = \frac{N_+ - N_-}{N_+ + N_-} = \begin{cases} -1.9\% \pm 0.4\% & \text{, for run 2771} \\ -2.0\% \pm 0.4\% & \text{, for run 2773} \end{cases}, \tag{5.32}$$

where $N_{+(-)}$ is the raw elastic event counts with helicity sign flag $\lambda_{\rm DAQ} > 0$ ($\lambda_{\rm DAQ} < 0$). Therefore, $\Phi_{\rm DAQ}$ can be determined by comparing $A_{\rm Raw}$ with theory calculations [20]:

$$\Phi_{\rm DAQ} = \text{sign}\left[\frac{A_{\rm Elastic}}{A_{\rm Raw}}\right] / \left(\Phi_{\rm IHWP} \cdot \text{sign}\left[\cos\phi_{\rm HallA}\right]\right) \tag{5.33}$$

$$= -1 \tag{5.34}$$

Therefore combining the $\Phi_{\rm DAQ}$ and $\phi_{\rm HallA}$ studies, the following relation was de-

[19] Field direction of PHI=0° was towards the beam dump (also called down stream).

[20] $A_{\rm Raw}$ was much larger than the beam charge asymmetry, which was on the order of 0.1%. Therefore, the sign of $A_{\rm Raw}$ was consistent with the sign of the yield asymmetry, which was normalized by beam charge.

termined for this experiment, both 1-pass and 5-pass beam configurations:

$$\lambda_e = \begin{cases} +\lambda_{\rm DAQ} & \text{, when IHWP was taken out} \\ -\lambda_{\rm DAQ} & \text{, when IHWP was inserted} \end{cases} \tag{5.35}$$

Cross-check of the Sign

Additional Asymmetry Measurements: $\Phi_{\rm DAQ}$ has been crosschecked by using similar procedures as discussed above, but based on additional elastic, quasi-elastic, and DIS data using the ^{3}He target. These data were taken during the sister experiments of E06-010: E06-014 [174], E05-015 [215] and E05-102 [175]. These experiments used the same electronics and analysis software for the helicity signal, and therefore shared the $\Phi_{\rm DAQ}$. The results are consistent with Eq. (5.34), which was also partially crosschecked by Dr. D. Parno (Carnegie Mellon University), *et. al.* from the E06-014 collaboration [216] and Dr. G. Jin (University of Virginia), *et. al.* from the E05-102 collaboration [217].

The Parity DAQ ran in parallel with the main DAQ to monitor the luminosity asymmetries. The helicity signals observed by the Parity DAQ and that by Møller polarimeter have a reversed sign. This sign convention has been cross-checked before [218, 219] and after [220, 221] experiment E06-010. The relative signs between the Parity DAQ and the E06-010 main DAQ were directly measured during the commissioning period of this experiment, by introducing an arbitrary large beam charge asymmetry. As shown in Fig. 5-24, the data points in asterisks are from the main DAQ. Consistent beam charge asymmetries (red: for target Spin $= +1$ and green for target Spin $= -1$) and T1+T3 overall event count asymmetries ($A_{\rm Raw}$ as of Eq. (5.32)) were observed. The grey dots were the charge asymmetry observed in Parity DAQ. Around 5 AM, this asymmetry was balanced in the accelerator and both DAQ's observations were also consistent with zero. Therefore, when beam charge asymmetry was non-zero, both DAQs observed this asymmetry but with opposite signs. Therefore their observed helicity signal also have opposite signs. Therefore, the E06-010 main

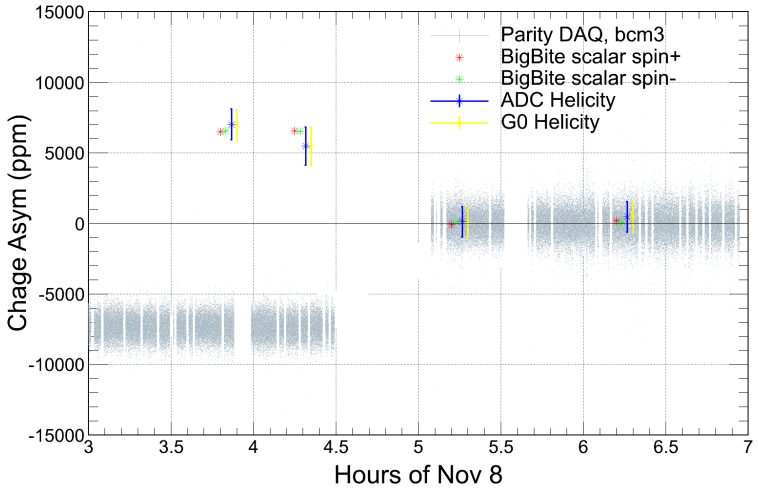

Figure 5-24: Direct check of the relative helicity signs between the Parity DAQ and the E06-010 main DAQ by introducing an arbitrary large beam charge asymmetry. See text for details.

DAQ and the Møller polarimeter should share the same helicity sign convention. During Experiment E06-010, the Møller polarimeter observed a positive physical helicity with helicity signal=+1 when the IHWP was OUT, consistent with Eq. (5.22).

5.6.3 Single-Arm HRS Asymmetries

As shown in Figs. 5-25 and 5-26, the double spin asymmetries (DSAs) were measured using the Left-HRS, which provided clean PID and background. For each panel, the left side shows DSA with vertical target spins and the right side is for transverse target spins. For both target spin orientations, Spin= +1 states are shown in red data points and Spin= −1 states were colored in blue. The particle species are

Pions (Fig. 5-25): the DSA for vertical target spins were consistent with zero, which is required by parity conservation. For the transverse target spin directions, 3-σ or larger asymmetries were observed. The transverse DSAs reversed in sign for opposite target spin states, which is consistent with parity conservation too. Opposite asymmetries were also observed for π^+ and π^-.

Proton+K^+ (Fig. 5-26a): in positive polarity, the dominant hadron, which was

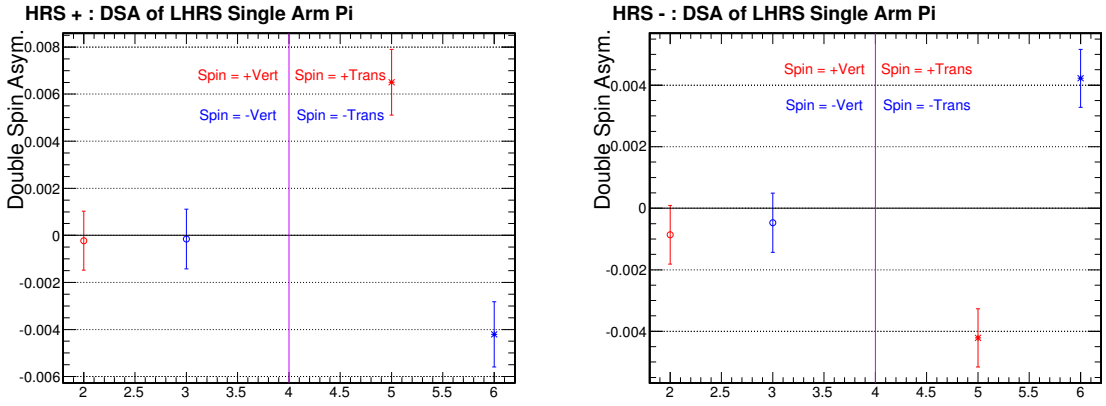

(a) (b)

Figure 5-25: Single pion DSA in Left-HRS for (a) π^+ and (b) π^-

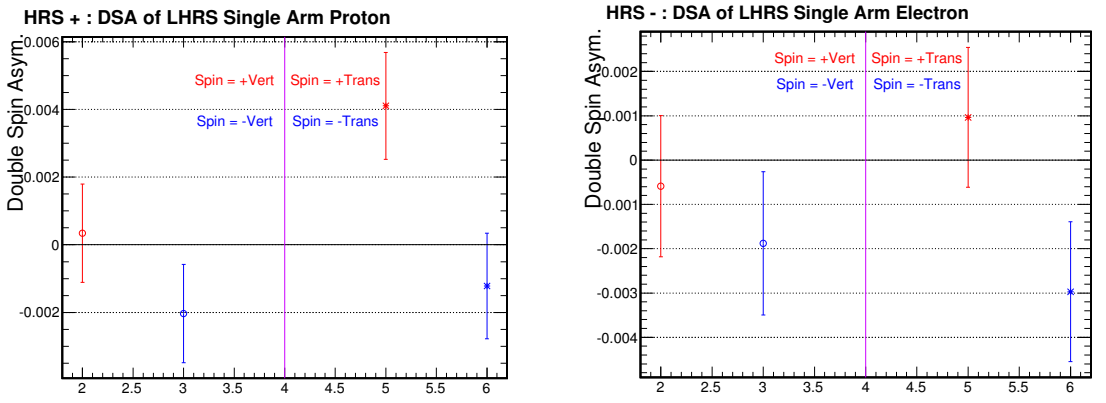

(a) (b)

Figure 5-26: Single particle DSA in Left-HRS for (a) proton+K^+ and (b) electron

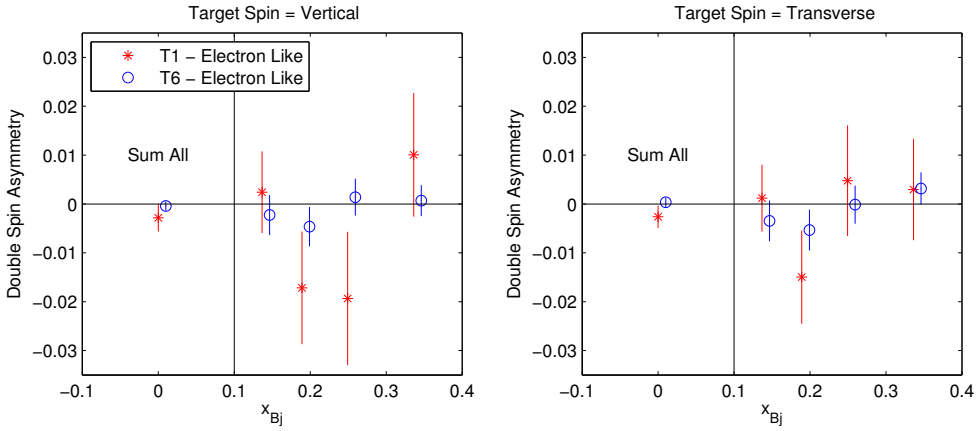

Figure 5-27: Preliminary single electron DSA in BigBite.

below the threshold of the A1 aerogel Cerenkov detector, was dominated by protons. A small fraction of K^+ was also in the sample. The vertical DSA was consistent with zero; and a 2.5-σ transverse DSA was observed combining both target spin states.

Electron (Fig. 5-26b): the HRS electron kinematics were at $x \sim 0.16$, $Q^2 \sim 1.1$ GeV^2 and $W \sim 2.3$ GeV. The transverse DSA corresponded to the nitrogen-diluted ^{3}He DIS $A_\perp$ and related to the polarized g_1 and g_2 structure functions [222]. The observed asymmetries were consistent with zero within statistical fluctuations.

The Left-HRS had a limited acceptance around the horizontal beam plane. Due to parity conservation of the EM and strong interactions, the vertical DSA are suppressed and DSAs reverse their sign for opposite target spin states. The observation is consistent with this expectation, which demonstrated the reliability of this measurement.

5.6.4 Single-Arm BigBite Asymmetries

Similar studies were also performed for the BigBite spectrometer. The optimized PID cuts and contamination for this single-arm measurement, which are different from the coincidence SIDIS one, are still under analysis. Therefore, the results shown

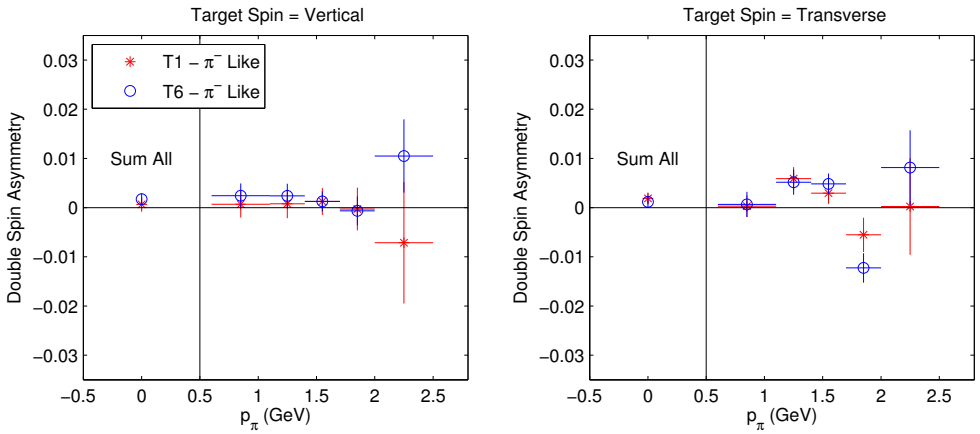

Figure 5-28: Preliminary single-arm BigBite DSA in for π^--like events

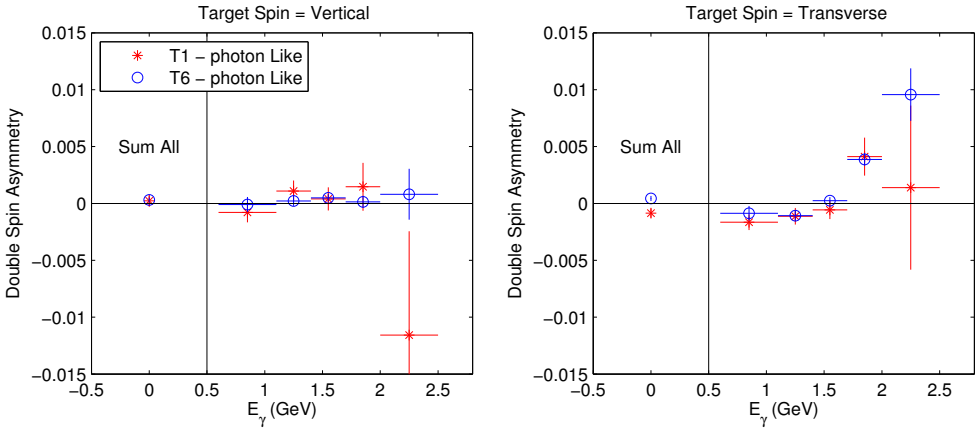

Figure 5-29: Preliminary single-arm BigBite DSA for photon-like events

are preliminary[21]. The results are shown in Figs. 5-27, 5-28 and 5-29, which are plotted with the following format:

- For each fig, the DSAs for vertical and transverse target spin are shown in the left and right panels, respectively. Events were summed over both Spin=±1 states and the sign followed that for Spin=+1. The vertical DSAs were consistent with zero, as required by parity conservations.

- During production data taking, BigBite was in negative polarity and covered a larger acceptance compared to the Left-HRS. Therefore, multiple kinematic bins are provided on the right-hand sides of each plot, and the left-hand side

[21] These preliminary results are not used for the primary analysis of this thesis (discussed in Sec. 6.1 and 6.2).

shows the asymmetries summed over all events.

- As discussed in Sec. 3.5.2, there were two major triggers for BigBite, a lower-threshold T1 trigger and a higher-threshold T6 trigger , which are shown by the red and blue data points, respectively. The asymmetries produced by both triggers were consistent with each other within their statistical fluctuations.

The following particle species were analyzed:

Electron (Fig. 5-27): the electron DSA are plotted against the Bjorken scaling variable x_{Bj}. The T6 data points were shifted by 0.01 in x_{Bj}. The asymmetries are consistent with zero.

π^- (Fig. 5-28): the DSA for π^--like events are plotted against their momentum p_π with central angle around 30 degrees relative to the beam direction. The transverse asymmetries suggest a possible sign change around $p_\pi \sim 1.7\,\text{GeV}$.

Photons (Fig. 5-28): the DSA for photon-like events are plotted against the energy deposition in the main cluster of the calorimeter E_γ. No track was found for such events. A positive asymmetry trend is suggested by the data as E_γ increases with a possible sign change around $E_\gamma \sim 1.5\,\text{GeV}$.

5.6.5 Coincidence Asymmetries

For the BigBite-HRS coincidence channels, the DSAs are shown in Figs. 5-30 to 5-32. In the case that two panels are presented, the left panel is corresponds to positively charged particles in the Left-HRS and the right panel is for negatively charged particles. For each panel, the DSAs are plotted against kinematic variables on the right side and the left side data point is averaged over all events. The data for vertical and transverse target spin orientations is shown in red and blue, respectively. Events are summed over both Spin=$\pm$1 states and the sign followed that for Spin=+1. The vertical data points are shifted slightly towards the right. The following channels are studied:

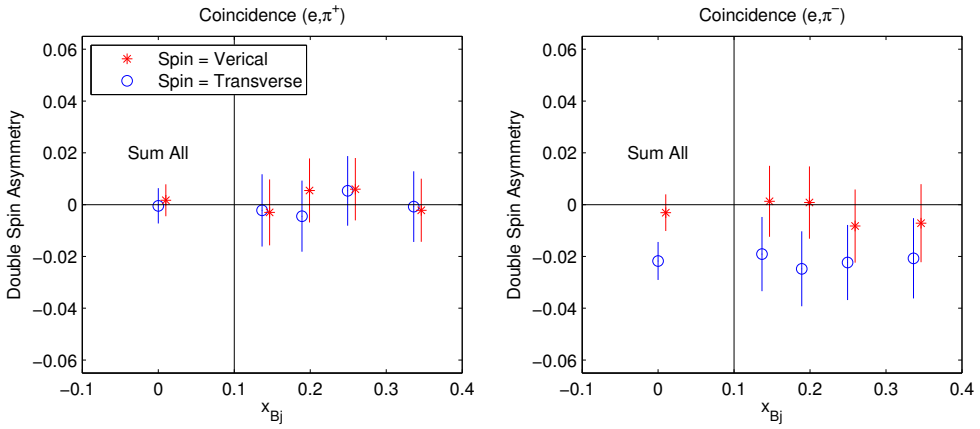

Figure 5-30: DSAs for SIDIS electroproduction of π^+ (left) and π^- (right) in the Left-HRS with electron detected in BigBite

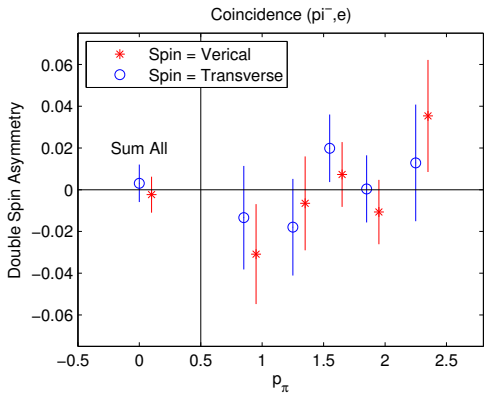

Figure 5-31: Preliminary coincidence DSA for electroproduction of π^- in BigBite with electrons detected in the Left-HRS

SIDIS Electroproduction of Charged Pions are shown in Figs. 5-30 and 5-31. For Fig. 5-30 electrons were detected in BigBite and charged pions were detected in the Left-HRS; and for Fig. 5-31, electrons were detected in the Left-HRS and π^- were detected in BigBite In Fig. 5-30, the DSAs for π^+ were consistent with zero; for π^-, the vertical asymmetries were consistent with zero as suppressed by parity conservation; a negative transverse asymmetry is indicated for all the x-bins. The DSA for π^- for all events showed a 3.0-σ asymmetry below zero. The preliminary DSA in Fig. 5-31, where $x \sim 0.16$ and $Q^2 \sim 1.1$ GeV^2, were consistent with zero.

Electroproduction of Protons (Fig. 5-32), for which the DIS cut was removed and

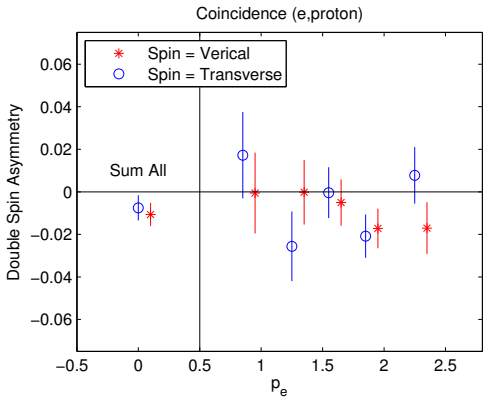

Figure 5-32: Preliminary coincidence DSA for electroproduction of protons in the Left-HRS with electrons detected in BigBite

$W > 1.5$ GeV was used. The results are consistent with zero. Limited by the beam energy, the proton production is dominated by the target fragmentation.

Chapter 6

Results and Discussions

The main physics result of this thesis, the ^{3}He $A_{LT}^{\cos(\phi_h-\phi_S)}$ asymmetry, which is sensitive to the g_{1T} TMD, is discussed in this Chapter. The derivative studies of neutron asymmetries and the quark TMD extractions in the simple parton model are presented following the main result.

6.1 ^{3}He $A_{LT}^{\cos(\phi_h-\phi_S)}$ Asymmetry

6.1.1 Overview

The azimuthal beam-target double spin asymmetry (DSA) $A_{LT}^{\cos(\phi_h-\phi_S)}$ was formed from the measured yields as in Eqs. (2.26) and (2.34), which is repeated as following[1]:

$$\begin{aligned} A_{LT}\left(\phi_h,\phi_S\right) &\equiv \frac{1}{|P_B S_T|}\frac{Y^+\left(\phi_h,\phi_S\right)-Y^+\left(\phi_h,\phi_S+\pi\right)-Y^-\left(\phi_h,\phi_S\right)+Y^-\left(\phi_h,\phi_S+\pi\right)}{Y^+\left(\phi_h,\phi_S\right)+Y^+\left(\phi_h,\phi_S+\pi\right)+Y^-\left(\phi_h,\phi_S\right)+Y^-\left(\phi_h,\phi_S+\pi\right)} \\ &\approx A_{LT}^{\cos(\phi_h-\phi_S)}\times\cos\left(\phi_h-\phi_S\right) \end{aligned} \tag{6.1}$$

where P_B is the polarization of the lepton beam, S_T is the transverse polarization of the target w.r.t. the virtual photon direction, and $Y^{\pm}\left(\phi_h,\phi_S\right)$ is the normalized yield for beam helicity of ±1. The relation in Eq. (6.1) becomes equal when the

[1] It is worth noting that, in the convention for the COMPASS collaboration [118, 119] and some literatur [85], this azimuthal asymmetry is defined differently, which is corresponding to $A_{LT}^{\cos(\phi_h-\phi_S)}/\left\langle\sqrt{1-\varepsilon^2}\right\rangle$ in the convention for this analysis (Eq. (6.1)). For this experiment, the averaged kinematic factor $\left\langle\sqrt{1-\varepsilon^2}\right\rangle$ was approximately 0.9 as shown in Table 5.2.

subleading-twist terms, the $\cos\phi_h$ and $\cos 2\phi_h$ azimuthal modulation on the unpolarized cross section are negligible, as explicitly shown in Eq. (2.26). The azimuthal asymmetry $A_{LT}^{\cos(\phi_h-\phi_S)}$ in each x-bin was extracted directly using an azimuthally unbinned maximum likelihood estimator (MLE, discussed in Appendix. C) taking into account the accumulated beam charge, the data acquisition livetime, and the beam and target polarizations. The azimuthally unbinned MLE is equivalent to a Fourier decomposition of the asymmetry for perfectly balanced beam and target polarization and in the limit of very small θ_S, ϕ_h and ϕ_S bins. The estimator was based on the ^{3}He cross section model:

$$\begin{aligned} d\sigma \quad (\phi_h,\, \phi_S,\, \theta_S) = \quad & d\sigma_{UU} \times \Big(1 + \lambda_e \left|P_B P_{Targ}\right| \sin\theta_S \cos(\phi_h - \phi_S)\, A_{LT}^{\cos(\phi_h-\phi_S)} \\ & + \lambda_e \left|P_B P_{Targ}\right| (-\cos\theta_S)\; A_{LL}\Big)\;. \end{aligned} \tag{6.2}$$

The neglected terms from Eq. (2.5) will be discussed in Sec. 6.1.4. Experimentally, the direct observable is the overall yield, which is diluted from Eq. (6.2) by the nitrogen and charge symmetric background. Therefore, the ^{3}He asymmetry was extracted as

$$A_{LT,\,^3\mathrm{He}}^{\cos(\phi_h-\phi_S)} = \frac{1}{(1-f_{\mathrm{N}_2})\,(1-f_{\mathrm{pair}})} A_{LT,\,\mathrm{raw}}^{\cos(\phi_h-\phi_S)} + \Delta A_{LL}\,, \tag{6.3}$$

where $A_{LT,\,\mathrm{raw}}^{\cos(\phi_h-\phi_S)}$ is the MLE fit result based on the model of Eq. (6.2) and assuming $A_{LL} = 0$ (Sec. 6.1.2). f_{N_2} and f_{pair} are dilution factors for the nitrogen and pair-produced background (Sec. 6.1.3), respectively. This MLE-based extraction of $A_{LT,\,\mathrm{raw}}^{\cos(\phi_h-\phi_S)}$ was cross-checked by an independent binning-and-fitting procedure [140, 145, 131]. ΔA_{LL} is a small correction to $A_{LT}\,(\phi_h, \phi_S)$ due to the DSA A_{LL}, where A_{LL} were calculated from the results of the DSSV[2] 2008 global fit [17]. The $P_{h\perp}$ dependence for A_{LL} was assumed to be the same as that for proton, which was measured recently by the CLAS collaboration [58]. The connection between A_{LL} and ΔA_{LL} was parametrized using MLE and Eq. (6.2) as discussed in Sec. 6.1.3.

[2]DSSV is the acronym of the family name for the authors of Ref. [17]

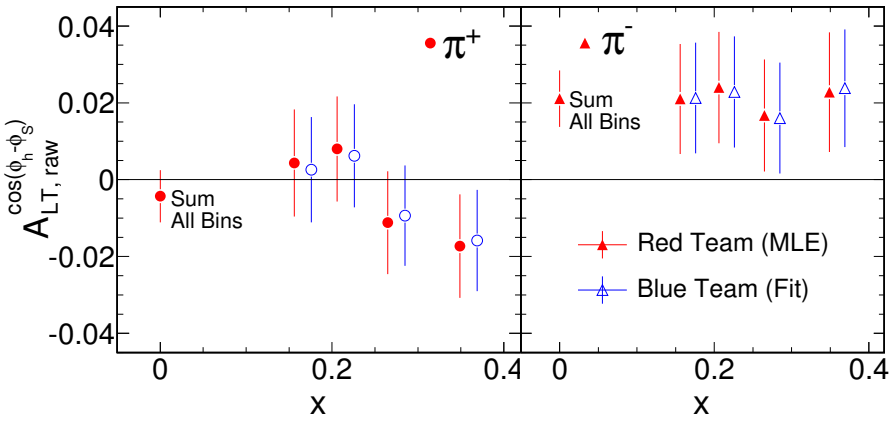

Figure 6-1: The raw azimuthal asymmetry, $A_{LT,\,\mathrm{raw}}^{\cos(\phi_h-\phi_S)}$ as analyzed, by the Red Team (solid points) and Blue Team (hollow points, slightly shifted in x) (see text). The asymmetry extracted by summing data of all bins is shown at $x = 0$ (only Red Team results shown). The left panel corresponds to the SIDIS π^+ production and the right panel is for π^- .

6.1.2 Raw Azimuthal Asymmetries

The raw azimuthal asymmetry, $A_{LT,\,\mathrm{raw}}^{\cos(\phi_h-\phi_S)}$, was formed assuming the overall cross section follows Eq. (6.2) and $A_{LL} = 0$. Therefore, it is diluted by the nitrogen and pair-produced background and biased by a non-zero A_{LL}. Normalizations for the accumulated beam charge, the data acquisition livetime, and the beam and target polarizations were also applied in this step. Since $A_{LT,\,\mathrm{raw}}^{\cos(\phi_h-\phi_S)}$ is the basis of this analysis as shown in Eq. (6.3), this result was extensively cross-checked.

Two Team Analysis and Cross-Check

Two independent analyses of $A_{LT,\,\mathrm{raw}}^{\cos(\phi_h-\phi_S)}$ were carried out to cross-check the results :

The Red Team[3] used the maximum likelihood estimator for the helicity based asymmetry, Eq. (C.42). Only one modulation term, $\lambda_e\,|P_B P_{Targ}|\,\sin\theta_S\cos(\phi_h - \phi_S)\,A_{LT}^{\cos(\phi_h-\phi_S)}$, was assumed for this step:

$$A_{LT,\,\mathrm{raw}}^{\cos(\phi_h-\phi_S)} = \frac{\sum_{\mathrm{ev}} \lambda_e \cdot P \cdot M^{(1)} - N \cdot \tilde{A}_L^{(1)}}{\sum_{\mathrm{ev}} P^2 \left(M^{(1)}\right)^2 - N\left(\tilde{A}_L^{(1)}\right)^2} \tag{6.4}$$

$$\triangle_{\mathrm{stat.}} A_{LT,\,\mathrm{raw}}^{\cos(\phi_h-\phi_S)} = \sqrt{\sum_{\mathrm{ev}} P^2 \left(M^{(1)}\right)^2 - N\left(\tilde{A}_L^{(1)}\right)^2} \tag{6.5}$$

$$P = |P_B P_{Targ}| \tag{6.6}$$

$$M^{(1)} = \sin\theta_S \cos(\phi_h - \phi_S)\,, \tag{6.7}$$

where $\sum_{\rm ev}$ is sum over all events, λ_e is the beam helicity for each event[4], and N is the total event count. $\tilde{A}_L$ as defined in Eq. (C.35), corrects for the effects due to the luminosity and DAQ livetime asymmetry between two helicity states. Through an active feedback system [123], the beam charge asymmetry between the two helicity states was controlled to less than 150 ppm over a typical 20 minute period between target spin-flips, and less than 10 ppm for the entire experiment. Therefore, the overall correction on $A_{LT,\,\rm raw}^{\cos(\phi_h-\phi_S)}$ from $\tilde{A}_L^{(1)}$ was less than 30 ppm for the π^+ bins and less than 20 ppm for the π^- bins, which are negligible compared with $\triangle_{\rm stat.} A_{LT,\,\rm raw}^{\cos(\phi_h-\phi_S)} \sim 1.5\%$.

The Blue Team [140, 145, 131] first obtained the SIDIS yields by normalizing the number of identified SIDIS events by the accumulated beam charge and the data acquisition livetime. For each target spin state, the data were divided into a pair of measurements in opposite beam helicity states to extract the raw asymmetries for2-D (ϕ_h, ϕ_S) bins

$$A_{LT}\left(\phi_h,\phi_S\right) \equiv \frac{1}{P}\frac{Y^+\left(\phi_h,\phi_S\right) - Y^-\left(\phi_h,\phi_S\right)}{Y^+\left(\phi_h,\phi_S\right) + Y^-\left(\phi_h,\phi_S\right)} \tag{6.8}$$

$$\approx A_{LT,\,\rm raw}^{\cos(\phi_h-\phi_S)} \left\langle \sin\theta_S \right\rangle \cos\left(\phi_h - \phi_S\right)\,. \tag{6.9}$$

The raw azimuthal asymmetry, $A_{LT,\,\rm raw}^{\cos(\phi_h-\phi_S)}$, was obtained by fitting the asymmetries in 2-D (ϕ_h, ϕ_S) bins[5].

Both teams used the same detector calibrations, PID cuts and polarization tables. The analysis software was based on different methods and was highly independent on the coding level. The results were cross checked for each kinematic bin as shown in

[4] As discussed in Sec. 5.6.2, the beam helicity state is controlled by the laser polarization direction at the beam source, which is recorded for each event.

[5] $\langle \sin\theta_S \rangle$ was averaged for each 2-D (ϕ_h, ϕ_S) bin and included in the fit.

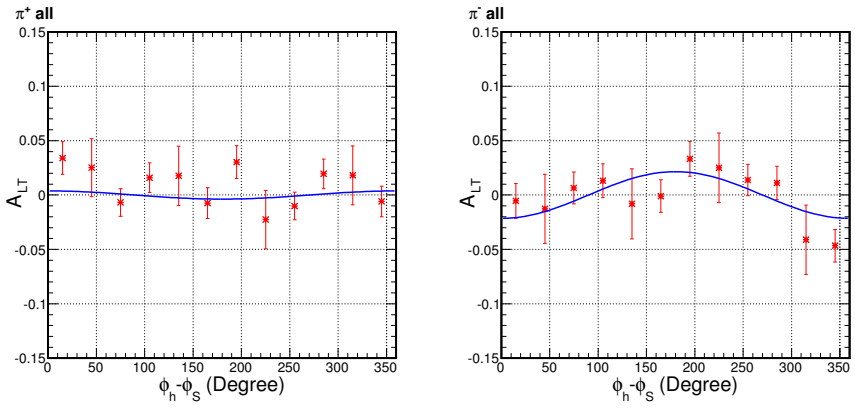

Figure 6-2: A_{LT} extraction for sum all x bins for π^+ (left) and π^- productions using the MLE based azimuthal bin and fit method (see text).

Fig. 6-1. The minor difference[6] between results of both teams can be attributed to the azimuthal binning effect, forming asymmetries within local periods of data and minor difference in the selection of good SIDIS events .

Although the analyses of both teams were based on the yield difference between two helicity states, the extraction of $A_{LT,\,\mathrm{raw}}^{\cos(\phi_h-\phi_S)}$ was effectively a beam-target double spin asymmetry as defined in Eq. (2.26) due to the frequent target spin reversal. Systematic biases, including beam single spin asymmetries (beam-SSAs), target single spin asymmetries (target-SSAs) and target single-spin-dependent final state interactions cancel automatically, as shown in Eq. (2.26). The residual effects will be discussed in the following sections.

Besides the one-step MLE extraction of $A_{LT,\,\mathrm{raw}}^{\cos(\phi_h-\phi_S)}$, Red Team also tested an extraction in two steps:

1. bin data into 12 $(\phi_h - \phi_S)$ azimuthal bins and extract $A_{LT}\,(\phi_h, \phi_S)$ for each bin using MLE;

2. perform an azimuthal fit for the $\cos\,(\phi_h - \phi_S)$ modulation.

The result for the sum of all four x-bins are shown in Fig. 6-2, where red data points are the yield asymmetry as Eq. (6.8) and blue curves are the fit. The χ^2/N_{dof} are

[6]The intrinsic difference between the two analysis methods is negligible for this experiment. Using a Monte-Carlo simulation (discussed in Sec. 5.4.1), results from both methods were shown to be highly consistent as shown in Sec. 6.1.4, Fig. 6-12.

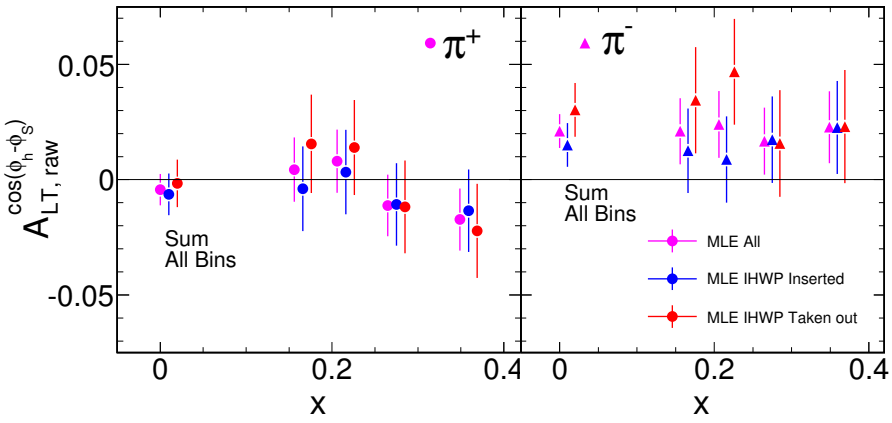

Figure 6-3: The raw azimuthal asymmetry, $A_{LT,\,\mathrm{raw}}^{\cos(\phi_h-\phi_S)}$, with data summed regardless of IHWP status (magenta), with IHWP inserted (blue, shifted 0.01 in x) and with IHWP taken out (red, shifted 0.02 in x). The sign was corrected in regards to the physical helicity asymmetry (see text for discussions). The asymmetry extracted by summing data of all bins is shown at $x \sim 0$. The left panel corresponds to the SIDIS π^+ production and the right panel is for π^- .

16.2/11 and 10.3/11 for π^+ (left) and π^- (right) productions, respectively. The fit results and those for one-step MLE (Fig. 6-1, data points labeled "sum all") are consistent within 6×10^{-4}, much smaller than the statistical precision.

Cross-Check Using Passive Helicity Reversal

As discussed in Sec. 3.2.1, the polarized electrons were were excited from a superlattice GaAs photocathode by a circularly polarized laser [122] at the injector of the CEBAF accelerator. The laser polarization, and therefore the electron beam helicity λ_e, was "actively" reversed at 30 Hz using a voltage-controlled Pockels cell. An electrical signal, which was related to the voltage applied on the Pockels cell, was used to flag the relative sign of beam helicity (using Eq. (5.22)) and was recorded for each event as λ_{DAQ}. Roughly half of the data were accumulated with an extra insertable half-wave plate (IHWP) inserted in the path of the laser at the CEBAF beam source, "passively" reversing the beam helicity with minimal change to the experiment as shown in Eqs. (5.22) and (5.23) on page 177. Therefore, the asymmetry for yield Y

which is flagged by $\lambda_{\rm DAQ} = \pm 1$

$$A^{\lambda_{\rm DAQ}} = \frac{1}{|P_{\rm Beam} P_{\rm Target}|} \frac{Y^{\lambda_{\rm DAQ}=+1} - Y^{\lambda_{\rm DAQ}=-1}}{Y^{\lambda_{\rm DAQ}=+1} + Y^{\lambda_{\rm DAQ}=-1}} \tag{6.10}$$

reverse its sign as the IHWP is inserted (IN status) or taken out (OUT status), while the physical-helicity-based yield asymmetry $A = \Phi_{\rm IHWP} \cdot A_{\lambda_{\rm DAQ}}$ (as used in other parts of this Chapter and defined in Eqs. (6.1) and (6.8)) remains on the same sign and amplitude. In the case that there is a artificial asymmetry which is correlated to the electrical level in the DAQ (e.g., related to the voltage of the helicity signal $\lambda_{\rm DAQ}$) but not related with the physical beam helicity λ_e, the observed $A^{\lambda_{\rm DAQ}}$ will not exactly reverse in sign and A will not be consistent with respect to the change in the IHWP status. Therefore this passive helicity reversal using IHWP provided an independent cross-check of the systematic uncertainty.

The physical-helicity-based asymmetries for data with IHWP inserted,taken out and sum of all data are shown in Fig. 6-3. The $A_{LT,\,\rm raw}^{\cos(\phi_h - \phi_S)}$ of IHWP IN and OUT were consistent with each other within their statistical fluctuations, which indicates that the helicity-signal-correlated systematic bias is small relative to the statistical uncertainty. A noticeable $+2.9\sigma$ asymmetry is observed for the π^- $A_{LT,\,\rm raw}^{\cos(\phi_h - \phi_S)}$ asymmetry by summing all four x-bins and the corresponding asymmetries with IHWP IN and OUT are consistent in the signs and amplitudes. This indicates that the observed asymmetry is not an artificial effect due to instrument or analysis bias, but it is related to the physical beam helicity. In the following discussions, the asymmetry results are always physical-helicity-based and summed in events regardless of the IHWP status.

6.1.3 Corrections

The corrections applied in Eq. (6.3) are discussed in this subsection.

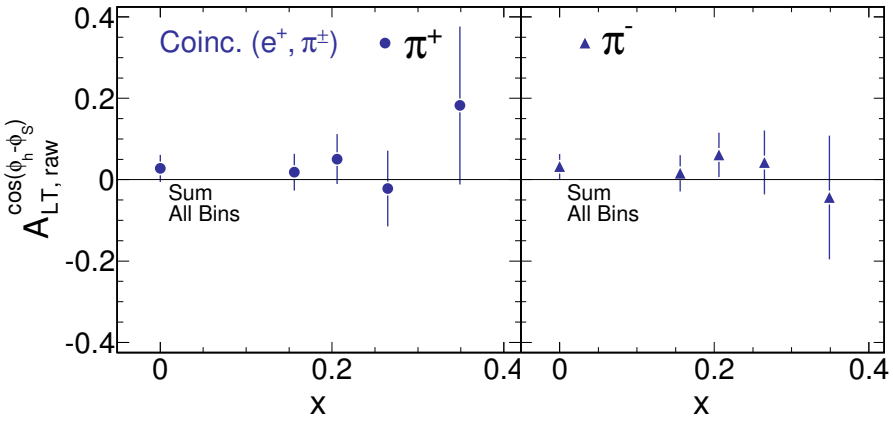

Figure 6-4: The raw azimuthal asymmetry, $A_{LT,\,\mathrm{raw}}^{\cos(\phi_h-\phi_S)}$ for the coincidence (e^+, $\pi^\pm$) sample. The asymmetry extracted by summing data of all bins is shown at $x = 0$, which are consistent with zero. The left panel corresponds to the SIDIS π^+ production and the right panel is for π^-.

Nitrogen Dilution

A small amount of unpolarized N_2 was required by the spin-exchange optical pumping of ^{3}He as discussed in Sec. 4.1.2.1. It diluted the measured asymmetry, which was corrected for the nitrogen dilution as in Eq. (6.3) and

$$f_{N_2} \equiv \frac{N_{N_2}\sigma_{N_2}}{N_{^3He}\sigma_{^3He} + N_{N_2}\sigma_{N_2}}\,, \tag{6.11}$$

where N is the density and σ is the unpolarized SIDIS cross section. The ratio $\sigma_{^3He}/\sigma_{N_2}$ was measured periodically in dedicated runs on targets filled with known amounts of pure unpolarized ^{3}He and N_2 as described in Sec. 5.5.3. Using the density of N_2 and ^{3}He in the production cells, f_{N_2} was found to be around 10%.

Pair-Produced Background

The dominant systematic effect for the lower x-bins was the contamination from photon induced charge-symmetric $e^\pm$ pair production, in which the e^- was detected in BigBite. The relative yield of (e^+, $\pi^\pm$) coincidences was measured by reversing the magnetic field of BigBite as discussed in Sec. 5.5.2. As shown in Table 5.3, the percentage of the background event, f_{pair}, ranged from 24% to 1% for the lower

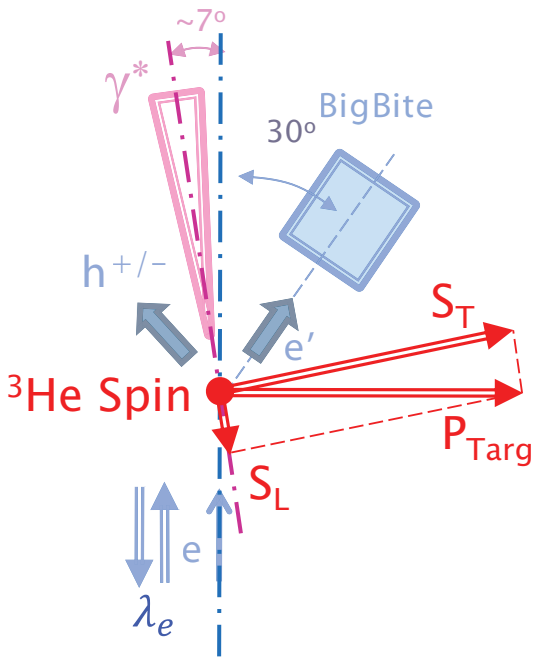

Figure 6-5: On top of Fig. 3-1, an illustration of the non-zero longitudinal component (S_L) of the target polarization with respect to (w.r.t.) the virtual photon direction. The target spin P_{Targ} is perpendicular w.r.t. the beam direction and in the central e-e' scattering plane.

x-bins to higher ones. This asymmetry for such background was estimated by looking at coincidence events in the production runs with positively bended electron-like particles in the BigBite spectrometer. Since the measured azimuthal asymmetry as shown in Fig. 6-4 was consistent with zero, the contamination was treated as a dilution and corrected in a similar way as the nitrogen dilution as shown in Eq. (6.3).

A_{LL} Corrections and Its Uncertainties

During Experiment E06-010, the target spin was always transverse with respect to (w.r.t.) the beam direction. As shown in Fig. 6-5, when the target spin is in the central e-e' scattering plane[7], it can be decomposed w.r.t. the virtual photon (γ^*) to a transverse spin component (S_T) and a 5-20% longitudinal component (S_L). Due to the nonzero S_L, a small bias on $A_{LT}\,(\phi_h, \phi_S)$ was introduced, which is proportional

[7]The central e-e' scattering plane is defined using the nominal electron beam e and the central line of the BigBite spectrometer which detected the scattered electron e'. In Hall A, this plane is horizontal at the height of the target center.

to longitudinal DSA A_{LL}. The corresponding correction, ΔA_{LL}, as in Eq. (6.3) is discussed in this section.

Comparing Eq. (6.2) to the leading-twist terms in the SIDIS cross section, Eq. (2.5), A_{LL} can be expressed in structure functions as

$$A_{LL} \;=\; \sqrt{1-\varepsilon^2}\,\frac{F_{LL}}{(1+\varepsilon R)\;F_{UU,T}}\,, \tag{6.12}$$

which is analog to Eq. (2.28). As discussed in Sec. 2.3.3, in the simple quark model A_{LL} can be expressed at leading-order (LO) using the helicity distribution (g_{1L}), the unpolarized distribution (f_1) and the unpolarized fragmentation function (D_1):

$$A_{LL} = \sqrt{1-\varepsilon^2}\,\frac{\Big[g_{1L}\otimes D_1\Big]}{\Big[f_1\otimes D_1\Big]}\,. \tag{6.13}$$

A_{LL} is a function of x, y, z, Q^2 and $P_{h\perp}$, where the y dependence is from the depolarization factor [41],

$$\sqrt{1-\varepsilon^2} \approx \frac{(2-y)\,y}{1+(1-y)^2}\,. \tag{6.14}$$

.A_{LL} and its uncertainty were estimated with the following factors:

- The estimation of A_{LL} was based on the $P_{h\perp}$ integrated SIDIS A_1^h,

$$A_1^h(x,\,Q^2,\,z) \;=\; \frac{\langle F_{LL}\rangle_{P_{h\perp}}}{\langle F_{UU,T}\rangle_{P_{h\perp}}} \tag{6.15}$$

$$\langle F\rangle_{P_{h\perp}} \;=\; \int d^2\vec{P}_{h\perp} F\,. \tag{6.16}$$

  As shown in Fig.6-6, A_1^h for charged pion and kaon production on a longitudinally polarized ^{3}He target were evaluated at fine-grained (binned in 80 x-bins) kinematic center of (x, Q^2, z) using the next-to-leading order (NLO) DSSV 2008 global fit by Dr. R. Sassot, *et. al.* [17]. The uncertainties, which corresponds to $\chi^2 = (\chi^2)_{\text{minimum}} + 2\%$ of the global fit [17], were estimated at two x points for each pion species, which gave the approximate size of the uncertainty for these curves. To be conservative, the maxima of the four estimated uncertainties,

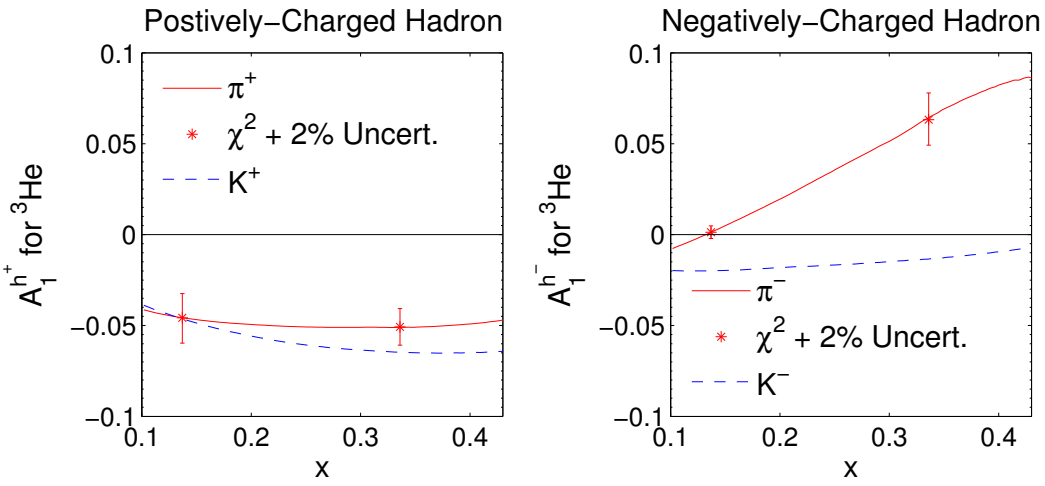

Figure 6-6: Next-to-leading order $A_1^{h\pm}$ of ^{3}He for positively-charged hadrons (left, $h^+ = \pi^+, K^+$) and negatively-charged hadrons (right, $h^- = \pi^-, K^-$), calculated at central kinematics of this experiment and integrated over $P_{h\perp}$ [17]. The pion and kaon are shown in red-solid and blue-dash lines, respectively. The $\chi^2 + 2\%$ uncertainties were estimated at two x points for π^+ and π^-, which are shown in red error bars.

$\triangle A_1^h = 1.5\%$, was quoted as the uncertainty for A_1^h at any given point.

- The $P_{h\perp}$ dependence of A_{LL} was estimated using the LO-approximation basedGaussian-ansatz fit of the recent proton A_{LL} data from the CLAS collaboration [58]. As shown in Appendix A.3, A_{LL} can be expressed using the Gaussian ansatz and LO approximation as

$$\begin{aligned} A_{LL}(x,\, y,\, z,\, Q^2,\, P_{h\perp}) &= \frac{\sqrt{1-\varepsilon^2}}{(1+\varepsilon R)}\, C(P_{h\perp})\, A_1^h(x,\, Q^2,\, z) \qquad (6.17) \\ C(P_{h\perp}) &\equiv \frac{\langle K_T^2\rangle + \langle p_T^2\rangle\, z^2}{\langle K_T^2\rangle + \mu_2^2 z^2} \\ &\quad \times \exp\left[-P_{h\perp}^2 \left(\frac{1}{\langle K_T^2\rangle + \mu_2^2 z^2} - \frac{1}{\langle K_T^2\rangle + \langle p_T^2\rangle\, z^2}\right)\right] \end{aligned}$$

The best fit of the CLAS data for π^+ production on a longitudinally polarized proton target yielded $\mu_2^2/\langle p_T^2\rangle = 0.7 \pm 0.1$ with χ^2/d.o.f.=1.5 [58]. Using the central kinematics of each x bin, $C(P_{h\perp}) - 1$ was found as 1.0%, 2.6%, 4.6% and 6.9% for the kinematic bins at x =0.16, 0.21, 0.27 and 0.35, respectively, respectively. Due to the lack of experimental information on ^{3}He, the full correction estimated using proton data was quoted as the uncertainty for the $P_{h\perp}$

dependence of A_{LL} , $\triangle\left(C(P_{h\perp})-1\right)=|C(P_{h\perp})-1|$.

- The longitudinal virtual-photon cross section contributes a scaling correction of $1/\left(1+\varepsilon R\right)$. Since there is no high precision SIDIS data on R at this kinematic region to date[8], R was estimated using the SLAC-R1999 parametrization for DIS [224]. This center value for A_{LL} was not corrected; and this effect was included in the uncertainty as $\triangle A_{LL}/A_{LL}=\varepsilon R$ and $\triangle A_{LL}/A_{LL}$ =8.7%, 9.5%, 10.0% and 9.7% for the kinematic bins at x =0.16, 0.21, 0.27 and 0.35, respectively. .

- The uncertainty due to $\delta\theta_S\sim 2^\circ$ is also included. This uncertainty is dominated by the uncertainty on the target spin direction.

- As shown in Table 5.2, the kinematic factor (also called depolarization factor [41]), $\sqrt{1-\varepsilon^2}$, ranges from $\sqrt{1-\varepsilon^2}$ =96% to 87% for the lower x-bins to larger ones, i.e., most of the beam polarization is transferred to the struck quark through the virtual photon.

Using Eq. (6.2) and the MLE with unknown parameter $A_{LT}^{\cos(\phi_h-\phi_S)}$ and known parameter A_{LL} (Appendix C.4.2), ΔA_{LL} can be estimated as

$$\Delta A_{LL} = -\frac{\sum_{\rm ev} P^2 M^{(1)} M^{(2)} - N\tilde{A}_L^{(1)}\tilde{A}_L^{(2)}}{\sum_{\rm ev} P^2\left(M^{(1)}\right)^2 - N\left(\tilde{A}_L^{(1)}\right)^2}\times A_{LL} \tag{6.18}$$

$$M^{(2)} = -\cos\theta_S\,. \tag{6.19}$$

The $\Delta A_{LL}/A_{LL}$ ratios are +8%, +10%, +12% and +14% for the lower x-bins to larger ones and they are similar for both π^+ and π^-. The final ΔA_{LL} and its uncertainty are shown in Sec. 6.1.5, in the bottom panels of Fig. 6-14 and in Table 6.3. The overall size of the correction is less than half of the statistical uncertainty of the ^{3}He $A_{LT}^{\cos(\phi_h-\phi_S)}$ asymmetries. The contribution from the sub-leading twist structure function $\cos\theta_S\cdot F_{LL}^{\cos\phi_h}$ was neglected due to a lack of experimental information, a

[8]Future high-precision SIDIS measurement on R is planned following the Jefferson Lab 12 GeV upgrade [223].

general assumption that such effects are suppressed by $1/Q$ [41], and existing evidence for the suppression of subleading-twist effects in other observables of inclusive and semi-inclusive DIS[9] [15, 225, 74].

6.1.4 Additional Systematic Uncertainties

The systematic uncertainties of the ^{3}He $A_{LT}^{\cos(\phi_h-\phi_S)}$ asymmetries, besides those contributed by the corrections as discussed in Sec. 6.1.3, are estimated in this subsection.

Yield Drift and Density Fluctuation

During experiment E06-010, the beam helicity was reversed at 30 Hz. When forming beam-helicity-based asymmetries as in Eq. 2.26, the systematic uncertainties due to acceptance, detector response drift and target density fluctuations are suppressed by $\sqrt{\#\text{ of helicity pairs}} \sim 10^4$. With a detector efficiency that drifts by 10% and a 5% target density fluctuation, both of these contributions to the systematic uncertainty are negligible compared to the raw statistical uncertainty of this measurement ($\sim$ 1.5%). The luminosity stability was confirmed using the luminosity monitor, which measured a few *ppm* level luminosity asymmetry between two beam helicity states for the whole experiment.

Uncertainties for Angle Reconstruction

As shown in Eq. 6.4, the extraction of $A_{LT,\,\text{raw}}^{\cos(\phi_h-\phi_S)}$ dependents on the polar and azimuthal angular reconstruction for θ_S, ϕ_h and ϕ_S. Therefore, the uncertainties in these angles ($\delta\phi$) contributes to the systematic uncertainty for the azimuthal asymmetry. The azimuthal angles were calculated based on the reconstructed observables, including the target spin direction, the momentum of the incident electrons, scattered electrons and produced hadrons[10]. Using simple arguments[11], $\delta\phi$ contributes to the

[9] the sub-leading twist effect were found to be small for the g_1 PDF in DIS [15, 225], and the SIDIS cross section data in Hall C is consistent with the leading-twist quark model calculations [74].

[10] The radiative correction was studied separately.

[11] Considering fit for amplitude A for a 1-D distribution of x which is modulated with $A \cdot \sin x$. If x has a small shift $x \to x + \Delta x$, then result the fit result is biased by $A \cdot (1 - \cos \Delta x) \sim A \cdot \mathcal{O}(\Delta x^2)$ to the leading order.

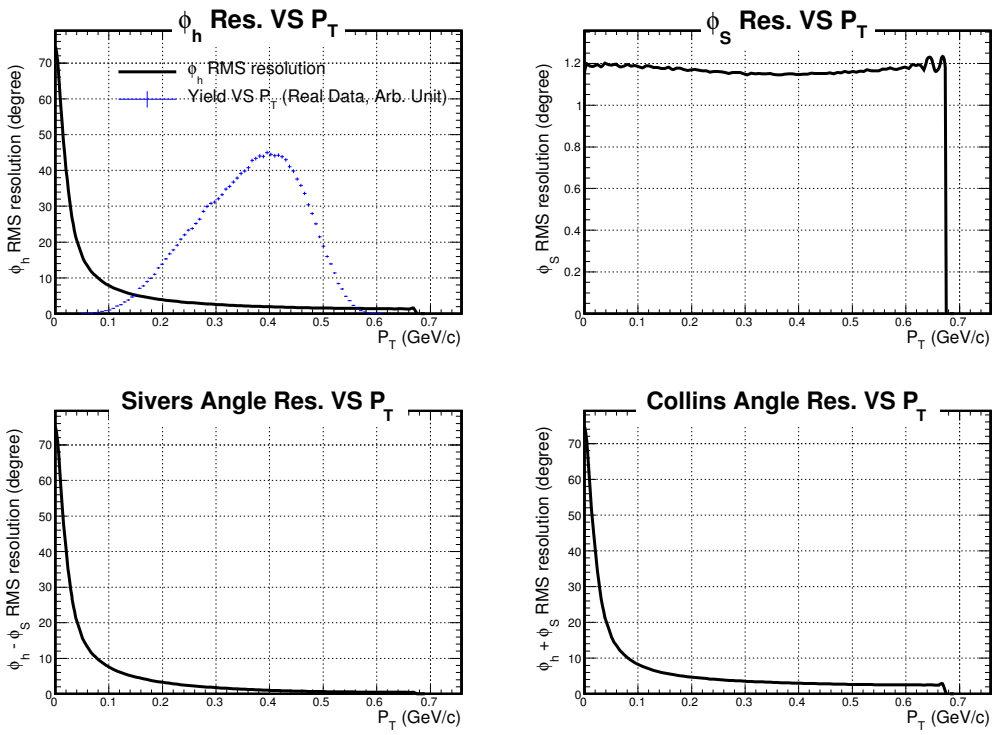

Figure 6-7: The RMS resolution for the azimuthal angles (ϕ_h and ϕ_S) and their combinations (Sivers Angle= $\phi_h - \phi_S$, Collins Angle= $\phi_h + \phi_S$), as functions of pion transverse momentum, $P_T = P_{h\perp}$. The P_T distribution of the E06-010 data with SIDIS kinematic cuts, is also shown in the left top panel.

systematic uncertainties of the azimuthal asymmetry at the level of $\mathcal{O}(\delta\phi^2)$ relative to the raw asymmetry. A MC study, based on a SIMC simulation (Sec. 5.4.1) with ~280 times more events than the E06-010 data, was performed to quantify this uncertainty:

There were two general categories of systematic uncertainties related to the reconstructed observables: resolution effects and a number of systematic offsets, which were simulated separately assuming an maximum bias effect as shown in Table 6.1. For the resolution effect, which mainly stems from the detector resolution of the beam energy measurements and the spectrometers momentum reconstructions, $\delta\phi_h$, $\delta\phi_S$ and their combinations are shown in Fig. 6-7. The RMS resolutions, weighted by the yield of the E06-010 data, are $\delta\phi_h \approx 2^\circ$, $\delta\phi_S \approx 1^\circ$, $\delta(\phi_h - \phi_S) \approx 1.5^\circ$, $\delta(\phi_h + \phi_S) \approx 3^\circ$ and $\delta(\sin\theta_S) \approx 1.5 \times 10^{-3}$. For each source of uncertainty, the general procedure was:

1. Take a SIMC sample with 200K events (statistical level of E06-010), which have

Source	Maximum Effect	Relative Sys. Uncert.
Spectrometer Resolution	In Sec. 5.2	0.1%
Bigbite Angular Offset	2 mrad Horizontal or Vertical	$< 0.01\%$
HRS Horizontal Offset	2 mrad	$< 0.01\%$
HRS Vertical Offset	2 mrad	0.02%
Vertical Target Spin	2°	0.05%
Transverse Target Spin	2°	0.1%
Sum	-	0.2%

Table 6.1: Systematic effect and their contribution to the systematic uncertainty in $|\delta A_{LT}/A_{LT}|$.

a 10% $A_{LT}^{\cos(\phi_h-\phi_S)}$ in the SIDIS cross section.

2. Extract $A_{LT,\,\mathrm{raw}}^{\cos(\phi_h-\phi_S)}$ with Eq. (6.4).

3. Add the resolution or offsets to the same event sample, recalculate azimuthal angles and perform the same fitting for the azimuthal asymmetry.

4. Compare the extracted asymmetries from step 2 and 3; the relative bias is normalized by the 10% initial asymmetry.

5. Repeat step 1-4 for ~280 independent samples and take the average effect.

6. Repeat step 1-5 for each x-bin; since the overall effect is small compared to the sum of other systematic uncertainties, the maximum effect out of the 4 bins was quoted as an estimation for the upper limit[12].

Due to the similarity of the phase space between positive and negative charged pions, only the π^+ channel was studied. The results are shown in Table 6.1. The overall systematic uncertainty for azimuthal asymmetries by quadratically summing over-all all contributions is no larger than $|\delta A_{LT}/A_{LT}|$=0.2%. This discussion excludes the uncertainty of ΔA_{LL} due to the angular reconstruction uncertainties, which was included in the systematic uncertainties for ΔA_{LL} in Sec. 6.1.3.

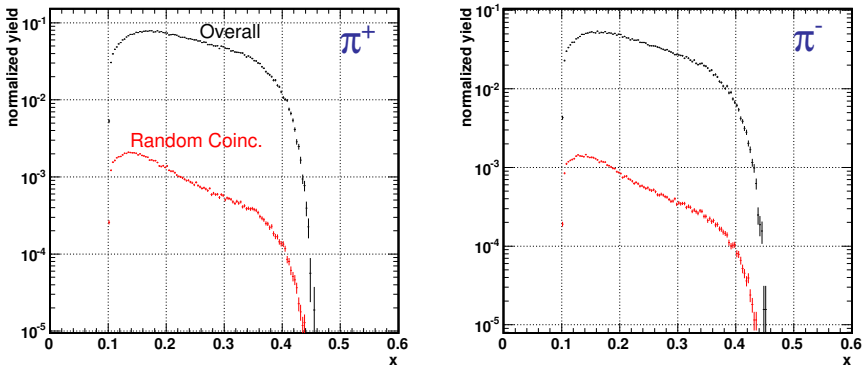

Figure 6-8: Normalized yield for the SIDIS sample within the 6 ns coincidence-timing window cuts (black) and the estimated yield for the random coincidence timing events for any 6 ns timing window (red). The left panel corresponds to random coincidence events with π^+ detected in Left-HRS and the right panel is for π^-.

Random Coincidence

As shown in Sec. 5.3.4, the SIDIS event sample was selected using two coincidence cuts: the coincidence timing (CT, also called coincidence time-of-flight) cut, which require the electrons and hadrons were produced at the same moment, and the coincidence vertex cut, which required they are produced at the same location. There was a small amount of random coincidence (also called accidental coincidence) events, which contaminated the A_{LT} measurement. The relative yields of the random coincidence-timing events were estimated as shown in Fig. 6-8. The black curve represents all overall events that passed the pion CT peak (Fig. 5-11) ± 3 ns cut; the red curve is the yield of random CT events in any 6 ns CT window, which was estimated using 108 ns random-CT bands outside any CT peaks. In addition, the coincidence vertex cut provided another factor of 4~5 suppression of the random coincidence background, which was determined for each x-bin using the random CT events. The yield ratio of the random coincidence events in the final SIDIS sample was estimated for each x-bins, ranging from 0.8%~0.2% for the smaller-x bins to larger ones. The azimuthal asymmetry for the random coincidence events was estimated using the same procedures as the one for coincidence data as shown in Fig. 6-9. The systematic effect

[12]For small effects, a precise estimation with both the upper and lower bounds require a simulation with larger statistics.

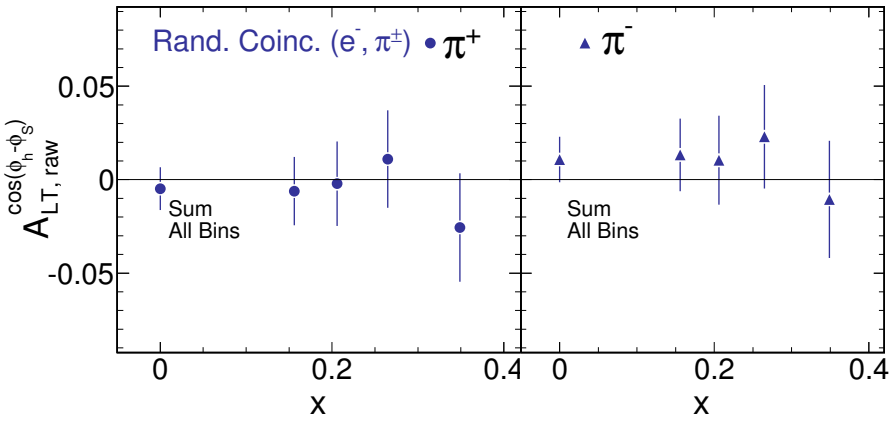

Figure 6-9: The raw azimuthal asymmetry, $A_{LT,\,\mathrm{raw}}^{\cos(\phi_h-\phi_S)}$ for the random coincidence (e^-, $\pi^\pm$) sample. The asymmetry extracted by summing data of all bins is shown at $x = 0$. The left panel corresponds to random coincidence events with π^+ detected in HRS and the right panel is for π^-.

for the SIDIS $A_{LT,\,\mathrm{raw}}^{\cos(\phi_h-\phi_S)}$ contributed by random coincidence was a product of the yield ratio and their asymmetry, which was not larger than 3×10^{-4} and 1/40 of the statistical uncertainty. Since the contribution is small, it was treated as a systematic uncertainty rather than a correction.

Contamination in the HRS Spectrometer

The HRS spectrometer detected charged pions for this measurement. With the standard pion cuts, the systematic uncertainty due to contamination of kaons, protons and electrons were addressed as following:

- As shown in Fig. 5-11, the CT ± 3 ns window included two hadron peaks, pion and kaon. However, the contamination of kaon was further suppressed by its low cross-section ($\leq 6\%$ for $\sigma_{K^+}/\sigma_{\pi^+}$ and $\leq 2\%$ for $\sigma_{K^-}/\sigma_{\pi^-}$) and the aerogel PID detector cut ($\sim 10:1$ kaon rejection in the pion sample) and result in ($\leq 0.6\%$ for N_{K^+}/N_{π^+} and $\leq 0.2\%$ for N_{K^-}/N_{π^-}). The azimuthal asymmetry for the coincidence (e^-, $K^\pm$) events was estimated using the same procedures as the one for coincidence data as shown in Fig. 6-10. The systematic uncertainties for the SIDIS $A_{LT,\,\mathrm{raw}}^{\cos(\phi_h-\phi_S)}$ contributed by kaon contamination was estimated using the product of the contamination yield ratio and their asymmetry, which were

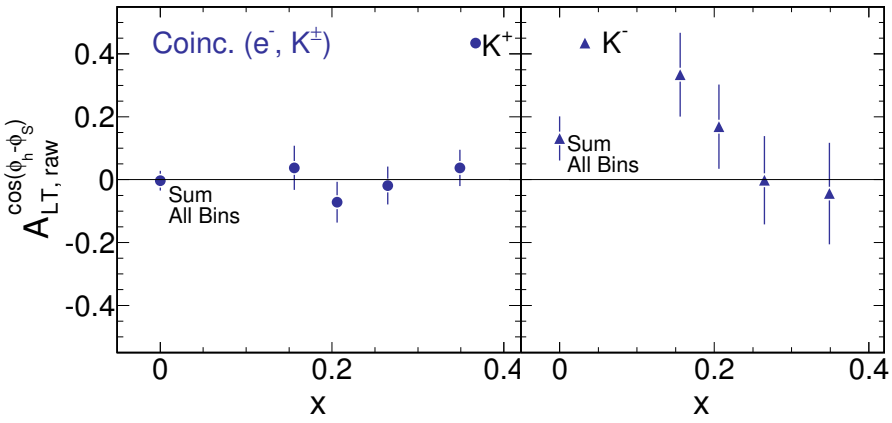

Figure 6-10: The raw azimuthal asymmetry, $A_{LT,\,\mathrm{raw}}^{\cos(\phi_h-\phi_S)}$ for the coincidence (e^-, $K^\pm$) sample. The asymmetry extracted by summing data of all bins is shown at $x = 0$. The left panel corresponds to the K^+ production and the right panel is for K^- .

not larger than 0.1% for each x-bin. And for the summation of all the x-bins, the uncertainties are $\Delta A\,(\pi^+) = 2 \times 10^{-4}$ for K^+ and $\Delta A\,(\pi^-) = 4 \times 10^{-4}$ for K^-.

- From the coincidence timing cut, the proton timing peak was $\sim 20\sigma$ away from the pion one. Therefore, the CT peaks of positively-charged pions and protons were well separated. The leak of proton into the SIDIS π^+ sample had to be in the random coincidence background and is further suppressed by the aerogel PID detector cut. Therefore the residual proton contribution is already included in the systematic uncertainty of random coincidence as discussed above.

- An electron rejection of $\sim 10^4 : 1$ was achieved [145] using the gas Cerenkov detector and the lead-glass detector. Since the yield for coincidence pion in the Left-HRS is larger than that for electrons, the contamination of e^- to the π^- sample is negligible.

Pion Contamination in the BigBite Spectrometer

The BigBite Spectrometer detected the scattered electrons. The electron PID was provided by the lead-glass calorimeter with a preshower-shower splitting. The positively charged particles were separated by the bending of the track (Sec. 5.3.2). The

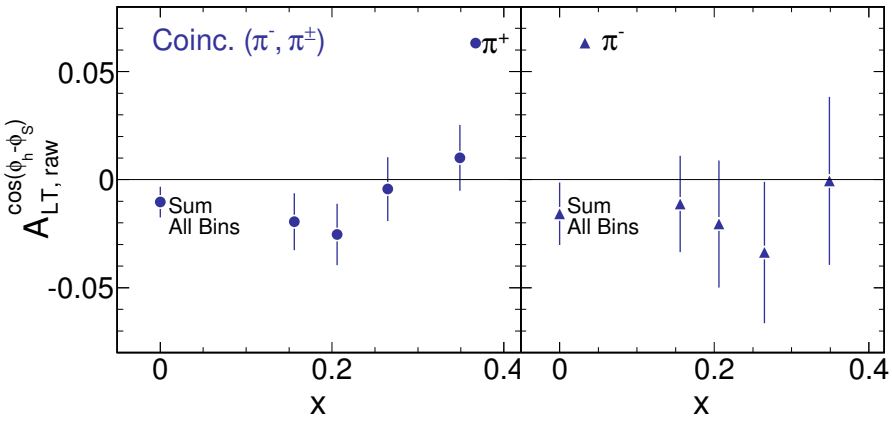

Figure 6-11: The raw azimuthal asymmetry, $A_{LT,\,\mathrm{raw}}^{\cos(\phi_h-\phi_S)}$ for the coincidence sample with negatively charged hadron in BigBite (π^- dominated) and charged pion in HRS. The asymmetry extracted by summing data of all bins is shown at $x = 0$. The left panel corresponds to coincidence events with π^+ detected in HRS and the right panel is for π^-.

ratio of negatively charged hadron contamination, which was dominated by π^-, was estimated by fitting the pion spectrum in the preshower detector ($E_{\mathrm{preshower}}$) with a Gaussian convoluted Landau function and counting its tail in the electron sample (cut with $E_{\mathrm{preshower}} > 200$ MeV) [131, 140]. From the smaller-x bins to larger ones, the pion contamination ratio[13] ranged from 1.7% to 0.2% for coincidence π^+ in HRS and from 0.5% to $< 0.1\%$ for coincidence π^- in HRS. The coincidence asymmetry for the BigBite π^- contamination was estimated by selecting hadron-like events using the calorimeter and extract their raw azimuthal asymmetry, $A_{LT,\,\mathrm{raw}}^{\cos(\phi_h-\phi_S)}$, as shown in Fig. 6-11. The systematic uncertainties for the SIDIS $A_{LT,\,\mathrm{raw}}^{\cos(\phi_h-\phi_S)}$ was estimated using the product of the pion contamination yield ratio and the asymmetry for the contaminated events. The result systematic uncertainty for the SIDIS pion production was not larger than $\delta A_{LT,\,\mathrm{raw}}^{\cos(\phi_h-\phi_S)} = 8 \times 10^{-4}$ for any x-bin.

Beam Single Spin Asymmetry, A_{LU}

The beam single spin asymmetry A_{LU} is related to the twist-three cross-section terms of $\lambda_e \sqrt{2\,\varepsilon(1-\varepsilon)}\,\sin\phi_h\,F_{LU}^{\sin\phi_h}$ in Eq. (2.5). Due to the frequent target spin reversal, the A_{LU} contribution was suppressed in the measured A_{LT} DSA as Eq. (2.26). A

[13] the number of contaminated π^- events/total electron sample

residual uncertainty contributed by ignoring A_{LU} during the analysis as Eq. (6.2) was estimated by adding the A_{LU} term into the cross section model and performing a two-free-term MLE fit following Eq. (C.42). The average changes on $A_{LT}^{\cos(\phi_h-\phi_S)}$ for this two-term fit compared to one-term fit is $\sim$ 190 ppm for π^+ and ~ -50 ppm for π^-. Since A_{LU} was assumed to be negligible in the extraction of $A_{LT,\,\mathrm{raw}}^{\cos(\phi_h-\phi_S)}$, this change was accounted into the systematic uncertainty of $\delta A_{LT,\,\mathrm{raw}}^{\cos(\phi_h-\phi_S)}$.

Target Single Spin Asymmetries, A_{UT}

In the measured A_{LT} double spin asymmetry, the target single spin asymmetry A_{UT} also cancels out due to the frequent target spin reversal. The residual effects were studied using SIMC (Sec. 5.4.1) following a similar procedure as that for the uncertainties for the azimuthal angle reconstruction as discussed the early part of this subsection. The final bias on A_{LT} is smaller than $|\delta A_{LT}/A_{LT}| = 1\%$, and it is much smaller than the rest of the systematic uncertainties of A_{LT}. Therefore, the systematic uncertainty for A_{LT} has included $|\delta A_{LT}/A_{LT}| = 1\%$ due to neglecting A_{UT} during the analysis. This uncertainty is much smaller than other (both statistical and systematical) uncertainties in this measurement as expected.

Unpolarized Azimuthal Asymmetries, A_{UU}

As shown in Eq. (2.5), the Cahn effect ($F_{UU}^{\cos\phi_h}$) and the Boer-Mulders effect ($F_{UU}^{\cos 2\phi_h}$) introduce $\cos\phi_h$ and $\cos 2\phi_h$ dependencies to the unpolarized SIDIS cross section, respectively. These modulations can be parametrized using the unpolarized azimuthal asymmetry, $A_{UU}^{\cos\phi_h}$ and $A_{UU}^{\cos 2\phi_h}$, as the ratios to the average cross section. The size of these asymmetries can be estimated using the preliminary HERMES proton and deuteron data [71] and an extrapolation to the E06-010 kinematic region, which leads to $\left|A_{UU}^{\cos\phi_h}\right| \sim 10\%$ and $\left|A_{UU}^{\cos 2\phi_h}\right| \sim 5\%$. As shown in Eq. 2.27, A_{UU} did not cancel naturally in the A_{LT} DSA since it do not inverse in sign with reversal of either the target spin or the beam helicity. They introduces a scaling effect at the level of $1 + A_{UU}$ (see denominator in Eq. 2.27) for experiments with the limited coverage of ϕ_h. A more precise estimation of this effect on $A_{LT}^{\cos(\phi_h-\phi_S)}$ was made using a SIMC

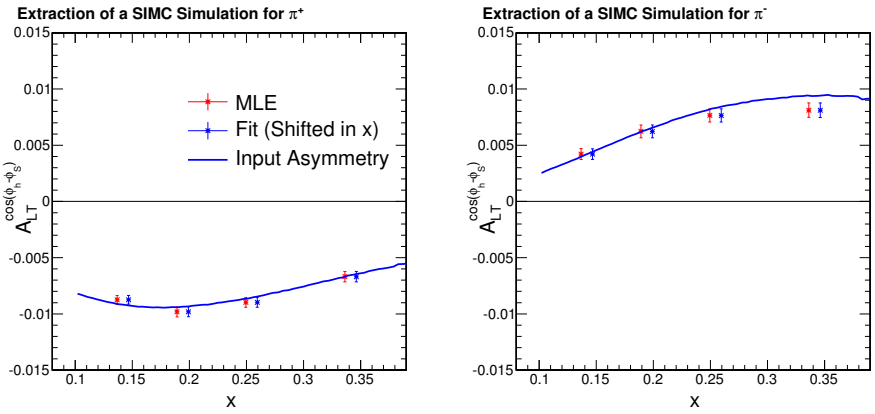

Figure 6-12: $A_{LT}^{\cos(\phi_h-\phi_S)}$ for π^+ (left) and π^- (right) extracted from a SIMC simulation with a built-in model asymmetry as the blue curve. Two extraction methods, MLE (red) and fit (blue), were used as discussed in Sec. 6.1.2, which yielded highly consistent results. The left panel corresponds to the SIDIS π^+ production and the right panel is for π^- .

simulation (Sec. 5.4.1) with the estimated A_{UU} and 10% of A_{LT}. Since A_{UU} for ^{3}He was not measured, the center value for A_{LT} was not corrected, and the relative bias on A_{LT} due to A_{UU} was taken into account of the systematic uncertainty δA_{LT}. For the Cahn effect, $|\delta A_{LT}/A_{LT}| = 10\% \sim 8\%$ for the smaller-x bins to larger ones and for the Boer-Mulders effect, $|\delta A_{LT}/A_{LT}| \sim 3\%$.

Bin Centering Effect

During the analysis, $A_{LT}^{\cos(\phi_h-\phi_S)}$ was assumed to be constant within each x-bin. However, $A_{LT}^{\cos(\phi_h-\phi_S)}$ can depend in a complex way on x, Q^2, z and $P_{h\perp}$. Therefore the extracted $A_{LT}^{\cos(\phi_h-\phi_S)}$ can deviate from the physical asymmetry corresponding to the kinematic center of each bin (Table 5.2). This deviation, which is also known as the bin centering effect, was estimated using a high statistics[14] SIMC simulation (Sec. 5.4.1) with a model $A_{LT}^{\cos(\phi_h-\phi_S)}$ asymmetry using the WW-type approximations [106, 107]. The same procedure, which was used to analyze the production data, was used to extract $A_{LT}^{\cos(\phi_h-\phi_S)}$ for each of the x bins as shown in Fig. 6-12. The relative deviation $|A_{extract} - A_{input}|\,/A_{extract}$ of extracted asymmetry $A_{extract}$ from the input asymmetry at the kinematic bin center A_{input} was used as the bin centering

[14] ~500 times of the statistics of the production data.

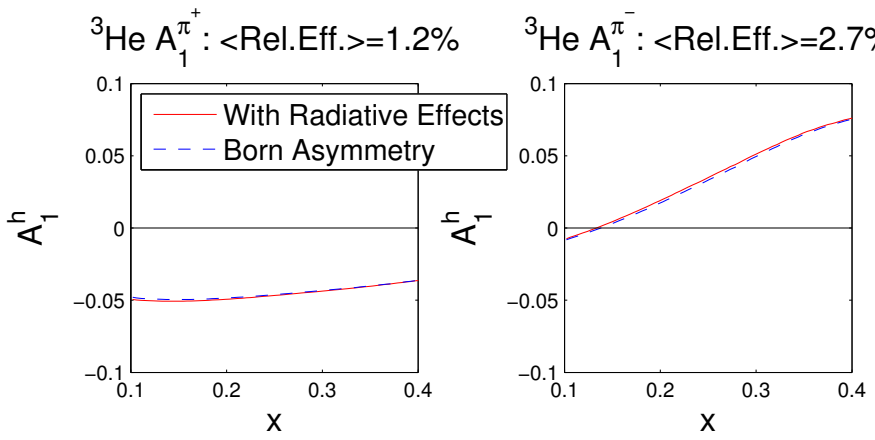

Figure 6-13: SIDIS ^{3}He $A_1^{\pi^\pm}$ (Eq. (6.15)) calculated using POLRAD2 [226] with radiative effects ON (red solid) and OFF (blue dash, also called Born Asymmetries) at the kinematics of this experiment. The difference between these two curves is the radiative effect, which is small (few percent).

uncertainty for the measured A_{LT}, i.e., $|\delta A_{LT}/A_{LT}|$ =4.1%, 5.1%, 6.2% and 10.4% for the π^+ smaller-x bins to larger ones and $|\delta A_{LT}/A_{LT}|$ =13%, 12%, 8.6% and 14% for the π^- bins[15].

Radiative Effects

The SIDIS cross section and models as discussed in Sec. 2.2 assumed one photon exchange between the scattering electron and the nucleon, i.e., the Born approximation. During the experiment, the electrons can radiate photons when they pass through the target materials and when scattering with the nucleon, which is known as the external and internal radiative effects, respectively. Both radiative effects cause the observed asymmetry to deviate from the Born asymmetry. The spin independent part of the radiative effects were corrected by shifting the observed central kinematics by an average radiative loss using the SIMC simulation as Sec. 5.4.1.

[15]Both the center value of the simulated deviation $A_{extract} - A_{input}$ and the simulation statistical uncertainty $\Delta\left(A_{extract} - A_{input}\right)$ were taken into account to estimate the expected ranges of bin centering effect, i.e.,

$$|\delta A_{LT}/A_{LT}| = \left|\sqrt{(A_{extract}-A_{input})^2+(\Delta(A_{extract}-A_{input}))^2}/A_{extract}\right| .$$

$|\delta A_{LT}/A_{LT}|$ were dominated by the statistical uncertainty for the simulation, especially for the π^- lower-x bins where the modeled A_{LT} are small. Therefore the uncertainty was larger for those bins.

The spin dependent radiative effect was estimated using POLRAD2 [226]. There is yet no experimentally verified model of A_{LT}, which is necessary for a precise spin dependent radiative correction. Therefore, the rough magnitude of this effect was estimated using a well-established procedure for radiative correction for SIDIS ^{3}He $A_1^{\pi^\pm}$ (Eq. (6.15)) as shown in Fig. 6-13, where the $A_1^{\pi^\pm}$ asymmetries with radiative effects ON and OFF were simulated for this experiment setup.The differences between these two asymmetries is the radiative effect. Their sizes relative to the asymmetries are small, i.e., $|(A_{rad.\,ON} - A_{rad.\,OFF})/A_{rad.\,ON}| \sim 1\%$ for π^+ and 3% for π^-[16]. Therefore, no correction was made on A_{LT} and $|\delta A_{LT}/A_{LT}| \sim |(A_{rad.\,ON} - A_{rad.\,OFF})/A_{rad.\,ON}|$ was included in the systematic uncertainty for A_{LT}.

Contamination from Low-W Events due to Radiative Effects

The low-W events, which have significantly lower W or W' than the SIDIS events, are mainly from resonance and exclusive productions. Although $W > 2.3\,\text{GeV}$ and $W' > 1.6\,\text{GeV}$ cuts were applied during the SIDIS analysis, the low-W events can contaminate into the SIDIS sample through radiative energy loss of the beam or scattered electron. The yield ratio of this contamination was estimated using the SIMC simulation by normalizing to the observed cross section of the coincidence data. The upper limit for the contamination was 3% and 4% for π^+ and π^-, respectively. The asymmetry for such low-W events were roughly estimated by extracting $A_{LT}^{\cos(\phi_h-\phi_S)}$ with inverse W cuts, i.e., $W < 2.3\,\text{GeV}$ and $W' < 1.6\,\text{GeV}$. With these cuts, $A_{LT,\,\text{low-}W}^{\cos(\phi_h-\phi_S)} = 2.8 \pm 1.2\%$ for π^+ and $0.0\% \pm 1.6\%$ for π^-. Their contribution to the systematic uncertainty was estimated by multiplying the contamination ratio and $A_{LT,\,\text{low-}W}^{\cos(\phi_h-\phi_S)}$, which lead to $\delta A_{LT} \leq 7 \times 10^{-4}$ for π^+ and 9×10^{-4} for π^-.

Sub-Leading Twist Modulations

Associated with A_{LT}, there are two subleading-twist $\cos\phi_S$ and $\cos(2\phi_h - \phi_S)$ modulations, which stem from the twist-three structure functions of $F_{LT}^{\cos\phi_S}$ and $F_{LT}^{\cos(2\phi_h-\phi_S)}$ as shown in Eq. (2.5), respectively. Because of the limited kinematic coverage and

[16]The region where $A_1^{\pi^-}$ crosses zero was avoided when averaging $|(A_{rad.\,ON} - A_{rad.\,OFF})/A_{rad.\,ON}|$ for π^- , since the relative effect diverges when $A_1^{\pi^-} \to 0$.

statistics for this experiment, the leading-twist $\cos(\phi_h - \phi_S)$ modulation can not be separated from the two subleading-twist ones in $A_{LT}(\phi_h, \phi_S)$ in this analysis. The current experimental information on the neutron subleading-twist effects can be roughly estimated using the preliminary deuteron [118] and proton [119, 121, 120] results from the COMPASS and HERMES collaboration. No statistical significant non-zero asymmetry was observed from these preliminary results; and therefore they suggest subleading-twist effects in neutron $A_{LT}(\phi_h, \phi_S)$ are consistent with zero for the current world data precision (preliminary). However, the uncertainties on neutron subleading-twist effect are larger than the statistical uncertainty for this measurement. Therefore the current world data (still preliminary) cannot put an effective limit on the uncertainty contributed by the subleading-twist A_{LT} modulations.

The uncertainties from neglecting the subleading-twist $\cos\phi_S$ and $\cos(2\phi_h - \phi_S)$ modulations in the leading-twist extraction procedure of A_{LT} (Eq. (6.1)) were not included in the systematic uncertainties for the following reasons:

- Lack of experimental information, both from this experiment and from the current world data, as discussed above,
- A general assumption that such effects are suppressed by $1/Q$ as shown in Ref. [41],
- There is a considerable body of experimental evidence in inclusive DIS and SIDIS supporting the general suppression of subleading-twist effects: the analyses of polarized DIS data in Ref. [15, 225] allowed the extractions of subleading-twist contributions to the subleading-twist helicity distribution $g_1(x, Q^2)$. This study showed that for the kinematics of this experiment, the subleading-twist effects are less than 20% of the leading twist distributions, which is much smaller than the statistical uncertainty for this experiment. Moreover, the Q^2-dependencies of the SIDIS cross sections for the π^+ and π^- production on hydrogen and deuterium targets measured at JLab in Hall C [74] are consistent with the leading-twist parton model calculations in kinematics very similar to this experiment. Nevertheless, this work has laid the foundation for future

high-precision mapping of A_{LT} following the JLab 12 GeV upgrade [35] and at an electron-ion collider [36], which will cover a broader Q^2 range will enable an accurate determination of the subleading-twist A_{LT} moments.

Diffractive ρ Contamination

Some of the detected events may originate from the decay of diffractive vector meson production, which is dominated by the ρ meson production for the pion channels. The underlying physics of this process can be described as the virtual photon fluctuating into a vector meson, that subsequently can interact with the nucleon through multiple gluon (Pomeron) exchange. Unlike SIDIS, the diffractive production do not carry parton information in the nucleon through virtual photon exchanges, and therefore, presents a background for the SIDIS study. The contamination in the identified SIDIS events from decays of diffractively produced ρ mesons was estimated to range from 3-5% (5-10%) for π^+ (π^-) using PYTHIA6 [227], which was also used by the HERMES [228, 50], JLab Hall B [58] and Hall C experiments [74]. The asymmetry data from diffractive rho is scarce[17] and there is no experimental information on the rho induced A_{LT} asymmetry at our kinematic range. Consistent with other SIDIS asymmetry analyses, no corrections on the central values of A_{LT} were applied for this contamination and this contamination is not included in the systematic uncertainties for A_{LT} [228, 50, 58, 54].

Summary

In addition to the previously discussed systematic uncertainties, the beam and target polarimetry contributed $|\delta A_{LT}/A_{LT}| \leq 5\%$ each as discussed in Sec. 3.2.6 and 4.7, respectively. The contributions to the systematic uncertainty are summarized in Table 6.2 and were added in quadrature for each of the x-bins as shown in Fig. 6-14. As discussed above, the systematic uncertainty due to diffractively produced ρ and the sub-leading twist contributions are not included.

[17] Preliminary asymmetry results for ρ production on a longitudinally polarized proton target are reported by the CLAS collaboration in Ref. [229]. The preliminary asymmetry for pions from ρ decay is also reported in the same talk.

Source	Format	Uncertainty	
		π^+	π^-
Beam Polarimetry	$\lvert\delta A_{LT}/A_{LT}\rvert$	4.6%	
Target Polarimetry	$\lvert\delta A_{LT}/A_{LT}\rvert$	4.9%	
Yield Drift and Density Fluctuation	-	Negligible	
Azimuthal Angle Reconstruction	$\lvert\delta A_{LT}/A_{LT}\rvert$	$\leq 0.2\%$	
Single Track Cut in HRS	-	Negligible	
N_2 Dilution	$\lvert\delta A_{LT}/A_{LT}\rvert$	~1%	
Charge-Symmetric Background	$\lvert\delta A_{LT}/A_{LT}\rvert$	$6\% \sim 0.5\%$	$6\% \sim 1\%$
A_{LL} Correction	$\delta A_{LT,\,^3\mathrm{He}}^{\cos(\phi_h-\phi_S)}$	0.2%~0.3%	0.1%~0.3%
Random Coincidence	$\delta A_{LT,\,\mathrm{raw}}^{\cos(\phi_h-\phi_S)}$	$\leq 3\times10^{-4}$	$\leq 2\times10^{-4}$
Kaon in HRS Pion	$\delta A_{LT,\,\mathrm{raw}}^{\cos(\phi_h-\phi_S)}$	$\leq 8\times10^{-4}$	$\leq 9.5\times10^{-4}$
Proton and Electron in HRS Pion	-	Negligible	
π^- in BigBite Electron	$\delta A_{LT,\,\mathrm{raw}}^{\cos(\phi_h-\phi_S)}$	$(8\sim1)\times10^{-4}$	$(4\sim3)\times10^{-4}$
Beam Single Spin Asymmetry	$\left\langle \delta A_{LT,\,\mathrm{raw}}^{\cos(\phi_h-\phi_S)} \right\rangle$	$\sim 2\times10^{-4}$	$\leq 1\times10^{-4}$
Target Single Spin Asymmetries	$\lvert\delta A_{LT}/A_{LT}\rvert$	$\leq 1\%$	
Boer-Mulders Effect ($A_{UU}^{\cos 2\phi_h}$)	$\lvert\delta A_{LT}/A_{LT}\rvert$	$10\% \sim 8\%$	
Cahn Effect ($A_{UU}^{\cos\phi_h}$)	$\lvert\delta A_{LT}/A_{LT}\rvert$	$\sim 3\%$	
Bin Centering Effect	$\lvert\delta A_{LT}/A_{LT}\rvert$	$4\% \sim 10\%$	$\leq 14\%$
Radiative Effect	$\lvert\delta A_{LT}/A_{LT}\rvert$	$\leq 1\%$	$\leq 3\%$
Low-W Contamination	$\delta A_{LT,\,\mathrm{raw}}^{\cos(\phi_h-\phi_S)}$	$\leq 7\times10^{-4}$	$\leq 9\times10^{-4}$
Total	$\sqrt{\sum(\delta A_{LT})^2}/\Delta_{\mathrm{Stat.}}A_{LT}$	$0.2 \sim 0.3$	$0.4 \sim 0.3$

Table 6.2: Summary for the systematic uncertainties of ^{3}He $A_{LT}^{\cos(\phi_h-\phi_S)}$, where A_{LT} was used as $A_{LT}^{\cos(\phi_h-\phi_S)}$ to save space. In the case that a range is given, the numbers are given in the order from smaller-x bins to larger ones. The contributions are added in quadrature and shown as the ratios to the statistical uncertainty, $\Delta_{\mathrm{Stat.}}A_{LT}$.

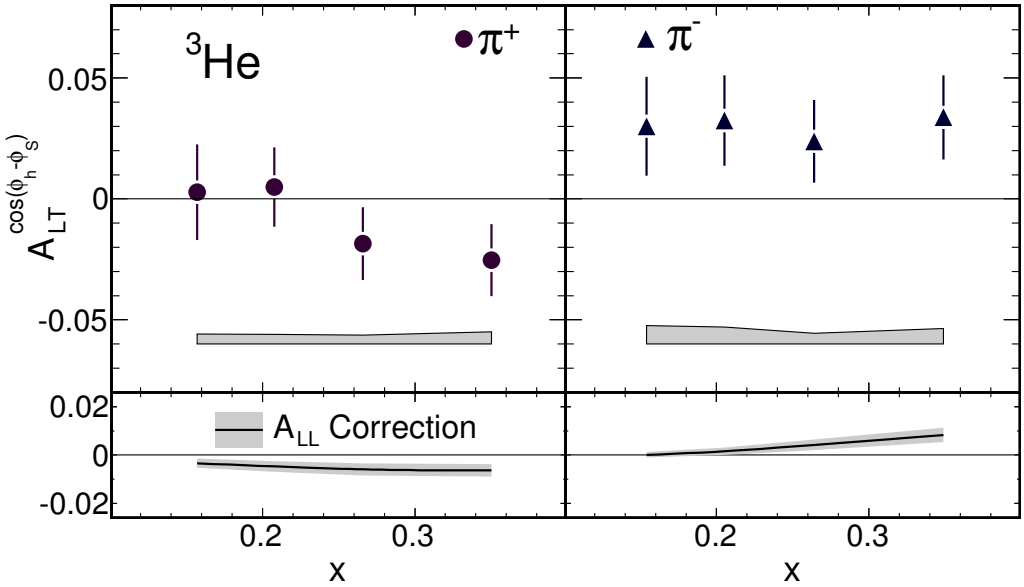

Figure 6-14: The ^{3}He $A_{LT}^{\cos(\phi_h-\phi_S)}$ azimuthal asymmetry plotted against x for positive (top left) and negative (top right) charged pions. The systematic uncertainties are shown in the grey bands. The A_{LL} corrections (ΔA_{LL}) , which were applied to the central value of $A_{LT}^{\cos(\phi_h-\phi_S)}$, and the uncertainties for ΔA_{LL}, which were combined to the total systematic uncertainty for $A_{LT}^{\cos(\phi_h-\phi_S)}$, are shown in the bottom panels on the left-hand and right-hand side for π^+ and π^-, respectively. This figure is from a manuscript (Ref. [230]) submitted to Phys. Rev. Lett.

6.1.5 Result and Discussions

^{3}He $A_{LT}^{\cos(\phi_h-\phi_S)}$ Result

The results for the ^{3}He $A_{LT}^{\cos(\phi_h-\phi_S)}$ asymmetry as defined in Eq. 6.3 are shown in Fig. 6-14 and in Table 6.3. For all four x-bins, the precision is dominated by the statistical uncertainties. The kinematic center for each bin is shown in Table 5.2. Combining the data from all four x-bins , including both statistical and systematic uncertainties, we have observed a positive asymmetry with 2.8 σ significance for π^- production on ^{3}He, while the π^+ asymmetries are consistent with zero. This is the first indication of a non-zero A_{LT} for SIDIS, which suggests a non-zero g_{1T}^q and quark S-P wave interference.

x	A_{LL} Correction π^+	A_{LL} Correction π^-	^{3}He $A_{LT}^{\cos(\phi_h-\phi_S)}$ π^+	^{3}He $A_{LT}^{\cos(\phi_h-\phi_S)}$ π^-
0.156	-0.003 ± 0.002	0.000 ± 0.001	$0.003 \pm 0.020 \pm 0.004$	$0.030 \pm 0.020 \pm 0.008$
0.206	-0.005 ± 0.002	0.002 ± 0.002	$0.005 \pm 0.016 \pm 0.004$	$0.032 \pm 0.019 \pm 0.007$
0.265	-0.006 ± 0.003	0.004 ± 0.002	$-0.019 \pm 0.015 \pm 0.004$	$0.024 \pm 0.017 \pm 0.004$
0.349	-0.006 ± 0.003	0.008 ± 0.003	$-0.025 \pm 0.015 \pm 0.005$	$0.034 \pm 0.017 \pm 0.006$

Table 6.3: Tabulated results for the measured ^{3}He $A_{LT}^{\cos(\phi_h-\phi_S)}$ asymmetries. The format for the A_{LL} correction follows "central value" ± "systematic uncertainty"; the format for the ^{3}He $A_{LT}^{\cos(\phi_h-\phi_S)}$ asymmetries follows "central value" ± "statistical uncertainty" ± "systematic uncertainty" .

6.2 Neutron $A_{LT}^{\cos(\phi_h-\phi_S)}$ Extraction

6.2.1 Introduction

As discussed in Sec. 4.1.1, the ground state ^{3}He wavefunction is dominated by the S-state, in which the two proton spins cancel and the nuclear spin resides entirely on the single neutron [149]. Therefore, a polarized ^{3}He target is the optimal effective polarized neutron target. In the extraction of the neutron double spin asymmetry from the measured ^{3}He asymmetry in the DIS region, the common approach is to use the effective nucleon polarization:

$$\sigma^{^3\mathrm{He}} = \sigma^n + 2\sigma^p \tag{6.20}$$

$$\Delta\sigma^{^3\mathrm{He}} = P_n \cdot \Delta\sigma^n + P_p \cdot 2\Delta\sigma^p \tag{6.21}$$

The effective neutron and proton polarizations in ^{3}He, $P_n = 0.86^{+0.036}_{-0.02}$ and $P_p = -0.028^{+0.009}_{-0.004}$, were reviewed by Zheng, *et. al.* [151] based on various nuclear model calculations and reviews of Refs. [149, 231, 153, 232]. Following this approach, the asymmetry of ^{3}He can be expressed using the asymmetry of the proton ($A^p = \Delta\sigma^p/\sigma^p$) and the neutron ($A^n = \Delta\sigma^n/\sigma^n$) as

$$A^{^3\mathrm{He}} = \frac{\Delta\sigma^{^3\mathrm{He}}}{\sigma^{^3\mathrm{He}}} = P_n \cdot (1 - f_p) \cdot A^n + P_p \cdot f_p \cdot A^p \,, \tag{6.22}$$

where the proton dilution factor is defined as $f_p \equiv 2\sigma_p/\sigma_{^3\mathrm{He}}$. This approximation neglects the nuclear effects, including nuclear binding, Fermi motion of the nucleon, the off-shellnesss of the nucleon, the presence of non-nucleonic degrees of freedom and final state interactions (FSIs). Experiment E05-102 ,[175] which is currently under analysis, will help understand the ^{3}He system beyond this simple approximation. Future experimental and theoretical studies are needed to precisely understand these effects, which are important for the next-generation high-precision neutron measurements [35, 233, 234].

6.2.2 Extraction

General Approach

Following Eq. (6.22), the neutron asymmetry was extracted from the ^{3}He asymmetry using the effective polarization approximation, given by

$$A_{LT}^{n} = \frac{A_{LT}^{^3\mathrm{He}} - f_p \cdot P_p \cdot A_{LT}^{p}}{(1 - f_p)\, P_n}\,, \tag{6.23}$$

where the proton dilution factor f_p was measured with unpolarized ^{3}He and hydrogen gas targets in identical kinematics, including the uncertainties from spin-independent final state interactions (FSI) as shown in Sec. 5.5.4. To facilitate the following discussions, Eq. (6.23) is expanded into two terms regarding their dependence on the proton asymmetry, i.e., $A_{LT}^{n} = \widehat{A}_{LT}^{^3\mathrm{He}\to n} - \widehat{A}_{LT}^{p\to n}$:

- The first term is the "direct" neutron asymmetry, which is equal to the final A_{LT}^{n} only if the proton asymmetry is zero,

$$\widehat{A}_{LT}^{^3\mathrm{He}\to n} \equiv \frac{A_{LT}^{^3\mathrm{He}}}{(1 - f_p)\, P_n}\,, \tag{6.24}$$

  i.e., the neutron asymmetry is directly related with the observed ^{3}He asymmetry through a dilution f_p from proton and the effective neutron polarization in ^{3}He P_n. $\widehat{A}_{LT}^{^3\mathrm{He}\to n}$ and its systematic uncertainty is shown with the data point and the grey bands in Fig. 6-15. As discussed in Sec. 5.5.4, f_p was measured using

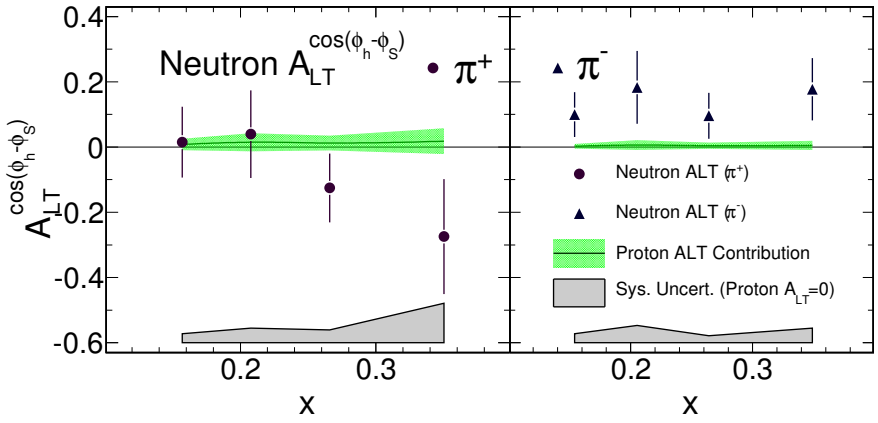

Figure 6-15: The "direct" neutron asymmetries $\widehat{A}_{LT}^{^3\mathrm{He}\to n}$ (data points) and the possible ranges for proton corrections $\widehat{A}_{LT}^{p\to n}$ (green bands). See text for descriptions. The left panel corresponds to the SIDIS π^+ production and the right panel is for π^-. The bottom grey bands show the systematic uncertainties for $\widehat{A}_{LT}^{^3\mathrm{He}\to n}$.

dedicated data with unpolarized ^{3}He and hydrogen gas targets. The results on $(1-f_p)$ are shown in Table 5.5, which are $0.1 \sim 0.2$ for π^+ and $0.2 \sim 0.35$ for π^-. Therefore, the overall scale factors $\frac{1}{(1-f_p)P_n}$ are 6 11 for π^+ and $3 \sim 6$ for π^-.

- The second term is the correction due to a non-zero proton asymmetry A_{LT}^p,

$$\widehat{A}_{LT}^{p\to n} \equiv \frac{f_p \cdot P_p}{(1-f_p)\, P_n} \cdot A_{LT}^p \tag{6.25}$$

which is estimated as in the following text:

Proton Asymmetry

There is no high precision experimental information for A_{LT}^p at the kinematics region of this experiment. However, with a model assistance, the limits on A_{LT}^p can be extrapolated from the preliminary results from the COMPASS [119] and HERMES [120] collaboration. By averaging the three larger-x data points at $0.1 \le x \le 0.3$ from the preliminary COMPASS results (shown in Fig. 2-8 and published in Ref. [119]), the upper limit on the deviation of the WW-type prediction[18] [106] from the averaged

[18] As discussed in Sec. 2.4.3.2, the WW-type calculations relate the g_{1T} TMD to the collinear PDF g_1 by assuming (mainly) the subleading-twist contributions are negligible.

A_{LT}^{p} data, was found to be 0.14 for π^+ and 0.12 for π^-. The recently reported preliminary HERMES proton A_{LT} [120] (Fig. 2-9) are consistent within this range. This limit was quoted as the uncertainty of A_{LT}^{p} for this experiment, whose central value was calculated using the same WW-type calculation. Following Eq. (6.25), the proton correction terms $\widehat{A}_{LT}^{p\to n}$ were estimated. Their allowed ranges are shown by the green bands in Fig. 6-15.

Since at the kinematic range of this experiment the current data on A_{LT}^{p} (and therefore on $\widehat{A}_{LT}^{p\to n}$) cannot distinguish between a zero asymmetry and the model calculations, $\widehat{A}_{LT}^{p\to n}$ was not used to correct the central value for the final A_{LT}^{n}. Instead, the possible ranges for the proton correction $\widehat{A}_{LT}^{p\to n}$ (green bands in Fig. 6-15) were combined quadratically with the systematic uncertainties for $\widehat{A}_{LT}^{^3\mathrm{He}\to n}$ to form the systematic uncertainties for the final A_{LT}^{n} as shown in the result section, Fig. 6-16.

Final State Interaction (FSI)

After pions are produced on the nucleon, they can interact with the spectator nucleons and affect the physics observables. The size of this effect was estimated as described below and quoted in the systematic uncertainty. The general size of the FSI was suppressed by choosing the kinematics at pion momentum of $P_h = 2.35$ GeV and at $z \sim 0.5$.

- Spin-independent FSI changes the SIDIS cross section and therefore the f_p measurement. The possible effect of FSI was estimated using pion multiplicity data [207] and the Lund string model-based calculation of the pion absorption probability [208], which showed $\sim$ 3.5% drop of SIDIS cross section for ^{3}He nuclei relative to two free protons and one neutron, which was discussed in Refs. [54, 169]. More detailed study are needed to pin down this number, therefore a 3.5% relative uncertainty for the SIDIS cross section was included.

- Target single-spin-dependent FSI effects on the DSA were canceled by the frequent target spin flips in Eq. (2.26), which results in a negligible uncertainty in the extracted neutron A_{LT}.

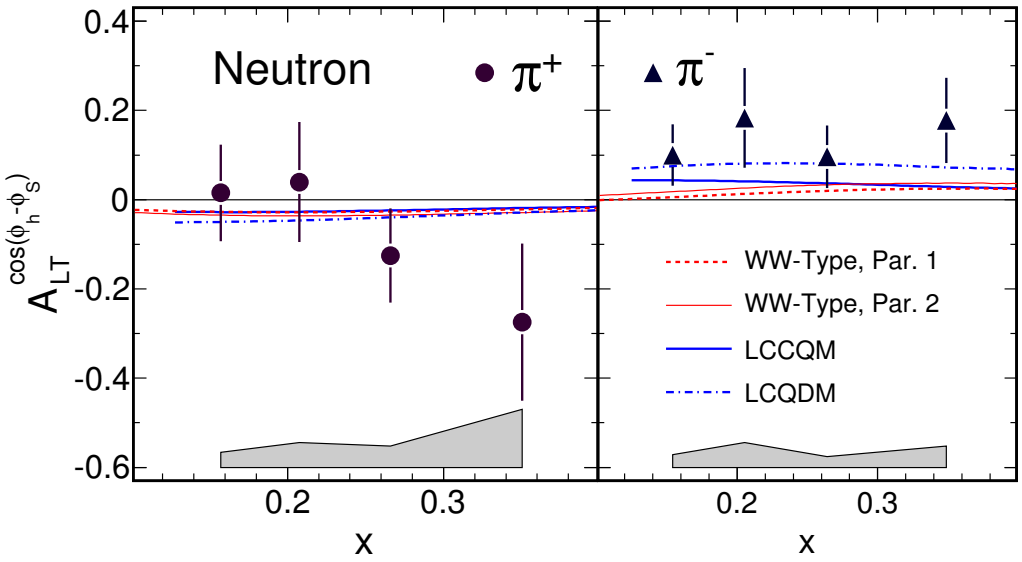

Figure 6-16: Neutron $A_{LT}^{\cos(\phi_h-\phi_S)}$ azimuthal asymmetry for positive (left) and negative (right) charged pions vs x. See text for the theory calculations. The left panel corresponds to the SIDIS π^+ production and the right panel is for π^-. This figure is from a manuscript (Ref. [230]) submitted to Phys. Rev. Lett.

- The beam-target double-spin-dependent FSI requires a beam-SSA of SIDIS on an unpolarized proton and for the pion to interact with a polarized spectator neutron through a target-SSA. SIDIS beam-SSA was measured in this experiment to be less than 6%; the neutron target-SSA due to spin-dependent FSI were estimated with a simple Glauber rescattering model to be well below 1% across the entire x range [54]. Therefore the overall effect is suppressed by the sizes of both asymmetries to a negligible level.

6.2.3 Results and Discussions

The extracted neutron $A_{LT}^{\cos(\phi_h-\phi_S)}$ for the π^+ and π^- productions ($A_{LT}^n(\pi^+)$ and $A_{LT}^n(\pi^-)$) are shown in Table 6.4 and Fig. 6-16. They are compared to several model calculations (shown in Sec. 2.5.4), including WW-type approximations with parametrizations from Ref. [106] (Par. 1) and Ref. [106, 107] (Par. 2), a light-cone constituent quark model (LCCQM) [94, 85] and a light-cone quark-diquark model

x	π^+	π^-
0.156	$+0.02 \pm 0.11 \pm 0.03$	$+0.10 \pm 0.07 \pm 0.03$
0.206	$+0.04 \pm 0.13 \pm 0.06$	$+0.18 \pm 0.11 \pm 0.06$
0.265	$-0.13 \pm 0.11 \pm 0.05$	$+0.10 \pm 0.07 \pm 0.02$
0.349	$-0.27 \pm 0.18 \pm 0.13$	$+0.18 \pm 0.10 \pm 0.05$

Table 6.4: Tabulated results for the extracted neutron $A_{LT}^{\cos(\phi_h - \phi_S)}$ asymmetries. The format follows "central value" ± "statistical uncertainty" ± "systematic uncertainty" .

(LCQDM) evaluated using Approach Two[19] in Ref. [82]. While the extracted $A_{LT}^n(\pi^+)$ is consistent with zero within the uncertainties, $A_{LT}^n(\pi^-)$ is consistent in sign with these model predictions but favors a larger magnitude. Sizable asymmetries could be expected for future experiments, including the corresponding SIDIS asymmetries for a proton target and the double-polarized asymmetry in Drell-Yan dilepton production. While the π^+ and π^- data are consistent with the interplay between S-P and P-D wave interference terms predicted by the LCCQM and LCQDM models, the magnitude of the measured π^- asymmetry suggests a larger total contribution from such terms than that found in the LCCQM. The larger magnitude of the data compared to the WW-type calculations suggests a possible different $P_{h\perp}$ dependence of A_{LT} than assumed in the calculations and a possible significant role for subleading-twist effects, or both. The statistical precision and kinematic coverage of the present data cannot distinguish between these scenarios.

As discussed in Sec. 2.4.3.1, many models supported the relation that the two "worm-gear" TMD distributions g_{1T}^q and $h_{1L}^{\perp q}$ take opposite signs, which can be tracked to the assumption of rotational invariance of the nucleon system [101]. The $h_{1L}^{\perp q}$ distribution describes the transverse quark polarization in a longitudinally polarized nucleon and it can be studied by measuring the $\sin 2\phi_h$ dependence of the target single spin asymmetry $A_{UL}^{\sin 2\phi_h}$ using a longitudinally polarized nucleon target. In the

[19]Two approaches on the estimation of the TMDs were introduced in Ref. [82]: Approach One directly calculated the TMD functions using the LCQDM model; Approach Two utilized the information on the unpolarized distributions and the transverse movement dependencies, which were extracted from experimental data using global analyses [80, 60]. The author argued that Approach Two give more reasonable predictions and provided prediction for this experiment according to this approach.

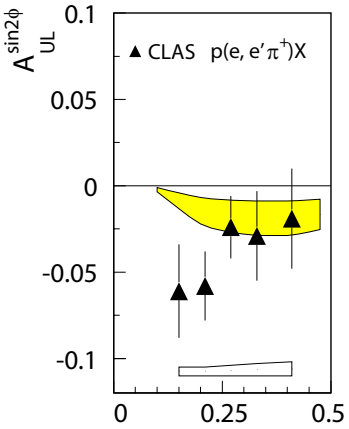

Figure 6-17: $A_{UL}^{\sin 2\phi_h}$ for π^+ production on a longitudinally polarized proton target, measured by the JLab CLAS collaboration with systematics shown in the lower bands. This figure was from Ref. [58]. The yellow band is a prediction using a chiral quark-soliton model [235, 112].

simple quark model (Sec. 2.3.3), $A_{UL}^{\sin 2\phi_h}$ is proportional to the convolution of $h_{1L}^{\perp q}$ and the Collins fragmentation function $H_1^{\perp}$ (Sec. 2.3.2). It is worth noting that the sign of $A_{LT}^{n}(\pi^-)$ suggested by this experiment is opposite to the sign of $A_{UL}^{\sin 2\phi_h}$ in π^+ production on the proton measured by the JLab CLAS collaboration (Fig. 6-17). Although the current precision on both asymmtries are limited, this indication of opposite signs is consistent with many models which support that g_{1T}^{u} and $h_{1L}^{\perp u}$ have opposite signs [101]. Future higher precision measurements [234, 236] will enable a comprehensive study on the relations between g_{1T}^{q} and $h_{1L}^{\perp q}$.

6.3 Probing the Quark Distributions with Naive Quark Models

In this section, the A_{LT} results are interpreted using the parton distributions at the leading-twist and in the leading-order (LO) quark/parton model. At the kinematics for this experiment, SIDIS data and theory tools, which can be used to determine effects beyond this simple approximation, including nuclear effects on ^{3}He, sub-leading twists and higher order effects, are very limited. These effects will be studied using the future high-precision SIDIS measurements following the JLab 12 GeV upgrade [35]

and at an electron-ion collider [36].

6.3.1 Charge Difference Asymmetry

Introduction

The charge-difference asymmetry, a flavor and charge non-singlet observable for which the contribution from exclusive ρ^0 mesons cancels, is defined as

$$A_{LT}^{\pi^+-\pi^-}(\phi_h, \phi_S) \equiv \frac{1}{|P_B S_T|} \frac{(\sigma_{+T}^{\pi^+} - \sigma_{+T}^{\pi^-}) - (\sigma_{-T}^{\pi^+} - \sigma_{-T}^{\pi^-})}{(\sigma_{+T}^{\pi^+} - \sigma_{+T}^{\pi^-}) + (\sigma_{-T}^{\pi^+} - \sigma_{-T}^{\pi^-})} \tag{6.26}$$

$$\approx A_{LT}^{\pi^+-\pi^-} \cos(\phi_h - \phi_S) \ , \tag{6.27}$$

the double spin asymmetry (DSA) in the difference between π^+ and π^- cross sections for opposite beam-helicity states, indicated by $\pm$ subscripts. In the plane-wave impulse approximation, ignoring the small polarization of the protons in ^{3}He and assuming charge symmetry and quark-flavor and hadron-species independent p_T-dependence, this asymmetry probes the combination for the LO valence quark transverse momentum dependent parton distributions (TMD), $4g_{1T}^{d_v} - g_{1T}^{u_v}$ [237]. Under these assumptions and further aid of the simple quark model with the Gaussian ansatz (Appendix A.3), $A_{LT}^{\pi^+-\pi^-}$ is proportional to the valence quark ratio $\left(4g_{1T}^{(1)d_v} - g_{1T}^{(1)u_v}\right) / \left(2f_1^{d_v} + 7f_1^{u_v}\right)$ as Eq. (A.20).

Analysis

$A_{LT}^{\pi^+-\pi^-}$ can also be defined using the cross section ratio of $\pi^\pm$ and the ^{3}He $A_{LT}^{\cos(\phi_h-\phi_S)}$ (Sec. 6.1.5):

$$A_{LT}^{\pi^+-\pi^-} = \frac{\sigma_{UU}^{\pi^+} \cdot A_{LT}^{\cos(\phi_h-\phi_S),\,\pi^+} - \sigma_{UU}^{\pi^-} \cdot A_{LT}^{\cos(\phi_h-\phi_S),\,\pi^-}}{\sigma_{UU}^{\pi^+} - \sigma_{UU}^{\pi^-}} \ , \tag{6.28}$$

where $\sigma_{UU}^{\pi^{+(-)}}$ are the cross sections for $\pi^+(\pi^-)$ production on ^{3}He. The difference of using Eq. (6.27) and Eq. (6.28) are negligible, as shown by a simulated data in

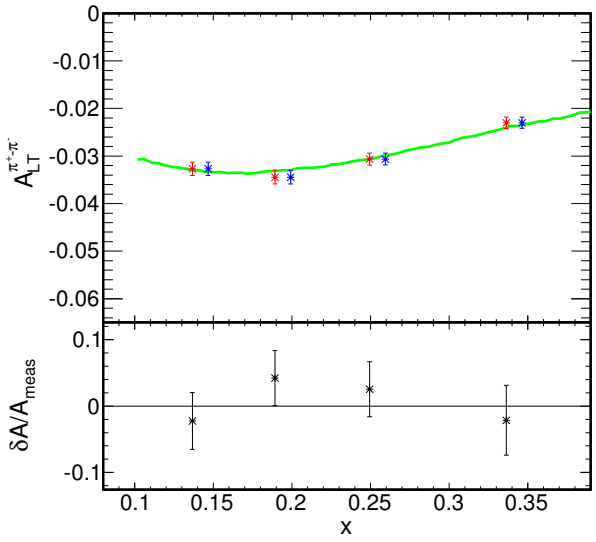

Figure 6-18: Extraction of $A_{LT}^{\pi^+-\pi^-}$ with a high statistics data set simulated by SIMC. The event generator used a WW-type calculation of nucleon $A_{LT}^{\cos(\phi_h-\phi_S)}$ [106, 107] and a simple nuclear model of ^{3}He based on the effective polarization approximation. Top panel: the green curve is the input $A_{LT}^{\pi^+-\pi^-}$ evaluated in fine-grained x-bins; the red and blue (shifted in x) data points were extracted using Eq. (6.27) and Eq. (6.28), respectively. The bottom panel is the relative residual.

Fig. 6-18[20]. This study used SIMC, which is a Monte-Carlo simulation tool developed for this SIDIS measurement as discussed in Sec. 5.4.1. The residual including the simulation uncertainty were quantified as the upper limit of the bin centering effect for $A_{LT}^{\pi^+-\pi^-}$ and included in the systematic uncertainty, $\left|\delta A_{LT}^{\pi^+-\pi^-}/A_{LT}^{\pi^+-\pi^-}\right| \sim 5\%$. Other systematic sources include:

- The major uncertainty was due to the Cahn ($\left|A_{UU}^{\cos\phi_h}\right| \sim 10\%$) and Boer-Mulders ($\left|A_{UU}^{\cos 2\phi_h}\right| \sim 5\%$) modulations of the unpolarized cross section. This effect was studied by introducing A_{UU} in the SIMC simulation as shown in Fig. 6-19. Four combinations of the signs were studied for each effect, and the maximum bias was quoted in the systematic uncertainty: for the smaller-x bins to larger ones, $\left|\delta A_{LT}^{\pi^+-\pi^-}/A_{LT}^{\pi^+-\pi^-}\right|$ =49%, 40%, 33% and 30% due to the Cahn effect, and $\left|\delta A_{LT}^{\pi^+-\pi^-}/A_{LT}^{\pi^+-\pi^-}\right|$ =21%, 18%, 12% and 9% due to the Boer-Mulders effect.

[20] In general, σ_{UU} and $A_{LT}^{\cos(\phi_h-\phi_S)}$ are not statistically independent. However, during the analysis, less than 20% of data were used to extract the ratio, $\sigma_{UU}^{\pi^+}/\sigma_{UU}^{\pi^-}$, which is mostly statistically independent from $A_{LT}^{\cos(\phi_h-\phi_S)}$ based on the full data sets.

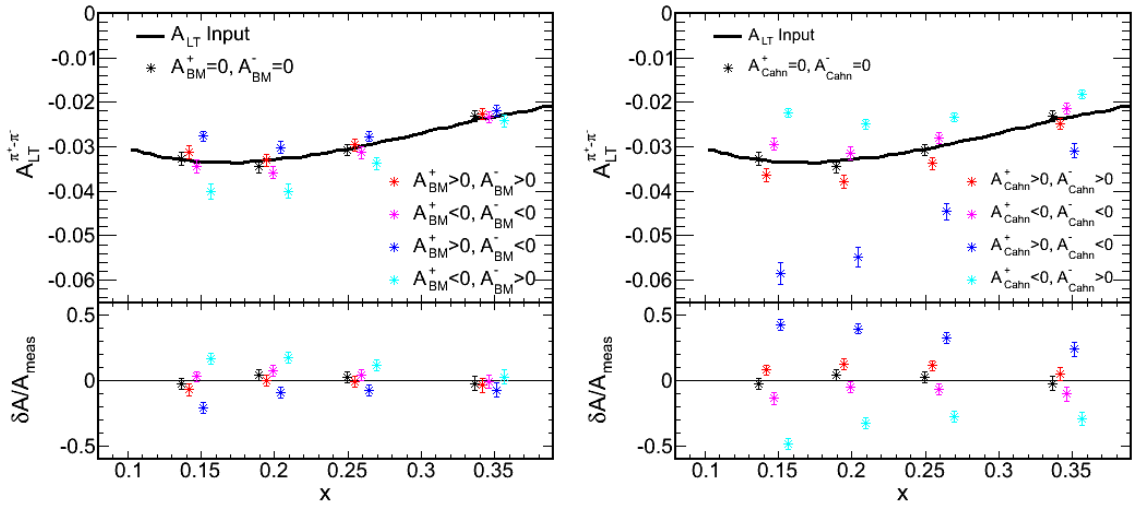

(a) (b)

Figure 6-19: Systematic effects on $A_{LT}^{\pi^+-\pi^-}$ due to (a) Boer-Mulders (BM) effect ($\left|A_{\rm BM}^{\pm}\right| = 10\%$, where $A_{\rm BM} \equiv A_{UU}^{\cos 2\phi_h}$) and (b) Cahn effect ($\left|A_{\rm Cahn}^{\pm}\right| = 5\%$, where $A_{\rm BM} \equiv A_{UU}^{\cos \phi_h}$). The superscript $+(-)$ stand for $\pi^+(\pi^-)$. The color coding is corresponding to the combination of signs, which was studied separately based on a high statistics SIMC simulation. The extracted $A_{LT}^{\pi^+-\pi^-}$ is shown in the top panel and its residual relative to the input $A_{LT}^{\pi^+-\pi^-}$ (thick black curve) was shown in the bottom panel.

- As discussed in Sec. 5.5.5, the unpolarized cross section ratio $\sigma_{UU}^{\pi^+}/\sigma_{UU}^{\pi^-}$ was measured with an systematic uncertainty better than 7% (excluding A_{UU} contributions) by flipping the polarity of the HRS spectrometer.

- The polarimetry introduced systematic uncertainty of $|\delta A_{LT}/A_{LT}| \sim 4.6\%$ for the beam polarization and $|\delta A_{LT}/A_{LT}| \sim 4.9\%$ for the target polarization, consistent with Table 6.2.

- The rest of systematic uncertainties for ^{3}He $A_{LT}^{\cos(\phi_h-\phi_S)}$ were combined using error propagation according to Eq. (6.28).

Results

The preliminary results are shown in Fig. 6-20. The "A_{UU}" band is the uncertainty resulting from the Cahn and Boer-Mulders modulations of the unpolarized cross section, while the "other" band contains all other systematic uncertainty contributions.

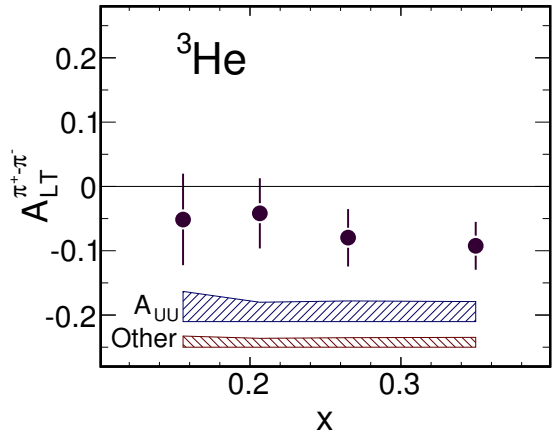

Figure 6-20: The preliminary ^{3}He charge-difference asymmetries, $A_{LT}^{\pi^+-\pi^-}$, vs x. The systematic uncertainties due to the Boer-Mulders (BM) effect ($A_{UU}^{\cos 2\phi_h}$) and the Cahn effect ($A_{UU}^{\cos \phi_h}$) are shown in the top error band (labeled "A_{UU}"), separated from the rest of the systematic uncertainties, which are shown by the lower error band (labeled "Other").

After combining the statistical and systematic uncertainties in quadrature for the highest x-bin, an $1.8\,\sigma$ negative asymmetry is observed . This indication suggests a negative value of $4g_{1T}^{d_v} - g_{1T}^{u_v}$, which is consistent with the sign expected by many model predictions [93, 94, 95, 96, 97, 99, 82, 98] and the pioneering lattice calculations [90, 92].

6.3.2 Naive Extraction of Quark Distribution

As shown in Fig. 2-4, the neutron cross section at the kinematics of experiment E06-010 is dominated by u and d quarks for the three larger-x bins. Besides using the assumptions in the last subsection, if one further *assumes* that the antiquarks and s-quark contributions are negligible, one can solve for the PDF of the u and d quarks based on the two neutron asymmetries $A_{LT}^{n\to\pi^\pm}$ under the naive quark model. More specifically, using Eq. (A.23), the $g_{1T}^{(1)}/f_1$ ratios for u and d quarks were extracted with the following assumptions:

- Leading-order interpretation of SIDIS cross section using transverse momentum dependent parton distributions (TMDs) as in Ref. [41].

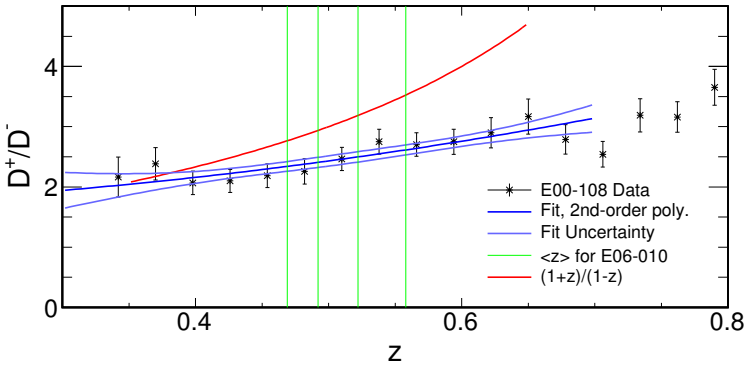

Figure 6-21: The favored and unfavored fragmentation function ratio, $R_D = D^+/D^-$, from the E00-108 data [74] and its fit (see text).

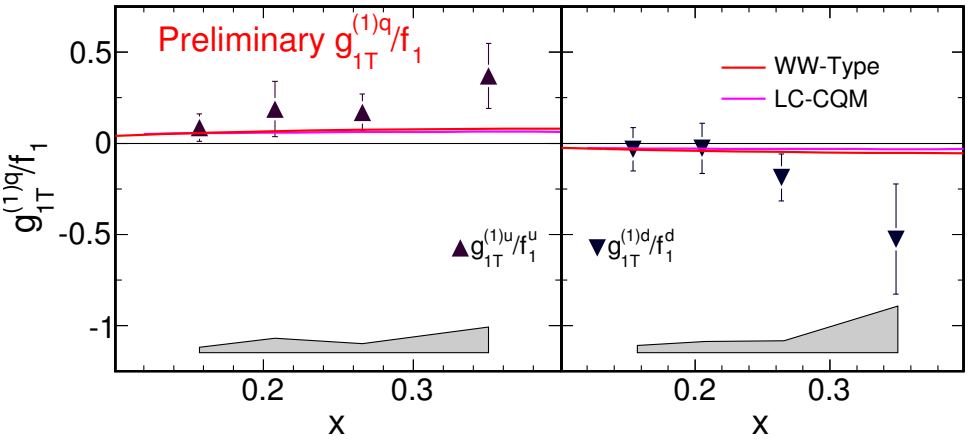

Figure 6-22: Naive extraction of $g_{1T}^{(1)q}/f_1$ based on Eq. (A.23) under the assumptions summarized in the text. The red curves are model calculations using WW-type approximations [107, 106]; the magenta curves were predicted using LCCQM [94, 85]. The left panel is for the u quarks and the right panel is for the d quarks.

- The Gaussian transverse momentum dependencies for TMDs and FFs, which are formulated in Appendix A. The Gaussian widths are assumed to be quark-flavor and hadron-species independent. $\langle p_T^2 \rangle = 0.25(\mathrm{GeV}/c)^2$ and $\langle K_T^2 \rangle = 0.20(\mathrm{GeV}/c)^2$ following the global analysis of [201]. μ_1^2 is assumed to be $0.10\,(\mathrm{GeV}/c)^2$ following A. Prokudin, *et.al.* [107].

- The antiquark contribution is *assumed* to be negligible. This assumption does not necessary hold for the kinematics of this experiment. As shown in Fig. 2-4, the the contribution to the unpolarized cross section from $\bar{u}$ and $\bar{d}$ in the

naive quark model is not larger than 25% for the three larger-x bins and is not larger than 5% for the highest x-bin at $x = 0.35$. The contribution from s and $\bar{s}$ is smaller than 1% for all x-bins. Eq. (A.23), which is the basis for this naive analysis, does not hold with large fractions of antiquark and s-quark contributions. With a significant contributions from $\bar{u}$ and $\bar{d}$, it is corrected to a more complex quark combinations as shown in Eq. (A.24).

- Charge symmetry for the pion fragmentation functions were assumed.

The ratios introduced in Eq. (A.23) were extracted with experimental data:

- $R_D = D^+/D^-$ was interpolated from data of experiment E00-108 [74] in Hall C at Jefferson Lab, which share a similar kinematics region with this measurement. As shown in Fig. 6-21, the data were fit with a second order polynomial and interpolated to an average z for each of the x-bins.

- The π^+ over π^- cross-section ratio on neutron R_σ^n was extracted based on data of this experiment using the cross section ratio of ^{3}He $R_\sigma^{^3\mathrm{He}}$ (also called R as extracted in Sec. 5.5.5) and the proton dilution factor (Sec. 5.5.4) $f_p^{\pi^\pm}$,

$$R_\sigma^n = R_\sigma^{^3\mathrm{He}} \cdot \frac{1 - f_p^{\pi^+}}{1 - f_p^{\pi^-}} \,. \tag{6.29}$$

  The result R_σ^n are close to 1 for this experiment.

The preliminary result is shown in Fig. 6-22. This naive extraction suggests that sign of $g_{1T}^{(1)}/f_1$ is consistent with model predictions [106, 107, 94, 85] for the larger-x bins. The preliminary systematic uncertainties do not include those due to the assumptions listed in the early part of this section, $F_{UU,L}$ and the A_{UU} contributions. This study also hints that the signs of g_{1T}^q are consistent with those of h_1^q [59, 60] as suggested by the QCD Parton Model [102, 103, 104].

6.4 Conclusion

The first measurement of the double spin asymmetry $A_{LT}^{\cos(\phi_h-\phi_S)}$ in semi-inclusive deep-inelastic scattering using a polarized electron beam on a transversely polarized ^{3}He target was discussed. The neutron A_{LT} was also extracted for the first time using the effective polarization approximation. Systematic uncertainties were minimized by forming the raw asymmetry between beam helicity states with minimal charge asymmetry due to the fast helicity reversal. A positive asymmetry was observed for $^3\mathrm{He}\,(e,e'\pi^-)\,X$ and $n\,(e,e'\pi^-)\,X$, providing the first experimental indication of a non-zero A_{LT}, which at leading twist leads to a non-zero g_{1T}^q and a non-zero interference between quark states with different orbital angular momentum. These new data will provide unique information on the quark-flavor decomposition of the transverse momentum dependent parton distribution (TMD), g_{1T}^q, during the future global analysis together with complementary A_{LT} measurements using proton and deuteron targets. In addition, the extracted $A_{LT}^{\pi^+-\pi^-}$ asymmetry suggests a negative sign at large x for the valence quark combination $4g_{1T}^{d_v} - g_{1T}^{u_v}$, which is consistent with the expectations of many models and the pioneering lattice work. This work has laid the foundation for the future high-precision mapping of A_{LT} following the JLab 12 GeV upgrade [35, 233, 234] and at an electron-ion collider [36], which will provide a comprehensive understanding of the g_{1T}^q TMD.

THIS PAGE INTENTIONALLY LEFT BLANK

Chapter 7

Future SIDIS Experiments with the SoLID Device and Polarized ^{3}He Targets

7.1 Overview for the SoLID SIDIS experiments

This thesis work provided the first measurement of the ^{3}He and neutron A_{LT} for SIDIS charged pion productions and laid the foundation for future high precision measurements. Several experiments have been proposed and approved to continue this study in the near future with significant improvement in precision and kinematic coverages. Three of the experiments shares a newly approved Solenoidal Large Intensity Device (SoLID) at JLab Hall A and are planned following the 12 GeV energy upgrade of CEBAF at Jefferson Lab:

- Experiment E12-10-006 (fully approved with full beam time awarded) [233] uses a transversely polarized ^{3}He target and focus on the measurement of target-SSAs. The primary goal is to study the TMD distributions for Sivers, Transversity and Pretzelosity.

- Experiment E12-11-007 (fully approved with full beam time awarded) [234] uses a longitudinally polarized ^{3}He target and studies the worm-gear distributions

(longitudinal transversity $h_{1L}^{\perp}$ and transversal helicity g_{1T}[1]).

- Experiment E12-11-108 (conditionally approved) [238] will use a transversely polarized polarized ammonia (hydrogen) target. The neutron and proton data from E12-10-006 and E12-11-108, respectively, have matching precision, which enables the quark flavor decomposition for the targeted TMDs.

This family of experiments will cover six out of the seven polarized transverse momentum dependent parton distributions (TMD) and will provide high precision data for this study. All asymmetries will be measured with a large kinematic coverage in a 4-D phase space of x, z, $P_{h\perp}$ and Q^2, which is required by the study of nucleon structure in multi-dimensions. The major new instrument, the SoLID detector is largely shared with another approved experiment, which measures the parity violating asymmetry over a broad DIS kinematic region [239]. In this chapter, I will summarize the E12-11-007 experiment [234], which has a direct link to the work presented in this thesis.

7.2 Scientific Case

The scientific motivations for the E12-11-007 experiment were covered in Chapter 2 and is summarized as follows:

- Extracting the "worm-gear" functions (g_{1T} and $h_{1L}^{\perp}$ distribution functions) by measuring the $A_{LT}^{\cos(\phi_h-\phi_S)}$ and $A_{UL}^{\sin 2\phi_h}$ asymmetry with multidimensional binning, respectively. The g_{1T} (or transversal helicity) and $h_{1L}^{\perp}$ (or longitudinal transversity) functions, describe the probability of finding a longitudinally polarized quark inside a transversely polarized nucleon and a transversely polarized quark inside a longitudinally polarized nucleon, respectively. They represent the real part of an interference between nucleon wave functions that differ by one unit of orbital angular momentum, while the imaginary parts are related to the better studied $f_{1T}^{\perp}$ (Sivers functions) and $h_1^{\perp}$ (Boer-Mulders functions) [84, 40].

[1]The majority of the g_{1T} will be shared with Experiment E12-10-006 by requiring a high beam polarization.

- Extracting the p_T^2-moments of the "worm-gear" functions, which were studied in the pioneer lattice QCD work in Refs. [90, 92] using a simplified definition of the distribution functions.

- Testing the WW-type approximations and provide constraints on the Transversity distribution through its link to $h_{1L}^{\perp}$.

- Testing model relations among TMDs: The most simple one of the model relations,

$$g_{1T}^{q} = -h_{1L}^{\perp q} \tag{7.1}$$

  which is flavor-independent, can be tested by this experiment within identical kinematic regions. Pioneering calculations in lattice QCD have indicated that the relation (7.1) may indeed be approximately satisfied [90, 92]. The experimental test that to which extent Eq. (7.1) is conserved or broken indicates the validity of the remaining flavor-independent relations: $h_1^q + \frac{\boldsymbol{k}_\perp^2}{2M^2}\, h_{1T}^{\perp q} = g_{1L}^q$ and $\left(g_{1T}^q\right)^2 + 2h_1^q\, h_{1T}^{\perp q} = 0$. These relations can be further used to make predictions in a generic way for the Pretzelosity distribution, $h_{1T}^{\perp q}$, which is experimentally challenging to measure due to the small predicted asymmetries.

- This experiment will also provide high precision data on the neutron A_{LL} asymmetry. Once included in the global analysis, these results will improve the precision of the polarized PDF for Δd. In addition, existing data [58] and models [240, 107] suggested a $P_{h\perp}$ dependence on A_{LL}. A possible interpretation of the $P_{h\perp}$-dependence of the double-spin asymmetry may involve different widths of the transverse momentum distributions of quarks with different flavor and polarizations [240], which results from the different orbital motion of quarks polarized in the direction of the nucleon spin [241]. The $P_{h\perp}$-dependence of A_{LL} will be mapped by this measurement.

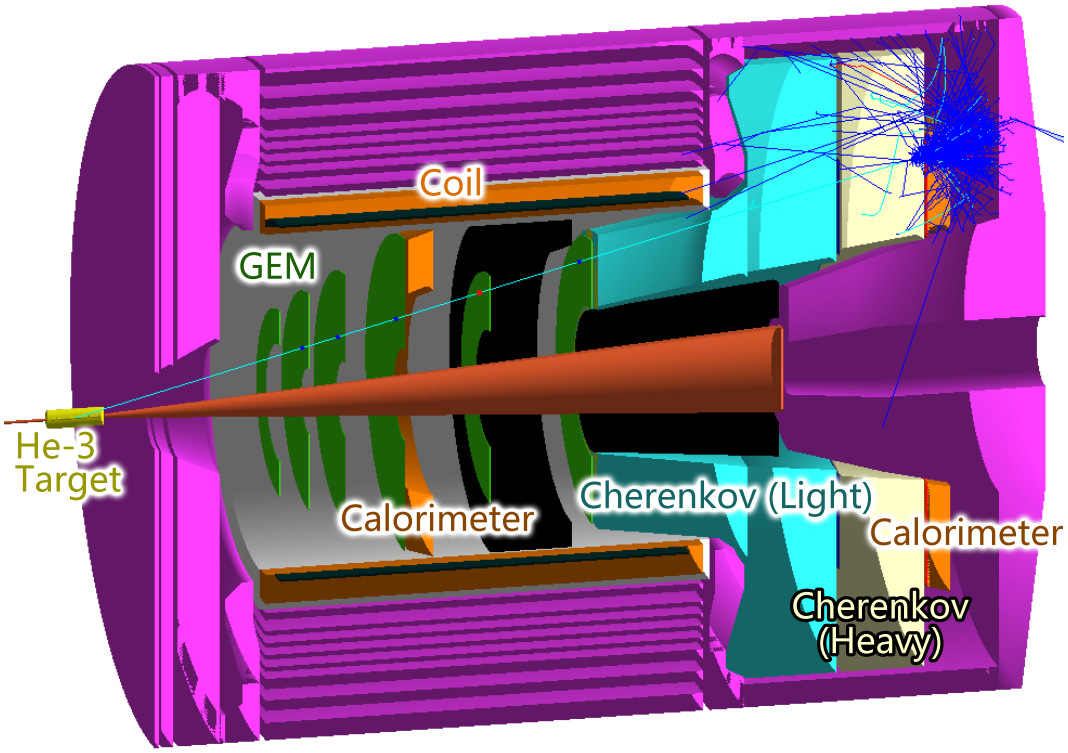

Figure 7-1: The SoLID spectrometer configured for the SIDIS measurement. A electron event is displayed [234, 242]. See text for description of the detectors.

7.3 Experimental Design

To achieve the physics goals, a new generation of polarized SIDIS measurement is required, which will precisely map the targeted asymmetries over a large kinematic space. Therefore, the detector should have large acceptance to take full advantage of the state-of-the-art high luminosity of the polarized ^{3}He target and conserve the azimuthal symmetry to improve the systematic uncertainties. The SoLID spectrometer is being to satisfy the specific needs for this measurement.

The experiment layout is shown in Fig. 7-1. The polarized electron beam scatters on a longitudinally polarized high-luminosity polarized ^{3}He target, located upstream of the spectrometer. Similar to Experiment E06-010, the target spin and beam helicity frequently reverse to reduce the systematic uncertainty due to the acceptance, detector response drift and target density fluctuations. The SoLID spectrometer consists of a superconducting solenoid magnet, a detector system of forward-angle detectors

and large-angle detectors. The acceptance, which is almost rotational symmetric, is divided into large-angle and forward-angle regions. The forward angle detectors cover the polar angle from 6.6 to 12 degrees while the large angle side covers 13 to 22 degrees[2]. Six layers of Gas Electron Multiplier (GEM) detectors [243] will be placed inside the coils to provide charged particle tracking. A combination of an electromagnetic calorimeter, gas Čerenkov counters, a layer of Multi-gap Resistive Plate Chamber (MRPC) [244] and a thin layer of scintillator will be used for particle identification in the forward-angle region. As only electrons are designed to be clearly identified in the large-angle region, a "shashlyk"-type [245] electromagnetic calorimeter will be sufficient to provide the pion rejection. The DAQ system for SoLID will utilize the recently developed high speed, fully pipelined VME Switched Serial (VXS) modules [246] by the Jefferson Lab DAQ group. The estimated rate will be about 50 kHz with a 36 ns coincidence window and the total raw data rate is expected to be 200 MB/s.

To ensure the deep-inelastic criteria, the following kinematic cuts will be used, in consistent with the E06-010 analysis: $Q^2 > 1(\mathrm{GeV}/c)^2$, $W > 2.3\mathrm{GeV}$ and $W' > 1.6\mathrm{GeV}$. The final kinematic coverage is $x = 0.05 - 0.65$, within which $A_{UL}^{\sin 2\phi_h}$ and $A_{LT}^{\cos(\phi_h - \phi_S)}$ are predicted to reach the maximum signals predicted by models (see Fig. 7-2 and 7-3). By combining the data with two beam energies settings (8.8 and 11 GeV), the Q^2 range covers from $1.0 - 8.0(\mathrm{GeV}/c)^2$; $P_{h\perp}$ covers $0 - 1.6\mathrm{GeV}/c$. We choose to detect the leading pions with $0.3 < z < 0.7$ to favor the current fragmentation.

Corresponding data on proton are necessary to provide a comprehensive flavor-decomposition. The longitudinally polarized proton data in a similar kinematic domain was provided by the CLAS collaboration [58]. The precision from that measurement will be significantly improved by the CLAS12 experiment E12-07-107 [236]. A joint global analysis between this experiment and E12-07-107 will provide a good understanding of $h_{1L}^{\perp q}$ with the aid of models. Experiment E12-11-108, which shares

[2]The final angular coverage depends on the final choice of the magnet. This particular number was for the design with the CDF magnet.

the same SoLID setup and uses a transversely polarized proton target, will provide the matching complementary proton data regarding g_{1T}.

7.4 Data Projections

Experiment E12-11-007 was approved for 35 days of beam time with a 15uA beam current and an 85% polarization. In addition, beam polarization for the E12-10-006 experiment (using transversely polarized ^{3}He target) was requested to be 85% to produce high precision data on $A_{LT}^{\cos(\phi_h-\phi_S)}$. The data will be binned in 4-dimensional space of $(x, P_{h\perp}, z, Q^2)$ for more than 1000 kinematic bins. The typical statistical uncertainty for each bin for the neutron will be 0.5% for $A_{UL}^{\sin 2\phi_h}$ and 0.4% for $A_{LT}^{\cos(\phi_h-\phi_S)}$ and for A_{LL} [234]. The systematic uncertainty is expected to be $\delta A/|A| \sim 7\%$, which is minimized by the frequent target spin and beam helicity reversals [234].

For a typical z and Q^2 bin ($0.40 < z < 0.45$, $2\text{GeV}^2 < Q^2 < 3\text{GeV}^2$, one of the forty-eight z-Q^2 bins), data projections are shown in Figs. 7-2 and 7-3, for $A_{UL}^{\sin 2\phi_h}$ and $A_{LT}^{\cos(\phi_h-\phi_S)}$, respectively. For each plot, the center of each red point corresponds to the kinematics center of each x and $P_{h\perp}$ bin and the error bar corresponds to the statistical uncertainty of the asymmetry for each 4-dimensional $(x, P_{h\perp}, z, Q^2)$ bin. The scale of the asymmetries and uncertainties are shown on the right side axis. For the model predictions: the *blue curve* is predicted by a light-cone constituent quark models [94, 85]; the *black curve* is based on a light-cone quark-diquark model [247, 82]; The *magenta dash-dot curve* is a prediction based on the WW-type relations [107, 105, 106]. All theory predictions are integrated over $P_{h\perp}$. The E06-010 results on $A_{LT}^{\cos(\phi_h-\phi_S)}$ are also shown on Fig. 7-3. Full projections for all bins and all targeted asymmetries can be found in Appendix B of Ref. [234] and similar coverages and precision as that shown in Fig. 7-3 will be archived for each of the targeted asymmetries.

7.5 Summary

In summary, as the next generation for this thesis experiment, the SoLID family of experiments, in particular the E12-11-007 [234] will provide comprehensive experimental information on the poorly constrained "worm-gear" TMDs using the high luminosity polarized ^{3}He target. Experiment E12-11-007 will provide the first data on SIDIS target-SSA with a longitudinally polarized effective neutron target. The systematic uncertainties are minimized by using fast target spin flips and a symmetric coverage in the azimuthal angles. All targeted asymmetries will be measured with a high precision and a large kinematic coverage in a 4-D phase space of x, z, $P_{h\perp}$ and Q^2 to allow a model independent extraction of the the g_{1T} and $h_{1L}^{\perp}$ distribution functions and therefore provide comprehensive information on the correlations between quark spin and its orbital motion in the nucleon.

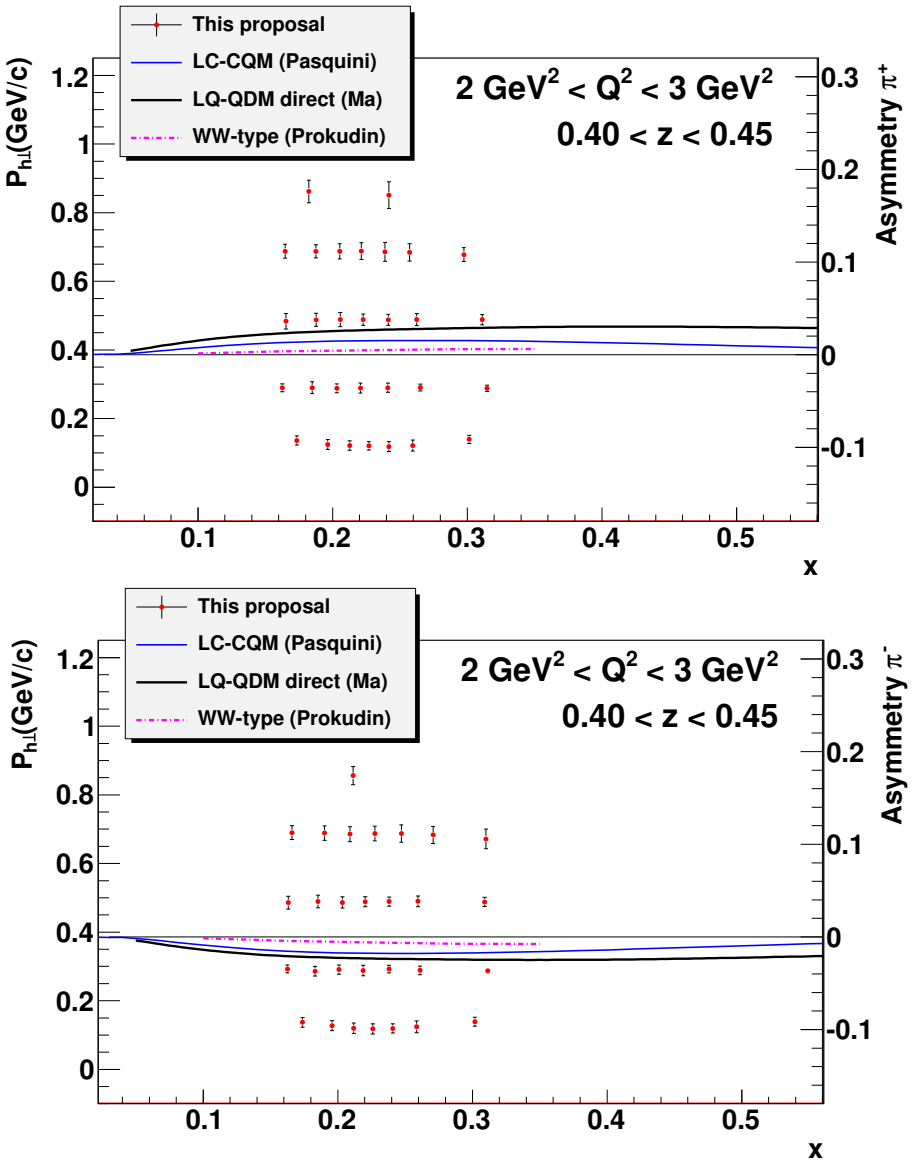

Figure 7-2: Projections of $A_{UL}^{\sin 2\phi_h}$ for coincidence $e'\pi^+$ channel (upper plot) and $e'\pi^-$ channel (lower plot) in one of the forty-eight z and Q^2 bins.

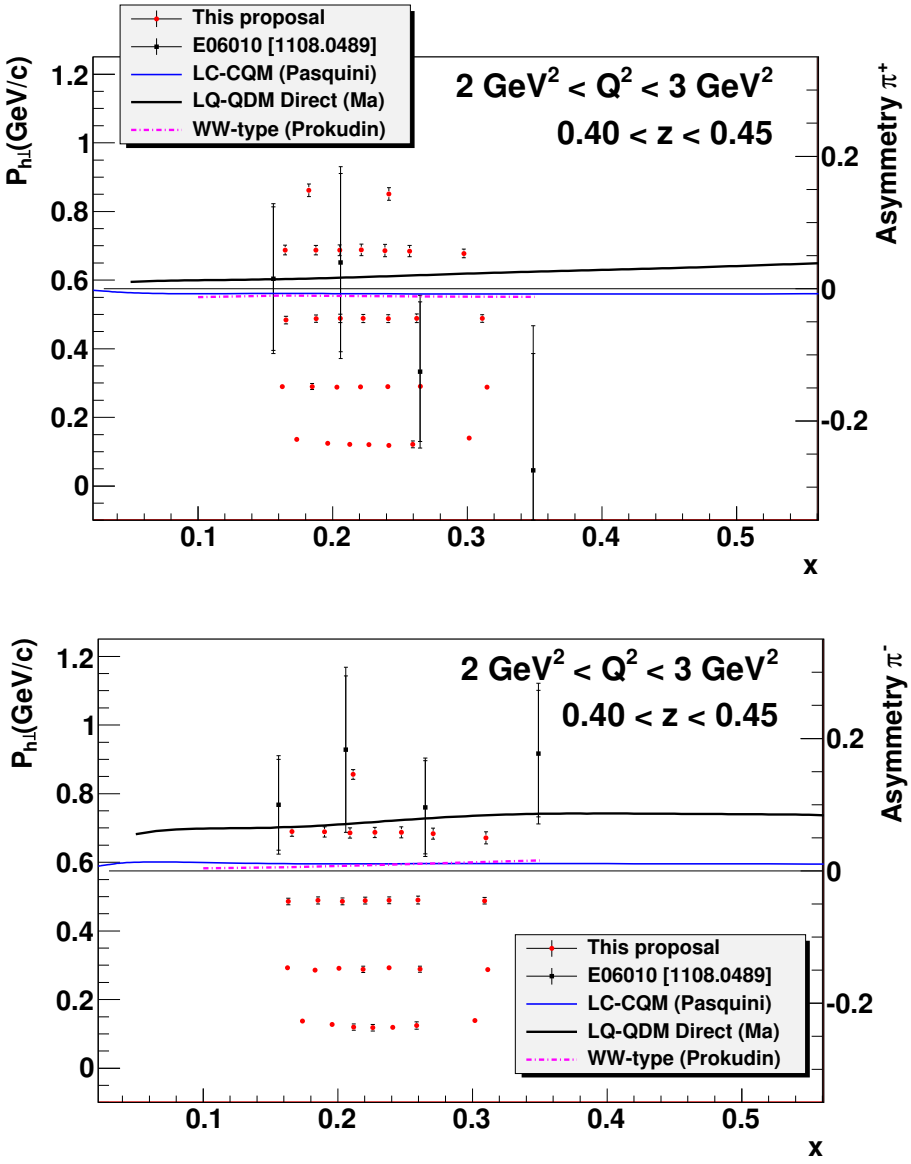

Figure 7-3: Projections of $A_{LT}^{\cos(\phi_h - \phi_S)}$ for coincidence$e'\pi^+$ channel (upper plot) and $e'\pi^-$ channel (lower plot) in one of the forty-eight z and Q^2 bins.

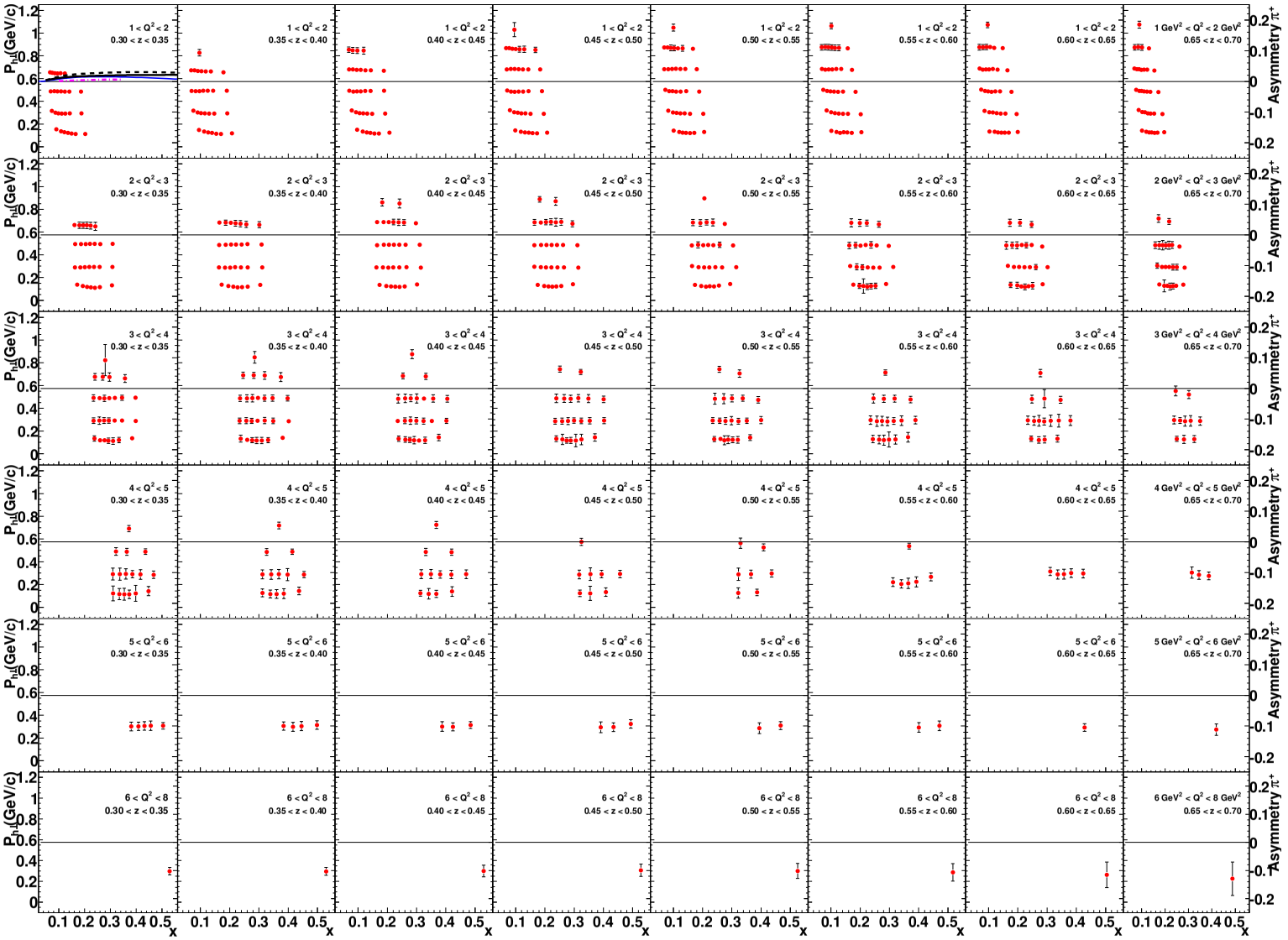

Figure 7-4: Projections of $A_{UL}^{\sin 2\phi_h}$ for coincidence $e'\pi^+$ channel for all z and Q^2 bins. The legend for these plots is identical to that of Fig. 7-2. Full projections for the other five targeted asymmetries can be found in Appendix B of Ref. [234].

Appendix A

Related Formulas

This appendix contains TMD related formulas frequently used in the thesis.

A.1 Definition of TMD Distributions Using Quark-Quark Correlation Function

In this section, I briefly summarize the definition of leading-twist TMDs using the decomposition of the quark-quark correlation function, as shown in Refs. [37, 38] and in a review [39] with a complete parametrization. The quark-quark correlation function for a spin one-half target is defined in a matrix form as

$$\Phi_{ij}(P,p,S) = \int \frac{d^4\xi}{(2\pi)^4}\, e^{ip\cdot\xi}\, \langle P,S \,|\, \bar{\psi}_j(0)\, \mathcal{W}(0,\xi)\, \psi_i(\xi) \,|\, P,S\rangle\,, \tag{A.1}$$

where ψ is the quark field. The target state is characterized by its four-momentum P and the covariant spin vector S. As discussed in details in Ref. [42], the covariant spin vector was defined following $S^2 = -1,\ P\cdot S = 0$. p denotes the momentum of the quark. The Wilson line $\mathcal{W}(0,\xi|n_-)$ guarantees color gauge invariance of the correlator [40, 41]. The transverse momentum dependent ($\boldsymbol{p}_T$-dependent) correlator,

$$\Phi(x,\boldsymbol{p}_T,S) = \int dk^-\, \Phi(P,p,S)\,, \tag{A.2}$$

enters the description of hard scattering processes like semi-inclusive DIS and the Drell-Yan process. The $\boldsymbol{p}_T$-dependent correlator can be specified in terms of all possible Dirac traces Γ, $\Phi^{[\Gamma]} = \mathrm{Tr}[\Phi(x, \boldsymbol{p}_T, S)\,\Gamma]$. The leading-twist terms contain eight independent scalar amplitudes, which are know as the leading-twist TMDs:

$$\Phi^{[\gamma^+]} = f_1 - \frac{\epsilon_T^{\rho\sigma} p_{T\rho} S_{T\sigma}}{M} f_{1T}^{\perp}\,, \tag{A.3}$$

$$\Phi^{[\gamma^+\gamma_5]} = S_L\, g_{1L} - \frac{p_T \cdot S_T}{M}\, g_{1T}\,, \tag{A.4}$$

$$\begin{aligned}\Phi^{[i\sigma^{\alpha+}\gamma_5]} &= S_T^{\alpha}\, h_1 + S_L\, \frac{p_T^{\alpha}}{M}\, h_{1L}^{\perp} \\ &\quad - \frac{p_T^{\alpha} p_T \cdot S_T - \frac{1}{2}\, p_T^2\, S_T^{\alpha}}{M^2}\, h_{1T}^{\perp} - \frac{\epsilon_T^{\alpha\rho} p_{T\rho}}{M}\, h_1^{\perp}\,,\end{aligned} \tag{A.5}$$

where α is restricted to be transverse indices in the light-cone coordinates and $\varepsilon_T^{ij} \equiv \varepsilon^{-+ij}$. S_L and S_T are the longitudinal and transverse components of the covariant spin vector with respect to the momentum of the nucleon [41][1], respectively.

A.2 Weighted TMDs and FFs

For convenience in the discussions, $\boldsymbol{p}_T$-moments of a general TMDs, $f^q(x, p_T^2)$, and FFs, $D^q(z, K_T^2)$, are defined [2] as follows:

$$f^q(x) \equiv \int d^2\boldsymbol{p}_T f^q(x, p_T^2)\,, \tag{A.6}$$

$$f^{q(n)}(x) \equiv \int d^2\boldsymbol{p}_T \left(\frac{p_T^2}{2M^2}\right)^n f^q(x, p_T^2)\,, \tag{A.7}$$

$$D(z) \equiv \int d^2\boldsymbol{K}_T D^q(z, K_T^2)\,, \tag{A.8}$$

$$D^{(n)}(z) \equiv \int d^2\boldsymbol{K}_T \left(\frac{K_T^2}{4z^2 M_h^2}\right)^n D^q(z, K_T^2)\,, \tag{A.9}$$

[1] S_L and S_T defined in this section is different from those used in Sec. 2.2, where they are defined with respect to the virtual photon direction. The difference is on the order of $1/Q^2$ and $1/Q$ for S_L and S_T [41], respectively.

[2] Using, e.g., a Gaussian parametrization of the transverse momentum dependence as a working assumption, the integrals for the TMD moments are well-defined.

where n is a positive half integer.

A.3 Gaussian Ansatz of the Transverse Momentum Dependence

Gaussian functions are a common ansatz for the transverse momentum dependence of TMDs and FFs [201, 248, 240, 106, 249, 107], i.e.

$$f_1(x,p_T^2) = f_1(x)\frac{1}{\pi\langle p_T^2\rangle}\exp\left(-\frac{p_T^2}{\langle p_T^2\rangle}\right) \quad (A.10)$$

$$D_1(z,K_T^2) = D_1(z)\frac{1}{\pi\langle K_T^2\rangle}\exp\left(-\frac{K_T^2}{\langle K_T^2\rangle}\right) \quad (A.11)$$

$$g_{1T}(x,p_T^2) = g_{1T}(x)\frac{1}{\pi\mu_1^2}\exp\left(-\frac{p_T^2}{\mu_1^2}\right) \quad (A.12)$$

$$= g_{1T}^{(1)}(x)\frac{2M^2}{\pi\mu_1^4}\exp\left(-\frac{p_T^2}{\mu_1^2}\right) \quad (A.13)$$

$$g_{1L}(x,p_T^2) = g_{1L}(x)\frac{1}{\pi\mu_2^2}\exp\left(-\frac{p_T^2}{\mu_2^2}\right) \quad (A.14)$$

where $\langle p_T^2\rangle$ and $\langle K_T^2\rangle$ were studied through global analysis in Ref. [201, 248, 249] and the Lattice QCD calculations [92]. In principal these Gaussian width factors can be quark flavor dependence. However they were assumed to be flavor independent following the theory study of Ref. [106, 59, 60]. There is still no experimental study on μ_1^2. The best fit on the CLAS data of π^+ production on a longitudinally polarized proton target yielded that $\mu_2^2/\langle p_T^2\rangle = 0.7\pm0.1$ with χ^2/d.o.f.=1.5 [58].

With this assumption, the convolution in SFs (Sec. 2.3.3) can be integrated analytically

$$F_{UU,T} = \left[f_1\otimes D_1\right]$$
$$= \frac{1}{\pi\left(\langle K_T^2\rangle + \langle p_T^2\rangle z^2\right)}\exp\left(-\frac{P_{h\perp}^2}{\langle K_T^2\rangle + \langle p_T^2\rangle z^2}\right)\sum_q e_q^2 f_1^q(x)D_1^q(z)$$

$$F_{LT}^{\cos(\phi_h-\phi_S)} = \left[\frac{\hat{\boldsymbol{h}}\cdot\boldsymbol{p}_T}{M}g_{1T}\otimes D_1\right]$$

$$= \frac{2Mz\ |\boldsymbol{P}_{h\perp}|}{\pi\left(\langle K_T^2\rangle + \mu_1^2 z^2\right)^2} \exp\left(-\frac{P_{h\perp}^2}{\langle K_T^2\rangle + \mu_1^2 z^2}\right) \sum_q e_q^2 g_{1T}^{(1)q}(x) D_1^q(z)\,.$$

$A_{LT}^{\cos(\phi_h-\phi_S)}$ as function of $(x, y, z, P_{h\perp})$ could be expressed as a function of $g_{1T}^{(1)}(x)$, $f_1(x)$ and $D_1(z)$ [106, 107], similar to Equation 2.37,

$$\begin{aligned}
A_{LT}(x,y,z,|P_{h\perp}|) &= \sqrt{1-\varepsilon^2}\,\frac{F_{LT}^{\cos(\phi_h-\phi_S)}}{(1+\varepsilon R)\ F_{UU,T}} \\
&= \mathcal{N}\,|\boldsymbol{P}_{h\perp}| \exp\left(-P_{h\perp}^2 W_{P_{h\perp}^2}\right) \frac{\sum_q e_q^2 g_{1T}^{(1)q}(x) D_1^q(z)}{\sum_q e_q^2 f_1^q(x) D_1^q(z)} \qquad \text{(A.15)} \\
\mathcal{N} &\equiv 2Mz \frac{1}{1+\varepsilon R} \frac{(2-y)\,y}{1+(1-y)^2} \frac{\langle K_T^2\rangle + \langle p_T^2\rangle\, z^2}{\left(\langle K_T^2\rangle + \mu_1^2 z^2\right)^2} \qquad \text{(A.16)} \\
W_{P_{h\perp}^2} &\equiv \frac{1}{\langle K_T^2\rangle + \mu_1^2 z^2} - \frac{1}{\langle K_T^2\rangle + \langle p_T^2\rangle\, z^2}\,, \qquad \text{(A.17)}
\end{aligned}$$

where $\frac{(2-y)y}{1+(1-y)^2}$ is an approximation of the depolarization factor $\sqrt{1-\varepsilon^2}$ at the $\gamma = \frac{2Mx}{Q} \to 0$ limit.

Eq. (A.15) can also be expressed as function of an unweighted $g_{1T}(x)$. However, it is easier for the theory comparisons to extract weighted functions, which were predicted by a Lattice calculation [90, 92], Lorentz Invariance Relations [105, 106, 107] and a light-cone model [94, 85]. With assumptions on the parametrization, Eq. (A.15) can be illustrated in Fig. A-1. Similar approach can be used to calculate $A_{LL}(x, y, z, |P_{h\perp}|)$:

$$\begin{aligned}
A_{LL}(x,y,z,|P_{h\perp}|) &= \frac{\langle K_T^2\rangle + \langle p_T^2\rangle\, z^2}{\langle K_T^2\rangle + \mu_2^2 z^2} \exp\left[-P_{h\perp}^2\left(\frac{1}{\langle K_T^2\rangle + \mu_2^2 z^2} - \frac{1}{\langle K_T^2\rangle + \langle p_T^2\rangle\, z^2}\right)\right] \\
&\quad \times \frac{\sum_q e_q^2 g_{1L}^q(x) D_1^q(z)}{\sum_q e_q^2 f_1^q(x) D_1^q(z)} \qquad \text{(A.18)}
\end{aligned}$$

In the plane-wave impulse approximation, ignoring the small polarization of the protons in ^{3}He (i.e. $F_{LT}^{\cos(\phi_h-\phi_S)}\,(^3\text{He} \to \pi^\pm) \approx P_n \cdot F_{LT}^{\cos(\phi_h-\phi_S)}\,(n \to \pi^\pm)$) and assuming charge symmetry, isospin symmetry for the pion fragmentation functions, the ^{3}He charge difference asymmetry as defined in Eq. (6.27) can be expressed using a simple

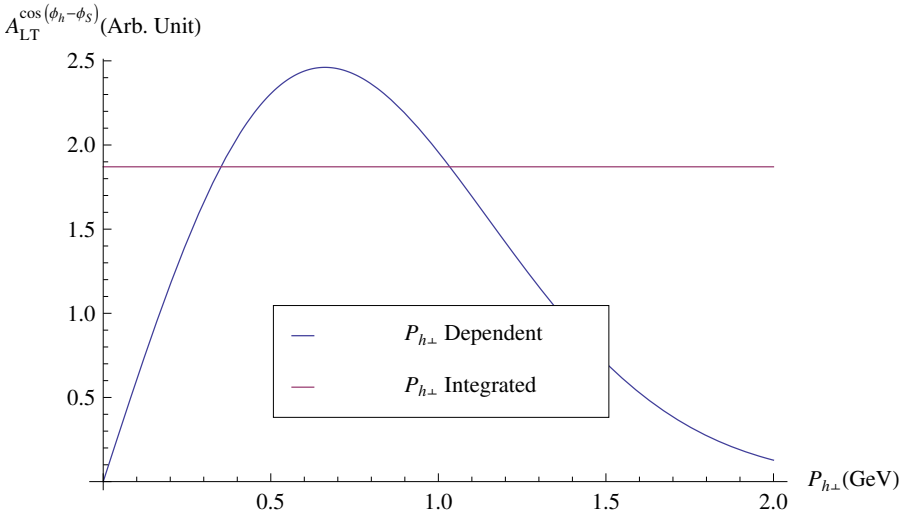

Figure A-1: Illustration of the transverse momentum dependence of $A_{LT}^{\cos(\phi_h-\phi_S)}$ using the Gaussian Ansatz as Eq. (A.15), where $\langle p_T^2\rangle = 0.38\,(\mathrm{GeV})^2$ and $\langle K_T^2\rangle = 0.16\,(\mathrm{GeV})^2$ following the global analysis of [249]. μ_1^2 was assumed to be $0.15\,(\mathrm{GeV})^2$ following A. Prokudin, *et.al.* [106]. $z = 0.5$ was used, following the approximate kinematic center of experiment E06-010. The relative value of the $P_{h\perp}$ integrated $A_{LT}^{\cos(\phi_h-\phi_S)}$ is also drawn as the horizontal line.

ratio of valence quark TMDs with these Gaussian ansatzes:

$$A_{LT}^{\pi^+-\pi^-} \approx P_n \frac{\sqrt{1-\varepsilon^2}}{(1+\varepsilon R)} \frac{F_{LT}^{\cos(\phi_h-\phi_S)}\left(n\to\pi^+\right) - F_{LT}^{\cos(\phi_h-\phi_S)}\left(n\to\pi^-\right)}{F_{UU,T}\left({}^3\mathrm{He}\to\pi^+\right) - F_{UU,T}\left({}^3\mathrm{He}\to\pi^-\right)} \quad \text{(A.19)}$$

$$= P_n \cdot \mathcal{N} \cdot |\boldsymbol{P}_{h\perp}| \cdot \exp\left(-P_{h\perp}^2 W_{P_{h\perp}^2}\right) \frac{4g_{1T}^{(1)d_v} - g_{1T}^{(1)u_v}}{2f_1^{d_v} + 7f_1^{u_v}} \quad \text{(A.20)}$$

where the valance PDF $f^{q_v} \equiv f^{q_v} - f^{\bar{q}}$ which is defined for both f_1^q and $g_{1T}^{(1)q}$.

A.4 TMD Extraction with a Naive Model

During E06-010, the kinematic acceptance is limited within a single x-bin. Therefore, to leading order, $A_{LT}^{\cos(\phi_h-\phi_S)}$ measured at each bin could be considered as corresponding asymmetry of kinematics center $(\langle x\rangle, \langle y\rangle, \langle z\rangle, \langle P_{h\perp}\rangle)$. Also we further naively *assume* the contribution from the antiquarks and the s quarks is negligible (noted as

$\bar{q} \to 0$ together) in the E06-010 kinematics. Then Eq. A.15 can be simplified to

$$A_{LT}^{n\to\pi^\pm} \overset{\bar{q}\to 0}{=} \mathcal{N}\,|P_{h\perp}| \exp\left(-P_{h\perp}^2 W_{P_{h\perp}^2}\right) \frac{e_d^2 g_{1T}^{(1)u} D_1^\mp + e_u^2 g_{1T}^{(1)d} D_1^\pm}{e_d^2 f_1^u D_1^\mp + e_u^2 f_1^d D_1^\pm} \tag{A.21}$$

where $u(d)$ are quarks flavor in proton, $D_1^\pm$ are the flavored/unflavored pion FFs.

Therefore, with further inputs of ratio

$$\begin{aligned} R_D &= \frac{D_1^+}{D_1^-} \\ R_\sigma^n &= \frac{\sigma^{n\to\pi^+}}{\sigma^{n\to\pi^-}} \\ &\overset{\bar{q}\to 0}{=} \frac{e_d^2 f_1^u D_1^- + e_u^2 f_1^d D_1^+}{e_d^2 f_1^u D_1^- + e_u^2 f_1^d D_1^+} \end{aligned} \tag{A.22}$$

g_{1T} functions could be extracted as ratio to f_1

$$\begin{aligned} \left(\frac{g_{1T}^{(1)u}}{f_1^u}\right)_{\bar{q}\to 0} &= \mathcal{N}' \frac{R_\sigma^n A_{LT}^{n\to\pi^+} - R_D A_{LT}^{n\to\pi^-}}{R_\sigma^n - R_D} \\ \left(\frac{g_{1T}^{(1)d}}{f_1^d}\right)_{\bar{q}\to 0} &= \mathcal{N}' \frac{R_D R_\sigma^n A_{LT}^{n\to\pi^+} - A_{LT}^{n\to\pi^-}}{R_D R_\sigma^n - 1} \\ \mathcal{N}' &= \left(\mathcal{N}\,|\boldsymbol{P}_{h\perp}| \exp\left(-P_{h\perp}^2 W_{P_{h\perp}^2}\right)\right)^{-1} \end{aligned} \tag{A.23}$$

For the E06-010 kinematics, $R_D \approx 3$ and $R_\sigma \approx 1$, which ensured sensitivity in this extraction by avoiding a near zero denominator.

As shown in Fig. 2-4, the contribution from the $\bar{u}$ and $\bar{d}$ is not necessary small for the E06-010 experiment, while the contribution from s and $\bar{s}$ is smaller than 1% for all x-bins. The quark interpretation of the on the left sides of Eqs. (A.23) is modified when the $\bar{u}$ and $\bar{d}$ are not negligible:

$$\begin{aligned} \left(\frac{g_{1T}^{(1)u}}{f_1^u}\right)_{\bar{q}\to 0} &\to \left(\frac{e_d^2 g_{1T}^{(1)u} + e_u^2 g_{1T}^{(1)\bar{d}}}{e_d^2 f_1^u + e_u^2 f_1^{\bar{d}}}\right)_{s,\bar{s}\to 0} \\ \left(\frac{g_{1T}^{(1)d}}{f_1^d}\right)_{\bar{q}\to 0} &\to \left(\frac{e_u^2 g_{1T}^{(1)d} + e_u^2 g_{1T}^{(1)\bar{u}}}{e_u^2 f_1^d + e_u^2 f_1^{\bar{u}}}\right)_{s,\bar{s}\to 0} \end{aligned} \tag{A.24}$$

Appendix B

Collection of Experimental Records

B.1 Left-HRS Sieve Slit

A removable Sieve slit was used to calibrate angular reconstruction for the Left-HRS. The slit and its mount are shown in Fig. B-1 and B-2, respectively. The sieve slit is shown as the yellow plate before the HRS entrance in Fig. B-4.

B.2 Survey Report

The offset for the Left-HRS spectrometer and its sieve slit were surveyed as shown in Fig. B-3.

B.3 Target Material and Thickness

The 3-D model of the target area is shown in Fig. B-4, where the thickness and calculated collision energy loss is summarized in Tab. B.1.

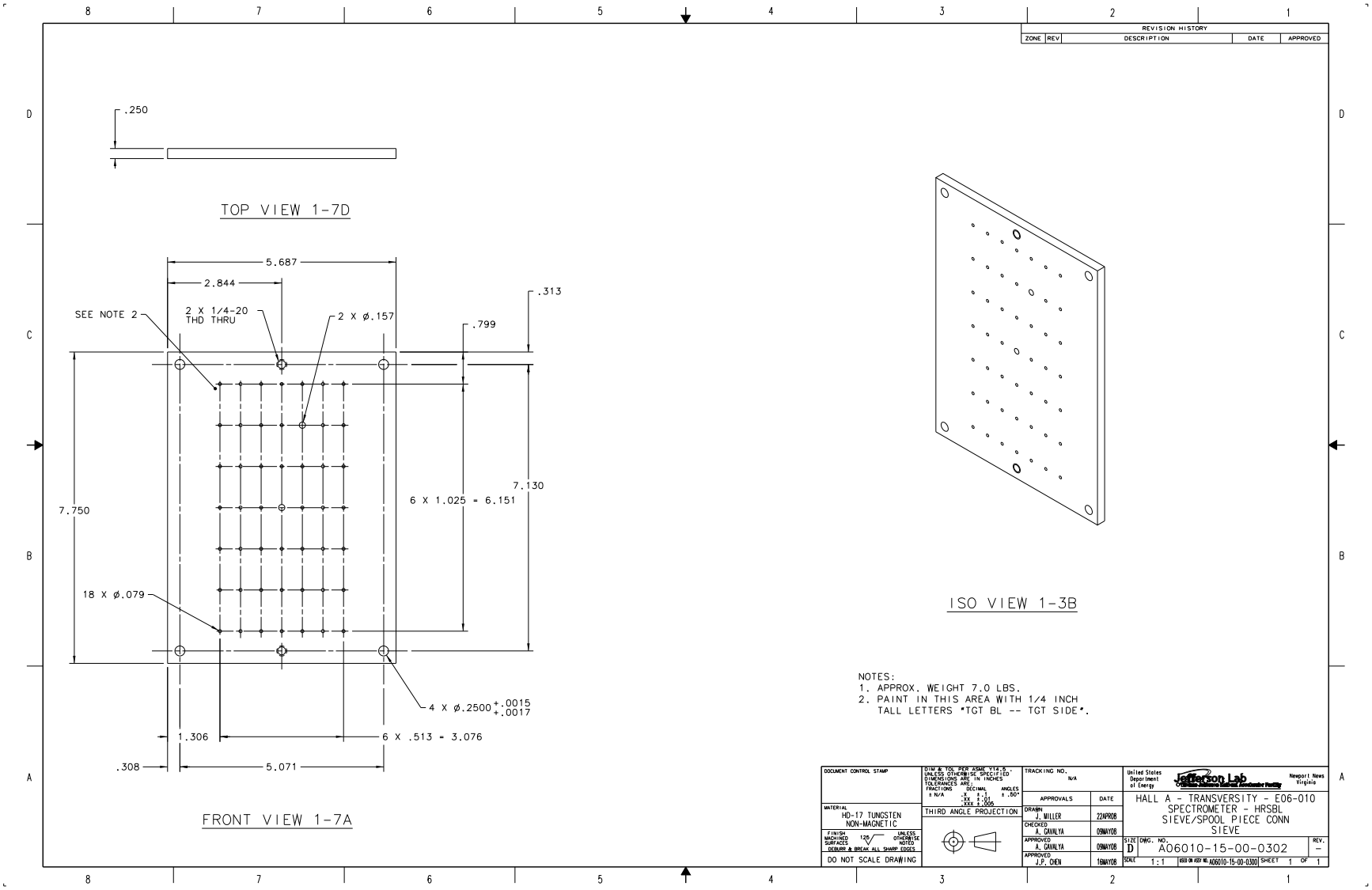

Figure B-1: Left-HRS sieve slit

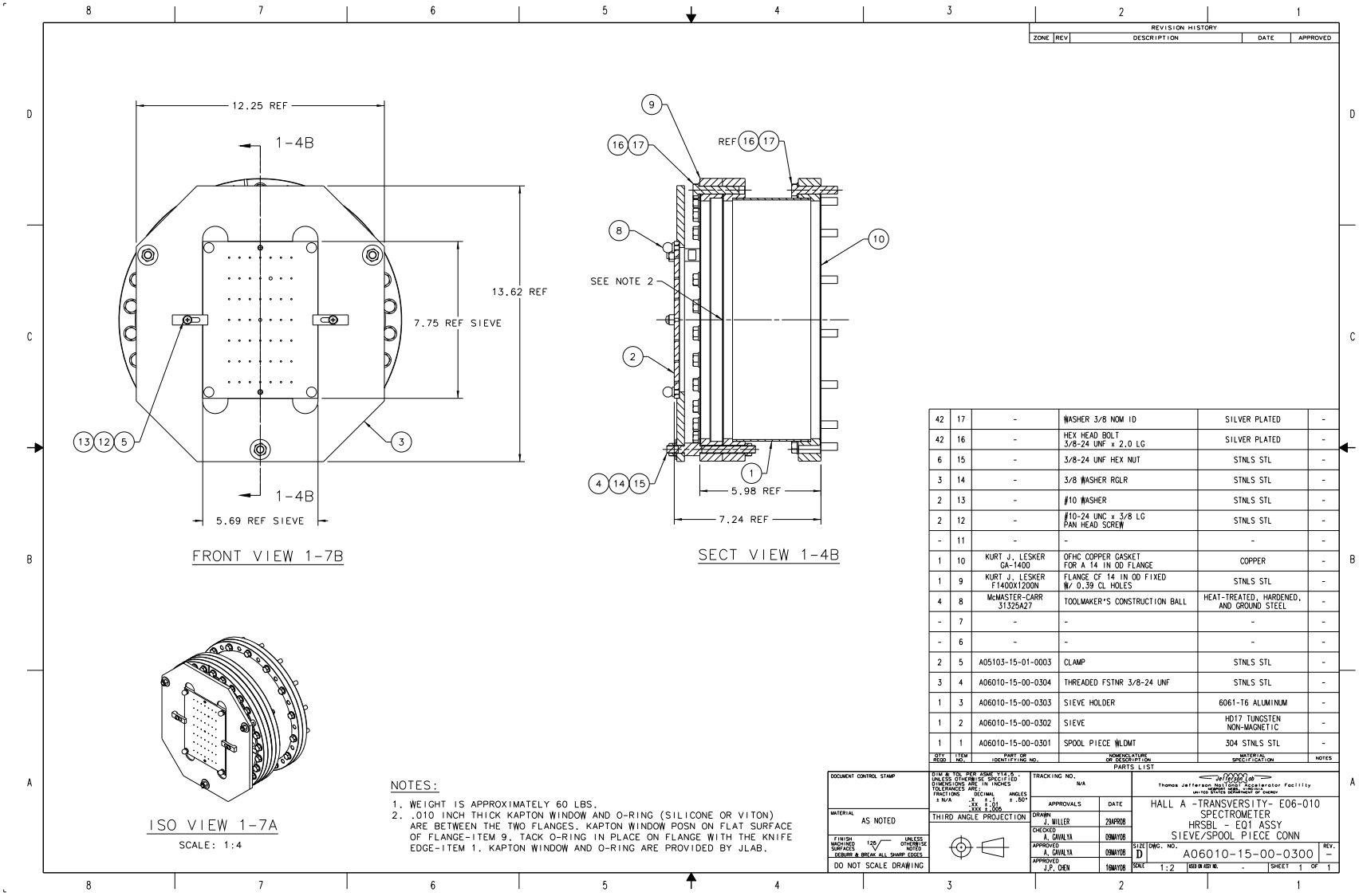

Figure B-2: Mount for the Left-HRS sieve slit

Jefferson Lab Alignment Group

Data Transmittal

TO: J.P. Chen, J. LeRose		**DATE:** 23 Oct 2008
FROM: Chris Curtis	**Checked:**	**# :** A1189

DETAILS:

Below are the results from the survey of the left spectrometer, the new spectrometer slits, superharps, calorimeter and the BCM carried out on 14th October, 2008. The values represent the difference in millimeters from the ideal position of each fiducial, except for the calorimeter which represents the centerline. A positive X value is to the beam left, a positive Y is too high.

========== RESULTS ========== E101408A

The central ray of the spectrometer is at -15.993 degrees.
It is missing the defined target center by 1.63 mm upstream,
and 0.98 mm vertically (positive = up).

If the offset is corrected by secondary alignment, the
spectrometer will be at -16.004 degrees.

*.9PR : 0.128 *.3DD : 2.01

Spectrometer Slit: (DX/DY from spectrometer centerline; DZ from target)

	DX	DY	DZ
	-0.34	4.49	1157

Superharps

	DX	DY
SH1H01A	0.11	0.00
SH1H01B	0.19	-0.01
SH1H01C	0.22	0.03
SH1H02A	-0.78	-0.20
SH1H02B	-0.72	-0.18
SH1H02C	-0.73	-0.14

Cavity BPMs

BCM1H1B	0.07	-0.44
BCM1H1C	0.02	-0.35
BCM1H2A	-0.82	-0.29
BCM1H2D	-0.29	-0.32

Calorimeter

IFY1H04	-0.35	-0.33

Figure B-3: Survey report A1189, which included the HRS pointing offset and sieve slit offset.

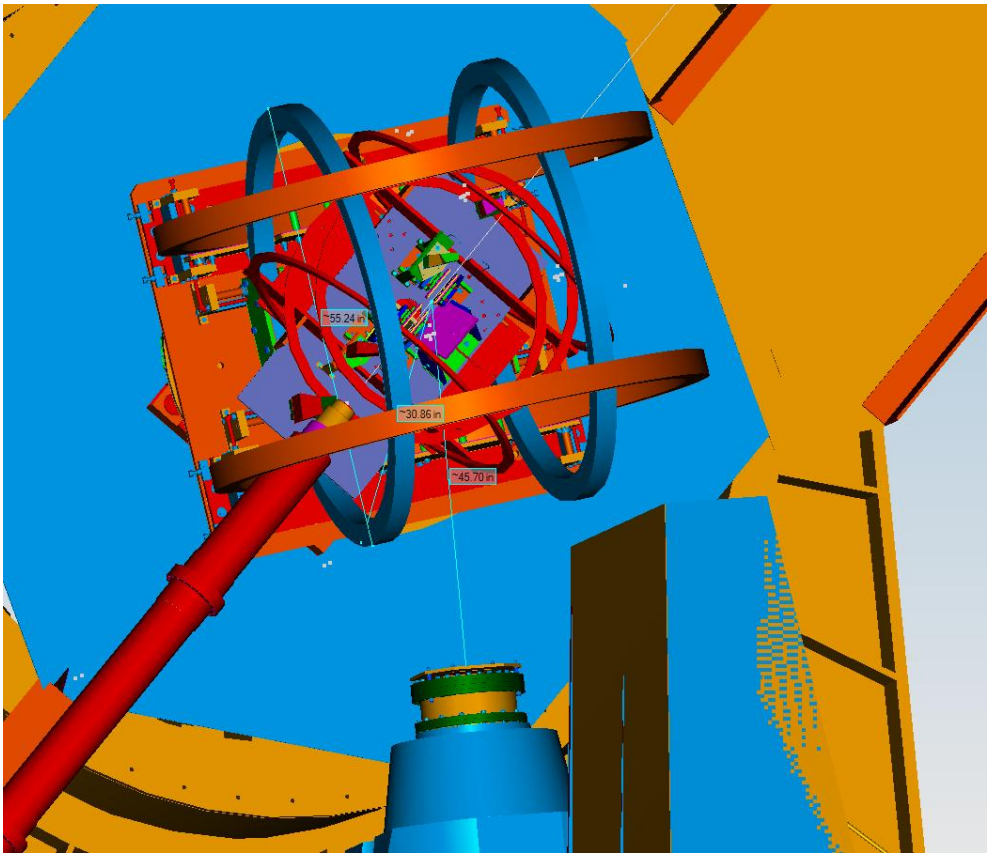

Figure B-4: Target setup and approximate distances. The beam came from top right corner and the upstream beam pipe, which exits through the Be beam window, is not drawn. The center is the targets ladder (Sec. 4.2.4.2). The G11/FR5 target enclosure was mounted on the coils, which was filled with ^{4}He gas. The Left HRS entrance was on the right bottom side, which was covered by an Kapton entrance window.

Material	Unit Loss [250] $\text{MeV} \cdot \text{g}^{-1} \cdot \text{cm}^{-2}$	Density $\text{g} \cdot \text{cm}^{-2}$	Thickness cm	Collision Loss MeV
Be, Beam Window	1.91	1.9	0.025	0.09
BeO, Foil Target	2.02	3.0	0.071	0.43
Carbon, Foil Target	2.13	1.7	0.027	0.11
^{3}He Gas, per ATM per cm	3.79	1.3×10^{-4}	-	4.8×10^{-4}
^{4}He Gas, per ATM per cm	2.85	1.7×10^{-4}	-	4.7×10^{-4}
H_2 Gas, per ATM per cm	5.66	8.4×10^{-5}	-	4.7×10^{-4}
Air, per cm	2.69	1.2×10^{-3}	-	3.2×10^{-3}
Glass Cell Wall, per mm	2.11	2.2	-	0.47
G11/FR5, Target Enclosure	-	-	0.078	0.4 (Guess)
Kapton, L-HRS Entrance	2.21	1.4	0.025	0.080

Table B.1: Materials in the target area, their thickness and collision energy loss for 1.23 GeV electron (1-pass beam).

THIS PAGE INTENTIONALLY LEFT BLANK

Appendix C

A Maximum Likelihood Estimator for SIDIS Azimuthal Asymmetry Analysis[1]

C.1 Introduction

Semi-inclusive deep inelastic scattering (SIDIS), in which a hadron from the fragmentation of the struck quark is detected in coincidence with the scattered lepton, provides access to transverse momentum dependent parton distributions (TMDs), which describes the quark structure of the nucleon in all three dimensions of momentum space [37]. All the leading twist TMDs can be accessed in SIDIS. Each of the TMD distributions is related to a term in the SIDIS cross section with a characteristic polarization dependency and a azimuthal angular modulation [41]. To reduce the experimental systematic uncertainties, they are usually measured as spin asymmetries. Several experiments has been proposed and carried out at Jefferson Lab, including 6 GeV experiments, CLAS [58], E06-010 (this experiment) and future 12 GeV experiments E12-07-107 [236], E12-09-009 [251], E12-10-006 [233] and E12-11-007 [234]. Existing SIDIS experiments which probes TMDs were reviewed in Ref. [34].

[1]This appendix is based on a draft of the E06-010 analysis note, written by the author this this thesis and Dr. Yi Qiang <yqiang@jlab.org>.

Maximum likelihood estimation (MLE) is a popular method used to fit a statistical model to data, and provide estimates for the model's parameters [6]. According to the features of these SIDIS experiments, we provide a set of efficient and low-biased maximum likelihood (ML) based estimators for the angular moments of the spin asymmetries. This method is design to take the advantage of the target spin and beam helicity flips, including various experimental corrections. To assist with the illustration of how the ML method works, we will frequently quote the specifications of Experiment E06-010 (this thesis experiment), which measured the target single spin asymmetry (target-SSA) and beam-target double spin asymmetry (DSA) in the SIDIS $^3\mathrm{He}^{\uparrow}(\overrightarrow{e}, e'\pi^{+/-}/K^{+/-})X$ reactions using a polarized electron beam and a transversely polarized ^{3}He target.

C.1.1 The Cross Section Model

Assuming the single photon exchange approximation and detection of an unpolarized final state hadron, the SIDIS cross section can be expressed in a model-independent way by a set of 18 structure functions (SFs) [41]. Each structure function is related to a characteristic a beam-target polarization and a azimuthal angular modulation. The cross section can be generalized as

$$\begin{aligned}\sigma &= \sigma_0 \times \Bigg(1 + \sum_i A_{UU}^{(i)} M_{UU}^{(i)}(\phi_h) \\ &\quad + P_{\mathrm{Target}} \cdot \sum_i A_{UX}^{(i)} M_{UX}^{(i)}(\phi_h, \phi_S, \theta_S) \\ &\quad + \lambda \cdot P_{\mathrm{Beam}} \cdot \sum_i A_{LU}^{(i)} M_{LU}^{(i)}(\phi_h) \\ &\quad + \lambda \cdot P_{\mathrm{Beam}} \cdot P_{\mathrm{Target}} \cdot \sum_i A_{LX}^{(i)} M_{LX}^{(i)}(\phi_h, \phi_S, \theta_S)\Bigg), \end{aligned} \tag{C.1}$$

where σ_0 is the unpolarized and azimuthal-averaged cross section; $P_{\mathrm{Beam(Target)}}$ is polarization of beam (target), $0 \sim 100\%$; $\lambda = \pm 1$ is the beam helicity; ϕ_h and ϕ_S are the azimuthal angles of the detected hadron, target spin, defined in the virtual photon frame as Fig. 2-2. θ_S is the polar angle of the target spin with respect to the virtual photon direction and $\tan\theta_S \equiv -|S_T|/S_L$. These terms are grouped by their

helicity-and-spin dependencies into five categories:

(I) unpolarized angular independent cross section σ_0, to which the Eq. (C.1) was normalized. It corresponds to the sum of structure functions $F_{UU,T}$ and $\epsilon\, F_{UU,L}$.

(II) unpolarized angular dependent cross section, relating to $A_{UU}^{(i)}$

(III) target single spin dependent cross section, relating to $A_{UX}^{(i)}$

(IV) beam single spin dependent cross section, relating to $A_{LU}^{(i)}$

(V) beam-target double spin dependent cross section, relating to $A_{LX}^{(i)}$

Terms in categories (II-V) are described as a product of angular modulation function $M^{(i)}$ and related moments of asymmetry $A^{(i)}$, which are defined following Eq. (2.5). The leading twist terms are listed in Tables C.1 and C.2. The subscripts indicate their categories with respect to beam and target polarization (X stand for either transversely ,T, or longitudinally, L, polarized target).

The dependence of the cross section and azimuthal moments on the kinematic variables, such as the Bjorken scaling variable, x and four momentum transfer, Q^2, is included implicitly in Eq. (C.1). Since this note concerns the extraction of the angular moments, the kinematic dependence is ignored in the following discussions, which is reasonable in the limit of a small kinematic binning. The systematic effect for ignoring such dependence can be studied separately as bin center corrections.

Comparing to the SIDIS cross section in Ref. [41], the moments of the asymmetry, $A^{(i)}$, are proportional to the ratios of polarized structure functions and σ_0. Meanwhile, the longitudinal and transverse target spin components are converted to combinations of the spin polar angle and target polarization, $S_L = -|P_{\text{Target}}|\cos\theta_S$ and $|S_T| = |P_{\text{Target}}|\sin\theta_S$, of which the polar angle part is absorbed into $M^{(i)}$. The polarized leading-twist terms, $A^{(i)}$, $M^{(i)}$ and their leading order TMD interpretations are listed in Tables C.1 and C.2.

C.1.2 Typical Data Structure and Assumptions

For the experiments this note concerns, the data were taken with several target spin directions, S, defined by the target magnetic field. The target spins are either parallel to this direction (S^+) or anti-parallel to it (S^-). In the case of experiment E06-010, there were two directions: vertical up/down ($V^\pm$) and transverse-in-plane beam-right/left ($T^\pm$). Within each so-called target spin state, the spin direction is held constant (for around 20 min in E06-010) while the beam helicity flips at a higher rate. Between two spin states, the target spin is flipped to exactly the opposite direction. In experiment E06-010, there are roughly 3000 spin states. They were approximately equally distributed between the transverse and vertical target directions. The average event count in each state is at the order of magnitude of 10^2 for $e'pi$ coincidence events and $\leqslant 10$ for $e'K$ coincidence events [169].

From the data, the following information was extracted as the inputs for this analysis:

- For each target spin state, $\left(S_i^\pm\right)$[2]
  - target/beam polarization is $P_{\text{Target}}^{S_i^\pm}/P_{\text{Beam}}^{S_i^\pm}$ [3]
  - target density is $\rho_{S_i^\pm}$, in the unit of #nucleon per unit area
  - total beam charge is $C_{S_i^\pm}$, and DAQ/electronics live time is $LT_{S_i^\pm}$.

  In this note, the effective accumulated luminosity is defined as

$$\tilde{L}_{S_i^\pm} \equiv \rho_{S_i^\pm} \times C_{S_i^\pm} \times LT_{S_i^\pm}. \tag{C.2}$$

  Furthermore, if helicity based asymmetries are considered, the luminosity should be determined separately by the helicity states, and an additional subscript, λ, will be assigned, e. g. $\tilde{L}_{\lambda,\, S_i^\pm}$.

- for each event, the following information is analyzed

[2] For example, S_i^+ stands for the i-th target spin state along the direction of S^+

[3] One can use different beam polarizations for different helicity state too.

– spin/helicity state, to which the events belong

– angular variables, i.e., ϕ_h, ϕ_S and θ_S

Additional assumptions for this note are

- The yields are stable. Experimental yields can drift due to a slow change in the detection efficiency and acceptance. This effect is suppressed by fast spin or/and helicity flips, and hence. it is not concerned in this part of analysis. Such effect was later included in the systematic uncertainty, as discussed in Sec. 6.1.4.

- The unpolarized angular dependent part of the cross section (category (II), $A_{UU}^{(i)}$) will be ignored in this step of analysis. The associated systematic uncertainties can be studies with the direct simulation, which is discussed in Sec. 6.1.4.

C.1.3 Construct Probability Function and Log Likelihood Function

From Eq. (C.1), the normalized SIDIS yield (event counts per unit effective charge per unit angular coverage) can be expressed as

$$\begin{aligned} y_{\lambda,\, S_i^{\pm}}(\phi_h, \phi_S, \theta_S) \;=\; & \rho_{S_i^{\pm}} \cdot \sigma_0 \cdot a_{S^{\pm}}(\phi_h, \phi_S, \theta_S) \times \\ & \Bigg(1 + P_{\text{Target}}^{S_i^{\pm}} \cdot \sum_i A_{UX}^{(i)} M_{UX}^{(i)}(\phi_h, \phi_S, \theta_S) \\ & + \lambda \cdot P_{\text{Beam}}^{S_i^{\pm}} \left(\sum_i A_{LU}^{(i)} M_{LU}^{(i)}(\phi_h) + P_{\text{Target}}^{S_i^{\pm}} \cdot \sum_i A_{LX}^{(i)} M_{LX}^{(i)}(\phi_h, \phi_S, \theta_S) \right) \Bigg) \end{aligned} \tag{C.3}$$

where $a_{S^{\pm}}(\phi_h, \phi_S, \theta_S)$, which can take values between 0% and 100%, is the acceptance and detector efficiency function for a spin direction, $S^{\pm}$. For measurements with an unpolarized target, one can assign each data section as a spin state S_i^{+} with zero target polarization and arbitrary values for ϕ_S and θ_S.

The function $a_{S^{\pm}}(\phi_h, \phi_S, \theta_S)$ has properties, which is useful for later simplifications:

- Due to the complete reversal of the spin direction,

$$a_{S^+}(\phi_h, \phi_S, \theta_S) = a_{S^-}(\phi_h, \phi_S + \pi, \pi - \theta_S) \tag{C.4}$$

- Also due to the target spin rotations,

$$a(\phi_h) \equiv \iint a_{S^\pm}(\phi_h, \phi_S, \theta_S) d\phi_S d\theta_S \tag{C.5}$$

  is independent of target spin directions, $S^\pm$. Therefore, one can define a universal integral of $a_{S^\pm}$ as

$$\tilde{a} \equiv \iiint a_{S^\pm}(\phi_h, \phi_S, \theta_S) d\phi_h d\phi_S d\theta_S \,. \tag{C.6}$$

Each SIDIS event can be treated as a sampling over a universal probability density function (pdf) of discrete random variables of the target spin state ($S_i^\pm$), beam helicity state (λ), and continuous random variables of azimuthal and polar angles,

$$f(\lambda, S_i^\pm, \phi_h, \phi_S, \theta_S) \;\; = \;\; \frac{1}{\mathcal{N}} C_{S_i^\pm} \times LT_{S_i^\pm} \times y_{\lambda, S_i^\pm}(\phi_h, \phi_S, \theta_S) \,, \tag{C.7}$$

where the normalization function $\mathcal{N}$ is defined so that this pdf is normalization to 1

$$\mathcal{N} \equiv \sum_\lambda \sum_{S_i^\pm} C_{S_i^\pm} \times LT_{S_i^\pm} \iiint f(\lambda, S_i^\pm, \phi_h, \phi_S, \theta_S) d\phi_h d\phi_S d\theta_S. \tag{C.8}$$

Here $\sum_\lambda$ is summing over two helicity states, ± 1 and $\sum_{S_i^\pm}$ is sum over all target spin states. Both the pdf and $\mathcal{N}$ contain the unknown parameters of the azimuthal moments, which are to be extracted.

The full data set with N events is independent and identically distributed (i.i.d.) with each event following the probability function (Pr) of $\Pr(\lambda, S_i^\pm, \phi_h, \phi_S, \theta_S)$. Therefore, the log likelihood function is

$$\ln L = \sum_{\text{ev}} \ln \Big(f(\lambda, S_i^\pm, \phi_h, \phi_S, \theta_S) \Big) \,, \tag{C.9}$$

Name	$M_{UX}^{(i)}(\phi_h, \phi_S, \theta_S)$	$A_{UX}^{(i)}$	LO TMD[5]
Collins	$\sin\theta_S \sin(\phi_h + \phi_S)$	${}^{\varepsilon F_{UT}^{\sin(\phi_h+\phi_S)}}/_{F_{UU,T}}$	$\propto h_1 \otimes H_1^\perp$
Sivers	$\sin\theta_S \sin(\phi_h - \phi_S)$	${}^{F_{UT,T}^{\sin(\phi_h-\phi_S)}}/_{F_{UU,T}}$	$\propto f_{1T}^\perp \otimes D_1$
pretzelosity	$\sin\theta_S \sin(3\phi_h - \phi_S)$	${}^{\varepsilon F_{UT}^{\sin(3\phi_h-\phi_S)}}/_{F_{UU,T}}$	$\propto h_{1T}^\perp \otimes H_1^\perp$
worm-gear	$-\cos\theta_S \sin(2\phi_h)$	${}^{\varepsilon F_{UL}^{\sin 2\phi_h}}/_{F_{UU,T}}$	$\propto h_{1L}^\perp \otimes H_1^\perp$

Table C.1: Leading twist azimuthal modulations, which can be accessed through the target single spin asymmetries with an unpolarized beam

where $\sum_{\text{ev}}$ is sum over all events. the ML estimators for the azimuthal moments can be found by maximizing $\ln L$.

The following two sections will simplify $\ln L$ and solve for the estimators based on two general categories of asymmetries:

- Target single spin asymmetry (target-SSA) with an unpolarized beam[4], in which the cross section terms of category (III) and $A_{UX}^{(i)}$ can be accessed

- Beam single spin asymmetry (beam-SSA), in which terms of category (IV) and $A_{LU}^{(i)}$ can be accessed.

With both polarized beam and target, terms of category (V) and $A_{LX}^{(i)}$ can be accessed in both methods of target-SSA and beam-SSA. The analysis of experiment E06-010 showed consistent results. However, since the beam helicity flip rate is much higher than that of target spin flips, the beam SSA method is usually preferred due to smaller systematic uncertainties.

C.2 Estimation of Azimuthal Target Single Spin Asymmetries

C.2.1 Introduction

In the case of a polarized target and an unpolarized lepton beam, the SIDIS cross section, Eq. (C.1), and pdf, Eq. (C.7), can be simplified as

$$\sigma = \sigma_0 \times \left(1 + P_{\text{Target}} \cdot \sum_i A_{UX}^{(i)} M_{UX}^{(i)}(\phi_h, \phi_S, \theta_S)\right) \tag{C.10}$$

$$f(S_i^{\pm}, \phi_h, \phi_S, \theta_S) = \frac{1}{\mathcal{N}} \cdot \tilde{L}_{S_i^{\pm}} \cdot a_{S^{\pm}}(\phi_h, \phi_S, \theta_S) \times \left(1 + P_{\text{Target}}^{S_i^{\pm}} \cdot \sum_i A_{UX}^{(i)} M_{UX}^{(i)}(\phi_h, \phi_S, \theta_S)\right). \tag{C.11}$$

The combinations of modulation and moments includes, but is not limited to, the leading twist terms as shown in Table C.1. The SSA modulations all flip signs during a target spin flip

$$M_{UX}^{(i)}(\phi_h, \phi_S, \theta_S) = -M_{UX}^{(i)}(\phi_h, \phi_S + \pi, \pi - \theta_S), \tag{C.12}$$

which is useful for simplifying the following calculations.

C.2.2 Definitions

- Total number of event is N

- angular moments of acceptance is defined as below

$$\tilde{a}_{S^+}^{(i)} \equiv \frac{1}{\tilde{a}} \iiint a_{S^+}(\phi_h, \phi_S, \theta_S) M_{UX}^{(i)}(\phi_h, \phi_S, \theta_S) d\phi_h d\phi_S d\theta_S \tag{C.13}$$

$$\tilde{a}_{S^-}^{(i)} \equiv \frac{1}{\tilde{a}} \iiint a_{S^-}(\phi_h, \phi_S, \theta_S) M_{UX}^{(i)}(\phi_h, \phi_S, \theta_S) d\phi_h d\phi_S d\theta_S \tag{C.14}$$

[4] An effective unpolarized beam can be formed by sum data regardless of beam helicity, given a small beam charge asymmetries provided by CEBAF [126].

and from Eq. (C.4) and (C.12), a unified moment for opposite spin directions,

$$\tilde{a}_S^{(i)} \equiv \tilde{a}_{S^+}^{(i)} = -\tilde{a}_{S^-}^{(i)} \tag{C.15}$$

Estimation of $\tilde{a}_S^{(i)}$ will be discussed in Section C.4.1.1.

- The polarization-and-acceptance-weighted effective luminosity asymmetry is defined as

$$\tilde{A}_L^{(i)} \equiv \frac{\sum_{S_j^\pm} \tilde{a}_S^{(i)} \left(\widetilde{L}_{S_j^+} P_{\text{Target}}^{S_i^+} - \widetilde{L}_{S_j^-} P_{\text{Target}}^{S_i^-} \right)}{\sum_{S_j^\pm} \left(\widetilde{L}_{S_j^+} + \widetilde{L}_{S_j^-} \right)}, \tag{C.16}$$

where $\sum_{S_j^\pm}$ is a summation over all target spin states.

- Event sums are defined as

$$\sum \left[P M^{(k)} \right] \equiv \sum_{\text{ev}} P_{\text{Target}} M_{UX}^{(k)}(\phi_h, \phi_S, \theta_S) \tag{C.17}$$

$$\sum \left[P^2 M^{(j)} M^{(k)} \right] \equiv \sum_{\text{ev}} P_{\text{Target}}^2 M_{UX}^{(j)}(\phi_h, \phi_S, \theta_S) M_{UX}^{(k)}(\phi_h, \phi_S, \theta_S), \tag{C.18}$$

where $\sum_{\text{ev}}$ is sum over all events

- Useful matrices and vectors are

$$\begin{aligned}
\mathbf{F} &\equiv \begin{pmatrix} \sum \left[P^2 M^{(1)} M^{(1)} \right] - N \tilde{A}_L^{(1)} \tilde{A}_L^{(1)} & \sum \left[P^2 M^{(1)} M^{(2)} \right] - N \tilde{A}_L^{(1)} \tilde{A}_L^{(2)} & \dots \\ \sum \left[P^2 M^{(2)} M^{(1)} \right] - N \tilde{A}_L^{(2)} \tilde{A}_L^{(1)} & \sum \left[P^2 M^{(2)} M^{(2)} \right] - N \tilde{A}_L^{(2)} \tilde{A}_L^{(2)} & \dots \\ \vdots & \vdots & \ddots \end{pmatrix} \\
\boldsymbol{B} &\equiv \begin{pmatrix} \sum \left[P M^{(1)} \right] - N \tilde{A}_L^{(1)} \\ \sum \left[P M^{(2)} \right] - N \tilde{A}_L^{(2)} \\ \vdots \end{pmatrix} \\
\boldsymbol{A} &\equiv \begin{pmatrix} A_{UX}^{(1)} \\ A_{UX}^{(2)} \\ \vdots \end{pmatrix}
\end{aligned} \tag{C.19}$$

C.2.3 Estimator and Uncertainty

The estimators for $\boldsymbol{A}$ can be calculated by numerically solving the following ML equation,

$$\begin{aligned} 0 = {}^{\partial \ln L}/_{\partial A_{UX}^{(k)}} &= \sum_{\text{ev}} \frac{P_{\text{Target}} M_{UX}^{(k)}(\phi_h, \phi_S, \theta_S)}{1 + P_{\text{Target}} \cdot \sum_i A_{UX}^{(i)} M_{UX}^{(i)}(\phi_h, \phi_S, \theta_S)} \\ &\quad - N \frac{\tilde{A}_L^{(k)}}{1 + \sum_i A_{UX}^{(i)} \tilde{A}_L^{(i)}}. \end{aligned} \tag{C.20}$$

Further, since the raw SIDIS asymmetry are usually small, the above equation can be expanded to leading order, so that the analytical estimators are given by

$$\hat{\boldsymbol{A}} = \mathbf{F}^{-1} \boldsymbol{B}, \tag{C.21}$$

The deviation of $\hat{\boldsymbol{A}}$ from the exact solution of Eq. (C.20) is at the level of third order with respect to the raw asymmetries. Since for most SIDIS experiments, the raw asymmetries are small; therefore, the analytical estimator is very close to the exact solution of the ML equation (Eq. (C.20)) which is efficient and approximately unbiased. Meanwhile, the benefit of this approximation is obvious: Eq. (C.21) is simple to calculate since it is just a summation over events.

The covariance matrix can be calculated by using the Gaussian approximation for the likelihood function and expanding to the leading orders of the raw asymmetries,

$$\begin{aligned} \mathbf{V}\left[\hat{\boldsymbol{A}}\right] &= \left[-\frac{\partial \ln L}{\partial A_{UX}^{(j)} \partial A_{UX}^{(k)}} \bigg|_{\hat{\boldsymbol{A}}} \right]^{-1}_{jk} \\ &= \mathbf{F}^{-1}. \end{aligned} \tag{C.22}$$

For the idealized case with zero effective luminosity asymmetry, $\tilde{A}_L^{(k)} = 0$, and 100% target polarization, the above estimator becomes the same as that in Ref. [252].

Name	$M_{LX}^{(i)}(\phi_h, \phi_S, \theta_S)$	$A_{LX}^{(i)}$	LO TMD[6]
Helicity	$-\cos\theta_S$	$\sqrt{1-\varepsilon^2}\,F_{LL}/F_{UU,T}$	$\propto g_{1L} \otimes D_1$
worm-gear	$\sin\theta_S \cos(\phi_h - \phi_S)$	$\sqrt{1-\varepsilon^2}\,F_{LT}^{\cos(\phi_h-\phi_S)}/F_{UU,T}$	$\propto g_{1T} \otimes D_1$

Table C.2: Leading twist azimuthal modulations, which can be accessed through the beam single spin asymmetries with a polarized target

C.3 Estimation of Azimuthal Beam Helicity Asymmetries

C.3.1 Introduction

With a polarized lepton beam, additional terms in Eq. (C.1) can be accessed. This section concerns the extraction of azimuthal moments of beam SSA. In the case of a polarized target, the moments of beam-target double spin asymmetries can also be extracted under a unified frame. In this case, the cross section and pdf model, Eq. (C.1) and (C.7), are

$$\sigma = \sigma_0 \times \Bigg(1 + \lambda \cdot P_{\text{Beam}} \times \Bigg(\sum_i A_{LU}^{(i)} M_{LU}^{(i)}(\phi_h) + P_{\text{Target}} \cdot \sum_i A_{LX}^{(i)} M_{LX}^{(i)}(\phi_h, \phi_S, \theta_S)\Bigg)\Bigg) \tag{C.23}$$

$$f(\lambda, S_i^{\pm}, \phi_h, \phi_S, \theta_S) = \frac{1}{\mathcal{N}} \tilde{L}_{\lambda, S_i^{\pm}} \cdot \sigma_0 \cdot a_{S_\pm}(\phi_h, \phi_S, \theta_S) \cdot \Bigg(1 + \lambda \cdot P_{\text{Beam}}^{S_i^{\pm}} \times \Bigg(\sum_i A_{LU}^{(i)} M_{LU}^{(i)}(\phi_h) + P_{\text{Target}}^{S_i^{\pm}} \cdot \sum_i A_{LX}^{(i)} M_{LX}^{(i)}(\phi_h, \phi_S, \theta_S)\Bigg)\Bigg) \tag{C.24}$$

Here the data is divided into sections of target spin state, $S_i^{\pm}$. In the case of an unpolarized target, each data segment can be treated as one spin state, S_i^{+} with zero target polarization. For the leading-twist terms, the modulation and asymmetry moments are shown in Table C.2.

The cross section terms of categories (II) and (III) are ignored for this study. Their contribution to the interested moments were shown to be small relative to the statistical uncertainty for this experiment, as discussed in Sec. 6.1.4. In the same section, the additional systematic uncertainty due to ignoring these terms was studied

by simulations.

C.3.2 Definitions

- The total number of events is N
- a unified set of symbols are defined
  - for beam single spin dependent part of the cross section,

$$
\begin{aligned}
P^{(i)}_{S^\pm_i} &\equiv P^{S^\pm_i}_{\text{Beam}} && \text{(C.25)}\\
A^{(i)} &\equiv A^{(i)}_{LU} && \text{(C.26)}\\
M^{(i)}(\phi_h,\phi_S,\theta_S) &\equiv M^{(i)}_{LU}(\phi_h) && \text{(C.27)}\\
\tilde{a}^{(i)}_S &\equiv \tilde{a}^{(i)}_{S^+} \equiv \tilde{a}^{(i)}_{S^-} \\
&\equiv \frac{1}{\tilde{a}} \iiint a(\phi_h) M^{(i)}_{LU}(\phi_h) d\phi_h d\phi_S d\theta_S && \text{(C.28)}
\end{aligned}
$$

  - for beam-target double spin dependent cross sections

$$
\begin{aligned}
P^{(i+n_{LU})}_{S^\pm_i} &\equiv P^{S^\pm_i}_{\text{Beam}} \times P^{S^\pm_i}_{\text{Target}} && \text{(C.29)}\\
A^{(i+n_{LU})} &\equiv A^{(i)}_{LX} && \text{(C.30)}\\
M^{(i+n_{LU})}(\phi_h,\phi_S,\theta_S) &\equiv M^{(i)}_{LX}(\phi_h,\phi_S,\theta_S) && \text{(C.31)}\\
\tilde{a}^{(i+n_{LU})}_{S^+} &\equiv \frac{1}{\tilde{a}} \iiint \big[a_{S^+}(\phi_h,\phi_S,\theta_S) \\
&\quad \times M^{(i)}_{LX}(\phi_h,\phi_S,\theta_S) d\phi_h d\phi_S d\theta_S\big] && \text{(C.32)}\\
\tilde{a}^{(i+n_{LU})}_{S^-} &\equiv \frac{1}{\tilde{a}} \iiint \big[a_{S^-}(\phi_h,\phi_S,\theta_S) \\
&\quad \times M^{(i)}_{LX}(\phi_h,\phi_S,\theta_S) d\phi_h d\phi_S d\theta_S\big] && \text{(C.33)}\\
\tilde{a}^{(i+n_{LU})}_S &\equiv \tilde{a}^{(i+n_{LU})}_{S^+} = -\tilde{a}^{(i+n_{LU})}_{S^-} && \text{(C.34)}
\end{aligned}
$$

where n_{LU} is the total number of beam single spin dependent terms. For the modulated acceptance, $\tilde{a}^{(i+n_{LU})}_{S^+} = -\tilde{a}^{(i+n_{LU})}_{S^+}$ due to Eq. (C.4) and the sign flip of $M^{(i)}_{LX}(\phi_h,\phi_S,\theta_S)$ as the target spin flips. The estimation of $\tilde{a}^{(i)}_S$ will be discussed in Section C.4.1.1.

- The polarization-and-acceptance-weighted effective luminosity asymmetry is given by

$$\tilde{A}_L^{(i)} \equiv \frac{\sum_{S_j^\pm} \tilde{a}^{(i)}_{S_j^\pm} P^{(i)}_{S_i^\pm} \left(\widetilde{L}_{+,S_j^\pm} - \widetilde{L}_{-,S_j^\pm} \right)}{\sum_{S_j^\pm} \left(\widetilde{L}_{+,S_j^\pm} + \widetilde{L}_{-,S_j^\pm} \right)}, \tag{C.35}$$

- The event-by-event sums are

$$\sum \left[\lambda P M^{(k)} \right] \equiv \sum_{\text{ev}} \lambda \cdot P^{(k)} M^{(k)}(\phi_h, \phi_S, \theta_S) \tag{C.36}$$

$$\sum \left[P^2 M^{(j)} M^{(k)} \right] \equiv \sum_{\text{ev}} P^{(j)} P^{(k)} M^{(j)}(\phi_h, \phi_S, \theta_S) M^{(k)}(\phi_h, \phi_S, \theta_S) , \tag{C.37}$$

  where $P^{(k)} = P^{(k)}_{S_i^\pm}$ is the corresponding for the spin state $S_i^\pm$ which the event belongs as defined in Eqs. (C.25) and (C.29).

- The relevant Matrices

$$\mathbf{F} \equiv \begin{pmatrix} \sum \left[P^2 M^{(1)} M^{(1)} \right] - N \tilde{A}_L^{(1)} \tilde{A}_L^{(1)} & \sum \left[P^2 M^{(1)} M^{(2)} \right] - N \tilde{A}_L^{(1)} \tilde{A}_L^{(2)} & \dots \\ \sum \left[P^2 M^{(2)} M^{(1)} \right] - N \tilde{A}_L^{(2)} \tilde{A}_L^{(1)} & \sum \left[P^2 M^{(2)} M^{(2)} \right] - N \tilde{A}_L^{(2)} \tilde{A}_L^{(2)} & \\ \vdots & \vdots & \ddots \end{pmatrix} \tag{C.38}$$

$$\boldsymbol{B} \equiv \begin{pmatrix} \sum \left[\lambda P M^{(1)} \right] - N \tilde{A}_L^{(1)} \\ \sum \left[\lambda P M^{(2)} \right] - N \tilde{A}_L^{(2)} \\ \vdots \end{pmatrix} \tag{C.39}$$

$$\boldsymbol{A} \equiv \begin{pmatrix} A^{(1)} \\ A^{(2)} \\ \vdots \end{pmatrix} \tag{C.40}$$

C.3.3 Estimator and Uncertainty

As presented in the previous section, the ML estimator for $\boldsymbol{A}$ can be found by numerically solving for $0 = {}^{\partial \ln L}/_{\partial A^{(k)}}$,

$$0 = \sum_{\text{ev}} \frac{\lambda \cdot P^{(k)} \cdot M^{(k)}(\phi_h, \phi_S, \theta_S)}{1 + P^{(k)} \cdot \lambda \cdot \sum_i A^{(i)} M^{(i)}(\phi_h, \phi_S, \theta_S)} - N \frac{\tilde{A}_L^{(k)}}{1 + \sum_i A^{(i)} \cdot \tilde{A}_L^{(i)}}. \tag{C.41}$$

An alternative easy-to-calculate estimator is the leading order solution of the above equation

$$\hat{\boldsymbol{A}} = \mathbf{F}^{-1}\boldsymbol{B} \tag{C.42}$$

The deviation of $\hat{\boldsymbol{A}}$ from the exact solution of Eq. (C.41) is also at the level of third order with respect to the raw asymmetries, which is leads to a negligible uncertainty for the E06-010 experiment and most SIDIS experiments [34]. The covariance matrix can be determined using the Gaussian approximation for the likelihood function and expanding to the leading order with respect to the raw asymmetries:

$$\mathbf{V}\left[\hat{\boldsymbol{A}}\right] \;=\; \mathbf{F}^{-1}\,. \tag{C.43}$$

C.4 Discussions

C.4.1 Acceptance

C.4.1.1 Estimation of Modulated Acceptance

Modulated acceptances, $\tilde{a}_S^{(i)}$, defined in Eqs. (C.13) and (C.14) for the target-SSA, Eq. (C.28) for the beam-SSA and Eqs. (C.32) and (C.33) for the DSA, are used to calculate the correction terms related to the luminosity asymmetries, $\tilde{A}_L^{(i)}$as defined in Eqs. (C.16) and (C.35). These correction terms are applied to the estimator by including them in the matrices $\boldsymbol{B}$ and $\mathbf{F}$. For an idealized experiment with complete acceptance and perfect detection efficiency, $\tilde{a}_S^{(i)} = 0$.

At leading order, $\tilde{A}_L^{(i)} \approx P \times \tilde{a}_S^{(i)} \times A_L$, where the effective luminosity asymmetry, $A_L = \left(\widetilde{L}_{S_j^+} - \widetilde{L}_{S_j^-}\right) / \left(\widetilde{L}_{S_j^+} + \widetilde{L}_{S_j^-}\right)$ for target SSA and $A_L = \left(\widetilde{L}_{+,\,S_j^\pm} - \widetilde{L}_{-,\,S_j^\pm}\right) / \left(\widetilde{L}_{+,\,S_j^\pm} + \widetilde{L}_{-,\,S_j^\pm}\right)$ for beam SSA. Therefore, for an experiment with balanced beam charge, stable target density and small DAQ deadtime (1−livetime), the estimator is almost independent of acceptance. When A_L is small, a rough estimation of $\tilde{a}_S^{(i)}$ will be good enough for the purpose of the asymmetry extraction.

In principle, $\tilde{a}_S^{(i)}$ can be calculated through studying the acceptance and detector

efficiencies. Practically, $\tilde{a}_S^{(i)}$ can be roughly estimated with the same SIDIS data as the asymmetry analysis: following Eq. (C.3), one can form the weighted sum with unpolarized beam and polarized target

$$\tilde{a}_S^{(i)} \approx \frac{\sum_{\text{ev},\,S^+} M^{(i)}(\phi_h,\phi_S,\theta_S)/\widetilde{L}_{S^+} + h\cdot\sum_{\text{ev},S^-} M^{(i)}(\phi_h,\phi_S,\theta_S)/\widetilde{L}_{S^-}}{N_{S^+}/\widetilde{L}_{S^+} + N_{S^-}/\widetilde{L}_{S^-}}\,, \quad \text{(C.44)}$$

$$h = \begin{cases} +1 & \text{for the beam-SSAs, } A_{LU}^{(i)} \\ -1 & \text{for the target-SSAs, } A_{UX}^{(i)}\text{, and DSAs, } A_{LX}^{(i)} \end{cases} \quad \text{(C.45)}$$

For each the target spin direction of $S^\pm$, $N_{S^\pm}$ is the events number and $\sum_{\text{ev},\,S^\pm}$ represents sum of events. The statistical precision for these estimations are usually high ($O(1/\sqrt{N})$); the systematic effects include the ignored terms in the cross sections and the fluctuation of target polarization.

C.4.1.2 Partial Acceptance

For typically experiments, the acceptance is not complete and the detectors have inefficiencies so that $a_{S^\pm}(\phi_h,\phi_S,\theta_S) < 100\%$. The consequences are

- Possible correlations between the extracted azimuthal asymmetries. The off-diagonal terms of matrix **F** can be non-zero, which lead to
  - larger diagonal terms in the covariance matrix, i.e., larger statistical uncertainty for a single moment using a multi-term fit.
  - Non-zero diagonal terms in the covariance matrix and a correlation between the extracted moments, although the physical ones are not assumed to be correlated.
- It is important to keep the asymmetry A_L of the effective luminosities small, since the correction term $\tilde{A}_L^{(i)} \approx P \times \tilde{a}_S^{(i)} \times A_L$. It is also possible to reduce the correction and its uncertainties by designing an experiment with a symmetrical acceptance so that $\tilde{a}_S^{(i)}$ can be optimized to approximately zero. Future examples include the SIDIS experiments with using SoLID spectrometers [233, 234].

C.4.2 Estimation with Additional Known Modulations

This subsection concerns a special case when, there are total $n+m$ terms included in the cross section model, within which, the azimuthal moments of $A^{(n+1)}$ to $A^{(n+m)}$ are known. The estimators for the unknown moments $A^{(1)}$ to $A^{(n)}$ can be calculated by solving the ML equation, $0 = {}^{\partial \ln L}/_{\partial A_{UX}^{(k)}}$ for $k = 1 \cdots n$ with fixed parameters of $A^{(n+1)}$ to $A^{(m)}$[7]. New matrices and vectors, which are sub-matrices and sub-vectors of $\mathbf{F}$, $\boldsymbol{B}$ and $\boldsymbol{A}$, are defined as following:

$$\begin{aligned}
\mathbf{F}_n &\equiv \begin{pmatrix} [\mathbf{F}]_{1,1} & \dots & [\mathbf{F}]_{1,n} \\ \vdots & \ddots & \dots \\ [\mathbf{F}]_{n,1} & \vdots & [\mathbf{F}]_{n,n} \end{pmatrix} & \boldsymbol{A}_n &\equiv \begin{pmatrix} A^{(1)} \\ \vdots \\ A^{(n)} \end{pmatrix} & \boldsymbol{B}_n &\equiv \begin{pmatrix} [\boldsymbol{B}]_1 \\ \vdots \\ [\boldsymbol{B}]_n \end{pmatrix} \\
\mathbf{C} &\equiv \begin{pmatrix} [\mathbf{F}]_{1,n+1} & \dots & [\mathbf{F}]_{1,m} \\ \vdots & \ddots & \dots \\ [\mathbf{F}]_{n,n+1} & \vdots & [\mathbf{F}]_{n,m} \end{pmatrix} & \boldsymbol{A'} &\equiv \begin{pmatrix} A^{(n+1)} \\ \vdots \\ A^{(n+m)} \end{pmatrix}
\end{aligned} \tag{C.46}$$

The estimator and covariance matrix for the unknown moments are

$$\hat{\boldsymbol{A}}_n = \mathbf{F}_n^{-1} \left(\boldsymbol{B}_n - \mathbf{C}\boldsymbol{A'} \right) \tag{C.47}$$

$$\mathbf{V}\left[\hat{\boldsymbol{A}}_n\right] = \mathbf{F}_n^{-1} \tag{C.48}$$

The known moments, $\boldsymbol{A'}$, introduced a correction, $\mathbf{F}_n^{-1} \cdot \mathbf{C} \cdot \boldsymbol{A'}$, to the n-term-modeled estimators, $\mathbf{F}_n^{-1}\boldsymbol{B}_n$. The correction is proportional to, $\mathbf{C}$, the correlation between the modulations within the acceptance. Since the modulations are orthogonal to each other, an experiment that has full acceptance does not suffer from cross talks between the azimuthal moments.

[7] An alternative method is to first extract estimators with m unknown moments and apply additional $m-n$ constrains of $A^{(n+1)}$ to $A^{(m)}$. Both methods reach the same results.

C.4.3 Tests for the Experiment E06-010 Target-SSA Analysis

The analysis of small-statistics subsamples of a large-statistics SIMC simulation (Sec. 5.4.1) was performed in order to investigate the bias and efficiency of the MLE method used in the E06-010 target-SSA analysis. In figures C-1 and C-2, two high-statistics SIMC data sets each with 10% input Sivers or 10% Collins asymmetries, were subdivided into approximately 2400 trials with statistics equal to the K^- data of experiment E06-010. In both cases, at least within the statistical precision of the study, the results of the maximum-likelihood extraction (Eq. C.21) for any given trial are Gaussian-distributed about the input value, with a σ in very good agreement with the average estimated statistical uncertainty in the extraction (Eq. C.22).

This study shows that the maximum-likelihood estimators (MLE) used for the analysis are unbiased (the average extracted result for a "large" number of trials is equal to the "true" asymmetry) and efficient (the statistical uncertainty calculated in the MLE extraction equals the variance of the results obtained in a large number of independent trials, which defines the statistical uncertainty). Similar results are obtained for both Collins and Sivers asymmetries when the SIMC data are subdivided into approximately 50 trials with statistics equal to the π^+ data of E06-010.

C.5 Conclusion

In summary, a set of estimators for the SIDIS azimuthal moments of spin asymmetries is presented. This method is equivalent to a Fourier decomposition of the cross section model with perfectly balanced luminosity and very small ϕ_h, ϕ_S and θ_S binning. Its advantages include

- High efficiency and approximately unbiased. It is a good approximation of the exact ML solution for most SIDIS experiments.

- Easy to calculate with event summations .

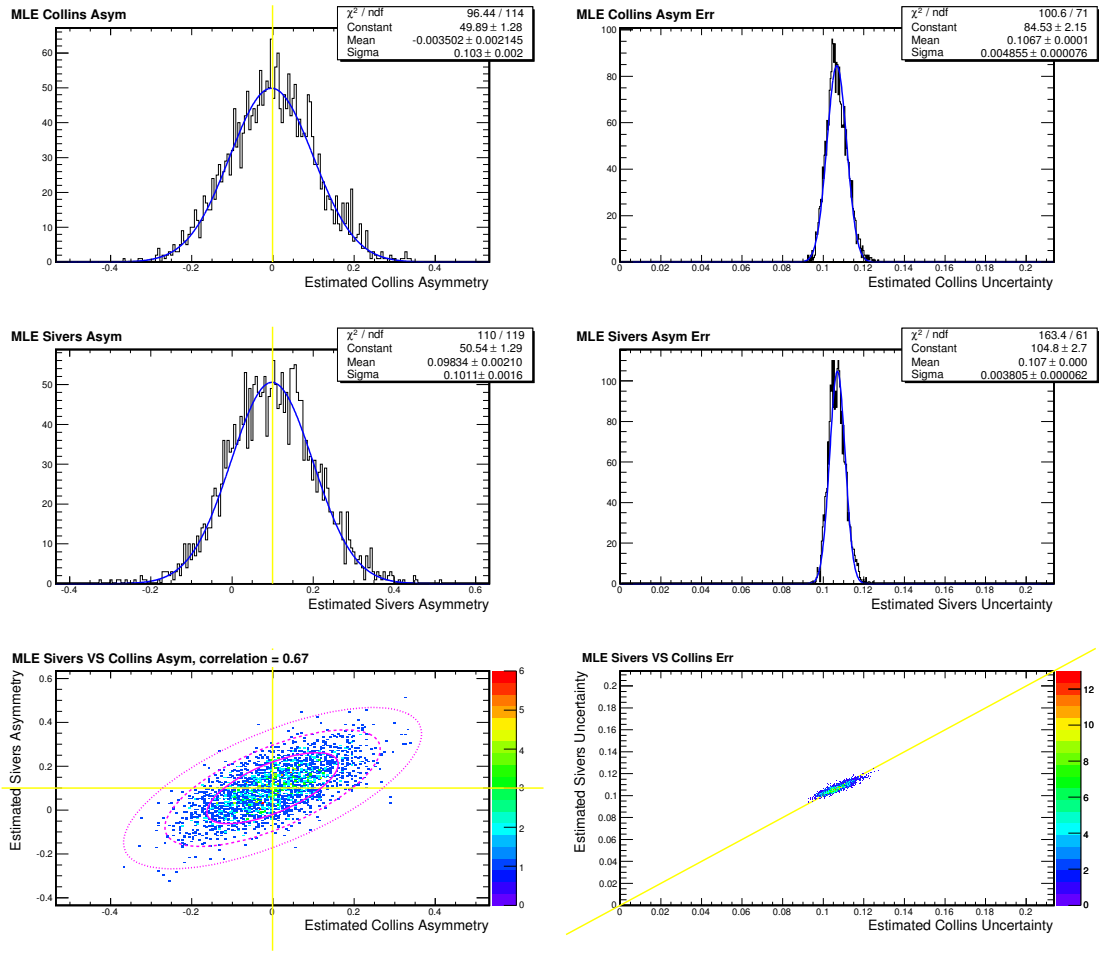

Figure C-1: Results of subdivision of a high-statistics SIMC run into 2400 trials with statistics equal to the K^- data from E06-010, for an input asymmetry of 10% Sivers and 0 Collins.

- With normalizations, including the luminosity asymmetry, the DAQ livetime asymmetry and the time dependence of the polarizations.

- The method does not require binning while extracting modulations in the 3-D angular space of ϕ_h, ϕ_S and θ_S. This is important for small event samples.

The estimators are given for the moments of target SSA (Eq. (C.21)), beam SSA and beam-target DSA (Eq. (C.42)). Exact equations of the ML estimators are also provided in Eqs. (C.20) and (C.41).

This set of estimators is useful for a wide spectrum of existing and future SIDIS asymmetry measurements. It has been successfully used for the DSA and SSA analysis

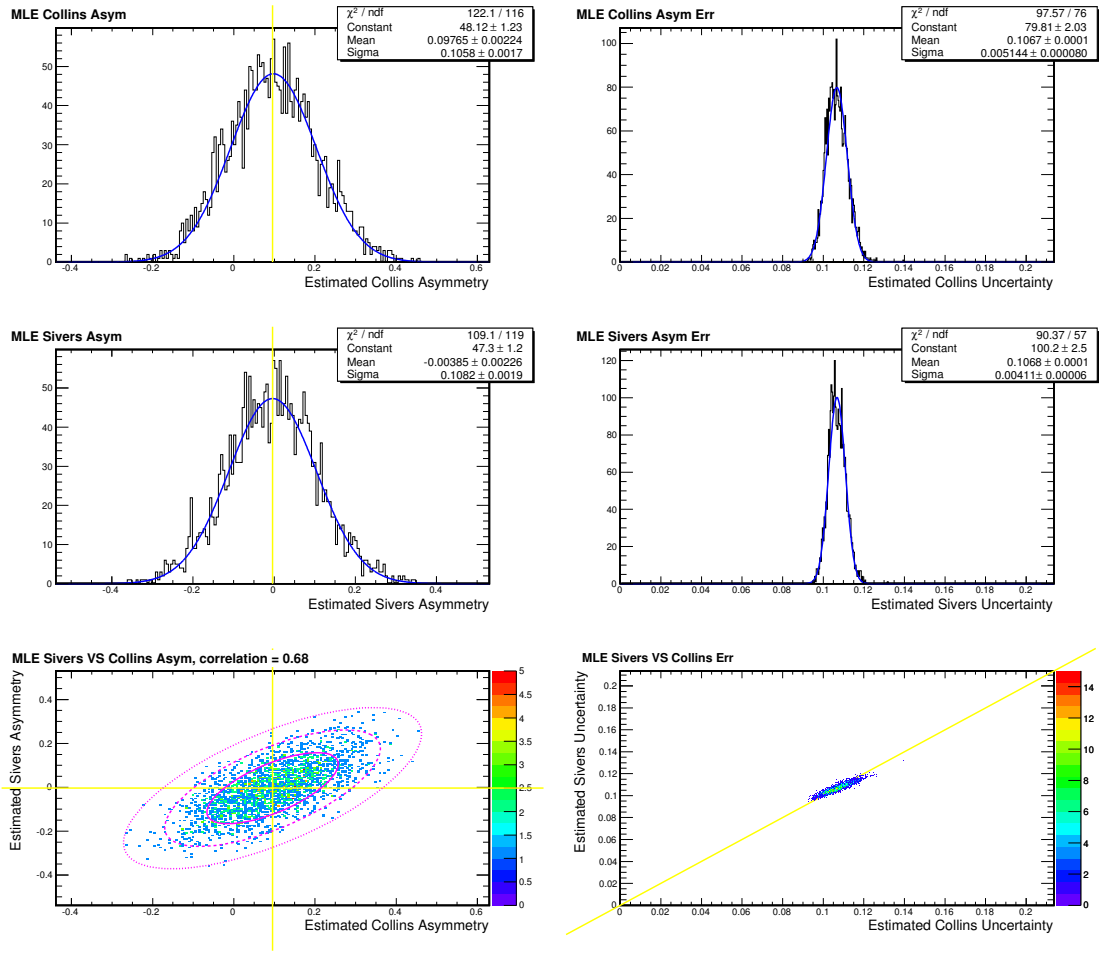

Figure C-2: Results of subdivision of a high-statistics SIMC run into 2400 trials with statistics equal to the K^- data from E06-010, for an input asymmetry of 0 Sivers and 10% Collins.

of experiment E06-010. Extensive cross checks between this estimator and a fitting method and a MC simulations demonstrated consistent results. With straightforward derivation, this method can also be applied to other asymmetry measurements, which are based on reversals of the beam helicity and/or target spins.

THIS PAGE INTENTIONALLY LEFT BLANK

Bibliography

[1] M. Bawin and S. Coon, Nucl.Phys. **A689**, 475 (2001), arXiv:nucl-th/0101005 [nucl-th] .

[2] R. Hofstadter, Rev. Mod. Phys. **28**, 214 (1956).

[3] M. Gell-Mann, Phys.Lett. **8**, 214 (1964).

[4] G. Zweig, Tech. Rep. 8419/TH. 412 (CERN, 1964).

[5] J. Bjorken, Phys.Rev. **179**, 1547 (1969).

[6] K. Nakamura *et al.* (Particle Data Group), J. Phys. G **G37**, 075021 (2010).

[7] S. Bethke, Eur. Phys. J. **C64**, 689 (2009), arXiv:0908.1135 [hep-ph] .

[8] M. Burkardt, A. Miller, and W. D. Nowak, Rept. Prog. Phys. **73**, 016201 (2010), arXiv:0812.2208 [hep-ph] .

[9] S. Drell and T.-M. Yan, Annals Phys. **66**, 578 (1971).

[10] V. Gribov and L. Lipatov, Sov.J.Nucl.Phys. **15**, 438 (1972).

[11] L. Lipatov, Sov.J.Nucl.Phys. **20**, 94 (1975).

[12] G. Altarelli and G. Parisi, Nucl.Phys. **B126**, 298 (1977).

[13] Y. L. Dokshitzer, Sov.Phys.JETP **46**, 641 (1977).

[14] A. Martin, W. Stirling, R. Thorne, and G. Watt, Eur. Phys. J. **C63**, 189 (2009), arXiv:0901.0002 [hep-ph] .

[15] E. Leader, A. V. Sidorov, and D. B. Stamenov, Phys. Rev. **D75**, 074027 (2007), arXiv:hep-ph/0612360 [hep-ph] .

[16] M. Hirai and S. Kumano (Asymmetry Analysis Collaboration), Nucl. Phys. **B813**, 106 (2009), arXiv:0808.0413 [hep-ph] .

[17] D. de Florian, R. Sassot, M. Stratmann, and W. Vogelsang, Phys. Rev. Lett. **101**, 072001 (2008), arXiv:0804.0422 [hep-ph] .

[18] D. de Florian *et al.*, Phys. Rev. **D80**, 034030 (2009), arXiv:0904.3821 [hep-ph] .

[19] A. Airapetian *et al.* (HERMES Collaboration), Phys.Rev.Lett. **92**, 012005 (2004), arXiv:hep-ex/0307064 [hep-ex] .

[20] A. Airapetian *et al.* (HERMES), Phys. Rev. **D71**, 012003 (2005), arXiv:hep-ex/0407032 .

[21] B. Adeva *et al.* (Spin Muon), Phys. Rev. **D58**, 112001 (1998).

[22] M. Alekseev *et al.* (COMPASS), Phys. Lett. **B680**, 217 (2009), arXiv:0905.2828 [hep-ex] .

[23] S. Alekhin, K. Melnikov, and F. Petriello, Phys.Rev. **D74**, 054033 (2006), arXiv:hep-ph/0606237 [hep-ph] .

[24] R. D. Ball *et al.* (NNPDF Collaboration), Nucl.Phys. **B809**, 1 (2009), arXiv:0808.1231 [hep-ph] .

[25] P. M. Nadolsky, H.-L. Lai, Q.-H. Cao, J. Huston, J. Pumplin, *et al.*, Phys.Rev. **D78**, 013004 (2008), arXiv:0802.0007 [hep-ph] .

[26] J. Ashman *et al.* (European Muon), Phys. Lett. **B206**, 364 (1988).

[27] R. Jaffe and A. Manohar, Nucl. Phys. **B337**, 509 (1990).

[28] X.-D. Ji, Phys.Rev.Lett. **78**, 610 (1997), arXiv:hep-ph/9603249 [hep-ph] .

[29] X.-d. Ji, Phys.Rev.Lett. **91**, 062001 (2003), arXiv:hep-ph/0304037 [hep-ph] .

[30] A. V. Belitsky, X.-d. Ji, and F. Yuan, Phys. Rev. **D69**, 074014 (2004), arXiv:hep-ph/0307383 [hep-ph] .

[31] A. Belitsky and A. Radyushkin, Phys.Rept. **418**, 1 (2005), arXiv:hep-ph/0504030 [hep-ph] .

[32] C. Lorce *et al.*, JHEP **05**, 041 (2011), arXiv:1102.4704 [hep-ph] .

[33] J. C. Collins and A. Freund, Phys.Rev. **D59**, 074009 (1999), arXiv:hep-ph/9801262 [hep-ph] .

[34] V. Barone, F. Bradamante, and A. Martin, Prog. Part. Nucl. Phys. **65**, 267 (2010), arXiv:1011.0909 [hep-ph] .

[35] H. Gao *et al.*, Eur. Phys. J.Plus **126**, 1 (2011), arXiv:1009.3803 [hep-ph] .

[36] M. Anselmino *et al.*, Eur. Phys. J. **A47**, 35 (2011), arXiv:1101.4199 [hep-ex] .

[37] P. J. Mulders and R. D. Tangerman, Nucl. Phys. **B461**, 197 (1996), arXiv:hep-ph/9510301 .

[38] D. Boer and P. J. Mulders, Phys. Rev. **D57**, 5780 (1998), arXiv:hep-ph/9711485 .

[39] K. Goeke, A. Metz, and M. Schlegel, Phys. Lett. **B618**, 90 (2005), arXiv:hep-ph/0504130 [hep-ph] .

[40] X.-D. Ji, J.-P. Ma, and F. Yuan, Nucl. Phys. **B652**, 383 (2003), arXiv:hep-ph/0210430 [hep-ph] .

[41] A. Bacchetta *et al.*, JHEP **02**, 093 (2007), arXiv:hep-ph/0611265 .

[42] T. Donnelly and A. Raskin, Annals Phys. **169**, 247 (1986).

[43] A. Bacchetta, U. D'Alesio, M. Diehl, and C. A. Miller, Phys. Rev. **D70**, 117504 (2004), arXiv:hep-ph/0410050 [hep-ph] .

[44] A. Bravar (Spin Muon), Nucl. Phys. Proc. Suppl. **79**, 520 (1999).

[45] A. Airapetian *et al.* (HERMES), Phys. Rev. Lett. **84**, 4047 (2000), arXiv:hep-ex/9910062 .

[46] A. Airapetian *et al.* (HERMES), Phys. Rev. **D64**, 097101 (2001), arXiv:hep-ex/0104005 .

[47] H. Avakian *et al.* (CLAS), Phys. Rev. **D69**, 112004 (2004), arXiv:hep-ex/0301005 .

[48] H. Avakian and L. Elouadrhiri (CLAS), Phys. Part. Nucl. **35**, S114 (2004).

[49] A. Airapetian *et al.* (HERMES), Phys. Rev. Lett. **94**, 012002 (2005), arXiv:hep-ex/0408013 .

[50] A. Airapetian *et al.* (HERMES), Phys. Lett. **B693**, 11 (2010), arXiv:1006.4221 [hep-ex] .

[51] M. G. Alekseev *et al.* (COMPASS), Phys. Lett. **B692**, 240 (2010), arXiv:1005.5609 [hep-ex] .

[52] V. Y. Alexakhin *et al.* (COMPASS), Phys. Rev. Lett. **94**, 202002 (2005), arXiv:hep-ex/0503002 .

[53] A. Kotzinian (COMPASS), (2007), 10.3360/dis.2007.107, arXiv:0705.2402 [hep-ex] .

[54] X. Qian *et al.* (The Jefferson Lab Hall A), Phys. Rev. Lett. **107**, 072003 (2011), arXiv:1106.0363 [nucl-ex] .

[55] A. Airapetian *et al.* (HERMES), Phys. Lett. **B562**, 182 (2003), arXiv:hep-ex/0212039 .

[56] A. Airapetian *et al.* (HERMES), Phys. Lett. **B622**, 14 (2005), arXiv:hep-ex/0505042 .

[57] M. G. Alekseev, V. Y. Alexakhin, Y. Alexandrov, G. D. Alexeev, A. Amoroso, *et al.* (COMPASS), Eur. Phys. J. **C70**, 39 (2010), arXiv:1007.1562 [hep-ex] .

[58] H. Avakian *et al.* (CLAS), Phys. Rev. Lett. **105**, 262002 (2010), arXiv:1003.4549 [hep-ex] .

[59] M. Anselmino, M. Boglione, U. D'Alesio, A. Kotzinian, F. Murgia, *et al.*, Phys. Rev. **D75**, 054032 (2007), arXiv:hep-ph/0701006 [hep-ph] .

[60] M. Anselmino, M. Boglione, U. D'Alesio, A. Kotzinian, F. Murgia, *et al.*, Nucl. Phys. Proc. Suppl. **191**, 98 (2009), arXiv:0812.4366 [hep-ph] .

[61] M. Gockeler *et al.* (QCDSF Collaboration, UKQCD Collaboration), Phys. Lett. **B627**, 113 (2005), arXiv:hep-lat/0507001 [hep-lat] .

[62] M. E. Peskin and D. V. Schroeder, *An Introduction to quantum field theory* (Westview Press, 1995).

[63] R.-b. Meng, F. I. Olness, and D. E. Soper, Nucl. Phys. **B371**, 79 (1992).

[64] R. Meng, F. I. Olness, and D. E. Soper, Phys. Rev. **D54**, 1919 (1996), arXiv:hep-ph/9511311 [hep-ph] .

[65] P. M. Nadolsky, D. Stump, and C. Yuan, Phys. Rev. **D61**, 014003 (2000), arXiv:hep-ph/9906280 [hep-ph] .

[66] X.-D. Ji *et al.*, Phys. Lett. **B638**, 178 (2006), arXiv:hep-ph/0604128 [hep-ph] .

[67] X.-D. Ji, J.-p. Ma, and F. Yuan, Phys. Rev. **D71**, 034005 (2005), arXiv:hep-ph/0404183 [hep-ph] .

[68] J. C. Collins and A. Metz, Phys. Rev. Lett. **93**, 252001 (2004), arXiv:hep-ph/0408249 [hep-ph] .

[69] M. Alekseev *et al.* (COMPASS), Phys. Lett. **B660**, 458 (2008), arXiv:0707.4077 [hep-ex] .

[70] K. Ackerstaff *et al.* (HERMES Collaboration), Phys. Rev. Lett. **81**, 5519 (1998), arXiv:hep-ex/9807013 [hep-ex] .

[71] L. A. Linden-levy, *On Extracting Hadron Multiplicities And Unpolarized Nucleon Structure Ratios From SIDIS Data at the HERMES Experiment*, Ph.D. thesis, UIUC (2008).

[72] T. Navasardyan *et al.*, Phys. Rev. Lett. **98**, 022001 (2007), arXiv:hep-ph/0608214 [hep-ph] .

[73] H. Mkrtchyan, P. Bosted, G. Adams, A. Ahmidouch, T. Angelescu, *et al.*, Phys. Lett. **B665**, 20 (2008), arXiv:0709.3020 [hep-ph] .

[74] R. Asaturyan *et al.*, (2011), arXiv:1103.1649 [nucl-ex] .

[75] J. C. Collins, Nucl. Phys. **B396**, 161 (1993), arXiv:hep-ph/9208213 .

[76] S. Kretzer, Phys. Rev. **D62**, 054001 (2000), arXiv:hep-ph/0003177 [hep-ph] .

[77] D. de Florian, R. Sassot, and M. Stratmann, Phys. Rev. **D75**, 114010 (2007), arXiv:hep-ph/0703242 [HEP-PH] .

[78] A. V. Efremov, K. Goeke, and P. Schweitzer, Phys. Rev. **D73**, 094025 (2006), arXiv:hep-ph/0603054 [hep-ph] .

[79] M. Anselmino, M. Boglione, U. D'Alesio, A. Kotzinian, S. Melis, *et al.*, AIP Conf.Proc. **1149**, 465 (2009).

[80] J. Pumplin *et al.*, JHEP **07**, 012 (2002), arXiv:hep-ph/0201195 .

[81] A. Kotzinian, Nucl. Phys. **B441**, 234 (1995), arXiv:hep-ph/9412283 .

[82] J. Zhu and B.-Q. Ma, Phys. Lett. **B696**, 246 (2011).

[83] A. Bacchetta, AIP Conf.Proc. **1149**, 447 (2009), arXiv:0902.2712 [hep-ph] .

[84] A. Bacchetta *et al.*, Phys. Rev. Lett. **85**, 712 (2000), arXiv:hep-ph/9912490 [hep-ph] .

[85] S. Boffi, A. V. Efremov, B. Pasquini, and P. Schweitzer, Phys. Rev. **D79**, 094012 (2009), arXiv:0903.1271 [hep-ph] .

[86] M. Burkardt, Phys.Rev. **D62**, 071503 (2000), arXiv:hep-ph/0005108 [hep-ph] .

[87] M. Diehl and P. Hagler, Eur. Phys. J. **C44**, 87 (2005), arXiv:hep-ph/0504175 [hep-ph] .

[88] B. Pasquini and C. Lorce, (2010), sch, arXiv:1008.0945 [hep-ph] .

[89] B. Pasquini and C. Lorce, in *GPD workshop at Trento*, edited by a (2010).

[90] P. Hagler *et al.*, Europhys. Lett. **88**, 61001 (2009), arXiv:0908.1283 [hep-lat] .

[91] B. Pasquini, S. Boffi, and P. Schweitzer, Mod. Phys. Lett. **A24**, 2903 (2009), arXiv:0910.1677 [hep-ph] .

[92] B. U. Musch, P. Hagler, J. W. Negele, and A. Schafer, Phys. Rev. **D83**, 094507 (2011), arXiv:1011.1213 [hep-lat] .

[93] R. Jakob, P. Mulders, and J. Rodrigues, Nucl. Phys. **A626**, 937 (1997), arXiv:hep-ph/9704335 [hep-ph] .

[94] B. Pasquini, S. Cazzaniga, and S. Boffi, Phys. Rev. **D78**, 034025 (2008), arXiv:0806.2298 [hep-ph] .

[95] A. Kotzinian, (2008), arXiv:0806.3804 [hep-ph] .

[96] A. V. Efremov, P. Schweitzer, O. V. Teryaev, and P. Zavada, Phys. Rev. **D80**, 014021 (2009), arXiv:0903.3490 [hep-ph] .

[97] H. Avakian, A. V. Efremov, P. Schweitzer, and F. Yuan, Phys. Rev. **D81**, 074035 (2010), arXiv:1001.5467 [hep-ph] .

[98] A. V. Efremov *et al.*, J. Phys. Conf. Ser. **295**, 012052 (2011), arXiv:1101.4035 [hep-ph] .

[99] A. Bacchetta *et al.*, Eur. Phys. J. **A45**, 373 (2010), arXiv:1003.1328 [hep-ph] .

[100] S. J. Brodsky and F. Yuan, Phys. Rev. **D74**, 094018 (2006), arXiv:hep-ph/0610236 .

[101] C. Lorce and B. Pasquini, (2011), arXiv:1104.5651 [hep-ph] .

[102] E. Di Salvo, Int. J. Mod. Phys. **A18**, 5277 (2003), arXiv:hep-ph/0207089 [hep-ph] .

[103] E. Di Salvo, Mod. Phys. Lett. **A22**, 1787 (2007), arXiv:hep-ph/0607184 [hep-ph] .

[104] E. Di Salvo, (2008), arXiv:0804.3545 [hep-ph] .

[105] A. M. Kotzinian and P. J. Mulders, Phys. Rev. **D54**, 1229 (1996), arXiv:hep-ph/9511420 .

[106] A. Kotzinian, B. Parsamyan, and A. Prokudin, Phys. Rev. **D73**, 114017 (2006), arXiv:hep-ph/0603194 [hep-ph] .

[107] A. Prokudin, (private communication).

[108] K. Goeke, A. Metz, P. Pobylitsa, and M. Polyakov, Phys. Lett. **B567**, 27 (2003), arXiv:hep-ph/0302028 [hep-ph] .

[109] A. Metz *et al.*, Phys. Lett. **B680**, 141 (2009), arXiv:0810.5212 [hep-ph] .

[110] U. D'Alesio, E. Leader, and F. Murgia, Phys. Rev. **D81**, 036010 (2010), arXiv:0909.5650 [hep-ph] .

[111] S. Wandzura and F. Wilczek, Phys. Lett. **B72**, 195 (1977).

[112] H. Avakian *et al.*, Phys. Rev. **D77**, 014023 (2008), arXiv:0709.3253 [hep-ph] .

[113] A. Accardi, A. Bacchetta, W. Melnitchouk, and M. Schlegel, JHEP **11**, 093 (2009), arXiv:0907.2942 [hep-ph] .

[114] A. Bacchetta, F. Conti, and M. Radici, Phys. Rev. **D78**, 074010 (2008), arXiv:0807.0323 [hep-ph] .

[115] A. Bacchetta, D. Boer, M. Diehl, and P. J. Mulders, JHEP **0808**, 023 (2008), arXiv:0803.0227 [hep-ph] .

[116] B. Musch, in *XIX International Workshop on Deep-Inelastic Scattering and Related Subjects (DIS 2011)* (2011).

[117] D. Boer, L. Gamberg, B. Musch, and A. Prokudin, (2011), arXiv:1107.5294 [hep-ph] .

[118] B. Parsamyan (COMPASS), Eur. Phys. J.ST **162**, 89 (2008), arXiv:0709.3440 [hep-ex] .

[119] B. Parsamyan, J. Phys. Conf. Ser. **295**, 012046 (2011), arXiv:1012.0155 [hep-ex] .

[120] L. L. Pappalardo, M. Diefenthaler, and f. t. H. Collaboration, (2011), arXiv:1107.4227 [hep-ex] .

[121] L. Pappalardo, in *XIX International Workshop on Deep-Inelastic Scattering and Related Subjects (DIS 2011)* (2011).

[122] C. Sinclair *et al.*, Phys. Rev. ST Accel. Beams **10**, 023501 (2007).

[123] D. Androic *et al.* (G0), Nucl. Instrum. Meth. **A646**, 59 (2011), arXiv:1103.0761 [nucl-ex] .

[124] J. Alcorn *et al.*, Nucl. Instrum. Meth. **A522**, 294 (2004).

[125] F. Gross, J.Phys.Conf.Ser. **299**, 012001 (2011).

[126] C. Leemann, D. Douglas, and G. Krafft, Ann. Rev. Nucl. Part. Sci. **51**, 413 (2001).

[127] X. Zheng, *Precision measurement of the neutron spin asymmetry A_1^n at large x_{Bj} using CEBAF at 5.7 GeV*, Ph.D. thesis, Massachusetts Institute of Technology (2002).

[128] A. Saha, "Arc Energy Measurement," Hall A Elog 249350 (2008), http://hallaweb.jlab.org/halog/log/html/0811_archive/081117103234.html.

[129] X. Zhan, *High Precision Measurement of the Proton Elastic Form Factor Ratio at Low Q^2*, Ph.D. thesis, Massachusetts Institute of Technology (2010), arXiv:1108.4441 [nucl-ex] .

[130] K. Unser, IEEE Trans. Nucl. Sci. **28**, 2344 (1981).

[131] X. Qian, *Measurement of Single Target-Spin Asymmetry in Semi-Inclusive $n^{\uparrow}(e, e'\pi^{+/-})$ Reaction on a Transversely Polarized ^{3}He Target*, Ph.D. thesis, Duke University (2010).

[132] W. Barry *et al.*, *JLab-TN-91-087*, Tech. Rep. (Jefferson Lab, 1991).

[133] M. Baylac, E. Burtin, C. Cavata, S. Escoffier, B. Frois, *et al.*, Phys.Lett. **B539**, 8 (2002), arXiv:hep-ex/0203012 [hep-ex] .

[134] D. Parno, M. Friend, F. Benmokhtar, G. Franklin, R. Michaels, *et al.*, J.Phys.Conf.Ser. **312**, 052018 (2011), arXiv:1106.4851 [physics.ins-det] .

[135] E.Chudakov, O.Glamazdin, *et al.*, "the Møller Polarimeter," Website, uRL: http://hallaweb.jlab.org/equipment/beam/beampol/beampolar.html, Old URL: http://www.jlab.org/~moller.

[136] Z.-E. Meziani, "Shift Summary, December 9,2008," Hall A Elog 252602 (2008), http://hallaweb.jlab.org/halog/log/html/0812_archive/081209000139.html.

[137] D. de Lange, H. Blok, D. Boersma, T. Botto, P. Heimberg, *et al.*, Nucl.Instrum.Meth. **A412**, 254 (1998).

[138] D. de Lange, J. Steijger, H. de Vries, M. Anghinolfi, M. Taiuti, *et al.*, Nucl.Instrum.Meth. **A406**, 182 (1998).

[139] R. W. Chan, "Construction and Characterization of Multi-wire Drift Chamber," Master Thesis, University of Virginia (2005).

[140] K. C. Allada, *Measurement of Single Spin Asymmetries in Semi-Inclusive Deep Inelastic Scattering Reaction* $n^{\uparrow}(e, e'\pi^{+})$ *at Jefferson Lab*, Ph.D. thesis, University of Kentucky (2010).

[141] A. Kolarkar, *Precision Measurements of the Neutron Electric Form Factor at High Momentum Transfers*, Ph.D. thesis, University of Kentucky (2008).

[142] K. Fissum, W. Bertozzi, J.-P. Chen, D. Dale, H. C. Fenker, *et al.*, Nucl.Instrum.Meth. **A474**, 108 (2001).

[143] Y. Qiang, *Search for Pentaquark Partners* Θ^{++}, Σ^{0} *and* N^{0} *in* $H\,(e,\, e'K(\pi))\,X$ *reactions at Jefferson Lab Hall A*, Ph.D. thesis, Massachusetts Institute of Technology (2007).

[144] M. Iodice, E. Cisbani, S. Colilli, R. Crateri, S. Frullani, *et al.*, Nucl.Instrum.Meth. **A411**, 223 (1998).

[145] C. Dutta, *Measurement of Single Target-Spin Asymmetry in the Electrproduction of Negative Pions in The Semi-Inclusive Deep Inelastic Reaction* $n^{\uparrow}(e, e'\pi^{-})$ *on a Transversely Polarized* ^{3}*He Target*, Ph.D. thesis, University of Kentucky (2010).

[146] E. Cisbani, S. Colilli, F. Cusanno, S. Frullani, R. Fratoni, *et al.*, , 36 (2005).

[147] "The coda data acuisition system," Jefferson Lab Data Acquisition Group, http://coda.jlab.org.

[148] "Experimental physics and industrial control system," Website, `http://www.aps.anl.gov/epics/`.

[149] F. R. P. Bissey, V. A. Guzey, M. Strikman, and A. W. Thomas, Phys. Rev. **C65**, 064317 (2002), arXiv:hep-ph/0109069 .

[150] Y. Qiang, AIP Conf.Proc. **1182**, 864 (2009).

[151] X. Zheng *et al.* (Jefferson Lab Hall A Collaboration), Phys. Rev. Lett. **92**, 012004 (2004), arXiv:nucl-ex/0308011 [nucl-ex] .

[152] B. Blankleider and R. Woloshyn, Phys. Rev. **C29**, 538 (1984).

[153] J. L. Friar, B. Gibson, G. Payne, A. Bernstein, and T. Chupp, Phys. Rev. **C42**, 2310 (1990).

[154] J. Singh *et al.*, AIP Conf. Proc. **1149**, 823 (2009).

[155] G. Breit and I. I. Rabi, Phys. Rev. **38**, 2082 (1931).

[156] M. V. Romalis, *Laser polarized He-3 target used for a precision measurement of the neutron spin structure*, a, Princeton University (1997).

[157] W. HAPPER, Rev. Mod. Phys. **44**, 169 (1972).

[158] W. Happer *et al.*, (2001), U.S. Patent No. 6,318,092.

[159] E. Babcock *et al.*, Phys. Rev. Lett. **91**, 123003 (2003).

[160] M. A. Bouchiat, T. R. Carver, and C. M. Varnum, Phys. Rev. Lett. **5**, 373 (1960).

[161] T. G. Walker, Phys. Rev. A **40**, 4959 (1989).

[162] B. Chann, E. Babcock, L. W. Anderson, and T. G. Walker, Phys. Rev. A **66**, 032703 (2002).

[163] A. Ben-Amar Baranga, S. Appelt, M. V. Romalis, C. J. Erickson, A. R. Young, G. D. Cates, and W. Happer, Phys. Rev. Lett. **80**, 2801 (1998).

[164] E. Babcock, Ph.D. thesis, University of Wisconsin (2005).

[165] W. C. Chen, T. R. Gentile, T. G. Walker, and E. Babcock, Phys. Rev. A **75**, 013416 (2007).

[166] "UVA Spin Physics Group," `http://galileo.phys.virginia.edu/research/groups/spinphysics/`.

[167] "Polarized Helium-3 Target Lab at The College of William & Mary," .

[168] Y. Zhang, "He-3 cell wall thickness and density measurements," (), e06-010 Internal Analysis Communications.

[169] K. Allada *et al.* (E06-010), *Analysis Note on the Hall-A Neutron Transversity Experiment (E06-010)*, Tech. Rep. (E06-010 Collaboration, 2011).

[170] "Selected list of glass properties," Webpage at UVa Spin Physics Group, http://galileo.phys.virginia.edu/research/groups/spinphysics/glass_properties.html.

[171] C. Chen and Z. Zhao, "thickness of the wall for the cell named hamlet is: 0.0641±0.00052inch," Private Communication.

[172] Z. Zhao, J. Liu, *et al.*, *Measurement of Transfer Tube Wall Thickness*, Tech. Rep. (Jefferson Lab, 2011).

[173] A. M. Kelleher, *A measurement of the neutron electric form factor at very large momentum transfer using polarized electrons scattering from a polarized ^3He target*, Ph.D. thesis, The College of William and Mary (2010).

[174] S. Choi, X. Jiang, Z. E. Meziani, B. Sawatzky, *et al.*, "JLab E6-014 : Precision Measurements of the Neutron dc: Towards the Electric XE and Magnetic XB Color Polarizabilities," (2006).

[175] S. Gilad, D. Higinbotham, W. Korsch, B. Norum, S. Sirca, *et al.*, "JLab E05-102 : Measurements of A_x and A_z Asymmetries in the Quasi-elastic ^{3}He$(e, e'D)$ Reaction," (2005).

[176] J. Huang, Y. Qiang, and C. Dutta, in *Hall A Weekly Meeting, Sept 16* (2008).

[177] A. Abragam, *Principles of Nuclear Magnetism* (Oxford University Press, 1961).

[178] D. J. Griffiths, *Introduction to Quantum Mechanics* (Pearson Prentice Hall, 2005).

[179] M. V. Romalis and G. D. Cates, Phys. Rev. A **58**, 3004 (1998).

[180] E. Arimondo, M. Inguscio, and P. Violino, Rev. Mod. Phys. **49**, 31 (1977).

[181] J. Emsley, *The Elements, Oxford Chemistry Guides* (Oxford Univ. Press, 1995).

[182] E. Babcock, I. A. Nelson, S. Kadlecek, and T. G. Walker, Phys. Rev. A **71**, 013414 (2005).

[183] J. Singh, A. M. Kelleher, and P. H. Solvignon, *Polarization Gradients in A Two Chambered Cell*, Tech. Rep. (University of Virginia, 2008) version 2.00.

[184] Q. Ye, G. Laskaris, H. Gao, W. Chen, W. Zheng, *et al.*, Eur. Phys. J. **A44**, 55 (2010), arXiv:0911.3647 [nucl-ex] .

[185] P. Dolph, J. Singh, *et al.*, "Gas dynamics in high-luminosity polarized ^{3}He targets using diffusion and convection," In preparation.

[186] J. Kestin *et al.*, J. Phys. Chem. Ref. Data **13**, 229 (1984).

[187] N. R. Newbury, A. S. Barton, G. D. Cates, W. Happer, and H. Middleton, Phys. Rev. A **48**, 4411 (1993).

[188] Y. Zhang, "Private Communications," ().

[189] G. D. Cates, D. J. White, T.-R. Chien, S. R. Schaefer, and W. Happer, Phys. Rev. A **38**, 5092 (1988).

[190] G. Cates, S. Schaefer, and W. Happer, Phys.Rev. **A37**, 2877 (1988).

[191] V. A. Pedroni, *Digital Electronics and Design with VHDL* (Morgan Kaufmann, 2008).

[192] Hall A Collaboration, "ROOT/C++ Analyzer for Hall A," website, http://hallaweb.jlab.org/podd/index.html.

[193] I. Antcheva, M. Ballintijn, B. Bellenot, M. Biskup, R. Brun, *et al.*, Comput.Phys.Commun. **182**, 1384 (2011).

[194] J. Huang, "Hrs optics optimizer reference guide," website (2009), http://www.jlab.org/ jinhuang/HRSOptics.

[195] Y. Wang, *Measurement of Target Single-Spin Asymmetry in Charged Kaon Electroproduction on a Transversely Polarized ^{3}He Target*, Ph.D. thesis, University of Illinois at Urbana-Champaign (2011).

[196] N. Liyanage, *Optics Calibration of the Hall A High Resolution Spectrometers using the C Optimizer*, Technote JLAB-TN-02-012 (Jefferson Lab, 2002) http://hallaweb.jlab.org/publications/Technotes/files/2002/02-012.pdf.

[197] "Minuit2 minimization package," website, `http://seal.web.cern.ch/seal/MathLibs/Minuit2/html/`.

[198] J. Huang, *Transversity Analysis Log 173*, Tech. Rep. (Jefferson Lab, 2009).

[199] R. Mankel, Rept. Prog. Phys. **67**, 553 (2004), arXiv:physics/0402039 [physics] .

[200] D. de Florian, R. Sassot, and M. Stratmann, Phys. Rev. **D76**, 074033 (2007), arXiv:0707.1506 [hep-ph] .

[201] M. Anselmino, M. Boglione, U. D'Alesio, A. Kotzinian, F. Murgia, *et al.*, Phys. Rev. **D71**, 074006 (2005), arXiv:hep-ph/0501196 [hep-ph] .

[202] M. Anselmino, M. Boglione, U. D'Alesio, A. Kotzinian, F. Murgia, *et al.*, Phys. Rev. **D72**, 094007 (2005), arXiv:hep-ph/0507181 [hep-ph] .

[203] E. Chudakov, "COMGEANT simulation at JLab," Http://www.jlab.org/ gen/simul/.

[204] D. E. Wiser, Ph.D. thesis, Univ. of Wisconsin (1997).

[205] L. Whitlow, *DEEP INELASTIC STRUCTURE FUNCTIONS FROM ELECTRON SCATTERING ON HYDROGEN, DEUTERIUM, AND IRON AT 0.6-GeV**2 <= Q**2 <= 30-GeV**2*, Ph.D. thesis (1990), ph.D. Thesis.

[206] J. Gomez, R. Arnold, P. E. Bosted, C. Chang, A. Katramatou, *et al.*, Phys.Rev. **D49**, 4348 (1994).

[207] A. Airapetian *et al.* (HERMES Collaboration), Nucl. Phys. **B780**, 1 (2007), arXiv:0704.3270 [hep-ex] .

[208] A. Accardi, V. Muccifora, and H.-J. Pirner, Nucl. Phys. **A720**, 131 (2003), arXiv:nucl-th/0211011 [nucl-th] .

[209] J. M. Grames *et al.*, Phys. Rev. ST Accel. Beams **7**, 042802 (2004).

[210] A. Amroun, V. Breton, J. Cavedon, B. Frois, D. Goutte, *et al.*, Nucl. Phys. **A579**, 596 (1994).

[211] M. Salomaa and H. Enge, Nuclear Instruments and Methods **145**, 279 (1977).

[212] A. Raskin and T. Donnelly, Annals Phys. **191**, 78 (1989).

[213] J. Katich, "EPR measurement," Hall A Elog 246458 (2008), `http://hallaweb.jlab.org/halog/log/html/0811_archive/081103141754.html`.

[214] Z. Ye, "NMR Measurement," Hall A Elog 246537 (2008), `http://hallaweb.jlab.org/halog/log/html/0811_archive/081103233859.html`.

[215] T. Averett, J. P. Chen, X. Jiang, *et al.*, "JLab E05-015 : Measurement of the Target Single-Spin Asymmetry in Quasi-Elastic $^3He(e,e')$," (2005).

[216] D. Parno, (private communication).

[217] G. Jin, (private communication).

[218] D. McNulty, "parity daq charge asymmetry," Hall A Elog 233758 (2008), `http://hallaweb.jlab.org/halog/log/html/0804_archive/080422105339.html`.

[219] E. Chudakov, "Charge asymmetry with Moller," Hall A Elog 233824 (2008), `http://hallaweb.jlab.org/halog/log/html/0804_archive/080422213153.html`.

[220] X. Deng, "sign check for new helicity board," Hall A Elog 297779 (2009), http://hallaweb.jlab.org/halog/log/html/0911_archive/091106095520.html.

[221] O. Glamazdin, "Moller sign check for new helicity board," Hall A Elog 297819 (2009), http://hallaweb.jlab.org/halog/log/html/0911_archive/091106134704.html.

[222] X. Zheng *et al.* (Jefferson Lab Hall A Collaboration), Phys. Rev. **C70**, 065207 (2004), arXiv:nucl-ex/0405006 [nucl-ex] .

[223] P. Bosted, R. Ent, and H. Mkrtchyan, "JLab E12-06-104 : Measurement of the Ratio R=sigmaL/sigmaT in Semi-Inclusive Deep-Inelastic Scattering," (2006).

[224] K. Abe *et al.* (E143 Collaboration), Phys. Lett. **B452**, 194 (1999), arXiv:hep-ex/9808028 [hep-ex] .

[225] J. Blumlein and H. Bottcher, Nucl. Phys. **B841**, 205 (2010), arXiv:1005.3113 [hep-ph] .

[226] I. Akushevich *et al.*, Comput. Phys. Commun. **104**, 201 (1997), arXiv:hep-ph/9706516 .

[227] T. Sjostrand, S. Mrenna, and P. Z. Skands, JHEP **0605**, 026 (2006), arXiv:hep-ph/0603175 [hep-ph] .

[228] A. Airapetian *et al.* (HERMES), Phys. Rev. Lett. **103**, 152002 (2009), arXiv:0906.3918 [hep-ex] .

[229] H. Avakian and L. Elouadrhiri (CLAS Collaboration), , 228 (2004).

[230] J. Huang *et al.* (Jefferson Lab Hall A Collaboration), (2011), submitted to Phys. Rev. Lett., ©American Physical Society, arXiv:1108.0489 [nucl-ex] .

[231] C. Ciofi degli Atti, S. Scopetta, E. Pace, and G. Salme, Phys. Rev. **C48**, 968 (1993), arXiv:nucl-th/9303016 [nucl-th] .

[232] A. Nogga, Ph.D. thesis, Ruhr-Universität Bochum, Bochum, Germany (2001).

[233] J. P. Chen, H. Gao, X. Jiang, J. Peng, X. Qian, *et al.*, "JLab E12-10-006 : Target Single Spin Asymmetry in Semi-Inclusive Deep-Inelastic Electro Pion Production on a Trasversely Polarized ^{3}He Target at 8.8 and 11 GeV, An update to PR12-09-014," (2010).

[234] J. P. Chen, J. Huang, Y. Qiang, W. Yan, and et al, "JLab E12-11-007 : Asymmetries in Semi-Inclusive Deep-Inelastic $(e, e'\pi^{\pm})$ Reactions on a Longitudinally Polarized ^{3}He Target at 8.8 and 11 GeV," (2011).

[235] A. Efremov, K. Goeke, and P. Schweitzer, Phys.Rev. **D67**, 114014 (2003), arXiv:hep-ph/0208124 [hep-ph] .

[236] H. Avakian, P. Bosted, K. Griffioen, K. Hafidi, P. Rossi, and et al, "JLab E12-07-107 : Studies of Spin-Orbit Correlations with Longitudinally Polarized Target," (2007).

[237] L. L. Frankfurt *et al.*, Phys. Lett. **B230**, 141 (1989).

[238] K. Allada, J. P. Chen, H. Gao, Z. Meziani, *et al.*, "JLab E12-11-108 : Target Single Spin Asymmetries in Semi-Inclusive Deep-Inelastic $(e, e'\pi^{\pm})$ Reactions on a Transversely Polarized Proton Target," (2011).

[239] P. Souder *et al.*, "JLab E12-10-007 : Precision Measurement of Parity-Violation in Deep Inelastic Scattering Over a Broad Kinematic Range," (2010).

[240] M. Anselmino *et al.*, Phys. Rev. **D74**, 074015 (2006), arXiv:hep-ph/0608048 [hep-ph] .

[241] H. Avakian *et al.*, Phys. Rev. Lett. **99**, 082001 (2007), arXiv:0705.1553 [hep-ph] .

[242] M. Ungaro *et al.*, "GEMC (GEant4 Monte-Carlo) framework," Website, `https://gemc.jlab.org/`.

[243] M. Altunbas, M. Capeans, K. Dehmelt, J. Ehlers, J. Friedrich, *et al.*, Nucl.Instrum.Meth. **A490**, 177 (2002).

[244] Y. Wang, J.-B. Wang, Q. Yan, Y.-J. Li, J.-P. Cheng, *et al.*, Chin.Phys. **C33**, 374 (2009).

[245] G. Atoian *et al.*, Nucl. Instrum. Meth. **A584**, 291 (2008), arXiv:0709.4514 [physics.ins-det] .

[246] "Trigger and DAq Electronics for 12GeV," Webpage, fast Electronics Group at Jefferson Lab.

[247] J. She, J. Zhu, and B.-Q. Ma, Phys. Rev. **D79**, 054008 (2009), arXiv:0902.3718 [hep-ph] .

[248] J. Collins, A. V. Efremov, K. Goeke, S. Menzel, A. Metz, *et al.*, Phys. Rev. **D73**, 014021 (2006), arXiv:hep-ph/0509076 [hep-ph] .

[249] P. Schweitzer, T. Teckentrup, and A. Metz, Phys. Rev. **D81**, 094019 (2010), arXiv:1003.2190 [hep-ph] .

[250] National Institute of Standards and Technology, "Stopping-power and range tables for electrons," website, `http://physics.nist.gov/PhysRefData/Star/Text/ESTAR.html`.

[251] H. Avagyan, M. Contalbrigo, K. Joo, Z. E. Meziani, B. Seitz, and et al, "JLab E12-09-009 : Studies of Spin-Orbit Correlations in Kaon Electroproduction in DIS with polarized hydrogen and deuterium targets," (2009).

[252] D. Besset, B. Favier, L. Greeniaus, R. Hess, C. Lechanoine, *et al.*, Nucl. Instrum. Meth. **166**, 515 (1979).